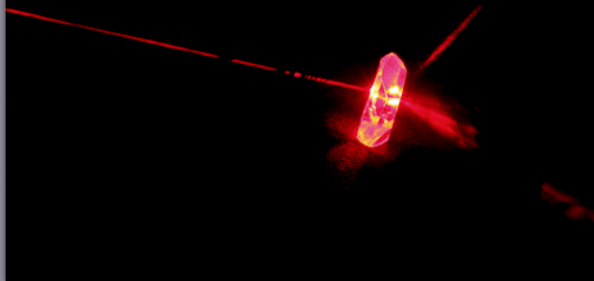


DE GRUYTER

*Theo Woike,
Dominik Schaniel (Eds.)*

STRUCTURES ON DIFFERENT TIME SCALES



Copyright 2018. De Gruyter. All rights reserved. May not be reproduced in any form without permission from the publisher, except fair uses permitted under U.S. or applicable copyright law.



Theo Woike and Dominik Schaniel (Eds.)
Structures on Different Time Scales

Also of Interest



Multiscale Materials Modeling. Approaches to Full Multiscaling

Siegfried Schmauder, Immanuel Schäfer (Eds.), 2016
ISBN 978-3-11-041236-9, e-ISBN (PDF) 978-3-11-041245-1,
e-ISBN (EPUB) 978-3-11-041251-2



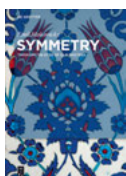
Superconductors at the Nanoscale. From Basic Research to Applications

Roger Würdenweber, Victor Moshchalkov, Simon Bending,
Francesco Tafuri (Eds.), 2017
ISBN 978-3-11-045620-2, e-ISBN (PDF) 978-3-11-045680-6,
e-ISBN (EPUB) 978-3-11-045624-0



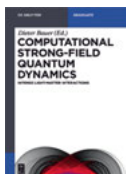
Multi-Component Crystals. Synthesis, Concepts, Function

Edward R. T. Tiekink, Julio Zukerman-Schpector (Eds.), 2017
ISBN 978-3-11-046365-1, e-ISBN (PDF) 978-3-11-046495-5,
e-ISBN (EPUB) 978-3-11-046495-5



Symmetry. Through the Eyes of Old Masters

Emil Makovicky, 2016
ISBN 978-3-11-041705-0, e-ISBN (PDF) 978-3-11-041714-2,
e-ISBN (EPUB) 978-3-11-041719-7



Computational Strong-Field Quantum Dynamics. Intense Light-Matter Interactions

Dieter Bauer (Eds.), 2017
ISBN 978-3-11-041725-8, e-ISBN (PDF) 978-3-11-041726-5,
e-ISBN (EPUB) 978-3-11-041934-4

Structures on Different Time Scales



Edited by
Theo Woike and Dominik Schaniel

DE GRUYTER

Physics and Astronomy Classification Scheme 2010

Primary: 61.05.C; Secondary: 31.15.E

Editors

Prof. Dr Theo Woike
TU Dresden
Institute of Structural Physics
Zellescher Weg 16
01069 Dresden
Germany
theo.woike@tu-dresden.de

Prof. Dr Dominik Schaniel
Université de Lorraine
Laboratoire de Cristallographie,
Résonance Magnétique et Modélisations
(CRM2 – UMR UL-CNRS 7036)
BP 70239 Boulevard des Aiguillettes
54506 Vandoeuvre les Nancy
France
dominik.schaniel@univ-lorraine.fr

ISBN 978-3-11-044209-0

e-ISBN (PDF) 978-3-11-043392-0

e-ISBN (EPUB) 978-3-11-043390-6

Library of Congress Cataloging-in-Publication Data

A CIP catalog record for this book has been applied for at the Library of Congress.

Bibliographic information published by the Deutsche Nationalbibliothek

The Deutsche Nationalbibliothek lists this publication in the Deutsche Nationalbibliografie; detailed bibliographic data are available on the Internet at <http://dnb.dnb.de>.

© 2018 Walter de Gruyter GmbH, Berlin/Boston

Typesetting: VTeX UAB, Lithuania

Printing and binding: CPI books GmbH, Leck

Cover image: Emmanuel Wenger, CRM2, Laboratoire de Cristallographie, Vandoeuvre les Nancy, France

☉ Printed on acid-free paper

Printed in Germany

www.degruyter.com

This book is dedicated to Niels K. Hansen

Contents

List of Contributors — IX

Dominik Schaniel and Theo Woike

Introduction — 1

Reinhard B. Neder

Static structural analysis of condensed matter: from single-crystal to amorphous — 13

Karlheinz Schwarz and Peter Blaha

DFT calculations of solids in the ground state — 67

Valerio Olevano

TDDFT, excitations, and spectroscopy — 101

Sébastien Pillet

Time-resolved structural analysis: probing condensed matter in motion — 143

Bruce D. Patterson

Ultrafast science — 221

Index — 269

List of Contributors

Prof. Dr Reinhard B. Neder

FAU Erlangen-Nürnberg
Department of Condensed Matter Physics
Staudstrasse 3
D-91058 Erlangen
Germany
reinhard.neder@fau.de

Prof. Dr Karlheinz Schwarz

Institut für Materialchemie
Technische Universität Wien
A-1060 Vienna
Getreidemarkt 9
Austria
kschwarz@theochem.tuwien.ac.at

Prof. Dr Peter Blaha

Institut für Materialchemie
Technische Universität Wien
A-1060 Vienna
Getreidemarkt 9
Austria
peter.blaha@tuwien.ac.at

Dr Valerio Olevano

Institut NEEL, CNRS, Grenoble, France
and
ETSF, European Theoretical Spectroscopy Facility
25 rue des Martyrs BP 166
38042 Grenoble cedex 9
France
valerio.olevano@grenoble.cnrs.fr

Dr Sébastien Pillet

CNRS
Laboratoire de Cristallographie, Résonance
Magnétique et Modélisations (CRM2 – UMR
UL-CNRS 7036)
Boulevard des aiguillettes, BP 70239
54506 Vandoeuvre les Nancy
France
sebastien.pillet@univ-lorraine.fr

Prof. Dr Bruce D. Patterson

Advanced Analytical Technologies
Empa Materials Science and Technology
Ueberlandstrasse 129
CH-8600 Dübendorf
Switzerland
bruce.patterson@bluewin.ch

Dominik Schaniel and Theo Woike

Introduction

Keywords: structure analysis, X-ray diffraction, electron density

1 Motivation and history

The purpose of this book is to provide an introduction into the field of time-resolved structural analysis. To this end, the fundamental notions of structural analysis and the concept of density functional theory and its extension to include time-dependent effects, i.e., excited nonequilibrium states, will be outlined, followed by a description of various techniques to determine structures of excited systems with life times in the range of femtoseconds to seconds. Further, the different diffraction patterns that can be expected upon various types of excitation from the ground state will be discussed and illustrated with examples. The possibilities opened by the X-ray free-electron laser, due to its extremely short and intense X-ray pulses, and a description of its operating principle conclude the topic.

The desire and necessity for following the movements of atoms in space and time have grown since the discovery of structure analysis by diffraction methods. The standard static structure analysis reveals the structural organization of the relaxed ground-state configuration with high precision. It is of considerable interest to know the structural configurations of excited nonequilibrium states to identify the changes in atomic distances relevant for the observed material properties. To be able to follow the atomic movements in time, one needs external sources for excitation that are synchronized with the X-ray source. Furthermore, the extension of structural analysis to the fourth dimension required significant developments of X-ray sources, X-ray detectors, and overall stability of the instruments.

The structure determination by X-ray diffraction is a success story, enabling much of our today's understanding of matter. An excellent review on this topic – covering up to the 1960s and highlighting the interplay between methodical, instrumental, and theoretical advances – has been given by Buerger in *Historical Atlas of Crystallography* [1]. With the development of ever more brilliant X-ray sources and faster two-dimensional X-ray detectors, the variable time became then accessible for structure determination in the second half of the twentieth century and is culminating today in the developments around the X-ray Free-Electron Lasers (XFELs) making time resolutions of a few femtoseconds or even beyond accessible. We shall give here only a brief recapitulation of the major steps and developments made toward time-resolved diffraction. A first phase of developments covers the period 1940–1975, and a short review on the historical development has been given by Green [2]. Starting as early

<https://doi.org/10.1515/9783110433920-001>

as 1942, Tsukerman and Avdeenko and one year later Altshuler reported the photographic recording of Laue diffraction patterns from aluminum single crystals with millisecond exposure times [3] and from steel samples with exposure times of 10^{-5} s [4]. In the 1950s, Schall [5, 6] and Schaaffs [7–9] developed experimental setups allowing for measurements with exposure times of 10^{-6} s. In 1966, Zavada and coworkers reached time resolutions of 10^{-7} s [10]. The subsequent development was mainly driven by the studies of shock-wave compressed materials, especially by Johnson and coworkers, who reached time resolutions of about 20 ns [11] (see also Whitlock and Wark [12]). During this first period, the development of X-ray flash techniques was important for the advancement of the experimental possibilities (see, e.g., review by Germer [13]). In the following period the instrumental developments of laser plasma sources [14] and the arrival of synchrotron radiation for X-ray diffraction [15] enabled major advancements. Among the first time-resolved diffraction experiments with synchrotron radiation sources, there was the study of the molecular mechanism responsible for muscle contraction with a time resolution in the range of 10^{-2} s [16–18]. Studies of laser heated crystals were also conducted at synchrotron sources with time resolutions of the order of 10^{-9} s [19]. Similarly, in the case of laser-plasma X-ray sources, first applications included time-resolved studies of biological samples with a time resolution of 10^{-9} s [20]. Furthermore, these laser-plasma X-ray sources allowed for straightforward synchronization between the X-ray pulse and the laser pulse, which, on the one hand, excites the sample under study and, on the other hand, generates the X-ray pulse via the laser-produced plasma. Consequently, studies of laser-heated crystals with time resolutions of 10^{-9} s were conducted, and the potential for increased time resolution by using shorter laser pulses was immediately recognized [21]. Following this line, soon picosecond ($5 \cdot 10^{-11}$ s) time-resolved X-ray diffraction studies were performed on laser-heated materials using laser plasma sources [22]. Shortly after, also femtosecond X-ray pulses were available [23], and corresponding X-ray diffraction studies were performed with a time resolution of about 10^{-13} s, e.g., on laser-heated organic films [24]. Using synchrotron radiation, time resolutions of a few tens of picoseconds were possible corresponding to the length of the electron bunches. Through combination with a streak camera, time resolutions around 10^{-12} s were achieved [25], and finally using laser slicing techniques, time resolutions of 10^{-13} s were obtained [26]. The latest developments yielding the highest time resolutions are made using XFELs, where pulses of only a few femtoseconds can be produced, and maybe in the near future even subfemtosecond time resolution can be expected [27–29]. The resolution accessible by attosecond pulses is actually needed to distinguish unambiguously between electronic excitation and nuclear motion, since, e.g., the hydrogen atom oscillation is in the range of 10 fs. Along with the high temporal resolution, the short X-ray pulses provide also extremely high intensities. Due to the high number of photons, even weak scattering processes can be investigated, and moreover nonlinear phenomena can be created, studied, and technologically exploited. For example, the wave mixing be-

tween an X-ray wave and a tunable wave in the optical spectrum [30] yields a spectral variability of X-ray frequencies with exceptionally high resolution.

2 About the book

This book is organized in five chapters, which can be separately studied. The reader is supposed to be familiar with the basic concepts of crystallography; however, all important notions will be detailed or illustrated via examples. We restrict ourselves to X-rays and X-ray diffraction. Concerning the developments made in time-resolved electron diffraction, we refer the reader to the book by Zewail [31].

We start the introduction to the topic with a survey on structural analysis from crystalline to amorphous materials, which illustrates to what extent and to which precision static structure determination is nowadays possible. R. Neder discusses these details explicitly on the example of atomic composition of nanoparticles using the pair distribution function (PDF) after a short outline of the structure analysis on crystalline materials.

K. Schwarz and P. Blaha discuss the quality that can be obtained by DFT calculations of the relaxed ground state, illustrated exemplarily on the example of BaBiO_3 using their program package Wien2k. More generally, they introduce the method of density functional theory through several examples, discuss the approximations that are made for the different functionals, and explain the LAPW method. One obtains the electron density distribution, electric field gradients, and magnetism quantities, which can also be obtained from the refinement of the experimental electron density by, e.g., a multipolar model and thus can be compared to the theoretical results. The band structure and density of states of solid-state materials are elementary results of the DFT.

Excited states, their structure, electron density distribution, and spectroscopic properties can be elucidated by time-dependent density functional theory (TDDFT). V. Olevano starts with the basic theoretical framework and explains through several examples the efficacy of TDDFT. Then an analysis of excitations with or without momentum transfer follows. On the example of silicon the outstanding challenges of TDDFT, especially with respect to the extension of the kernels, are discussed.

The chapter *Time-resolved structural analysis* by S. Pillet sums up a comprehensive overview of the various methods for observing structural changes by time-resolved X-ray diffraction. Different cases of the induced structural perturbations are discussed in real and reciprocal space through analysis of the diffraction patterns, illustrating what can be expected from such measurements and what quality is needed to be able to detect the corresponding phenomena. There follows a description of the experimental methods for time-resolved diffraction and excitations on different time scales. Finally, the question is discussed what information can currently be ob-

tained from the measurement of the time-dependent electron density distribution $\rho(\mathbf{r}, t)$.

To conclude, the chapter *Ultrafast science* by B. Patterson deals with the investigation of photoinduced coherent phenomena, the use of correlation techniques of short X-ray pulses for the structural analysis of molecules, and examples for nonlinear X-ray optics. The chapter concludes with a summary on the operating principle of the XFEL.

3 Electron density distribution and structure factors

The following chapters deal with an extension of static structure analysis to include the variable time. Mostly, and especially from the experimental point of view, this will be restricted to the analysis of the motion of nuclei. However, recall that X-rays are mainly scattered by the electrons, and therefore X-ray diffraction allows us in principle to investigate in detail the electron density distribution $\rho(\mathbf{r})$. The X-ray diffraction is described by the interaction of a radiation field with a quantum mechanical system in the first Born approximation, where the interaction between the photons and the scattering system is weak, and no excited states are involved in the elastic scattering. The scattering process changes the quantum mechanical system from the initial state $|\psi_m\rangle$ to the final state $|\psi_n\rangle$ and the incident wave with propagation vector \mathbf{k}_i to the outgoing wave with propagation vector \mathbf{k}_f . As will be detailed in the chapter *Static Structural Analysis*, the structure factor $F(\mathbf{H})$ is the Fourier transform of the electron density in the unit cell:

$$F(\mathbf{H}) = \hat{F}[\rho_{\text{uc}}(\mathbf{r})] = \int_{\text{uc}} \rho(\mathbf{r}) e^{2\pi i \mathbf{H} \cdot \mathbf{r}} d\mathbf{r}. \quad (1)$$

The measurement of the Bragg intensities for the scattering vectors \mathbf{H} allow therefore in principle for the determination of the electron density $\rho(\mathbf{r})$. However, due to the fact that the number of observed reflections is finite and only the moduli of the structure factors $F(\mathbf{H})$ are known but not their phases, a model of the electron density $\rho(\mathbf{r})$ has to be elaborated. In the following we shall discuss briefly the two main models applied today, the independent atom model (IAM) and the multipolar model (MM). For a more in-depth treatment of the subject, the interested reader is referred to the excellent textbook by Coppens [32] and the comprehensive overview about charge-density-related research edited by Gatti and Macchi [33].

3.1 The independent atom model IAM

In the independent atom model the unit cell electron density $\rho_{\text{uc}}(\mathbf{r})$ is approximated by a sum over atomic densities from isolated atoms, which consist of spherical symmetric

atomic densities $\rho_j(\mathbf{r})$ centered at the nuclear position \mathbf{r}_j of the atom j :

$$\rho_{\text{uc}}(\mathbf{r}) = \sum_j \rho_j(\mathbf{r}) \delta(\mathbf{r} - \mathbf{r}_j). \quad (2)$$

The structure factor is then given by

$$F(\mathbf{H}) = \hat{F}[\rho_{\text{uc}}(\mathbf{r})] = \sum_j f_j(\mathbf{H}) e^{2\pi i \mathbf{H} \cdot \mathbf{r}_j} \quad (3)$$

with the atomic form factor $f_j(\mathbf{H})$ given by the Fourier transform of the atomic density $\rho_j(\mathbf{r})$ at the scattering vector \mathbf{H} :

$$f_j(\mathbf{H}) = \int \rho_j(\mathbf{r}) e^{2\pi i \mathbf{H} \cdot \mathbf{r}} d\mathbf{r}. \quad (4)$$

Up to now, we have ignored that the observable electron density is in fact the result of a thermal average over many vibrational states due to the movement of the atoms. Within the Born–Oppenheimer approximation, the electrons follow the nuclei instantaneously. Assuming that the electrons can be assigned to specific nuclei, the thermally averaged electron density is a superposition of atomic densities that follow rigidly the motion of the nuclei. This can be expressed as a convolution of a probability density function $p_j(\mathbf{r})$, giving the probability of atom j to be displaced from its equilibrium position \mathbf{r}_j and a static atomic density $\rho_{j,\text{static}}(\mathbf{r})$. The unit cell density is then given by

$$\rho_{\text{uc}}(\mathbf{r}) = \sum_j [\rho_{j,\text{static}}(\mathbf{r}) * p_j(\mathbf{r})] * \delta(\mathbf{r} - \mathbf{r}_j). \quad (5)$$

In general the displacement models are harmonic, and this convolution approximation is termed the *rigid pseudo-atom approximation*. For the structure factor, it follows

$$F(\mathbf{H}) = \hat{F}[\rho_{\text{uc}}(\mathbf{r})] = \sum_j f_j(\mathbf{H}) T_j(\mathbf{H}) e^{2\pi i \mathbf{H} \cdot \mathbf{r}_j} \quad (6)$$

with $f_j(\mathbf{H})$ now the static atomic structure factor and T_j the atomic temperature factor, often referred to as the Debye–Waller factor

$$T_j(\mathbf{H}) = \int p_j(\mathbf{r}') e^{2\pi i \mathbf{H} \cdot \mathbf{r}'} d\mathbf{r}'. \quad (7)$$

The correct deconvolution of thermal motion and atomic structure factors is crucial for a meaningful description of the electron density distribution. Mostly harmonic approximations are applied for the description of the thermal motion, whereby isotropic or anisotropic displacements of the atoms are modeled by Gaussian probability distributions. If high-resolution data are available, applications of models beyond the harmonic approximation are possible.

The independent atom model is the main tool used for routine structure analysis based on X-ray diffraction, yielding reliable and precise models for the nuclear static structure. It is based on a spherical electron density distribution, so whenever asphericity or chemical bonding effects are negligible, it works perfectly. However, whenever the valence electrons constitute a significant part of the total electron density distribution, the IAM is not sufficient for an accurate description of the electron density. For example, in the case of the hydrogen atom, it leads to an underestimation of bond distances due to bonding effects. Considering a purely spherical electron density distribution, the one electron of the hydrogen involved in the chemical bonding results in an electron density distribution with its center shifted toward the atom it is bonding to. This effect is well known, and models for correction have been developed and may be applied in structure refinement programs. Another drawback of IAM is that it assumes the atoms in a crystal to be neutral. This is in general not the case due to charge transfer between atoms or due to asphericity of the electron density distribution, responsible for, e.g., molecular dipole moments. This effect is, for example, clearly visible in atoms such as oxygen via their so-called lone-pairs, i.e., the doubly filled nonbonding orbitals.

To improve the description of the electron density distribution, the IAM has been extended by adding a term accounting for charge transfer between atoms. In this so-called κ -formalism, one separates the scattering contributions due to valence and inner shell electrons, ρ_{core} and ρ_{val} , respectively, by writing

$$\rho_{\text{atom}} = \rho_{\text{core}} + P_v \kappa^3 \rho_{\text{val}}(\kappa r), \quad (8)$$

where P_v is the valence shell population parameter, and κ is a parameter allowing for contraction or expansion of the valence shell, i.e., it scales the radial coordinate r . Normalizing the atomic form factors to one electron and using the core electron population P_c , we obtain for the structure factor

$$F(\mathbf{H}) = \sum_j [\{P_{c,j} f_{\text{core},j}(H) + P_{v,j} f_{\text{val},j}(H/\kappa)\} e^{2\pi i \mathbf{H} \cdot \mathbf{r}_j} T_j(\mathbf{H})]. \quad (9)$$

The κ -model allows only changing the radial form of the electron density distribution by contraction or expansion. This might be helpful for simple cases like the hydrogen atom, where only one electron has to be treated. Therefore this model is rarely used on its own; however, it is very useful as a first step toward a more complex model.

3.2 The multipolar model

The multipolar model uses atom-centered multipolar functions for the description of the electron density. The most popular model used today is the so-called Hansen–Coppens model, introduced in 1978 [34]. It combines radial and angular functions to

describe the density of each atom as follows:

$$\rho_{\text{atom}} = P_c \rho_{\text{core}}(r) + P_v \kappa^3 \rho_{\text{val}}(\kappa r) + \sum_{l=0}^{l_{\text{max}}} \kappa'^3 R_l(\kappa' r) \sum_{m=0}^l P_{lm\pm} d_{lm\pm}(\theta, \varphi), \quad (10)$$

where the two first terms correspond to the κ -formalism introduced in the preceding paragraph, including the core and valence electron population parameters P_c and P_v . This type of multipolar model is termed valence-density formalism since it allows for contraction or expansion of the valence shell via the κ parameters in the radial terms R_l and an aspherical description via the angular terms d_{lm} , which accounts for chemical bonding effects. The choice of suitable radial and angular functions is crucial. Typically, single Slater functions ζ are employed.

The aspherical atomic form factor $f_j(\mathbf{H})$ and the corresponding structure factor $F(\mathbf{H})$ are then obtained by the Fourier transform:

$$\begin{aligned} f_j(\mathbf{H}) = & P_{c,j} f_{\text{core},j}(H) + P_{v,j} f_{\text{val},j}(H/\kappa) \\ & + 4\pi \sum_{l=0}^{l_{\text{max}}} \sum_{m=0}^l \sum_p P_{lm\pm} t^l \langle j_l(S/\kappa') \rangle d_{lm\pm}(\beta, \gamma) \end{aligned} \quad (11)$$

and

$$F(\mathbf{H}) = \sum_j f_j(\mathbf{H}) e^{2\pi i \mathbf{H} \cdot \mathbf{r}} T_j(\mathbf{H}). \quad (12)$$

In equation (11), $\langle j_l \rangle$ denotes the Fourier–Bessel transform

$$\langle j_l(S/\kappa') \rangle = \int j_l(2\pi S r) R_l(r) r^2 dr \quad (13)$$

with j_l the spherical Bessel functions. The density functions $d_{lm\pm}$ containing the spherical harmonics describe the charge density in the form of multipoles. Overall, the electron density distribution $\rho(\mathbf{r})$ is thus described as a sum of pseudo-atomic densities. Each of these is composed of a spherical part ρ_{core} for the core and ρ_{val} for the valence shell and of a set of spherical harmonic functions to describe the aspherical part. The multipoles can then be developed up to the degree (dipole, quadrupole, octupole, hexadecapole, etc.) adequate for the system under study. Note that the summation includes also monopoles ($l = 0$), which may be omitted for first- and second-row atoms but are necessary to describe the more diffuse outer s -electron shell of transition metal atoms. The description of the electron density distribution with a multipolar model such as the Hansen–Coppens model has the advantage that it gives quite an intuitive view of the electron distribution as we are used to by the orbital description of the electron clouds. Moreover, due to the fact that the density $\rho(\mathbf{r})$ is related to the probability of finding an electron in a certain volume according to $\rho(\mathbf{r}) \sim \psi\psi^*(\mathbf{r})$, it is a quantity that can be obtained by theory and thus allows for direct comparison between theory and experiment (see the chapter *DFT calculations of solids in the ground state*).

Once the electron density distribution is determined, by theory or experiment, we can perform a topological analysis and derive properties, such as the electrostatic potential, dipole moments, etc. A quantitative analysis of the topological properties of the density $\rho(\mathbf{r})$ is possible using the quantum theory of atoms in molecules (QTAIM) developed by Bader [35]. It is not the purpose of this book to describe these methods in detail, and we refer the reader to the specialized literature and the book of Bader [35]. Some examples are treated in the chapter *DFT calculations of solids in the ground state*.

We immediately recognize that the description with a multipolar model will significantly increase the number of parameters in the least square refinements. Therefore the requirements for experimental electron density determination in terms of data completeness, redundancy, and precision are high. Typically, we need complete data sets up to resolutions of $\sin \theta/\lambda \sim 1.2 \text{ \AA}^{-1}$. Special care must be taken to deconvolute the smearing of the electron density deformation due to thermal motion from the other effects we are interested in, such as chemical bonding, polarization, etc. It is the valence electron distribution, which is the most affected by the mentioned effects. Since this part of the electron density distribution is more diffuse in direct space than the core electron density distribution, it is more contracted in reciprocal space. This implies that the structure factors at low resolution $\sin \theta/\lambda$ are more affected than those at high resolution. As a consequence, in general, we first perform a so-called high-order refinement, using only data above a certain $\sin \theta/\lambda$ threshold, which allows us to obtain a good deconvolution of thermal motion. Typical threshold values are $\sin \theta/\lambda > 0.7 - 0.8 \text{ \AA}^{-1}$. Once the standard structural and thermal parameters are obtained from this kind of IAM refinement, we proceed to the refinement of the multipolar model including the whole data set. Most often, we start by calculating and inspecting so-called deformation electron density maps. The deformation density is defined as the difference between the total observed density ρ_{obs} and the spherical density $\rho_{\text{calc}}^{\text{IAM}}$ calculated with a spherical reference model (IAM). It corresponds thus to a Fourier difference map, yielding the residual density after a refinement according to IAM:

$$\Delta\rho(\mathbf{r}) = \rho_{\text{obs}} - \rho_{\text{calc}}^{\text{IAM}}. \quad (14)$$

These maps illustrate bonding features and aspherical electron density distributions and allow for proper choice of the multipolar expansion level needed. To test the validity of the refined model, there exists a large number of statistical tools, which should be applied systematically. Because the number of parameters is high, special attention has to be paid not to overinterpret the refinement results. Figure 1 shows in the left panel as an example the deformation electron density obtained after a spherical refinement (IAM) of the data calculated according to equation (14) for sodium nitroprusside ($\text{Na}_2[\text{Fe}(\text{CN})_5\text{NO}]2\text{H}_2\text{O}$, SNP) in the plane spanned by Fe, C2, and N4. SNP crystallizes in the orthorhombic space group *Pnmm*. The central iron atom of the

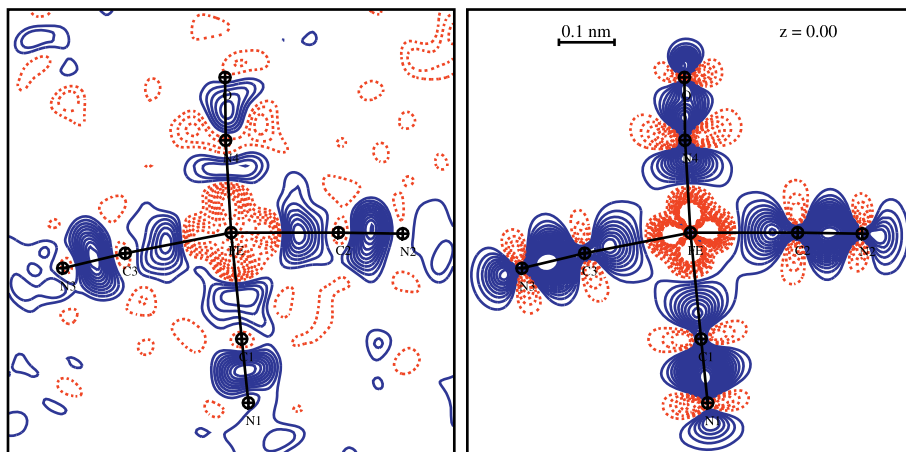


Figure 1: (Left) deformation electron density $\Delta\rho(\mathbf{r})$ and (right) static deformation electron density $\Delta\rho_{\text{static}}(\mathbf{r})$ in the Fe–C2–N4 plane of the $[\text{Fe}(\text{CN})_5\text{NO}]^{2-}$ anion. In blue (positive) and red (negative) contours drawn at $0.05 \text{ e}\text{\AA}^{-3}$ [36].

$[\text{Fe}(\text{CN})_5\text{NO}]^{2-}$ anion is octahedrally coordinated by one almost linear NO (Fe–N–O angle of 175.96°) and five CN ligands. The deformation map illustrates clearly the bonding features in the NO and CN groups and toward the central metal atom. The deformation electron density around the iron atom is highly anisotropic as can be seen from Figure 1. A multipolar model can account for all of these features and allows us to derive further quantities such as d -orbital populations, atomic charges, etc. [32]. After performing a successful multipolar refinement, we can calculate the electron density according to equation (10). From this the so-called *static deformation electron density* is calculated, which is the difference between the density calculated from the multipolar model and that calculated from the independent atom model:

$$\Delta\rho_{\text{static}}(\mathbf{r}) = \rho_{\text{calc}}^{\text{MM}} - \rho_{\text{calc}}^{\text{IAM}}. \quad (15)$$

This kind of deformation map has the advantage to be noise free and especially avoids the thermal smearing effects due to the atom motions (Debye–Waller factor), hence the name *static*. These maps are thus perfectly suited for comparison with *ab initio* calculations (see the chapter *DFT calculations of solids in the ground state*) since calculations are in general performed at $T = 0 \text{ K}$. Figure 1 shows in the right panel the static deformation electron density for the same plane as the deformation density in SNP. We immediately recognize the much more prominent bonding features, including the lone pairs on the oxygen and nitrogen atoms, which are now clearly visible due to the reduced thermal smearing. The anisotropic electron distribution around the central iron atom is now striking, and we can clearly see the depletion of the $d_{x^2-y^2}$ and d_{z^2} orbitals compared to the d_{xy} , d_{xz} , and d_{yz} orbitals (see also [37]).

Concerning time-resolved studies, the requirements with respect to data quality and completeness represent a considerable challenge, and currently a detailed modelling of time-resolved data based on the multipolar model are not possible. However, first steps toward the time-resolved study of the electron density distribution are made and will be discussed in the chapter *Time-resolved structural analysis*.

Bibliography

- [1] M. J. Buerger. *Brief History of Crystal Structure Determination*. Kluwer Academic Publishers: Dordrecht, 1990.
- [2] R. E. Green. First x-ray diffraction photograph of a shaped charge jet. *Rev. Sci. Instrum.*, 46:1257–1261, 1975.
- [3] V. A. Tsukerman and A. I. Avdeenko. *Zh. Tekh. Fiz.*, 12:185, 1942.
- [4] L. V. Al'tshuler. *Zh. Exsperim. Teor. Fiz.*, 13:388, 1943.
- [5] R. Schall. Feinstrukturaufnahmen in ultrakurzen Zeiten mit dem Röntgenblitzrohr. *Angew. Chem.*, 62:97–98, 1950.
- [6] R. Schall. *Arch. Tech. Mess. Z.*, 74:117, 1953.
- [7] W. Schaaffs. Die Erzeugung von Röntgenblitz-Interferenzen an polykristallinem Material. *Z. Naturforsch. A*, 5:631–632, 1950.
- [8] W. Schaaffs and K. H. Hermann. Aufbau und technische Eigenschaften von Hochvakuum-Röntgenblitzröhren. *Z. Angew. Phys.*, 6:23–35, 1954.
- [9] W. Schaaffs. Erzeugung und Anwendung von Röntgenblitzen. *Ergeb. Exakten Naturwiss.*, 28:1–46, 1955.
- [10] N. I. Zavada, M. A. Manakova, and V. A. Tsukerman. *Prib. Tekh. Exsp.*, 2:434, 1966.
- [11] Q. Johnson, R. N. Keeler, and J. W. Lyle. X-ray diffraction experiments in nanosecond time intervals. *Nature*, 213:1114–1115, 1967.
- [12] R. R. Whitlock and J. S. Wark. *X-ray Diffraction Dynamics of Shock-Compressed Crystals*. Oxford Science Publications: London, 1997.
- [13] R. Germer. X-ray flash techniques. *J. Phys. E, Sci. Instrum.*, 12:336–350, 1979.
- [14] P. J. Mallozzi, H. M. Epstein, R. G. Jung, D. C. Applebaum, B. P. Fairand, W. J. Gallagher, R. L. Uecker, and M. C. Muckerheide. Laser-generated plasmas as a source of x-rays for medical applications. *J. Appl. Phys.*, 45:1891–1895, 1974.
- [15] G. Rosenbaum, K. C. Holmes, and J. Witz. Synchrotron radiation as a source for x-ray diffraction. *Nature*, 230:434–437, 1971.
- [16] A. R. Faruqi. Application of nuclear instrumentation techniques to x-ray diffraction from muscle. *IEEE Trans. Nucl. Sci.*, 22:2066–2073, 1975.
- [17] H. E. Huxley. The structural basis of contraction and regulation in skeletal muscle. *Acta Anat. Nippon.*, 50:310–325, 1975.
- [18] H. E. Huxley, A. R. Faruqi, J. Bordas, M. H. J. Koch, and J. R. Milch. The use of synchrotron radiation in time-resolved x-ray diffraction studies of myosin layer line reflections during muscle contraction. *Nature*, 284:140–143, 1980.
- [19] B. C. Larson, C. W. White, T. S. Noggle, J. F. Barhorst, and D. M. Mills. Time-resolved x-ray diffraction measurement of the temperature and temperature gradients in silicon during pulsed laser annealing. *Appl. Phys. Lett.*, 42:282–284, 1983.
- [20] R. D. Frankel and J. M. Forsyth. Nanosecond x-ray diffraction from biological samples with a laser-produced plasma source. *Science*, 204:622–624, 1979.

- [21] J. G. Lunney, P. J. Dobson, J. D. Hares, S. D. Tabatabaei, and R. W. Eason. Time-resolved x-ray diffraction from silicon during pulsed laser annealing. *Opt. Commun.*, 58:269–272, 1986.
- [22] I. V. Tomov, P. Chen, and P. M. Rentzepis. Picosecond time-resolved x-ray diffraction during laser-pulse heating of an Au(111) crystal. *J. Appl. Crystallogr.*, 28:358–362, 1995.
- [23] A. Rousse, P. Audebert, J. P. Geindre, F. Fallies, J. C. Gauthier, A. Mysirowicz, G. Grillon, and A. Antonetti. Efficient $K\alpha$ x-ray source from femtosecond laser-produced plasmas. *Phys. Rev. E*, 50:2200–2207, 1994.
- [24] C. Rischel, A. Rousse, I. Uschmannand, P.-A. Albouy, J. P. Geindre, P. Audebert, J. C. Gauthier, E. Foerster, J.-L. Martin, and A. Antonetti. Femtosecond time-resolved x-ray diffraction from laser-heated organic films. *Nature*, 390:490–492, 1997.
- [25] B. Larsson, Z. Chang, E. Judd, P. J. Schuck, R. W. Falconeand, P. A. Heimannand, H. A. Padmore, H. C. Kapteyn, P. H. Bucksbaum, M. M. Murnaneand, R. W. Leeand, A. Machacek, J. S. Wark, X. Liu, and B. Shan. Ultrafast x-ray diffraction using a streak-camera detector in averaging mode. *Opt. Lett.*, 22:1012–1014, 1997.
- [26] R. W. Schoenlein, S. Chattopadhyay, H. H. W. Chong, T. E. Glover, P. A. Heimann, C. V. Shank, A. A. Zholents, and M. S. Zolotarev. Generation of femtosecond pulses of synchrotron radiation. *Science*, 287:2237–2240, 2000.
- [27] J. C. H. Spence. Approaches to time-resolved diffraction using an XFEL. *Faraday Discuss.*, 171:429–438, 2014.
- [28] F. X. Kärtner, F. Ahr, A.-L. Calendron, H. Çankaya, S. Carbajo, G. Chang, G. Cirmi, K. Dörner, U. Dorda, A. Fallahi, A. Hartin, M. Hemmer, R. Hobbs, Y. Hua, W. R. Huang, R. Letrun, N. Matlis, V. Mazalova, O. D. Mücke, E. Nanni, W. Putnam, K. Ravi, F. Reichert, I. Sarrou, X. Wu, A. Yahaghi, H. Ye, L. Zapata, D. Zhang, C. Zhou, R. J. D. Miller, K. K. Berggren, H. Graafsma, A. Meents, R. W. Assmann, H. N. Chapman, and P. Fromme. Axis: exploring the frontiers in attosecond x-ray science, imaging and spectroscopy. *Nucl. Instrum. Methods Phys. Res., Sect. A*, 829:24–29, 2016.
- [29] D. J. Dunning, B. W. J. McNeil, and N. R. Thompson. Towards zeptosecond-scale pulses from x-ray free electron lasers. *Phys. Proc.*, 52:62–67, 2014.
- [30] T. E. Glover, D. M. Fritz, M. Cammarata, T. K. Allison, S. Coh, J. M. Feldkamp, H. Lemke, D. Zhu, Y. Feng, R. N. Coffee, M. Fuchs, S. Ghimire, J. Chen, S. Shwartz, D. A. Reis, S. E. Harris, and J. B. Hastings. X-ray and optical wave mixing. *Nature*, 488:603–608, 2012.
- [31] A. H. Zewail and J. M. Thomas, editors. *4D Electron Microscopy*. Imperial College Press: London, 2010.
- [32] P. Coppens. *X-ray Charge Densities and Chemical Bonding*. Oxford Science Publications: London, 1997.
- [33] C. Gatti and P. Macchi, editors. *Modern Charge-Density Analysis*. Springer: Berlin, 2012.
- [34] N. K. Hansen and P. Coppens. Testing aspherical atom refinements on small-molecule data sets. *Acta Crystallogr., Sect. A*, 34:909–921, 1978.
- [35] R. F. W. Bader. *Atoms In Molecules. A Quantum Theory*. Clarendon Press: Oxford, 1990.
- [36] S. Dahaoui. Private communication. 2017.
- [37] E. Wenger, S. Dahaoui, P. Alle, P. Parois, C. Palin, C. Lecomte, and D. Schaniel. XPAD x-ray hybrid pixel detector for charge density quality diffracted intensities on laboratory equipment. *Acta Crystallogr. Sect. B*, 70:783–791, 2014.

Reinhard B. Neder

Static structural analysis of condensed matter: from single-crystal to amorphous

Keywords: X-ray scattering, structure analysis

Introduction

The main focus of this book is placed on the analysis of X-ray diffraction by dynamically changing structures. The details of the time-dependent formalism are presented in the chapter *Time-resolved structural analysis* of this book. Here the ground work for the time-resolved scattering is laid out, starting with the analysis of a static structure. Where relevant, differences between a static structure and the time-resolved structure are pointed out.

The time resolution limit in this chapter is down to the time-scale where the measurement still yields averaged positions, i.e., measurement/averaging time longer than typical vibration of atoms around equilibrium positions.

It is expected that the reader is familiar with a crystallographic description of crystals, which can be found in any textbook on crystallography, like Refs. [1–3]. Aspects of the structure determination from measured Bragg intensities can be found in textbooks [1, 4–8].

1 Basic diffraction algorithm

An atomic structure can be studied in a diffraction experiment with any radiation whose wavelength is of the order of interatomic distances or shorter. This holds for X-rays, electrons, and neutrons. It is obvious that X-rays, which are a section of the electromagnetic spectrum in the wavelength range from approximately 0.2 down to 0.001 nm, can be diffracted by a grating with dimensions of the same order of magnitude. In a classical description, electrons and neutrons are treated as particles. Since their mass is very small, a quantum mechanical description of electrons and neutrons with wave properties is more appropriate for diffraction experiments. Given the wave nature of electrons and neutrons, they can be diffracted by crystals just as well as X-rays. The strength of the interaction between matter and the radiation increases from neutrons to X-rays to electrons. For this reason, time-resolved neutron diffraction has not yet reached the very short time scale that can be achieved with X-rays. Another reason for the limited time resolution in a neutron experiment is the comparatively small neutron velocity. At a speed of approximately 2.2 km/s for thermal neu-

<https://doi.org/10.1515/9783110433920-002>

trons, the neutron will travel 2.2 nm per picosecond. Let us assume a crystal of just 100-nm diameter, which results in an extremely small volume for neutron diffraction. A thermal neutron requires 45 ps to traverse the sample. As a result, the neutron wave will see the entrance and the exit part of the crystal at considerably different times. Compare this to X-rays that travel at 300 000 km/s. A photon will traverse the same crystal in just 0.3 fs! Thus X-rays will inherently allow for much better time resolution. On the other hand, the very strong interaction between electrons and matter makes the quantitative treatment of their diffracted intensity much more complicated. A quantitative analysis of electron diffraction patterns is just emerging. Since time-resolved X-ray diffraction is the dominant experimental technique, this section focuses on the treatment of X-ray interaction with matter.

X-rays can interact with matter in a variety of processes, schematically shown in Figure 1. The incoming X-ray photon may be absorbed completely, and its energy be transferred to electrons within the structure. Alternatively, the X-ray photon may be scattered. Here we need to distinguish the elastic case where the scattered photon has the same energy as the incoming photon and the inelastic case where the energy of the scattered photon differs from the energy of the incoming photon. For structural analysis of the internal structure of condensed matter, the elastically scattered wave is of predominant interest. In the first inelastic scattering event, called Compton scattering, the photon may interact with a single electron and transfer part of its energy to the electron. The resulting scattering is isotropically distributed. As this process occurs randomly throughout the structure and independently at different atoms, it is an incoherent process. In a second type of inelastic scattering event, the X-ray photon can also interact with the collective vibrations of the crystal, the phonons. In this process the photon may lose or gain a small amount of energy depending on whether a phonon is excited or dampened. As the energy of X-rays is in the keV range and that of phonons in the meV range, the X-ray energy change is very small. This inelastic scattering is much more relevant in the realm of neutron scattering as the energy of neutrons with a wavelength around 1 Å is some tens of meV and thus much more similar to that of phonons. Finally, in another elastic scattering event, the X-ray photon may also interact with the magnetic moments of the structure, allowing insight into the order of these magnetic moments. With respect to fast structural changes, the

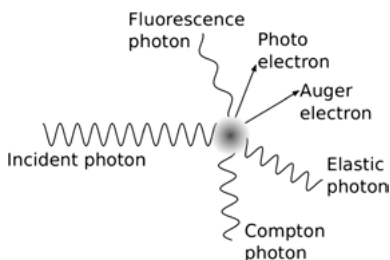


Figure 1: Schematic illustration of interaction between X-rays and matter.

elastic scattering is the most important part and is derived in detail in this introductory chapter.

Finally, let us briefly consider the absorption process. When an X-ray photon is absorbed, its energy is completely transferred to an electron, which may be excited into an unoccupied state within the crystal or may leave the crystal as a so-called photoelectron. The excited electron leaves behind a hole. Secondary processes will relax the crystal back into its ground state. Electrons from higher energy levels will relax into the lower level, and the energy difference will be released as electromagnetic radiation, so-called fluorescence radiation. As an alternative process, the energy released when an electron relaxes from a higher energy level to a lower level may in turn excite another electron, a process called Auger electron emission.

1.1 Diffraction by electrons, atoms, molecules, and crystals

In a diffraction experiment the relevant information thought after is the relative intensity of X-rays scattered by the atoms in the crystal. To derive an expression for this intensity, we need to start with the scattering process of the X-ray photon with a single electron. It turns out that this can be done quite well with a classical description. A detailed quantum mechanical derivation yields the same results; see, for example, Ref. [9].

Within this classical approach keep in mind that X-rays are part of the electromagnetic spectrum. The oscillating electric field vector of the incident X-ray photon causes an oscillating acceleration of the electron. The oscillating electron in turn will emit electromagnetic radiation with the same frequency as the incoming X-ray photon, and thus this process is called elastic as the frequencies and thereby the energies of incoming and scattered X-ray photons are identical.

The elastic scattering of X-rays by a single free electron is the most basic process. This process can be described in terms of a fundamental unit, the Thompson scattering length or classical electron radius. To derive this length, consider a scattering process at a single electron. A number of photons per second impinges on this electron and the scattered wave is observed by a detector at distance R over a solid angle $\Delta\Omega$ (Figure 2). This incoming flux Φ_0 , the number of photons per second and per unit area, is proportional to the square of the electric field strength and the speed of light.

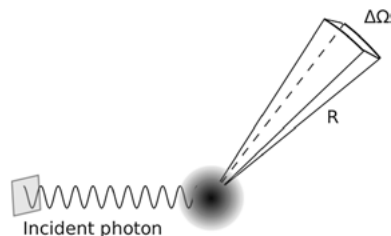


Figure 2: Schematic illustration of elastic X-ray scattering.

The latter follows from the consideration that all photons within a distance $c \cdot t$ pass through our unit area in time t , and we get $\Phi_0 \propto c|E|^2/\hbar\omega$. Here \hbar is the Plank constant divided by 2π , and ω is the circular frequency of the incoming radiation.

The intensity recorded by the detector in turn is proportional to the square of the scattered electric field strength, the speed of light, and the area of the detector. This area can be written as $R^2\Delta\Omega$, and we obtain $I_{SC} \propto c|E_{SC}|^2/\hbar\omega \cdot (R^2\Delta\Omega)$. The differential cross section that describes the strength of the scattering process is defined as the scattered intensity normalized for incoming flux and solid angle:

$$\left(\frac{d\sigma}{d\Omega}\right) = \frac{I_{SC}}{\Phi_0\Delta\Omega}. \tag{1}$$

Inserting the individual expressions for incident flux and measured intensity, we obtain

$$\left(\frac{d\sigma}{d\Omega}\right) = \frac{c|E_{SC}|^2/\hbar\omega \cdot (R^2\Delta\Omega)}{c|E_0|^2/\hbar\omega\Delta\Omega} = \frac{|E_{SC}|^2R^2}{|E_0|^2}. \tag{2}$$

Within our classical description, the oscillating incoming electric field forces the electron to oscillate, and this oscillating electric charge $-e$ in turn emits a spherical electromagnetic wave with modulus of the electric field $|E_{SC}| \propto -ee^{2\pi i\mathbf{kR}}/R$. Here we adopt the nomenclature to depict the length of the wave vector as $k = 1/\lambda$, rather than $2\pi/\lambda$. Consider a photon that travels along the positive x -axis with polarization direction of the electric field vector along the y -axis (Figure 3). If we observe the scattered radiation within the x - z plane, then we will see an effective acceleration a_y independent of the angle between the incoming and scattered radiation. If we observe the scattered radiation within the x - y plane, then we will see an effective acceleration $a_y \cos\psi$, where ψ is the angle between the positive x -direction and our observation direction. Initially, let us focus on the scattering in the x - z plane, where we can write the observed scattered electric field as a function of distance and time t as

$$E_{SC}(R, t) \propto \frac{-e}{R}a_y(t'). \tag{3}$$

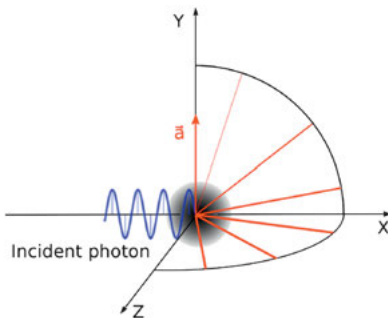


Figure 3: Schematic illustration of elastic X-ray scattering by a single electron.

We have to refer to the acceleration at time $t' = t - R/c$, since the scattered phonon has to travel the distance R with velocity c . The acceleration of the electron is proportional to its charge and the incoming electric field and inversely proportional to the electron mass: $a_y(t') = \frac{-eE_0}{m} e^{-2\pi i f \cdot t'}$. Here f is the regular frequency, and with $E_{\text{in}} = E_0 e^{-2\pi i f t}$ as the incoming time-dependent electric field, we obtain

$$a_y(t') = \frac{-eE_0}{m} e^{-2\pi i f \cdot (t-R/c)} = \frac{-eE_{\text{in}}}{m} e^{2\pi i f \cdot R/c} = \frac{-eE_{\text{in}}}{m} e^{2\pi i \cdot kR}. \quad (4)$$

This expression for the acceleration can be inserted into equation (3), and this equation, rearranged to reflect the ratio between the scattered and incident electric fields, becomes

$$\frac{E_{\text{SC}}(R, t)}{E_{\text{in}}} \propto \left(\frac{e^2}{m}\right) \frac{1}{R} e^{2\pi i \cdot kR}. \quad (5)$$

The next step in the development of the scattering theory is to consider a single atom. Instead of a single electron, we have a continuous electron density distribution around the nucleus. Thus we will have to integrate over all waves scattered throughout this density distribution. Figure 4 schematically shows the electron density distribution with two arbitrarily chosen scattering centers. Each is a point source of a scattered wave, and the scattered amplitude is proportional to the electron density at this point. Since the atomic dimensions are extremely small compared to sample-to-detector distances, a far-field approximation is well justified. In this approximation, we can treat both, the incoming and the outgoing waves as plane waves rather than spherical waves. The angle between the outgoing wave vectors \mathbf{k} is for all practical matters zero. The geometrical path difference between the rays I and II is the sum of the bold sections A and B with $A = -\mathbf{s}_0 \mathbf{r}$ and $B = \mathbf{s} \mathbf{r}$, where \mathbf{s}_0 and \mathbf{s} are the unit vectors in the direction of the wave vectors \mathbf{k}_0 and \mathbf{k} , respectively. The minus sign in the expression for A results from the fact that in this geometry the projection of \mathbf{r} onto \mathbf{s}_0 results in a vector that is opposite in direction to \mathbf{s}_0 . Thus we get, as the phase difference between the two scattered waves, $\Gamma = \frac{2\pi}{\lambda} (\mathbf{s} - \mathbf{s}_0) \mathbf{r} = 2\pi \mathbf{S} \mathbf{r}$ with the scattering vector $\mathbf{S} = (\mathbf{s} - \mathbf{s}_0)/\lambda$. Note that another customary depiction is to use a symbol \mathbf{Q} for the scattering vector with the definition $\mathbf{Q} = 2\pi(\mathbf{s} - \mathbf{s}_0)/\lambda = 2\pi \mathbf{S}$. Correspondingly, the wave vectors must now be defined with length $2\pi/\lambda$. The only difference between these

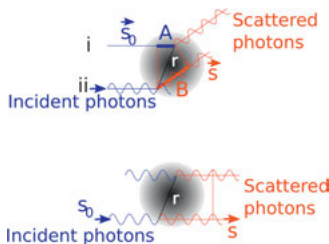


Figure 4: Schematic illustration of atomic form factor. In the forward direction, all waves scattered at different locations have the same phase. With increasing scattering angle the phase difference between the two waves increases.

nomenclatures is the question whether to include the factor of 2π within the scattering vector, respectively wave vector, or whether to write it as a separate factor. In this book we will write the factor 2π as a separate factor as is customary in crystallographic literature. As pointed out in the deduction of the scattering by a single electron, the scattered intensity by the scattered electron is proportional to its charge. Accordingly, the scattered intensity by a small volume $d\mathbf{r}$ is proportional to the electron density. For the interference of two waves scattered by different volumes, the absolute phase of the individual waves is not relevant. The main aspect is the phase shift between any two waves. Without loss of generality, we can therefore define the phase of a wave scattered at the origin to be zero. By placing the origin within the center of the atom, for the scattered amplitude, we obtain

$$A(\mathbf{S}) = r_0 \int_V \rho(r) e^{2\pi i \mathbf{S} \cdot \mathbf{r}} d\mathbf{r} = r_0 f(\mathbf{S}), \quad (6)$$

where $f(\mathbf{S})$ is known as the atomic form factor, and the integration is carried out over the volume V of the atom. For $\mathbf{S} = \mathbf{0}$, the integral will simply yield the total integral over the electron density, i.e., the number of electrons of the atom. For larger values of \mathbf{S} , the exact value of course depends on the exact electron density distribution. The values of the atomic form factor f have been calculated from quantum mechanical calculations and are tabulated, for example, in the International Tables for Crystallography, vol C [10]. These calculations have been carried out for an individual free atom or ion with the assumption of spherical symmetry for the electron density distribution. This approximation does neglect the effect of chemical bonds within a crystal and is known as the independent atom model (IAM). In the presence of chemical bonds, this assumption is no longer strictly valid, and small deviations from the spherical model can be observed. These deviations can be modeled and allow insight into the detailed electron density distribution of chemically bonded atoms; see the chapter *Introduction* in this book and further references therein. Within the assumption of the spherical electron density distribution, let us have a qualitative look at the consequences for the scattering by a single atom. Mathematically speaking, the integral in equation (6) is the Fourier transform of the electron density. Recall the following two properties of a Fourier transform $F(h)$ of a function $f(x)$: Scaling the amplitude of $f(x)$ translates into scaling the amplitude of $F(h)$: $\text{Fourier}[p \cdot f(x)] = p \cdot \text{Fourier}[f(x)]$. Scaling the x -coordinate of $f(x)$ translates into the inverse scaling of the h -coordinate of $F(h)$:

$$\text{Fourier}[f(a \cdot x)] = 1/a F(h/a). \quad (7)$$

The first almost trivial result is that if we compare two atoms with different number of electrons, then the scattered amplitude by the atom is proportional to the number of electrons. That is the reason why light elements like Hydrogen contribute much less to an X-ray scattering pattern than heavier elements. The second result is that if we

spread out the electron density by a factor a , then the atomic form factor shrinks by the reciprocal of this factor. To a very crude approximation, we can describe the radial electron density distribution by a Gaussian distribution

$$\rho(r) = \frac{1}{\sigma\sqrt{2\pi}} e^{-\frac{r^2}{2\sigma^2}}. \quad (8)$$

The Fourier transform of this Gaussian distribution is again a Gaussian distribution:

$$f(S) = \frac{\sigma}{\sqrt{2\pi}} e^{-\frac{1}{2}S^2\sigma^2}. \quad (9)$$

If we decrease the width σ , then the Fourier transform will become wider. Thus if we take the same number of electrons and place them with higher density closer to the nucleus, then the effect is that the atomic form factor will decrease slower with increasing diffraction angle. Thus heavier atoms tend to dominate X-ray diffraction patterns in two aspects. With their higher electron number, their scattering amplitude is larger, and since most of their electrons will be bound more closely to the nucleus, the decrease of their atomic form factor with increasing scattering angle is also slower.

We are now ready to group several atoms into a larger unit, either a molecule or an extended three-dimensional solid. Staying within the independent atom model, we can describe the continuous electron density distribution of the group by splitting it into a sum over individual atoms located at position \mathbf{r}_k and a sum over the electron density within each individual atom. The scattering by each atom can be described by the atomic form factor as treated in the previous paragraphs. The molecular electron density can thus be described as $\rho_M(\mathbf{r}) = \sum_{k=1}^N \rho(\mathbf{r} - \mathbf{r}_k)$. Here the sum runs over all N atoms k in the molecule. To calculate the scattered amplitude, we need to integrate over the entire molecule volume: $F_m(\mathbf{S}) = \int_V \sum_{k=1}^N \rho(\mathbf{r} - \mathbf{r}_k) e^{2\pi i \mathbf{S} \cdot \mathbf{r}}$. Within the independent atom model, we can now exchange the sequence of the integration and summation. Within the volume V_A of each atom, we define a temporary vector \mathbf{R}_j from the center of atom k to the local electron density:

$$F_m(\mathbf{S}) = \sum_{k=1}^N \int_{V_A} \rho(\mathbf{R}_j) e^{2\pi i \mathbf{S}(\mathbf{r}_k + \mathbf{R}_j)} d\mathbf{R}_j = \sum_{k=1}^N \left[\int_{V_A} \rho(\mathbf{R}_j) e^{2\pi i \mathbf{S} \mathbf{R}_j} d\mathbf{R}_j \right] e^{2\pi i \mathbf{S} \mathbf{r}_k}. \quad (10)$$

The term in square brackets is just the atomic form factor from equation (6), and we obtain

$$F_m(\mathbf{S}) = \sum_{k=1}^N f_k(\mathbf{S}) e^{2\pi i \mathbf{S} \mathbf{r}_k}. \quad (11)$$

This function is called the molecular form factor. In analogy to the atomic form factor, it describes the scattered amplitude by a single molecule and depends on the molecular shape, and thus its name. The molecular form factor in general is a smoothly varying function. As the molecule may possess no internal symmetry,

the molecular form factor has different values along the different components of the scattering vector \mathbf{S} .

Note that, in the derivation of the molecular form factor, no assumption was made with respect to the position of the individual atoms nor to the existence of any chemical bond. We can therefore use the same arguments to expand the expression to that of a crystal. With the exception of quasicrystals, we can describe the atom arrangement in a crystal as a sum of identical unit cells, each placed at a corner of the lattice. Each atom position can then be described as $\mathbf{r}_k = u\mathbf{a} + v\mathbf{b} + w\mathbf{c} + \mathbf{r}_j$, where vectors \mathbf{a} , \mathbf{b} , and \mathbf{c} are the base vectors of the lattice, and \mathbf{r}_j is a vector from the origin of the individual unit cell to the atom j . Indices u, v, w are integer numbers. From equation (11) we now get the scattered amplitude of the whole crystal as

$$F_{\text{Cr}}(\mathbf{S}) = \sum_{u=1}^U \sum_{v=1}^V \sum_{w=1}^W \sum_{j=1}^{N_{\text{unit}}} f_j(\mathbf{S}) e^{2\pi i \mathbf{S}(u\mathbf{a} + v\mathbf{b} + w\mathbf{c} + \mathbf{r}_j)}. \quad (12)$$

Here U, V, W are the numbers of unit cells in the crystal, and N_{unit} is the number of atoms per unit cell. By writing the sums over all nodes of the lattice as individual sums over the three base vectors we make the implicit assumption that the crystal is a block of $U \times V \times W$ unit cells. This does not affect the main purpose of the current derivation, the so-called structure factor. We can write this in more general terms as a sum over all lattice nodes irrespective of the outer shape of any limiting surface. The following arguments remain identical independent of the crystal shape we assume. As the content of each unit cell is identical to each other, the sum over the content is independent of the sum over all lattice nodes and can be factored out:

$$F_{\text{Cr}}(\mathbf{S}) = \left[\sum_{j=1}^{N_{\text{unit}}} f_j(\mathbf{S}) e^{2\pi i \mathbf{S} \mathbf{r}_j} \right] \left[\sum_{u=1}^U \sum_{v=1}^V \sum_{w=1}^W e^{2\pi i \mathbf{S}(u\mathbf{a} + v\mathbf{b} + w\mathbf{c})} \right] = F(\mathbf{S}) F_{\text{Lattice}}(\mathbf{S}). \quad (13)$$

The first factor is called the unit cell structure factor or more often just the structure factor F . Its value depends on the position of the atoms within a unit cell, i.e., the crystal structure, and thus its name. In the field of crystal structure analysis from (X-ray) diffraction data, this is the most important quantity as it relates the atomic position, i.e., the crystal structure, to the diffracted amplitudes. The second factor is related to the extent of the lattice and is of less importance, except for nanocrystalline samples. For a reasonably large crystal, the number of unit cells U, V, W will be very large, easily some tens of thousands. Under these circumstances, the lattice factor will be almost zero everywhere, except if the product $\mathbf{S}(u\mathbf{a} + v\mathbf{b} + w\mathbf{c})$ is integer. If this holds, then each of the complex exponents is simply one, and the sum is equal to the total number of unit cells in the crystal.

In the appendix to this chapter the properties of the Fourier transform are detailed. You will find a proof that the Fourier transform of an infinite sum of delta distributions equally spaced at a common distance is in turn an infinite sum of delta distributions spaced at the reciprocal distance. The second factor in equation (13) is such a Fourier

transform of a three dimensional lattice. In equation (114) in the appendix, the variable in the Fourier space S has to satisfy the condition that $S - \frac{h}{a} = 0$ for integer h . In three dimensions, this condition holds for every component of \mathbf{S} , and we can write this as $\mathbf{S}(u\mathbf{a} + v\mathbf{b} + w\mathbf{c}) = 1$. With \mathbf{S} written as a commonly known reciprocal space vector $\mathbf{S} = (h\mathbf{a}^* + k\mathbf{b}^* + l\mathbf{c}^*)$, we obtain that $(h\mathbf{a}^* + k\mathbf{b}^* + l\mathbf{c}^*)(u\mathbf{a} + v\mathbf{b} + w\mathbf{c}) = 1$.

This condition is fulfilled for any integer h, k, l and u, v, w if we defined the vectors \mathbf{a}^* , \mathbf{b}^* , and \mathbf{c}^* such that the products $\mathbf{a}^* \cdot \mathbf{a} = \mathbf{b}^* \cdot \mathbf{b} = \mathbf{c}^* \cdot \mathbf{c} = 1$ and all mixed products $\mathbf{a}^* \cdot \mathbf{b} = \mathbf{a}^* \cdot \mathbf{c} = \mathbf{b}^* \cdot \mathbf{a} = \mathbf{b}^* \cdot \mathbf{c} = \mathbf{c}^* \cdot \mathbf{a} = \mathbf{c}^* \cdot \mathbf{b} = 0$. This second set of conditions implies that any base vector of the direct space is normal to two base vectors in the reciprocal space and vice versa. The first condition supplies a proper scaling of the reciprocal space. If we write the three base vectors of the direct space as \mathbf{a}_i and the three base vectors of the reciprocal space as \mathbf{a}_j^* , then the definition can be written concisely as $\mathbf{a}_i \cdot \mathbf{a}_j^* = \delta_{ij}$. Here δ_{ij} is the Kronecker symbol with $\delta_{ii} = 1$ and $\delta_{ij, i \neq j} = 0$. An equivalent vectorial definition of reciprocal space is obtained of the vector product of any two real space base vectors, normalized by the unit cell volume: $\mathbf{a}^* = \frac{1}{V}(\mathbf{b} \wedge \mathbf{c})$, $\mathbf{b}^* = \frac{1}{V}(\mathbf{c} \wedge \mathbf{a})$, $\mathbf{c}^* = \frac{1}{V}(\mathbf{a} \wedge \mathbf{b})$. The unit cell volume in turn can be calculated from $V = \mathbf{a}(\mathbf{b} \wedge \mathbf{c}) = \mathbf{b}(\mathbf{c} \wedge \mathbf{a}) = \mathbf{c}(\mathbf{a} \wedge \mathbf{b})$.

Now let us look at the terms $\mathbf{a}_i \cdot \mathbf{a}_j^* = \delta_{ij}$. By our definition, $\mathbf{a}^* = \frac{1}{V}(\mathbf{b} \wedge \mathbf{c})$, which implies that \mathbf{a}^* is normal to \mathbf{b} and \mathbf{c} . Thus the scalar products $\mathbf{a}^* \cdot \mathbf{b} = \mathbf{a}^* \cdot \mathbf{c} = 0$. The scalar product is defined as $\mathbf{a} \cdot \mathbf{a}^* = |\mathbf{a}| |\mathbf{a}^*| \cos(\angle \mathbf{a}, \mathbf{a}^*)$. Here $|\mathbf{a}| \cos(\angle \mathbf{a}, \mathbf{a}^*)$ is the length d of a vector \mathbf{a} projected onto a vector \mathbf{a}^* , i.e., of a vector parallel to \mathbf{a}^* . This length d is exactly the distance between adjacent 100 lattice planes that are spanned by vectors \mathbf{b} and \mathbf{c} . This gives for the scalar product:

$$\mathbf{a} \cdot \mathbf{a}^* = d_{100} |\mathbf{a}^*| = d_{100} \frac{1}{V} (|\mathbf{b} \wedge \mathbf{c}|) = \frac{1}{V} [d_{100} |\mathbf{b}| |\mathbf{c}| \sin(\angle \mathbf{b}, \mathbf{c})]. \quad (14)$$

As d_{100} is the height of the parallelepiped spanned by vectors \mathbf{a} , \mathbf{b} , and \mathbf{c} , the term in square brackets is equal to the unit cell volume, and the scalar product is equal to 1. The other relationships hold in an analogous fashion. This implies the important general relationship that any reciprocal lattice vector $\mathbf{S} = (h\mathbf{a}^* + k\mathbf{b}^* + l\mathbf{c}^*)$ stands normal to the lattice plane with Miller indices hkl and has the inverse length of the lattice plane distance.

To illustrate the properties of this reciprocal lattice, let us have a look at the usual derivation of Bragg's law. In Figure 5, two atoms 1, 2 are symbolized on adjacent lattice

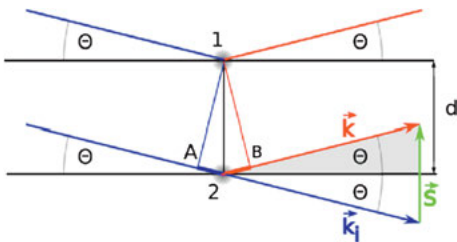


Figure 5: Schematic illustration of Bragg's law.

planes separated by distance d . Up to the line 1A, the two X-ray photons travel parallel at constant phase relationship. From line 1B onward the scattered photons travel parallel again at different but constant phase relationship. Here we have implicitly used the Fraunhofer approximation that the point of detection at which the two photons are observed is at a distance that is much longer than the distance d between the lattice planes. Under this approximation, very well justified for the very small interplanar distances in a crystal, the two scattered photons travel indeed along parallel lines. We thus have the geometrical detour taken along the lower path as the length of lines A2 and 2B. With the angle Θ between the plane and the incoming, respectively the scattered, photon paths, this geometrical detour is $\Gamma = \overline{A2} + \overline{2B} = 2d \sin(\Theta)$. The two scattered waves interfere constructively if this geometrical detour is an integer multiple of the wavelength, and we obtain Bragg's law: $n\lambda = 2d \sin(\Theta)$. Rather than to refer to higher orders of n , it is more convenient to divide this equation by n . On the right-hand side we will silently replace the original distance d between two lattice planes by d/n the distance between virtual lattice planes equally spaced at d/n : $\lambda = 2d \sin(\Theta)$.

Before we address the issue that any of the two atoms can be moved parallel to the lattice plane without affecting the phase difference, let us use this simple derivation to illustrate the meaning behind reciprocal space. In Figure 5 the wave vectors of the incoming and scattered waves are denoted as vectors \mathbf{k}_i and \mathbf{k} . As long as we are dealing with purely elastic scattering, the lengths of these two vectors are identical and equal to $|\mathbf{k}_i| = |\mathbf{k}| = 1/\lambda$. With this condition and as both vectors are at an angle Θ to the plane, the vector $\mathbf{S} = \mathbf{k} - \mathbf{k}_i$ stands normal to the lattice plane. Now consider the shaded triangle or, equivalently, the lower nonshaded one. In this triangle, we have $|\mathbf{S}|/2 = |\mathbf{k}| \sin(\Theta)$. With $|\mathbf{k}_i| = |\mathbf{k}| = 1/\lambda$, we obtain $|\mathbf{S}| = 2 \sin(\Theta)/\lambda$. This is equivalent to Bragg's law if we define the length of the vector $|\mathbf{S}|$ as the inverse of the lattice plane spacing, $|\mathbf{S}| = 1/d$.

This equality allows us to word Bragg's equation in terms of reciprocal vectors, i.e., vectors in a system with dimensions 1 over length. Define the system of vectors $\mathbf{S} = (h\mathbf{a}^* + k\mathbf{b}^* + l\mathbf{c}^*)$ that each are normal to the lattice plane with Miller indices hkl and that are of length $|\mathbf{S}(hkl)| = 1/d_{hkl}$. Waves scattered elastically by atoms on any lattice plane interfere constructively if the incoming wave vector and the scattered wave vector are of equal length $1/\lambda$ and form a triangle with vector \mathbf{S} . Geometrically, this relationship can be sketched by placing the end point of the incoming wave vector \mathbf{k}_i at the origin of reciprocal space and the scattered wave vector \mathbf{k} at the starting point of \mathbf{k}_i .

Drawing all possible vectors \mathbf{k} around the starting point of \mathbf{k}_i , we obtain a sphere, the Ewald sphere. If the reciprocal space is oriented so that the reciprocal origin is on the surface of the Ewald sphere, then constructive interference occurs if any reciprocal space vector is also on the surface of the Ewald sphere as this is the condition $\mathbf{S} = \mathbf{k} - \mathbf{k}_i$.

Figure 6 illustrates the derivation of Bragg's law again. This time, however, the atom 1 on the upper plane has been shifted by some arbitrary amount parallel to the plane. The geometrical beam path difference between the photons scattered in atoms 1

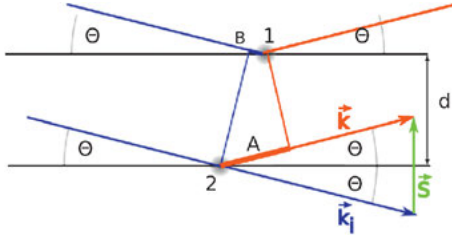


Figure 6: Schematic illustration of Bragg's law for atoms shifted parallel to the lattice plane.

and 2 is the difference between lines 1B and A2. With \mathbf{r} the vector between the two atoms, the length of line 1B is $\overline{1B} = \frac{\mathbf{r}\mathbf{k}}{|\mathbf{k}|}$, and that of A2 is $\overline{A2} = \frac{\mathbf{r}\mathbf{k}_i}{|\mathbf{k}_i|}$, which gives the overall beam path difference as

$$\Gamma = \overline{1B} - \overline{A2} = \frac{\mathbf{r}\mathbf{k}}{|\mathbf{k}|} - \frac{\mathbf{r}\mathbf{k}_i}{|\mathbf{k}_i|} = \frac{\mathbf{r}(\mathbf{k} - \mathbf{k}_i)}{|\mathbf{k}|}.$$

Notice that so far we have not really referenced the lattice plane at all. This derivation simply assumes the interference between the waves scattered by two atoms that are at a separation \mathbf{r} . Constructive interference is observed if the geometrical beam path difference is equal to an integer multiple of the wavelength λ ,

$$n\lambda = \frac{\mathbf{r}(\mathbf{k} - \mathbf{k}_i)}{|\mathbf{k}|}. \quad (15)$$

Now replacing the vector $\mathbf{k} - \mathbf{k}_i$ by the vector \mathbf{S} , the vector normal to the lattice plane, we obtain

$$n\lambda|\mathbf{k}| = \mathbf{r}\mathbf{S} \quad (16)$$

or

$$n = \mathbf{r}\mathbf{S}.$$

We observe constructive interference if the projection of the interatomic vector onto the vector normal to the lattice plane results in a vector whose length is an integer multiple of the interplanar spacing. As the length of this projection, i.e., the value of the scalar product $\mathbf{r}\mathbf{S}$, does not change when a vector normal to \mathbf{S} is added to \mathbf{r} , a shift of the atoms parallel to the lattice plane does not change the derivation of Bragg's law.

1.2 Structure factor

In Section 1.1 the basic scattering equation has been derived to yield the expression for the wave scattered by the crystal as

$$F_{\text{Cr}}(\mathbf{S}) = \left[\sum_{j=1}^{N_{\text{unit}}} f_j(\mathbf{S}) e^{2\pi i \mathbf{S} \mathbf{r}_j} \right] \left[\sum_{u=1}^U \sum_{v=1}^V \sum_{w=1}^W e^{2\pi i \mathbf{S}(u\mathbf{a} + v\mathbf{b} + w\mathbf{c})} \right] = F(\mathbf{S}) F_{\text{Lattice}}(\mathbf{S}). \quad (17)$$

The second factor in this equation is the reciprocal lattice, and the first factor is the so-called structure factor. In this section, we analyze the properties of the structure factor in more detail. As the crystal is considered to be strictly periodic, it is sufficient to carry out the summation over all atoms in a single unit cell, since the summation over all unit cells results in the second factor, the reciprocal lattice.

In the approximation of the independent atom model, the electron density distribution around each atom can be considered to have spherical symmetry. This means that the atomic form factor is a function of the reciprocal scattering vector length only. Usually, this is implicitly assumed, and the atomic form factor is denoted simply as f .

In this simplified notation, we can write the structure factor as

$$F(\mathbf{S}) = \left[\sum_{j=1}^{N_{\text{unit}}} f_j e^{2\pi i \mathbf{S} \mathbf{r}_j} \right]. \quad (18)$$

Using the equality $e^{2\pi i x} = \cos(2\pi x) + i \sin(2\pi x)$, we can write the structure factor equivalently as

$$F(\mathbf{S}) = \sum_{j=1}^{N_{\text{unit}}} f_j [\cos(2\pi \mathbf{S} \mathbf{r}_j) + i \sin(2\pi \mathbf{S} \mathbf{r}_j)]. \quad (19)$$

The scalar product can be written as

$$\mathbf{S} \mathbf{r}_j = (h\mathbf{a}^* + k\mathbf{b}^* + l\mathbf{c}^*)(x_j\mathbf{a} + y_j\mathbf{b} + z_j\mathbf{c}) = hx_j + ky_j + lz_j, \quad (20)$$

since the scalar product of a reciprocal and direct vector is either 1 or 0. At this point, it is convenient to write the last term as the product of a 1×3 row matrix with a 3×1 column matrix:

$$(h, k, l) \begin{pmatrix} x_j \\ y_j \\ z_j \end{pmatrix} = hx_j + ky_j + lz_j. \quad (21)$$

Thus the structure factor equivalently is

$$\begin{aligned} F(\mathbf{S}) &= \sum_{j=1}^{N_{\text{unit}}} f_j e^{2\pi i \mathbf{S} \mathbf{r}_j} = \sum_{j=1}^{N_{\text{unit}}} f_j [\cos(2\pi \mathbf{S} \mathbf{r}_j) + i \sin(2\pi \mathbf{S} \mathbf{r}_j)] \\ &= \sum_{j=1}^{N_{\text{unit}}} f_j [\cos(2\pi(hx_j + ky_j + lz_j)) + i \sin(2\pi(hx_j + ky_j + lz_j))] \\ &= \sum_{j=1}^{N_{\text{unit}}} a_j + i \sum_{j=1}^{N_{\text{unit}}} b_j \end{aligned} \quad (22)$$

with

$$a_j = f_j \cos(2\pi(hx_j + ky_j + lz_j)), \quad (23)$$

$$b_j = f_j \sin(2\pi(hx_j + ky_j + lz_j)). \quad (24)$$

All forms are identical, and we will use any form according to circumstance. The sums over the real and imaginary parts can be carried out independently to yield

$$F(\mathbf{S}) = A + iB = |F(\mathbf{S})|e^{i\phi} \quad (25)$$

with

$$A = \sum_{j=1}^{N_{\text{unit}}} f_j [\cos(2\pi(hx_j + ky_j + lz_j))], \quad (26)$$

$$B = \sum_{j=1}^{N_{\text{unit}}} f_j [\sin(2\pi(hx_j + ky_j + lz_j))]. \quad (27)$$

As for any complex number, its modulus is calculated as

$$|F(\mathbf{S})| = \sqrt{F(\mathbf{S})F^*(\mathbf{S})} = \sqrt{(A + iB)(A - iB)} = \sqrt{A^2 + B^2}, \quad (28)$$

and the phase angle is related to the real and imaginary parts by

$$\frac{B}{A} = \tan(\phi). \quad (29)$$

This complex number represents the wave scattered by the reciprocal lattice vector \mathbf{S} or, equivalently worded, the wave scattered at the lattice plane with Miller indices hkl . The amplitude of the scattered wave is the modulus of the structure factor, and its phase angle is given by ϕ .

The individual contributions (a_j, b_j) to the structure factor can be understood as a vector in the complex number plane. The total structure factor will have a large amplitude if all these individual complex vectors are parallel to each other. These complex vectors are parallel to each other if the scalar product $\mathbf{S} \cdot \mathbf{r}_k$ is of identical value. As $|\mathbf{S}| = 1/d_{hkl}$, the scalar product corresponds to the height of atom j between the lattice planes. Accordingly, the amplitude of the structure factor is high if all atoms are at (approximately) the same height between the lattice plane (hkl). The location of the main electron density determines the phase angle of the structure factor. If all (or most) electrons are on the lattice plane, then the phase angle is zero, and if most electrons are midway between the lattice plane, then the phase angle is 180° .

The actual intensity detected by the detector is proportional to the squared amplitude:

$$I(\mathbf{S}) = |F(\mathbf{S})|^2 = A^2 + B^2. \quad (30)$$

This intensity does not carry any information of the phase angle ϕ . Reconstruction of the atomic structure from the intensities measured in a diffraction experiment requires the phase angles to be reconstructed by a suitable algorithm. This is the scope of structure determination techniques; see, for example, Refs. [1, 4–8].

To compare the intensity of reflections \mathbf{S} and $-\mathbf{S}$, let us calculate these explicitly:

$$\begin{aligned}
 I(\mathbf{S}) &= F(\mathbf{S})F^*(\mathbf{S}) \\
 &= \left[\sum_{j=1}^{N_{\text{unit}}} f_j [\cos(2\pi(hx_j + ky_j + lz_j))] + i \sum_{j=1}^{N_{\text{unit}}} [f_j \sin(2\pi(hx_j + ky_j + lz_j))] \right] \\
 &\quad \cdot \left[\sum_{j=1}^{N_{\text{unit}}} f_j [\cos(2\pi(hx_j + ky_j + lz_j))] - i \sum_{j=1}^{N_{\text{unit}}} [f_j \sin(2\pi(hx_j + ky_j + lz_j))] \right] \\
 &= [A + iB] \cdot [A - iB] = [A^2 + B^2].
 \end{aligned} \tag{31}$$

The inversion of a vector \mathbf{S} inverts all signs of the Miller indices hkl , and we obtain:

$$\begin{aligned}
 I(-\mathbf{S}) &= F(-\mathbf{S})F^*(-\mathbf{S}) \\
 &= \left[\sum_{j=1}^{N_{\text{unit}}} f_j [\cos(-2\pi(hx_j + ky_j + lz_j))] + i \sum_{j=1}^{N_{\text{unit}}} [f_j \sin(-2\pi(hx_j + ky_j + lz_j))] \right] \\
 &\quad \cdot \left[\sum_{j=1}^{N_{\text{unit}}} f_j [\cos(-2\pi(hx_j + ky_j + lz_j))] - i \sum_{j=1}^{N_{\text{unit}}} [f_j \sin(-2\pi(hx_j + ky_j + lz_j))] \right] \\
 &= \left[\sum_{j=1}^{N_{\text{unit}}} f_j [\cos(2\pi(hx_j + ky_j + lz_j))] - i \sum_{j=1}^{N_{\text{unit}}} [f_j \sin(2\pi(hx_j + ky_j + lz_j))] \right] \\
 &\quad \cdot \left[\sum_{j=1}^{N_{\text{unit}}} f_j [\cos(2\pi(hx_j + ky_j + lz_j))] + i \sum_{j=1}^{N_{\text{unit}}} [f_j \sin(2\pi(hx_j + ky_j + lz_j))] \right] \\
 &= [A - iB][A + iB] = [A^2 + B^2] = I(\mathbf{S}).
 \end{aligned} \tag{32}$$

Thus the intensities of the wave scattered by the vector \mathbf{S} and the wave scattered by the vector $-\mathbf{S}$ are identical. This is known as Friedel's law. As this holds for any vector pair, reciprocal space symmetry always includes a center of inversion, even if the crystal structure itself does not. Friedel's law does break down if one or more atoms strongly absorb the incoming X-ray photons. Strong absorption occurs if the energy of the incident X-ray photon is close to the energy level of core electrons. Resonant effects result, and the atomic form factor takes on a more general form, $f - f' + if''$. For noncentrosymmetric structures, these complex atomic form factors result in different intensities for reflections hkl and $\bar{h}\bar{k}\bar{l}$.

The calculation of the structure factor includes the summation over all atoms in the unit cell. Instead of the explicit sum over all atoms, we can take an arbitrary atom 1 at x, y, z and apply all symmetry operations (\mathbf{W}, \mathbf{w}) of the space group to this atom. Let us denote the symmetry operation as $\mathbf{r}'_j = \mathbf{W}_j \mathbf{r}_1 + \mathbf{w}_j$, where the 3×3 matrix \mathbf{W}_j describes the rotational part of the symmetry operation, and the vector \mathbf{w}_j describes any translational part. The translational part may arise if the symmetry operation is a centering vector, a glide plane, or a screw axis or if the symmetry element is not

located at the unit cell origin. The structure factor for this equivalent set of atoms is

$$F(\mathbf{S}) = \sum_{j=1}^{N_{\text{unit}}} f_j e^{2\pi i \mathbf{S}[\mathbf{W}_j \mathbf{r}_1 + \mathbf{w}_j]}. \quad (33)$$

Applying a further arbitrary symmetry operation (\mathbf{U}, \mathbf{u}) to all symmetry operations of the group, we will generate exactly the same group. The symmetry elements will be in a different sequence, but this is irrelevant. The sum over all j symmetry operations will still copy atom 1 onto all atom positions in the unit cell. If a symmetry operation shifts an atom to a location outside the unit cell, then we can shift it back into the original cell. As the Miller indices hkl are restricted to integer numbers, the argument $2\pi(hx_j + ky_j + lz_j)$ to the cosine and sine functions remains effectively the same as we simply add an integer multiple of 2π to the argument. Thus our structure factor is

$$F(\mathbf{S}) = \sum_{j=1}^{N_{\text{unit}}} f_j e^{2\pi i \mathbf{S}(\mathbf{U}[\mathbf{W}_j \mathbf{r}_1 + \mathbf{w}_j] + \mathbf{u})} = \left[\sum_{j=1}^{N_{\text{unit}}} f_j e^{2\pi i \mathbf{S}\mathbf{U}[\mathbf{W}_j \mathbf{r}_1 + \mathbf{w}_j]} \right] e^{2\pi i \mathbf{S}\mathbf{u}}. \quad (34)$$

Since the vector \mathbf{u} is independent of the index j , it has been taken out of the summation. The term $\mathbf{S}\mathbf{U} = \mathbf{S}'$ is a symmetrically equivalent reciprocal space vector, and the equation can be written as

$$F(\mathbf{S}) = \left[\sum_{j=1}^{N_{\text{unit}}} f_j e^{2\pi i \mathbf{S}' \mathbf{r}_j} \right] e^{2\pi i \mathbf{S}\mathbf{u}} = F(\mathbf{S}') e^{2\pi i \mathbf{S}\mathbf{u}}, \quad (35)$$

and by rearranging we obtain

$$F(\mathbf{S}') = F(\mathbf{S}) e^{-2\pi i \mathbf{S}\mathbf{u}}. \quad (36)$$

If the scalar product $\mathbf{S} \cdot \mathbf{u}$ in the complex exponential $e^{-2\pi i \mathbf{S}\mathbf{u}}$ is equal to zero, then the two structure factors for a reciprocal vector \mathbf{S} and its symmetrically equivalent vector \mathbf{S}' are absolutely identical. If the scalar product is nonzero, then the amplitudes are still identical, but the phases of the two structure factors differ. As the intensity is the square of the amplitude, the intensities of all symmetrically equivalent reflections are identical. Since the translational components of the symmetry elements of the space group do not influence the intensities, the symmetry of reciprocal space is that of the point group to which the space group belongs.

Since Friedel's law always adds a center of symmetry, the reciprocal point group is the supergroup of the point group, which contains a center of symmetry. These 11 point groups are called Laue classes; see Table 1.

1.2.1 Systematic extinctions

Symmetry operations such as centering vectors, glide planes, and screw axes include a translational component that shifts the image in addition to the rotational part of

Table 1: Laue classes.

Laue group	Point groups		
$\bar{1}$	1	$\bar{1}$	
$2/m$	2	m	$2/m$
mmm	222	$mm2$	$2/m$ $2/m$ $2/m$
$4/m$	4	4	$4/m$
$4/mmm$	422	$4mm$	$42m$ $4/m$ $2/m$ $2/m$
$\bar{3}$	3	$\bar{3}$	
$\bar{3}2/m$	32	$3m$	$\bar{3}2/m$
$6/m$	6	6	$6/m$
$6/mmm$	622	$\bar{6}2m$	$6mm$ $6/m$ $2/m$ $2/m$
$m\bar{3}$	23	$m\bar{3}$	
$m\bar{3}m$	432	$\bar{4}3m$	$4/m\bar{3}2/m$

the symmetry operation. These symmetry operations have a systematic effect on the structure factors such that a subset of the structure factors systematically have zero intensity.

Centering vectors, most glide planes, and the 2_1 screw axes create a pair of symmetrically equivalent atoms. The d -glide planes and the other screw axis create a larger group. For any atom k in the asymmetric unit we can list the atoms created by this special symmetry operation in a subset $\{\mathbf{r}_k, [\mathbf{W}_1\mathbf{r}_k + \mathbf{w}_1], \dots\}$. The complete unit cell content is achieved by applying all other symmetry operations to this subset. The contribution of this subset to the structure factor is

$$f_k [e^{2\pi i \mathbf{S} \cdot \mathbf{r}_k} + e^{2\pi i \mathbf{S} \cdot [\mathbf{W}_1 \mathbf{r}_k + \mathbf{w}_1]} + \dots] = f_k [e^{2\pi i \mathbf{S} \cdot \mathbf{r}_k} + e^{2\pi i \mathbf{S} \cdot \mathbf{W}_1 \mathbf{r}_k} e^{2\pi i \mathbf{S} \cdot \mathbf{w}_1} + \dots]. \quad (37)$$

This contribution to the structure factor will not result in any special value for all possible and arbitrary atom positions \mathbf{r}_k , except for all those reciprocal space vectors for which the symmetry operation \mathbf{W} is a neutral operation with $\mathbf{S} = \mathbf{S}\mathbf{W}$. For the centering operations, the symmetry matrix \mathbf{W} is a unit matrix, and the relationship holds for all reciprocal space vectors. For glide planes, the relationship holds for those reciprocal space vectors that are within that plane through reciprocal origin that is parallel to the glide plane. Finally, for the screw axes, the relationship holds for all reciprocal space vectors along a line through reciprocal origin parallel to the screw axis. For this set of reciprocal space vectors, the contribution to the structure factor is

$$f_k e^{2\pi i \mathbf{S} \cdot \mathbf{r}_k} [1 + e^{2\pi i \mathbf{S} \cdot \mathbf{w}_1} + \dots]. \quad (38)$$

The value of the term in square brackets is independent of the atom position, and thus its value is a property of the space group, not a property of the special crystal structure. The term may be zero for a set of the reflections for which $\mathbf{S} = \mathbf{S}\mathbf{W}$. If this term is zero, then the contribution of this set of atoms to the structure factor is zero. The

complete structure factor will also be zero as the complete structure factor results from a sum over all atoms k in the asymmetric unit and all further symmetry operations.

At this point, it is easier to break the general discussion into sections for the individual symmetry types.

Let us first consider those centering operations that create exactly one copy of the original atoms. These are A-, B-, C-, and I-Bravais lattices. The term in square brackets in equation (38) consists of the first two terms $1 + e^{2\pi i \mathbf{S}\mathbf{w}}$. This term will be zero if the second term will be equal to -1 . The necessary condition for this is that the scalar product $\mathbf{S}\mathbf{w} = hw_x + kw_y + lw_z$ is equal to $\frac{1}{2}$ since $[1 + e^{2\pi i(1/2)}] = [1 - 1] = 0$. As an example, take the body-centered Bravais lattice. Here $\mathbf{w} = [1/2, 1/2, 1/2]$, and the condition for the term to be equal to zero is $\mathbf{S}\mathbf{w} = (h/2 + k/2 + l/2) = (h + k + l)/2 = 1/2$. This condition is fulfilled for all reciprocal space vectors for which $h + k + l$ is $2n + 1$, an odd number.

For the face-centered Bravais lattice, we have three centering operations with $\mathbf{w}_1 = [1/2, 1/2, 0]$, $\mathbf{w}_2 = [1/2, 0, 1/2]$, and $\mathbf{w}_3 = [0, 1/2, 1/2]$. Accordingly, the term of equation (38) in square brackets $[1 + e^{2\pi i \mathbf{S}\mathbf{w}_1} + e^{2\pi i \mathbf{S}\mathbf{w}_2} + e^{2\pi i \mathbf{S}\mathbf{w}_3}]$ will be equal to zero if one of the exponentials is equal to -1 and the other two cancel. This is fulfilled for any reciprocal space vector with $h + k = 2n + 1$, or $h + l = 2n + 1$, or $k + l = 2n + 1$. Table 2 lists the conditions for all Bravais lattice types.

Table 2: Centering operations and reflection conditions for Bravais lattices.

Bravais lattice	Centering operation(s)	Reflection condition	
		$l = 0$ for	$l \neq 0$ for
<i>P</i>	[0, 0, 0]	None	all
<i>A</i>	[0, 1/2, 1/2]	$k + l = 2n + 1$	$k + l = 2n$
<i>B</i>	[1/2, 0, 1/2]	$h + l = 2n + 1$	$h + l = 2n$
<i>C</i>	[1/2, 1/2, 0]	$h + k = 2n + 1$	$h + k = 2n$
<i>I</i>	[1/2, 1/2, 1/2]	$h + k + l = 2n + 1$	$h + k + l = 2n$
<i>F</i>	[0, 1/2, 1/2]	$h + k = 2n + 1$	$h + k = 2n$
	[1/2, 0, 1/2]	or $h + l = 2n + 1$	and $h + l = 2n$
	[1/2, 1/2, 0]	or $k + l = 2n + 1$	and $k + l = 2n$
<i>R</i>	[1/3, 2/3, 1/3]	$-h + k + l \neq 3n$	$-h + k + l = 3n$
	[2/3, 1/3, 2/3]		eee; ooo

The last column lists the reflection conditions as listed for each space group in the International Tables for Crystallography and in standard text books on diffraction. Keep in mind that some intensities may still be zero for a given crystal structure. This will, however, be a result of the special atom arrangement in this structure and not a systematic effect due to the presence of a symmetry operation that includes a translational component.

All but the d -glide planes produce a pair of atoms. Again, the term in square brackets of equation (38) is $1 + e^{2\pi i \mathbf{S}\mathbf{w}}$. Consider a c -glide plane normal to the b -axis with $\mathbf{w} = [0, 0, 1/2]$. The mirror operation is a neutral element for $[h, 0, l]$, and only these reciprocal space vectors are affected. With $\mathbf{S}\mathbf{w} = (h \cdot 0 + 0 \cdot 0 + l/2) = l/2 = 1/2$, the condition for the square term to be zero is $l = 2n + 1$. Analogous arguments hold for the other glide plane types and the other glide plane orientations. Table 3 lists the glide planes normal to a b -axis and the resulting conditions. For a full table, refer to the International Tables or to standard text books.

Table 3: Glide components and reflection conditions for glide planes normal to a b -axis.

Glide plane	Glide component(s)	Reflection condition	
		$l = 0$ for $h0l$ with	$l \neq 0$ for $h0l$ with
a	$[1/2, 0, 0]$	$h = 2n + 1$	$h = 2n$
c	$[0, 0, 1/2]$	$l = 2n + 1$	$l = 2n$
n	$[1/2, 0, 1/2]$	$h + l = 2n + 1$	$h + l = 2n$
d	$[1/4, 0, 1/4]$	$h + l \neq 4n$	$h + l = 4n$

For all screw axes, the rotational part of the symmetry operation results in a neutral operation for the reciprocal space vectors along the line through reciprocal origin that is parallel to the screw axis. As an example, consider a 2_1 screw axis parallel to the b -axis. The reciprocal space vectors affected by the screw axis are the $[0, k, 0]$ vectors. The translational component is $\mathbf{w} = [0, 1/2, 0]$, and the term in square brackets is zero since $\mathbf{S}\mathbf{w} = (0 \cdot 0 + k \cdot 1/2 + 0 \cdot 0) = k/2 = 1/2$. Accordingly, reciprocal space vectors $[0, k, 0]$ with $k = 2n + 1$ have zero intensity. Corresponding arguments hold for the other screw axis types.

1.2.2 Projections and slices in direct and reciprocal space

In this section, we derive the effect that the limitation of either the Fourier or direct space has on the other space. These considerations will be helpful later on when we consider the effect of limiting the diffraction signal to pure elastic scattering or to integrate the diffraction signal over all inelastically scattered components.

In its full form the structure factor is

$$F(hkl) = \sum_{j=1}^{N_{\text{unit}}} f_j [e^{2\pi i (hx_j + ky_j + lz_j)}]. \quad (39)$$

We can now arbitrarily consider a slice in reciprocal space at $l = 0$:

$$F(hk0) = \sum_{j=1}^{N_{\text{unit}}} f_j [e^{2\pi i (hx_j + ky_j + 0z_j)}]. \quad (40)$$

The net effect of the limitation to $l = 0$ is that all z components of the atoms have become irrelevant. The identical result will be achieved if we project all atoms along the c -axis into the $xy0$ plane. Essentially, we have done an integration of direct space along the c -axis.

1.3 Debye–Waller factor

So far we assumed that the atoms were at rest. As the book is concerned with time-resolved crystal structures, it should be obvious that we need to consider atoms in motion as well. Although the average crystal structure remains unchanged as a function of time, atoms are never at rest but will oscillate around their average position due to the thermal energy. Due to the interactions with the surrounding atoms, an individual atom is located within a potential well. The detailed shape of this potential depends on the chemical bonds involved and the local symmetry around the given atom. For the moment, we simplify this potential to a harmonic potential. This is in fact a fairly good approximation to any potential as long as the energy of the atom is small. Each atom moves around within this potential well. If we consider the motion of two atoms that are far apart, we can expect that the motions of these two atoms are completely independent. This breaks down as we consider atoms that are much closer to each other and ultimately are immediate neighbors. The displacement of one atom will exert a force on the neighboring atoms and will displace these neighboring atoms in turn. This correlated movement can be described as a common displacement wave or a collective excitation of the lattice, a phonon. These will be dealt with in more detail in later chapters.

Let us first use a bit of a hand-waving argument to derive the influence of this independent atom movement onto the scattered amplitude. We assume that the data collection time is long compared to the duration of a single oscillation of any given atom. With this assumption, we can describe the time-averaged atom position by a probability density function. Given a harmonic potential, the probability density function (pdf) of the atoms is a Gaussian distribution:

$$\text{pdf}(r) = \frac{1}{\sqrt{2\pi\sigma}} e^{-\frac{(r-r_0)^2}{2\sigma^2}}. \quad (41)$$

The time-averaged electron density of an atom can thus be described as the convolution of the electron density of an atom at rest by the probability density function

$$\rho_{\text{th}}(\mathbf{r}) = \rho_{\text{st}}(\mathbf{r}) \otimes \text{Gaussian}. \quad (42)$$

Since the scattered amplitude is the Fourier transform of the electron density, for the contribution by a single atom that is undergoing thermal motion around its average position, we obtain

$$\text{Fourier}(\rho_{\text{th}}(\mathbf{r})) = \text{Fourier}(\rho_{\text{st}}(\mathbf{r})) \cdot \text{Fourier}(\text{Gaussian}). \quad (43)$$

The Fourier transform of the electron density is the atomic form factor, and since the Fourier transform of a Gaussian distribution is again a Gaussian distribution, for the atomic form factor of an atom with thermal motion, we obtain

$$f_{\text{th}}(\mathbf{S}) = f_{\text{st}}(\mathbf{S}) \cdot e^{-8\pi^2 \langle u^2 \rangle \left(\frac{\sin(\Theta)}{\lambda}\right)^2}. \quad (44)$$

Here $\langle u^2 \rangle$ is the mean square displacement of the atom, which is in the range of 0.01 \AA^2 . The right factor in equation (44) is commonly called the Debye–Waller factor. The argument in the exponent can be expressed equally as

$$\begin{aligned} -8\pi^2 \langle u^2 \rangle \left(\frac{\sin(\Theta)}{\lambda}\right)^2 &= -2\pi^2 \langle u^2 \rangle \left(\frac{2\sin(\Theta)}{\lambda}\right)^2 = -\frac{1}{2}(2\pi)^2 h^2 \langle u^2 \rangle \\ &= -B \left(\frac{\sin(\Theta)}{\lambda}\right)^2 = -\frac{1}{2} Q^2 \langle u^2 \rangle. \end{aligned} \quad (45)$$

A comparison of the first and fourth expressions shows that $B = 8\pi^2 \langle u^2 \rangle$. The term B is more commonly used in the realm of neutron diffraction. Before we look at a more rigorous derivation, let us analyze the influence of the Debye–Waller factor on the structure factor and respectively the observed intensities. The exponent is a scalar function of the diffraction angle and respectively of the length of the reciprocal vector. Accordingly, the effect of the Debye–Waller factor is a dampening of the scattered amplitude with increasing scattering angle.

As the interaction time between the X-ray photon and the electron cloud of an atom is much faster than the vibrational speed of the atom itself, we can also describe the diffraction as the time average of many snapshots with the structure at rest but with the atoms slightly off their respective average position. As explained in the previous section, the structure factor decreases if the height distribution of the atoms between the lattice planes increases. Recall that the d -spacing of a lattice plane is the inverse value of the length of the reciprocal lattice vector $d_{hkl} = 1/|\mathbf{S}_{hkl}|$. With increasing distance to the origin of reciprocal space, i.e., with increasing Bragg angle Θ , the root mean square displacement $\sqrt{\langle u^2 \rangle}$ thus becomes an increasing fraction of the lattice plane spacing d_{hkl} . As a consequence, the atoms are more widely *spread* between the lattice planes, and accordingly the structure factor will diminish with increasing Bragg angle just as derived in the rough derivation above. A second consequence will become clear in the section on disordered structures and will be just mentioned at this point. If we consider the individual atomic vibrations as independent, then the structure can be considered as a disordered structure in which the atoms are randomly displaced from their ideal time-averaged positions. This random displacement will give rise to an isotropically distributed diffuse background intensity. Essentially, the intensity lost from the Bragg reflections is distributed into the reciprocal space between the Bragg reflections. If, on the other hand, the atoms vibrate collectively as phonons, then the displacement can be described by a displacement wave. The scattering effect of such a displacement wave is a satellite reflection at a distance that is the inverse

of the wavelength. A multitude of phonons with different wavelengths is excited in the crystal. These phonons have wavelength distributed over many multiples of the unit cell length. Thus the corresponding scattering is typically broadened into a diffuse peak underneath the Bragg reflections, the so-called thermal diffuse scattering. If the amplitude of phonons in a particular direction is especially strong, then we can observe a streak of diffuse scattering in reciprocal space.

Now let us look at a more rigorous derivation of the Debye–Waller factor; see also Refs. [11, 12]. At any instance in time, we can write the current atomic position as the sum of the average position plus a displacement:

$$\mathbf{r}_j = \langle \mathbf{r}_j \rangle + \mathbf{u}_j. \quad (46)$$

The structure factor can then be written as

$$F(\mathbf{S}) = \sum_{j=1}^N f_j(|\mathbf{S}|) e^{2\pi i(\mathbf{S}(r_j) + \mathbf{u}_j)} = \sum_{j=1}^N f_j(|\mathbf{S}|) e^{2\pi i(\mathbf{S}(r_j))} e^{2\pi i(\mathbf{S}\mathbf{u}_j)}. \quad (47)$$

This term needs to be averaged over time to yield:

$$\langle F(\mathbf{S}) \rangle = \left\langle \sum_{j=1}^N f_j(|\mathbf{S}|) e^{2\pi i(\mathbf{S}(r_j))} e^{2\pi i(\mathbf{S}\mathbf{u}_j)} \right\rangle. \quad (48)$$

The atomic form factor and the average atom position are of course time-independent variables and can be taken out of the average operation:

$$\langle F(\mathbf{S}) \rangle = \sum_{j=1}^N f_j(|\mathbf{S}|) e^{2\pi i(\mathbf{S}(r_j))} \langle e^{2\pi i(\mathbf{S}\mathbf{u}_j)} \rangle. \quad (49)$$

The time average of the last factor can be obtained by expanding this term in a power series:

$$\langle e^{2\pi i\mathbf{S}\mathbf{u}} \rangle_t = 1 - \frac{1}{2}(2\pi)^2 \langle (\mathbf{S}\mathbf{u})^2 \rangle_t + \frac{1}{24}(2\pi)^4 \langle (\mathbf{S}\mathbf{u})^4 \rangle_t - \dots \quad (50)$$

We can compare this power series to that of a Gaussian function, conveniently written as the Debye–Waller factor:

$$e^{-\frac{1}{2}(2\pi)^2 \langle (\mathbf{S}\mathbf{u})^2 \rangle_t} = 1 - \frac{1}{2}(2\pi)^2 \langle (\mathbf{S}\mathbf{u})^2 \rangle_t + \frac{1}{8}(2\pi)^4 \langle (\mathbf{S}\mathbf{u})^2 \rangle_t^2 - \dots \quad (51)$$

As the first two terms are identical, we can approximate for small displacements:

$$\langle e^{2\pi i\mathbf{h}\mathbf{u}} \rangle_t \approx e^{-\frac{1}{2}(2\pi)^2 \langle (\mathbf{h}\mathbf{u})^2 \rangle_t}, \quad (52)$$

which is exactly the expected result. Let us, however, test this approximation with commonly observed values for the atomic displacement parameter. With $\langle u^2 \rangle$ and

MoK α at 0.709 Å and a diffraction angle of 30°, the argument to the exponential function becomes

$$(2\pi)^2 \langle (\mathbf{S}\mathbf{u})^2 \rangle_t = (2\pi)^2 \frac{2 \sin^2(30^\circ) 0.01 \text{ \AA}^2}{(0.709 \text{ \AA})^2} = 0.785. \quad (53)$$

This is by no means a small value, and the cut off after the linear term is a gross approximation! This simple derivation apparently is flawed although it seems to give the correct result. The time average actually needs to be taken as an average over all individual modes of vibration:

$$\langle e^{2\pi i \mathbf{S}\mathbf{u}} \rangle_t = \langle e^{2\pi i \mathbf{h} \sum_k \mathbf{u}_k} \rangle_t. \quad (54)$$

In the harmonic approximation, all individual modes are independent, and the sum in the exponent can be replaced by a product of individual exponential terms:

$$\langle e^{2\pi i \mathbf{S} \sum_k \mathbf{u}_k} \rangle_t = \prod_k \langle e^{2\pi i \mathbf{S}\mathbf{u}_k} \rangle_t. \quad (55)$$

The amplitude of an individual mode is much smaller and the approximation by a power series terminated after the linear term is justified:

$$\langle e^{2\pi i \mathbf{S} \sum_k \mathbf{u}_k} \rangle_t = \prod_k \left(1 - \frac{1}{2} (2\pi \mathbf{S}\mathbf{u}_k)^2 \right) \approx e^{-\frac{1}{2} (2\pi)^2 \langle (\mathbf{S}\mathbf{u})^2 \rangle_t}. \quad (56)$$

The last approximation holds for the limit of large N , and we now have the result that

$$\langle e^{2\pi i \mathbf{S}\mathbf{u}} \rangle_t \approx e^{-\frac{1}{2} (2\pi)^2 \langle (\mathbf{S}\mathbf{u})^2 \rangle_t}. \quad (57)$$

Finally, we make the approximation that the individual modes are displaced isotropically, and we can separate the average over the scalar product into the average over the displacement to yield

$$\langle e^{2\pi i \mathbf{S}\mathbf{u}} \rangle_t \approx e^{-\frac{1}{2} (2\pi)^2 \langle \mathbf{S}^2 \rangle_t \langle u^2 \rangle_t}. \quad (58)$$

If the atomic displacements are not isotropically distributed, then we can describe their effect on the structure factor as

$$F(hkl) = \sum_{j=1}^N f_j(|hkl|) e^{2\pi i (hx_j + ky_j + lz_j)} e^{-2\pi^2 h_i U_{ij} h_j}. \quad (59)$$

Here the U_{ij} are dimensionless parameters that describe the effects of anisotropic displacements. We can now define the tensor \mathbf{U}_L as

$$\mathbf{U}_L = \begin{pmatrix} \frac{\langle \Delta x^2 \rangle}{\mathbf{a}^* \mathbf{a}^*} & \frac{\langle \Delta x \Delta y \rangle}{\mathbf{a}^* \mathbf{b}^*} & \frac{\langle \Delta x \Delta z \rangle}{\mathbf{a}^* \mathbf{c}^*} \\ \frac{\langle \Delta x \Delta y \rangle}{\mathbf{a}^* \mathbf{b}^*} & \frac{\langle \Delta y^2 \rangle}{\mathbf{b}^* \mathbf{b}^*} & \frac{\langle \Delta y \Delta z \rangle}{\mathbf{b}^* \mathbf{c}^*} \\ \frac{\langle \Delta x \Delta z \rangle}{\mathbf{a}^* \mathbf{c}^*} & \frac{\langle \Delta y \Delta z \rangle}{\mathbf{b}^* \mathbf{c}^*} & \frac{\langle \Delta z^2 \rangle}{\mathbf{c}^* \mathbf{c}^*} \end{pmatrix}. \quad (60)$$

This tensor can be transformed to its principal axes. In the transformed state the tensor elements along the main diagonal give access to the mean square displacements along each of these axes. Keep in mind that even the anisotropic atomic displacement parameters assume a harmonic potential. With higher-order terms the effect of an anharmonic potential can be described as well.

1.4 Patterson function

To understand the relationship between the observed intensities and the structure, especially the structure as a function of time, we start with a derivation of the so-called Patterson function. Recall that the intensity is the product of the structure factor with its conjugate complex, $I(\mathbf{S}) = F(\mathbf{S}) \cdot F^*(\mathbf{S})$. Now considering the inverse Fourier transform of the intensity, we obtain

$$\text{Fourier}^{-1}[I(\mathbf{S})] = \text{Fourier}^{-1}[F(\mathbf{S}) \cdot F^*(\mathbf{S})]. \quad (61)$$

The Fourier transform of the product on the right-hand side can be split into the convolution of the individual Fourier transforms:

$$\text{Fourier}^{-1}[I(\mathbf{S})] = \text{Fourier}^{-1}[F(\mathbf{S})] \otimes \text{Fourier}^{-1}[F^*(\mathbf{S})]. \quad (62)$$

If we consider X-ray diffraction, then the Fourier transform of the structure factor is the electron density $\rho(\mathbf{r})$. The Fourier transform of the conjugate complex structure factor is the conjugate complex of the electron density at $-\mathbf{r}$:

$$\begin{aligned} \text{Fourier}^{-1}[I(\mathbf{S})] &= \rho(\mathbf{r}) \otimes \rho^*(-\mathbf{r}) \\ &= \rho(\mathbf{r}) \otimes \rho(-\mathbf{r}) = P(\mathbf{u}). \end{aligned} \quad (63)$$

Here we have replaced the complex conjugate of the electron density by the electron density itself, since the electron density is of course a real-valued number. Thus the inverse Fourier transform of the intensity is the convolution of the electron density with the electron density inverted at the origin. Such a convolution is an autocorrelation function. An autocorrelation function has maxima at \mathbf{u} if the electron density has high values at \mathbf{r} and $\mathbf{r} + \mathbf{u}$. Thus the Patterson function $P(\mathbf{u})$ has maxima at the positions corresponding to interatomic vectors \mathbf{u} , schematically illustrated in Figure 7.

In the classical use of the Patterson function, the intensities are restricted to the integrated intensity at the reciprocal lattice points, i.e., at the points where $\mathbf{S} = h\mathbf{a}^* + k\mathbf{b}^* + l\mathbf{c}^*$. For this case, the Fourier transform in equation (63) reduces to a Fourier series:

$$P(\mathbf{u}) = \sum_{j=1}^{N_{\text{unit}}} |F(hkl)|^2 e^{-2\pi i(hu + kv + lw)}. \quad (64)$$

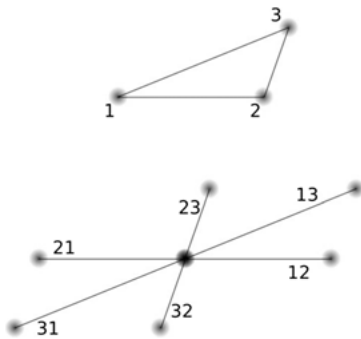


Figure 7: Relationship between a simple molecule, top, and the Patterson function, bottom. The numbers at the Patterson vectors indicate the corresponding atom pair.

Here $\mathbf{u} = u\mathbf{a} + v\mathbf{b} + w\mathbf{c}$ is the vector in the Patterson space. Although the Patterson space is a direct space with base vectors that have a dimension of lengths, it is a good idea to separate the Patterson space from the usual direct space of the crystal structure, since the information in the former is related to interatomic distances, not to the actual structure. The Patterson space has the identical periodicity as the direct space, as can easily be proven if we consider the value of the Patterson space at a point $\mathbf{u}' = (u + m)\mathbf{a} + (v + n)\mathbf{b} + (w + o)\mathbf{c}$ with integer numbers m, n, o :

$$\begin{aligned} P(\mathbf{u}') &= \sum_{hkl} |F(hkl)|^2 e^{-2\pi i(h(u+l) + k(v+m) + l(w+n))} \\ &= \sum_{hkl} |F(hkl)|^2 e^{-2\pi i(hu + kv + lw)} e^{-2\pi i(hm + kn + lo)}. \end{aligned} \quad (65)$$

As $(hm + kn + lo)$ is an integer number for any integer h, k, l and integer m, n, o , the second exponential function equals one, and thus $P(\mathbf{u}') = P(\mathbf{u})$.

If, on the other hand, the intensity distribution throughout complete reciprocal space is taken into the Fourier transform, a generalized Patterson function results. As the Fourier transform is now a Fourier integral rather than a Fourier series, the generalized Patterson function is no longer periodic. This generalized Patterson function is related to the pair distribution function obtained in a powder diffraction experiment and to the 3D-PDF.

1.5 X-ray scattering is integration in time, and neutron is purely elastic scattering

The Patterson function $P(\mathbf{u})$ defined in the previous section gives the probability to find a pair of atoms at distance \mathbf{u} . At first sight, it may sound unusual to refer to the Patterson function with a probability in mind. As long as we consider a perfect crystal structure with strict periodicity, the probability to find an atom pair at distance \mathbf{u} and an equivalent pair at distance $\mathbf{u}' = \mathbf{u} + m\mathbf{a} + n\mathbf{b} + o\mathbf{c}$, where m, n, o are integer numbers, is of course the same. As soon as we allow the structure to contain (randomly

distributed) defects, the concept of a probability to find a pair of atoms at a separation \mathbf{u} becomes more evident.

This concept can be extended into a consideration of the probability to find a pair of atoms not only at a given distance, but also after some time [13]. This generalized four-dimensional Patterson function is the autocorrelation function of the space and time-dependent electron density:

$$\begin{aligned} P(\mathbf{u}, t) &= \iint \rho(\mathbf{R}, T) \rho(\mathbf{u} + \mathbf{R}, t + T) d\mathbf{R} dT \\ &= \rho(\mathbf{r}, t) \otimes \rho(-\mathbf{r}, -t). \end{aligned} \quad (66)$$

In the previous section, we focused on a static structure. The Patterson function was defined as the inverse Fourier transform of the observed intensity. Accordingly, the intensity is the Fourier transform of the Patterson function. Likewise, we can now define the Fourier transform of the generalized time-dependent Patterson function. This will give a generalized intensity in the four-dimensional space,

$$|F(\mathbf{S}, \nu)|^2 = \iint P(\mathbf{u}, t) e^{2\pi i(\mathbf{S}\mathbf{u} + \nu t)} d\mathbf{u} dt. \quad (67)$$

Here $\mathbf{S} = \mathbf{k} - \mathbf{k}_i$ is the usual reciprocal space vector that describes the change of the incoming wave vector \mathbf{k} . The frequency ν describes the change of frequency between the incoming and scattered radiations.

The following special cases will help us to illustrate the concept of this generalized Patterson function and the information that is present in a diffraction experiment.

In general, the four-dimensional Patterson function $P(\mathbf{u}, t)$ describes the probability to find a pair of atoms separated by a vector \mathbf{u} after time t . At the special vector $\mathbf{u} = 0$ the generalized Patterson function describes the probability to find any atom at the same position after time t :

$$P(0, t) = \iint \rho(\mathbf{R}, T) \rho(\mathbf{R}, t + T) d\mathbf{R} dT. \quad (68)$$

As in any autocorrelation function, the integration over time T serves to collect all pairs of atoms at position \mathbf{u} at time interval t throughout all times T . The integration over space \mathbf{R} serves to average over all atoms irrespective of their actual position. At the point $\mathbf{u} = 0$ the generalized Patterson function is related to the diffusion of atoms. If the atoms do not diffuse away from their average position, then the value $P(0, t)$ is constant for all times larger than the vibrational period of the atoms. If atoms do undergo a diffusion process, then the probability to find an atom at the identical position decreases with increasing time interval t .

In a neutron diffraction experiment, it is possible to restrict the measured intensity to the purely elastic scattering. A corresponding X-ray experiment currently requires ultrahigh energy resolution, which in turn requires a long exposure time. Thus a purely elastic X-ray scattering experiment is usually not performed for time-resolved

experiments. Still, it is instructive for the moment to consider a purely elastic X-ray diffraction experiment. Accordingly, we obtain the generalized intensity at no change in frequency ν :

$$|F(\mathbf{S}, 0)|^2 = \int \int P(\mathbf{u}, t) e^{2\pi i(\mathbf{S}\mathbf{u})} d\mathbf{u} dt. \quad (69)$$

As the complex exponentiation is independent of time t , we can interchange the integrations and write

$$|F(\mathbf{S}, 0)|^2 = \int \left[\int P(\mathbf{u}, t) dt \right] e^{2\pi i(\mathbf{S}\mathbf{u})} d\mathbf{u}. \quad (70)$$

The integration over time t gives the time-averaged Patterson function or, in other words, the autocorrelation function of the time-averaged electron density. Recall the relationship between the structure factor $F(hk0)$ and the structure projected or averaged along the c -axis. This is the corresponding term in time. Thus the purely elastic scattering is related to the time-averaged electron density distribution.

At the other extreme, the measurement may include all inelastic contributions. This is the normal case for X-ray diffraction as most X-ray detectors do not have sufficient energy resolution to distinguish between purely elastically and inelastically scattered photons. At a common X-ray energy around 12 keV, the room-temperature phonon energy of 25 meV causes a very small energy change of the scattered photon. A very high resolution detector setup is required to detect this small energy change. This high resolution in turn requires long measurement times, excluding excellent time resolution for time-resolved experiments. Accordingly, the measured intensity usually is the integral over all frequencies ν :

$$\int |F(\mathbf{S}, \nu)|^2 d\nu = \int \int [P(\mathbf{u}, t) dt] e^{2\pi i(\mathbf{S}\mathbf{u})} \delta(t) d\mathbf{u} dt. \quad (71)$$

In analogy to the integration over all coordinates along the c -axis to obtain $F(hk0)$, we now have the integration over all frequencies to obtain the generalized Patterson function $P(\mathbf{u}, 0)$ at time difference zero:

$$\int |F(\mathbf{S}, \nu)|^2 d\nu = \int P(\mathbf{u}, 0) e^{2\pi i(\mathbf{S}\mathbf{u})} d\mathbf{u}. \quad (72)$$

This corresponds to a snapshot in time with a momentarily static structure. As the counting time for a diffraction experiment is nonzero, the actual measured intensity corresponds to a time average of these individual snapshots.

1.6 Averaging in time and space

In the previous section, we pointed out that the X-ray diffraction pattern corresponds to a snapshot in time. As the exposure time typically extends over a finite time span,

an average is performed over the various structure snapshots during this time span. Simultaneously, an average in space is performed as well. Here we need to distinguish two aspects of the average in space related to the coherence of the incoming X-rays and the structural coherence of the sample.

The term coherence length refers to the extend over which the incoming X-ray photons are coherent, i.e., have a fixed phase relationship. The coherence length varies widely for different experimental setups. Along the X-ray beam path, the longitudinal coherence length ranges from a few hundred nm for a laboratory source [14] to several μm at a well-collimated coherent synchrotron beam line. The transverse coherence length is typically roughly half as wide. With respect to the crystal structure, the coherence length refers to the extend over which the lattice is reasonably perfect. The structural coherence length is thus related to the mosaicity of the crystal structure. The structural coherence is thus a sample-dependent value that widely varies from a few hundred nm of an ideal imperfect crystal [1, 15, 16] to several mm in a perfect silicon crystal. Generally, however, it will, at least in the transverse direction, be larger than the X-ray coherence length. Figure 8 illustrates these aspects schematically. Within each 5×5 block, the structure is locally coherent, and small angle boundary dislocations and other similar defects separate these blocks from each other.

With respect to diffraction, the term coherent diffraction refers to the interference of waves with a strict phase relationship. The waves can add up constructively only if the phase difference is an integer multiple of 2π . The total intensity is the square of the sum of all individual amplitudes. If waves overlap incoherently, then no strict phase relationship exists, and the total intensity is the sum of the individual intensities. In Figure 8 the black waves are coherent with respect to each other but incoherent with respect to the red wave group.

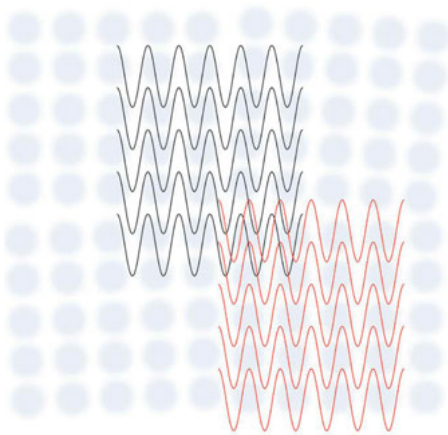


Figure 8: Schematic illustration of coherence within the structure and between the X-ray photons.

Recall that we split the equation for the structure factor, equation (17), into two parts, the sum over all atoms in one unit cell and the sum over all unit cells. The implicit assumption behind this separation is that the structure is structurally coherent in the sense that we assume that all unit cells are periodically spaced and that their unit cell contents are all equal. As the sum over all unit cells builds up the reciprocal lattice, we can see that the structural coherence is a necessary condition for the existence of Bragg reflections. At the same time, this separation implicitly assumes as well that the radiation is coherent as we assume a fixed and well-defined phase relationship in the propagating wave field. In the transverse direction, we assume identical phases and, in the longitudinal direction, a wave that is periodic in space. Without either of these two coherence aspects, the scattering at each individual atom would occur at a random phase, and the interference by the individual secondary waves radiated by each atom would produce random noise only.

The reverse conclusion is that if Bragg reflections are observed in an experiment the coherence conditions are met sufficiently well. In a standard analysis the intensity of the Bragg reflections is integrated over a finite region in reciprocal space and assigned to a triplet of integer hkl values. Within the scope of this analysis, we automatically assume that the crystal is strictly periodic in space.

In the following section on disordered structures, we deal in more detail with the average in space, and we defer the detailed discussion to that section. For a moment, it is sufficient to realize that as long as we can observe Bragg reflections, the crystal is periodic in space, at least on the average. Small deviations will affect the Bragg intensities only in a minor sense, similar to the effect of the thermal motion in Section 1.3 on the Debye–Waller factor. Under these conditions, we can describe the average electron density at a position \mathbf{r}_{unit} within a single average unit cell as

$$\langle \rho(\mathbf{r}_{\text{unit}}) \rangle = \frac{1}{N} \int \sum_{\mathbf{R}} \rho(\mathbf{r}_{\text{unit}} + \mathbf{R}, T) dT, \quad (73)$$

where the summation is over all N unit cells. We can write the contribution of an atom to the structure factor as the combination of the average atomic form factor at the average position with a local deviation: $f_j = \langle f \rangle + \Delta f_j$ and $\mathbf{r}_j = \langle \mathbf{r} \rangle + \Delta \mathbf{r}_j$ to obtain a general structure factor by calculating a sum over all atoms in the structure:

$$\langle F(\mathbf{S}) \rangle = \sum_{j=1}^{N_{\text{at}}} (\langle f \rangle + \Delta f_j) e^{2\pi i \mathbf{S}(\langle \mathbf{r} \rangle + \Delta \mathbf{r}_j)}. \quad (74)$$

The average atomic form factor and the average position are simply the arithmetic averages of the corresponding values. Note that at this point we have not specified whether the average is taken as a sum over all atom positions at fixed time or as the average over all states at a fixed position at different times or as a combination of both. If we exclude diffusion, then the time-averaged form factor will not change with time

at any position k but will remain identical to $f_j = \langle f \rangle + \Delta f_j$. We obtain the average form factor only by averaging in space over all symmetrically equidistant sites in all unit cells.

If a site in the unit cell is occupied by more than a single-atom species, then equation (73) can be split into the outer sum over all sites in the unit cell and the inner sum over all atom species that occupy this particular site. The average form factor at a site k in the unit cell can then be expressed as the individual form factors for atom type j multiplied by the probability to find an atom of type j at the site k . This probability is usually referred to as occupancy Occ_j of site k by atom type j , $\langle f_k \rangle = \sum_j \text{Occ}_j \cdot f_j$.

Due to thermal motion, the atom will always be displaced from the average position, at least by a possibly very small amount as long as we look at the structure at time differences that are smaller than the vibrational period of the atoms. As pointed out in the section on the Patterson function, the integration over all energies performed by the X-ray detector corresponds to a single snapshot in time with the structure momentarily frozen, and the X-ray intensity is the average over many such snapshots. Within such a single snapshot, the atoms at long distances are displaced independently from each other. At short distances, atoms tend to be displaced predominantly by acoustic phonons and, as a consequence, tend to be displaced along similar directions and by similar amounts. As a consequence, the interatomic distance distributions as seen by the pair distribution function (PDF) tend to be narrower at shorter distances, as will be discussed in more detail in the section on the PDF method later in this chapter. The average over all atom positions within such a single snapshot results in an electron density that is “smeared” out by the probability density function that describes the probability to find an atom at a given position.

Averaging the local position over many snapshots, we will see the atom subject to the same probability density function. At this state, the time average becomes identical to the space average. Currently, all X-ray diffraction patterns require an exposure time that is long compared to the vibrational periodicity of the individual atoms. The experimentally obtained diffraction pattern will therefore consist of many individual snapshots, which all see an individual atom at slightly different positions. Effectively, the long exposure time averages the structure in time.

This holds in a slightly different way for any stroboscopic experiment. In such an experiment the final exposure consists of a series of many individual short exposures that by themselves do not yield sufficient intensity. The sum of these individual exposures comprises the final data set. At first glance, this time average appears to be identical to the time average of a single long exposure, and indeed, for any exposure time beyond several picoseconds, it is exactly the same. During the time that it takes for the photon to travel the lateral coherence length, the scattering at a given position is coherent. Beyond this time, no well-defined phase relationship holds any longer. This leads to an incoherent average in time.

2 Disordered structures

No crystal is perfect in the strictest sense of mathematical abstraction. Trivially speaking, a perfect periodic lattice is infinite in size, and thus the surface of each crystal is a defect in itself. Even in thermodynamic equilibrium, no crystal is perfect since a – possibly very small – amount of impurities like wrong atom types or vacancies will be present. Many types of defects can be present within the average crystal structure [17–20]. Loosely, we can classify these defects into two classes. On the one hand, defects exist that modify the crystal on a large scale while the content of neighboring unit cells remains essentially the same. On the other hand, we have defects that modify the individual unit cells but leave the overall average lattice undisturbed. These are limiting cases, and defects will usually show both effects on the crystal structure. A feature common to the presence of any defect in a crystal structure is that the strict periodicity no longer holds. This in turn has two major effects. First of all, the strict adherence to the 230 space groups is no longer required. Due to the lack of strict periodicity, the crystal does not even belong to the space group $P1$ any longer, but has no symmetry at all. Most disordered crystals will still have a crystal structure that is close to that of the corresponding average structure and thus close in the local symmetry to that of the proper space group. The second aspect is the occurrence of additional broad diffuse scattering between the Bragg reflections. This diffuse scattering has a peak intensity several orders of magnitude less than that of the Bragg reflections. For highly disordered materials, the integral intensity of the diffuse scattering can, however, be a significant fraction of the total scattered intensity.

2.1 Types of disordered structures

To classify disordered structures, two aspects of the disorder need to be taken into account. The first aspect is the defect type present within the structure, and the second aspect is the distribution of these defects throughout the crystal. The two aspects are somewhat independent of each other. In combination with the relaxed symmetry constraints and the already large number of crystal structure types, these two aspects cause a very large number of observed disorder types.

The defect types that may be present in disordered materials can be characterized by their respective dimensions. The most basic defect type is point defects, which are ever present even in almost perfect crystal structures. These point defects may be individual wrong atom types on the site of regular atoms, missing atoms at a site, or interstitial atoms. As the individual interatomic distances between any atom pair are slightly different, point defects are usually accompanied by a local distortion of the neighboring atom positions. Thus point defects are not strictly zero-dimensional defects but slightly extended defects. This results in a small cluster if the immediate distorted environment of the point defect is also included. No sharp boundary exists to

extended clusters of a locally slightly different structure. Such point defects are the dominant defects in nonstoichiometric compounds like alloys. As a one-dimensional defect, we can classify inclusion compounds with linear channels. A prominent example is urea inclusion compounds. The urea molecules form a host structure with infinite channels that can host linear hydrocarbon molecules with a wide variety of chain lengths. Within a given channel, a zig-zag hydrocarbon chain can be present in one of three possible orientations that differ by a 120° rotation. Along each channel, the hydrocarbon molecules are placed with almost perfect periodic distance. The individual molecules are, however, not always in the same orientation. From any given channel to a neighboring channel there is no strict order of the hydrocarbon orientation. Thus these structures exhibit good (distance) periodicity along the channel axis and strong disorder in the plane normal to the channels. Planar two-dimensional defects are common in layered materials. Here an individual layer has perfect periodicity within each layer. The stacking sequence of the layers along the third axis is subject to disorder. Common examples are clay minerals, micas, and materials that can be described on the basis of the closed-packed structure types. As the energy differences between the cubic closed-packed structure and the hexagonal closed-packed structure are very small, defects are likely to occur. Finally, three-dimensional defects are extended clusters of a (slightly) different structure within a host material.

Apart from these defect types, we need to consider their distribution throughout the host crystal. As the simplest type of distribution, we can have a random distribution of individual defects. This distribution type is typically present if the defect concentration is low. Under these circumstances, the local distortions around the defect will have subsided to sufficiently small values not to cause an interaction between the position of one defect and another. At higher defect concentrations the local changes of the structure will affect the location of nearby defects, and the defects will no longer be distributed at random. Instead, the location of two defects will be correlated. In contrast to the periodic structure of a perfect crystal, the resulting order of the defect distribution is not perfect. A well defined distance relationship between defect pairs tends to exist for short distances only. With increasing distance, this order will eventually die out, and defects that are separated by distances of several unit cells will bear no distance correlation. This order is referred to as a short-range order.

2.2 Basic diffuse scattering theory

To point out the fundamental aspects of diffuse scattering, we need to extend the basic intensity equation that was derived for the intensity of a perfect crystal structure:

$$I(\mathbf{S}) = \sum_{i=1}^{N_{\text{at}}} \sum_{j=1}^{N_{\text{at}}} f_i f_j e^{2\pi i \mathbf{S} \cdot (\mathbf{r}_i - \mathbf{r}_j)}. \quad (75)$$

In a disordered material, atoms i and j may be replaced by another atom type and may be displaced from the corresponding position in the average structure. Thus the actual atomic form factor at positions i and j can be written as $\langle f \rangle + \Delta f$, where $\langle f \rangle$ is the average atomic form factor at this site, and Δf is the deviation from this average atomic form factor at a specific position. Likewise, the position can be represented as an average position plus a local deviation, $\langle \mathbf{r} \rangle + \Delta \mathbf{r}$. As the crystal is no longer periodic, the summation needs to be carried out over all atoms of the crystal, not just the atoms in a single unit cell. This yields

$$I(\mathbf{S}) = \sum_{i=1}^{N_{\text{at}}} \sum_{j=1}^{N_{\text{at}}} (\langle f \rangle_i + \Delta f_i) (\langle f \rangle_j + \Delta f_j) e^{2\pi i \mathbf{S} \cdot ((\langle \mathbf{r} \rangle_i + \Delta \mathbf{r}_i) - (\langle \mathbf{r} \rangle_j + \Delta \mathbf{r}_j))}. \quad (76)$$

This equation can be split into the individual sums by separating the average and local deviation of the atomic form factors:

$$\begin{aligned} I(\mathbf{S}) &= \sum_{i=1}^{N_{\text{at}}} \sum_{j=1}^{N_{\text{at}}} (\langle f \rangle_i) (\langle f \rangle_j) e^{2\pi i \mathbf{S} \cdot ((\langle \mathbf{r} \rangle_i + \Delta \mathbf{r}_i) - (\langle \mathbf{r} \rangle_j + \Delta \mathbf{r}_j))} \\ &+ \sum_{i=1}^{N_{\text{at}}} \sum_{j=1}^{N_{\text{at}}} (\langle f \rangle_i) (\Delta f_j) e^{2\pi i \mathbf{S} \cdot ((\langle \mathbf{r} \rangle_i + \Delta \mathbf{r}_i) - (\langle \mathbf{r} \rangle_j + \Delta \mathbf{r}_j))} \\ &+ \sum_{i=1}^{N_{\text{at}}} \sum_{j=1}^{N_{\text{at}}} (\Delta f_i) (\langle f \rangle_j) e^{2\pi i \mathbf{S} \cdot ((\langle \mathbf{r} \rangle_i + \Delta \mathbf{r}_i) - (\langle \mathbf{r} \rangle_j + \Delta \mathbf{r}_j))} \\ &+ \sum_{i=1}^{N_{\text{at}}} \sum_{j=1}^{N_{\text{at}}} (\Delta f_i) (\Delta f_j) e^{2\pi i \mathbf{S} \cdot ((\langle \mathbf{r} \rangle_i + \Delta \mathbf{r}_i) - (\langle \mathbf{r} \rangle_j + \Delta \mathbf{r}_j))}. \end{aligned} \quad (77)$$

To demonstrate the effects of disorder on the diffraction pattern, we can look at two illustrating limiting situations: pure substitutional disorder, where the atomic displacements from the ideal sites are zero or at least completely uncorrelated, and pure displacement disorder, where all deviations from the average atomic form factors are zero. In the first case, the uncorrelated atomic displacements cause an effect equivalent to the Debye–Waller factor. If, for a moment, we set the atomic displacements to zero, we obtain

$$\begin{aligned} I(\mathbf{S}) &= \sum_{i=1}^{N_{\text{at}}} \sum_{j=1}^{N_{\text{at}}} (\langle f \rangle_i) (\langle f \rangle_j) e^{2\pi i \mathbf{S} \cdot (\langle \mathbf{r} \rangle_i - \langle \mathbf{r} \rangle_j)} \\ &+ \sum_{i=1}^{N_{\text{at}}} \sum_{j=1}^{N_{\text{at}}} (\langle f \rangle_i) (\Delta f_j) e^{2\pi i \mathbf{S} \cdot (\langle \mathbf{r} \rangle_i - \langle \mathbf{r} \rangle_j)} \\ &+ \sum_{i=1}^{N_{\text{at}}} \sum_{j=1}^{N_{\text{at}}} (\Delta f_i) (\langle f \rangle_j) e^{2\pi i \mathbf{S} \cdot (\langle \mathbf{r} \rangle_i - \langle \mathbf{r} \rangle_j)} \\ &+ \sum_{i=1}^{N_{\text{at}}} \sum_{j=1}^{N_{\text{at}}} (\Delta f_i) (\Delta f_j) e^{2\pi i \mathbf{S} \cdot (\langle \mathbf{r} \rangle_i - \langle \mathbf{r} \rangle_j)}. \end{aligned} \quad (78)$$

The first term describes the contribution by the pure average structure, and the terms are identical within each unit cell. By its very definition, the average atomic form factor is identical from unit cell to unit cell. Likewise, the average atom positions are identical within all unit cells, and we can factor out this first summation into a contribution by a single unit cell and a lattice factor. This is exactly the formalism used to derive the structure factor in Section 1.2. Thus this term describes the Bragg intensities. Note that the value of the first sum does not depend on the distribution of the local deviations from the average atomic form factor. The intensity of the Bragg reflections is not affected at all by the local distributions of the specific atoms! The remaining three sums are due to the distribution of the local deviations from the average atomic form factor. The detailed intensity that is derived from these three sums depends on the distribution of the local deviations from the average atomic form factors. The distribution of these defects is not periodic; otherwise, we would have a new perfect crystal structure. As a consequence, the intensity distribution is no longer limited to the Bragg positions but is continuously distributed throughout reciprocal space. Generally, all atomic form factors decrease in magnitude with increasing length of the reciprocal space vector \mathbf{S} . Correspondingly, the deviations from the average atomic form factor also decrease. For pure substitutional disorder, the diffuse scattering tends to decrease in intensity with increasing distance to the origin of reciprocal space, i.e., with increasing Bragg angle 2θ .

In the other limiting case, we can assume pure displacement disorder. At each given site a position is occupied by the average atom, and thus all deviations Δf are zero. In this case, only the first term in equation (77) remains:

$$\begin{aligned}
 I(\mathbf{S}) &= \sum_{i=1}^{N_{\text{at}}} \sum_{j=1}^{N_{\text{at}}} \langle f \rangle_i \langle f \rangle_j e^{2i\pi\mathbf{S} \cdot ((\mathbf{r})_i + \Delta\mathbf{r}_i) - ((\mathbf{r})_j + \Delta\mathbf{r}_j)} \\
 &= \sum_{i=1}^{N_{\text{at}}} \sum_{j=1}^{N_{\text{at}}} \langle f \rangle_i \langle f \rangle_j e^{2i\pi\mathbf{S} \cdot (\mathbf{r}_i - \mathbf{r}_j)} e^{2i\pi\mathbf{S} \cdot (\Delta\mathbf{r}_i - \Delta\mathbf{r}_j)}. \tag{79}
 \end{aligned}$$

If the individual deviations $\Delta\mathbf{r}$ from the average position are distributed throughout the crystal structure with no correlation to each other and all deviations are isotropically oriented, then we obtain the case of an ideal crystal with pure random atomic displacement. The scattering consists of the Bragg reflections whose intensity is dampened by a Debye–Waller term and additional diffuse scattering. The diffuse scattering itself is isotropically distributed throughout the reciprocal space. The argument of the last factor in this equation increases linearly with $|\mathbf{S}|$. Correspondingly, this term modifies the intensity more and more with increasing distance from the reciprocal origin. Generally speaking, the pure displacement diffuse scattering tends to increase with increasing distance from the reciprocal origin. In the cases where the atomic displacements are parallel to each other, a systematic extinction of the diffuse scattering can be observed in those sections of reciprocal space where the scalar product $\mathbf{S} \cdot (\Delta\mathbf{r}_i - \Delta\mathbf{r}_j)$

is zero, i.e., where the reciprocal vector is normal to the displacements. This extinction rule is used, for example, to distinguish longitudinal and transverse displacement waves.

These two cases are usually not really present in their pure form in a crystal structure. In case of substitutional disorder, the replacement of one atom by another at a given site in the unit cell is accompanied by at least small positional deviations as the individual atomic radii will differ. Likewise, displacements of atoms from their average site position are often accompanied and influenced by local changes in the composition. To treat these general cases, the exponent in equation (75) is usually separated into terms equivalent to equation (79):

$$\begin{aligned}
 I(\mathbf{S}) &= \sum_{i=1}^{N_{\text{at}}} \sum_{j=1}^{N_{\text{at}}} (\langle f \rangle_i + \Delta f_i)(\langle f \rangle_j + \Delta f_j) e^{2i\pi\mathbf{S} \cdot ((\mathbf{r}_i + \Delta\mathbf{r}_i) - (\mathbf{r}_j + \Delta\mathbf{r}_j))} \\
 &= \sum_{i=1}^{N_{\text{at}}} \sum_{j=1}^{N_{\text{at}}} (\langle f \rangle_i + \Delta f_i)(\langle f \rangle_j + \Delta f_j) e^{2i\pi\mathbf{S} \cdot (\mathbf{r}_i - \mathbf{r}_j)} e^{2i\pi\mathbf{S} \cdot (\Delta\mathbf{r}_i - \Delta\mathbf{r}_j)}. \quad (80)
 \end{aligned}$$

In the next step the last factor can be approximated by a power series:

$$\begin{aligned}
 I(\mathbf{S}) &= \sum_{i=1}^{N_{\text{at}}} \sum_{j=1}^{N_{\text{at}}} (\langle f \rangle_i + \Delta f_i)(\langle f \rangle_j + \Delta f_j) e^{2i\pi\mathbf{S} \cdot (\mathbf{r}_i - \mathbf{r}_j)} \\
 &\quad \cdot \left[1 + 2i\pi\mathbf{S} \cdot (\Delta\mathbf{r}_i - \Delta\mathbf{r}_j) - \frac{1}{2}(2\pi\mathbf{S} \cdot (\Delta\mathbf{r}_i - \Delta\mathbf{r}_j))^2 \right. \\
 &\quad \left. - \frac{1}{6}i(2\pi\mathbf{S} \cdot (\Delta\mathbf{r}_i - \Delta\mathbf{r}_j))^3 + \dots \right]. \quad (81)
 \end{aligned}$$

This equation contains both the Bragg reflections and the diffuse scattering. If the terms with the form factors are separated again into average parts and local deviations, then we can split off the Bragg reflections from this equation. In the remaining expressions, the four terms in the square brackets describe parts of the diffuse scattering, each depending on a different power of displacement. The first term is independent of the displacements and describes the effects of substitutional disorder, usually referred to as chemical short-range order (SRO). The second term with linear dependence on the displacements is commonly known as the size effect. The third term with square dependency is referred to as Huang scattering and thermal diffuse scattering.

The terms with even powers of the displacement cause diffuse scattering that is symmetric around the Bragg reflections, whereas those with odd powers cause antisymmetric diffuse scattering. Careful analysis of the diffuse scattering distribution allows us to assess the character of the main disorder contributions. This analysis in the reciprocal space tremendously helps to build an initial disorder model.

Both Huang and thermal diffuse scatterings are caused by the distortions due to long-range part of the displacement field around a given defect [21]. Huang scattering refers to the pure static displacement fields caused by substitutional disorder when different ionic radii are involved or extended clusters distort their environment.

To gain insight into the different types of diffuse scattering and their relationship with the defects, we can describe the crystal as the sum of the average structure plus a sum over all defect types, each of these convoluted with the corresponding distribution:

$$\rho(\mathbf{r}) = \langle \rho(\mathbf{r}) \rangle + \sum_{\text{types}} \rho_{\text{defect, type}}(\mathbf{r}) \otimes \text{Distr}_{\text{type}}(\mathbf{r}). \quad (82)$$

The diffraction pattern is the Fourier transform of this electron density, and we obtain

$$F(\mathbf{S}) = F_{hkl}(\mathbf{S}) + \sum_{\text{types}} \text{Fourier}[\rho_{\text{defect, type}}(\mathbf{r})] \cdot \text{Fourier}[\text{Distr}_{\text{type}}(\mathbf{r})]. \quad (83)$$

The first term is the group of all Bragg reflections, and the second comprises all of the diffuse scattering. Lets analyze a few basic defect and distribution types.

If the defects are point defects or very small clusters, their Fourier transform is constant or at least varies very slowly throughout the reciprocal space with nonzero values essentially all over the reciprocal space. Next, let us assume linear defects like guest molecules in a 1D channel of the host structure. Without loss of generality, we can place the linear axis of the object parallel to the c -axis through the origin of the space. For a strictly one-dimensional guest molecule, all x and y coordinates are zero, and the structure factor of such an object is

$$F(\mathbf{S}) = \sum_{j=1}^N f_j e^{2\pi i(h0+k0+lz)} = \sum_{j=1}^N f_j e^{2\pi ilz}. \quad (84)$$

This structure factor is independent of both h and k . Apart from the form factor dependency, the structure factor is identical for all h and k . If the molecules are arranged periodically with repeat distance Δz along the c -axis, then the structure factor is limited to l values where $l\Delta z$ is integer. In combination with the constant values for all h and l , this gives a set of equidistant planes in reciprocal space. The distance between these planes need not be a simple multiple of the c^* length of the host crystal.

Next, let us consider planar defects, where we can write the structure factor as

$$F(\mathbf{S}) = \sum_{j=1}^N f_j e^{2\pi i(hx+ky+l0)} = \sum_{j=1}^N f_j e^{2\pi i(hx+kl)}. \quad (85)$$

This yields constant $F(S)$ values along \mathbf{c}^* . The most common planar defect consists of stacks of layers that are perfectly periodic within the ab -plane. This periodicity limits the structure factor to integer values of h and k , and the structure factor consists of lines of constant intensity parallel to \mathbf{c}^* through integer positions of h and k . As \mathbf{c}^* is normal to \mathbf{a} and \mathbf{b} , the diffuse scattering is limited to a line normal to the individual planes.

Finally, we consider extended three-dimensional defects like extended domains or exsolutions of a secondary phase. Their scattering is best described like that of an individual crystal with very limited dimensions. We can formally describe such an object as an infinite object multiplied in direct space by a shape function. Accordingly, the structure factor of such a defect is limited to the points of the respective reciprocal lattice. The peaks are widened due to the convolution with the Fourier transform of the shape function. Still, they are limited to small regions in the reciprocal space.

Similar arguments can now be developed for the distribution of the defects in the direct space. First, let us consider a random distribution of defects. This distribution can be described as a sum of origins of the respective defect with arbitrary positions:

$$\text{Distr}_{\text{type}}(\mathbf{r}) = \sum_{j=1}^N \delta(\mathbf{r} - \mathbf{r}_j). \quad (86)$$

The Fourier transform of a delta distribution at position \mathbf{r}_j is a complex number with unit modulus and phase defined by the scalar product of vectors \mathbf{S} and \mathbf{r} . Thus the Fourier transform of the distributions of origins is

$$\text{Fourier}(\text{Distr}_{\text{type}}(\mathbf{r})) = \sum_{j=1}^N e^{2\pi i(\mathbf{S}\mathbf{r}_j)}. \quad (87)$$

With a random distribution of the positions the sum is a random complex number. Thus the Fourier transform of the randomly distributed defect origins gives a homogeneously distributed noise in reciprocal space.

If the defects are correlated along a single direction in direct space and are completely uncorrelated along the other two directions, then we have a strictly one-dimensional distribution of defect origins along this one unique direction. We can place the line of one of these distributions into the origin of the direct space, and we have

$$\text{Distr}_{\text{type}}(z) = \sum_{j=1}^N \delta(z - z_j). \quad (88)$$

As all x and y coordinates are zero, the Fourier transform of this distribution is

$$\text{Fourier}(\text{Distr}_{\text{type}}(z)) = \sum_{j=1}^N e^{2\pi i(Lz_j)}. \quad (89)$$

Thus the Fourier transform is independent of h and k and thus constant within the a^*b^* plane of the reciprocal space. The random distribution of such one-dimensional defect distributions within the $a-b$ plane of the direct space only introduces a random phase similar to the completely random defect distribution. Along \mathbf{c}^* the structure factor depends on the specific distribution.

3 Pair distribution function

3.1 Theory

The data analysis of disordered materials that exist only as polycrystalline materials is hampered by the projection of all of reciprocal space into the one-dimensional powder pattern. This implies a loss of information as all vectors of identical length in reciprocal space fall onto a single data point in the powder pattern. The smooth diffuse scattering becomes even more featureless upon this projection. Thus the modulations that can be observed in the powder diffraction pattern can usually not be associated with a single diffuse feature. An interpretation is not straightforward and therefore requires the test of several disorder models.

Fortunately, the pair distribution function (PDF) technique exists that allows a much more straightforward interpretation and initial model building [22]. Essentially, the PDF is a histogram of all interatomic distances that can be derived by the Fourier transform of the properly corrected observed intensities. As such, it resembles the Patterson function used in single-crystal structure determination techniques, and its information content is similar. The important difference lies in the input that goes into the respective Fourier transforms. The Patterson function is based on the intensities of the integrated Bragg reflections only. Thus its Fourier coefficients are at the integer grid points of the reciprocal lattice. As a consequence, the Patterson function has the same translational periodicity of the crystal structure and does not yield information on disorder beyond the limited information within the Bragg reflections. The PDF in both its variants, the more commonly used powder PDF [22] and the single crystal or 3D PDF [23], uses all of reciprocal space as input into the Fourier transform. For this reason, the PDF is also referred to as total scattering since the total diffraction pattern, consisting of Bragg reflections and diffuse scattering, is used. Since the continuous data points underneath the Bragg reflections are used in the Fourier transform as well, the resulting function in direct space is no longer periodic. As such, it contains information on both the average periodic structure and the local deviations that reflect the disordered part of the structure.

After proper background subtraction, correction for absorption, inelastic thermal scattering, Compton scattering, and normalization, the experimental intensity $I(Q)$ is changed to yield a normalized scattering function $S(Q)$. Despite the name scattering function, we should keep in mind that this is still a pattern related to the intensity, rather than the crystallographic structure factor. The latter contains information on the amplitude and phase of the scattered wave, whereas both the intensity $I(Q)$ and the normalized scattering function $S(Q)$ contain information on the amplitude only. The experimental reduced pair distribution function is calculated through a sine Fourier transform according to

$$G(r) = \frac{2}{\pi} \int_{Q_{\min}}^{Q_{\max}} Q[S(Q) - 1] \sin(Qr) dQ. \quad (90)$$

The result of this Fourier transform is a diagram in direct space. It consists of peaks at positions r that correspond to interatomic distances. To illustrate this, we can derive a qualitative picture of the PDF by following the steps from the diffraction process back to the PDF. The structure factor $F(h)$ is the Fourier transform of the scattering density, i.e., the electron density if we focus on X-ray diffraction:

$$F(\mathbf{S}) = \text{Fourier}(\rho(\mathbf{r})). \quad (91)$$

As the next step, the intensity measured in a diffraction experiment is proportional to the structure factor squared:

$$I(\mathbf{S}) = |F(\mathbf{S})|^2 = F(\mathbf{S}) \cdot F^*(\mathbf{S}). \quad (92)$$

Next, we perform the inverse Fourier transform of the intensity and use the multiplication theorem, which states that the Fourier transform of a product is equal to the convolution of the Fourier transform of the individual factors:

$$\text{Fourier}[I(\mathbf{S})] = \text{Fourier}[F(\mathbf{S})] \otimes \text{Fourier}[F^*(\mathbf{S})], \quad (93)$$

where \otimes denotes the convolution of two terms. The Fourier transform of the structure factor is, of course, the original scattering density. The Fourier transform of the conjugate complex structure factor gives the conjugate complex scattering density at $-r$, and we obtain

$$\text{Fourier}[I(\mathbf{S})] = \rho(\mathbf{r}) \otimes \rho^*(-\mathbf{r}) = \rho(\mathbf{r}) \otimes \rho(-\mathbf{r}). \quad (94)$$

For the last equality, we have used the fact that the scattering function is a real-valued function. For any such function, the conjugate complex value is identical to the original value. This last result shows that the Fourier transform of the intensity is the convolution of the scattering density with the scattering density inverted at the origin. This convolution corresponds to the so-called autocorrelation function, which has peaks at distances r that separate positions in the scattering function with high values. These distances are the interatomic distances within the structure. Compare this development to the Patterson function derived in the initial section.

Note that in this qualitative derivation we did not rely on any assumptions on the internal order of the structure for which the structure factor and the intensity were calculated, or obtained from a diffraction experiment. Thus we can expect that the PDF yields information on the interatomic distances in any kind of structure, crystalline, disordered, amorphous, liquid, or even gaseous. This was actually the driving force behind the original PDF developments [24].

As $G(r)$ is calculated via the Fourier transform of the experimental data, it is influenced by two experimental conditions that need be considered in the choice of the appropriate experimental setup. The first aspect is the value of Q_{\max} in equation (90).

Compared to an idealized $G(r)$ where Q_{\max} is infinity, the effect of a finite Q_{\max} can be described as a multiplication of the powder pattern to infinite Q_{\max} by a box function with value 1 for $Q < Q_{\max}$ and zero for $Q > Q_{\max}$. The Fourier transform of this multiplication leads to the convolution of the experimental $G(r)$ by the Fourier transform of the box function:

$$G(r) = \text{Fourier}[I_{\infty}(Q) \cdot \text{Box}(Q_{\max})] = G_{\infty}(r) \otimes \text{Fourier}[\text{Box}(Q_{\max})]. \quad (95)$$

The Fourier transform of the box function is a sinc function:

$$\text{Fourier}[\text{Box}(Q_{\max})] = \frac{\sin(Q_{\max}r)}{Q_{\max}r}. \quad (96)$$

The effect of this convolution of the idealized $G(r)$ with the sinc function is a widening of the $G(r)$ peaks with decreasing Q_{\max} . The minimum Q_{\max} value that should be used is approximately 20 \AA^{-1} . Smaller values of Q_{\max} lead to rather wide PDF peaks and thus to considerable peak overlap.

The second experimental aspect to consider is the instrumental angular resolution. It is sufficient to simplify the experimental conditions a little bit by assuming that the resolution function is constant over the entire 2Θ region. We can then describe the effect of the instrumental resolution as a convolution of an idealized powder pattern. The Fourier transform of this convolution turns it into a regular multiplication:

$$G(r) = \text{Fourier}[I_{\text{ideal}}(Q) \otimes \text{Res}(Q)] = G_{\text{ideal}}(r) \cdot \text{Fourier}[\text{Res}(Q)]. \quad (97)$$

Under the assumption that the resolution function can be described by a Gaussian function with width σ , its Fourier transform is again a Gaussian with width $1/\sigma$. Thus the effect of a relaxed angular resolution is a dampening of the experimental $G(r)$ at increasing r . If the focus is placed on the very local order within the first tens of Å , then the instrumental resolution can be relaxed considerably in favor of increased intensity, which helps to improve the achievable time resolution. If, on the other hand, the focus is placed on the interpretation of extended domain structures at several tens to some 100 \AA , then the instrumental resolution must be optimized at a loss of intensity. Modern high resolution synchrotron powder beam lines typically offer a minimum wavelength around 0.3 \AA , which is sufficiently short to achieve a good value of Q_{\max} .

The calculated reduced pair distribution function can readily be calculated from a structural model according to

$$G(r) = \frac{1}{Nr} \sum_{i=1}^N \sum_{j=1}^N \frac{f_i f_j}{\langle f \rangle^2} \delta(r - r_{ij}) - 4\pi\rho_0 r. \quad (98)$$

Here N is the number of atoms in the structure model, r_{ij} is the distance between atoms i and j , and ρ_0 is the number density, i.e., the number of atoms per unit vol-

ume. The atomic form factors are commonly approximated by their values at a fixed Q -value, often either at $Q = 0$ or at a Q -value approximately equal to $Q_{\max}/2$. As the Q -dependence of the atomic form factor is not too different for different atom types, the actual value of Q at which the atomic form factor is calculated is not very critical, since a similar Q -dependence is present in the nominator and denominator.

This equation corresponds to a static structure with all atoms at rest, and thus it represents a snapshot in time. As long as the experiment corresponds to a time average, the displacements of the atoms from their average position need be modeled properly. Two different techniques can be applied to model the atomic distributions. If the structure model consists of a large number of atoms, then each atom can be displaced from its ideal position. The displacement distribution must be chosen to match the expected occupational probability density function. To model (an)isotropic thermal vibrations, a Gaussian distribution is adequate. Similar probability density distributions may be chosen to describe anharmonic displacements or static displacement within a disordered structure. As an effect of such a displacement, the distance distributions between atoms are widened. If the model consists of several thousand atoms, then the calculated PDF is a smoothly varying function.

For smaller models that consist of a few atoms or a few hundred atoms, an alternative approximation is commonly used. The initial calculated PDF of equation (98) is convoluted with a Gaussian distribution $D(r) = \frac{1}{\sqrt{2\pi}\sigma} e^{-\frac{r^2}{2\sigma^2}}$, which also effectively widens the peaks of the calculated PDF. As the PDF in equation (98) corresponds to the projection of all interatomic distance vectors into the one-dimensional space, it is not straightforward to describe an anisotropic displacement. At distances beyond approximately 2 nm, this model proves to be a very good approximation for thermal and random static displacements. Any two atoms are displaced independently from each other, and the σ of the Gaussian distribution corresponds to the sum of the two isotropic displacement parameters u_i . At shorter distances, this model neglects correlated displacement of neighboring atoms. As a good deal of the atomic displacements from the average position is due to acoustic phonons, atoms at close distances tend to be displaced at any given moment in time into a similar direction. Time averaging these correlated displacements result in approximately the same distance as if the atoms were at rest. As a consequence, the peaks in a PDF have a width that increases as a function of interatomic distance r . The effect is described either by a $1/r$ or by a $1/r^2$ dependence that needs be subtracted from the width at long distances:

$$\sigma(r) = \sigma - \frac{c_{\text{lin}}}{r}; \quad \sigma(r) = \sigma - \frac{c_{\text{quad}}}{r^2}. \quad (99)$$

Here c_{lin} and c_{quad} are two sample-dependent parameters [22]. In the future with XFEL sources, a single exposure of a very small sample volume in a time frame of ps may become available.

3.2 Experiments

Fundamentally, a diffraction experiment for a powder PDF does not differ from a standard powder diffraction experiment. As pointed out in the previous section, a crucial requirement for a good PDF is a high value of $Q = 4\pi \sin(\Theta)/\lambda$. With Cu K_α radiation, a maximum value of $Q = 8 \text{ \AA}^{-1}$ can be achieved, which is not sufficient for a well-resolved PDF. Starting with Mo K_α and $Q_{\max} = 17 \text{ \AA}^{-1}$, reasonable values are achieved. Predominantly, however, synchrotron radiation from specialized high-energy X-ray beam lines is used. At the moment, these are 11-ID-B at the APS, ID15 and ID31 at the ESRF, and in the near future beam lines at PETRA, DIAMOND, and NSLS II. Future beam lines can be expected to follow as the number of PDF based experiments is increasing rapidly. These beam lines provide a very intense beam, typically with primary beam energies near 60 or 90 keV, which correspond to wavelengths of approximately 0.2 or 0.14 \AA , respectively. At these short wavelengths a maximum value of $Q_{\max} = 20$ to 40 \AA^{-1} is readily achieved. At the same time, these beam lines provide sufficient flux to perform a good PDF measurement within a second. Several of the existing beam lines will be upgraded, and the measurement time can be expected to drop down to a range close to 0.1 s. Although this is a very long time compared to the timescale of chemical reactions, stroboscopic experiments will give access to time-resolved experiments in the near future.

To achieve these Q_{\max} and time-scale values, the typical setup follows the design reported by Chupas et al. [25]. The primary beam impinges onto a capillary or flat sample in transmission mode. Without further collimation, the diffracted beams are detected by a large and fast area detector. Currently, these are mostly detectors originally developed for medical applications and use amorphous silicon as a primary detector material. As the absorption of high energy X-rays by silicon is actually low, new detector designs are starting to be available that use Ge or CdTe as a primary absorber. As the detection efficiency increases considerably, the minimum detection time can be reduced accordingly. These detector types allow a repetition rate of up to kHz, at least for a few seconds.

The available detectors offer an area of approximately $40 \times 40 \text{ cm}^2$. If the primary beam is placed onto the center of the detector, then the largest diffraction angle at the side point of the detector is

$$2\Theta_{\max} = \tan^{-1}\left(\frac{W}{2D}\right), \quad (100)$$

where W is the full width of the detector, and D is the sample to detector distance. At a width of 40 cm and a sample to detector distance of 20 cm this gives $2\Theta_{\max} = 45^\circ$. Up to this point, all powder rings are complete, which gives the optimum measured intensity. As 2Θ is increased, the powder rings are partially outside the active detector area, reducing the initially measured intensity. This reduction is easily corrected, however, the signal-to-noise ratio increases as less and less of the powder ring is recorded.

At the corner of the detector the maximum diffraction angle is

$$2\Theta_{\max} = \tan^{-1}\left(\frac{W}{\sqrt{2} \cdot D}\right) \quad (101)$$

with $2\Theta_{\max} = 54^\circ$ for the width and distances as given in the previous example.

A further increase of $2\Theta_{\max}$ can be achieved if the detector is placed asymmetrically behind the primary beam. At the utmost extreme, the detector can be placed such that the primary beam is close to one corner, which gives the maximum 2Θ angle in the opposite corner as

$$2\Theta_{\max} = \tan^{-1}\left(\frac{\sqrt{2}W}{D}\right) \quad (102)$$

with $2\Theta_{\max} = 70^\circ$. With the typical wavelengths of 0.2 \AA and 0.1 \AA , the different settings yield maximum Q values of 36 \AA^{-1} and 72 \AA^{-1} , respectively (Table 4).

Table 4: Maximum Q_{\max} values for different experimental configurations.

Primary beam position	$2\Theta_{\max}$	$Q_{\max} [\text{\AA}^{-1}]$ for $\lambda = 0.2 \text{ \AA}$	$Q_{\max} [\text{\AA}^{-1}]$ for $\lambda = 0.1 \text{ \AA}$
center	45° at the edge	24	48
corner	54° at the corners	28	57
corner	70° at opposite corner	36	72

The table shows that a large Q_{\max} value is readily achieved even if only the central part of the detector up to the edges is used. A measurement that fully uses the large Q_{\max} values, of course, requires longer counting times as the elastically scattered intensity decreases with increasing Q_{\max} whereas the inelastic contribution (mostly Compton scattering) increases.

As pointed out in the theory section, the value of Q_{\max} partially determines the width of the PDF peaks. For room temperature measurements, the thermal motion of atoms add a substantial contribution to the PDF peak widths. A Q_{\max} in excess of 30 \AA^{-1} will not significantly reduce the peak width any longer as it is now dominated by thermal motion. Thus, for most applications, a Q_{\max} value of 20 to 25 \AA^{-1} gives a good compromise between the opposing requirements to reduce the PDF peak width and to decrease counting times.

As the general setup for a PDF experiment is simple, a few constraints exist to set up additional sample environment options. These options include cooling and heating devices, as well as more complex sample environments. The latter were, for example, used to study nanoparticle synthesis [26–28] and the interaction between nanoparticles and the surrounding fluid [29].

3.3 Data treatment

Several steps are needed to transform the initial 2D area detector signal into the experimental PDF. These steps include:

- (1) radial integration
- (2) background subtraction
- (3) corrections for Compton scattering and further experimental features
- (4) the actual Fourier transform

The initial data treatment requires to integrate the 2D diffraction data into a one-dimensional conventional powder diffraction pattern. Several routines are available that perform this task more or less automatically (Refs. [30, 31]). A main step that the user has to be aware of and that requires careful handling is the treatment of detector defects. Any 2D area detector will have several pixels that systematically miscount the intensity, and these pixels will have to be masked out prior to integration. Otherwise, erroneous intensities in the diffraction pattern will result, particularly if the defect consists of an extended line of defect pixels.

The background in an experiment intended to obtain the PDF will not differ from the background in any other powder diffraction experiment. For a classical analysis of a powder diffraction experiment in reciprocal space like a Rietveld refinement, the background can be treated as a polynomial that is fitted to the data in addition to the Bragg intensities. For a PDF analysis, the whole diffraction pattern will eventually undergo the Fourier transform. The data will include the very high Q -region. In this part of the diffraction pattern, all Bragg reflections will have diminished in peak intensity and have broadened to overlap almost completely. Therefore, the background can no longer be identified with any certainty. Instead, the background has to be measured in a separate experiment. Care has to be taken to ensure that the background intensity is measured with sufficient counting time to avoid any statistical noise at high Q -values.

The further treatment is most commonly performed in a semiempirical manner within the software package PDFgetX3. This software allows the user to tune the sample composition, the background scale factor, and an empirical polynomial. The sample composition is used to calculate and subtract the Compton scattering and should ideally be obtained in a separate analysis. Likewise, the background scale should correspond to the counting time ratios. If the sample absorption cannot be neglected, but is not known exactly, we can tune the background scale factor slightly to account for the reduced scattering by the part of the sample holder that is partly shielded by the sample.

3.4 Analysis and refinement

The exact analysis of an experimental PDF, of course, depends on the actual sample at hand and the information we seek to obtain about the sample. The PDF technique

is most useful for samples that are disordered or even amorphous. Well crystalline materials that exhibit sharp Bragg peaks and little or no diffuse scattering are more easily analyzed in reciprocal space with Rietveld methods. Especially, if very good time resolution requirements are crucial, then a powder pattern for Rietveld analysis can be measured in much less time than a pattern for proper PDF analysis. For this analysis, the limiting factor for the time resolution is really still the detector read out time.

Thus the main emphasis in this section is placed on strategies to unravel the local order at a scale of a few nm. For truly amorphous samples like glasses or liquids, no structural correlation exists in atom positions beyond the first few neighbor shells.

Three different approaches have become very popular. The first approach is essentially a transfer of the Rietveld method into direct space, whereas the second and third approaches attempt to model larger sections of a structure or whole nanoparticles.

In the first approach, the sample is modeled as a single unit cell or as a block of a few unit cells. Extended distances are calculated with periodic boundary conditions. The approach allows us to refine atom coordinates, atomic displacement parameters, and occupancies with a standard least-squares algorithm. Thus the algorithm is very fast and well suited to follow structural changes in time-resolved experiments. As the structure is modeled as a single unit cell or a few unit cells, the capability of this approach to model extended disorder is limited. As periodic boundary conditions are used to derive the PDF peaks at distances beyond the diameter D of the initial box, the structure effectively is periodic beyond this diameter. Any defect to be analyzed has to fit inside a radius that corresponds to half the box diameter. Longer distances r correspond to the same atom pair at $D - r$ in the opposite direction. Despite this limitation, the method has been used very successfully to analyze changes in the local order beyond the box diameter. To achieve this effect, the refinement is limited to a finite distance range from r_{\min} to r_{\max} . If the sample at hand consists, for example, of small domains, then a refinement limited to short distances reflects the structure within a single domain, whereas a refinement restricted to longer distances reflects the average crystal structure.

In the second approach, the sample is modeled as a large box that consists of several thousand to ten thousand atoms. Periodic boundary conditions are applied beyond this large box. The so-called reverse Monte Carlo algorithm is used to modify the structure to achieve a good agreement between experimental and calculated PDFs. Small random modifications of the initial structure such as individual shifts or an exchange of two atoms are applied. If such a modification results in an improved agreement, then the modification is accepted. Otherwise, the modification may still be accepted, but the probability to accept such a bad modification decreases with a Boltzmann distribution probability. Thus by accepting some bad modifications the algorithm maintains the ability to jump out of a local energy minimum. Under ideal conditions,

the structure can be an arbitrary guess, and we do not have to know anything beyond the average chemical composition. An educated guess, of course, tremendously speeds up the convergence. Once the algorithm has converged to a good agreement between the observed and calculated PDFs, the structure needs to be analyzed with respect to the defects and the local ordering scheme that has evolved. This algorithm is particularly well suited for highly disordered materials such as glasses or liquids.

The third approach uses tools to expand an initial unit cell to a large block and to introduce defects and disorder into this block of atoms. Periodic boundary conditions may be applied, but the algorithm allows us equally well to calculate the diffraction pattern or PDF from a finite set of atoms. This enables the algorithm to model inherently nonperiodic objects like decorated nanoparticles. In contrast to the reverse Monte Carlo algorithm, a reasonably good estimate of the defect structure must be developed prior to the refinement.

3.5 3D PDF

As the powder PDF is based on a powder diffraction experiment, it inherits all the advantages and disadvantages of a powder diffraction experiment, especially with respect to time-resolved data collection. The main advantage is the comparatively short exposure time required and the ease to add extended experimental setups for the control of external conditions like temperature, pressure, and electric and magnetic fields. The main disadvantage is the projection of the original three-dimensional reciprocal space into a one-dimensional diffraction pattern. All points in reciprocal space at identical modulus of the scattering vector \mathbf{S} end up at the same point in the powder diffraction experiment. All information on the relative orientation of the reciprocal space vectors is lost. As a consequence, it becomes much more difficult to analyze diffuse scattering in a powder diffraction experiment. The analysis of diffuse scattering from a single crystal retains the full information on the orientation of the diffuse scattering within three-dimensional reciprocal space. The main disadvantage with respect to time-resolved measurements is the long counting time, which even at a synchrotron source is in the range of an hour.

As an alternative approach to the powder PDF technique, the 3D PDF and particularly the 3D Δ -PDF have been developed. This 3D-PDF is calculated from the experimental intensity data via the Fourier transform as well. In contrast to the powder PDF, the intensity data are those of a single crystal experiment that include both the Bragg reflections and the diffuse intensity. A complete three-dimensional volume of reciprocal space is needed for the Fourier transform. In this respect the 3D-PDF corresponds closely to the classical Patterson function analysis. As pointed out in the section on the PDF, the Patterson function is a periodic function in direct space. If the total scattering is used to calculate the Fourier transform, then the resulting generalized Patterson function in 3D, i.e., the 3D-PDF is no longer periodic.

3.6 Nanoparticle example ZnSe

In this section, we illustrate the PDF technique using ZnSe as an example (from [32] and [33]). Figures 9 and 10 show an overview of the full experimental PDF of nanocrystalline ZnSe together with that of crystalline ZnSe measured under identical conditions. The PDF peaks for the nanocrystalline ZnSe are insignificantly small starting

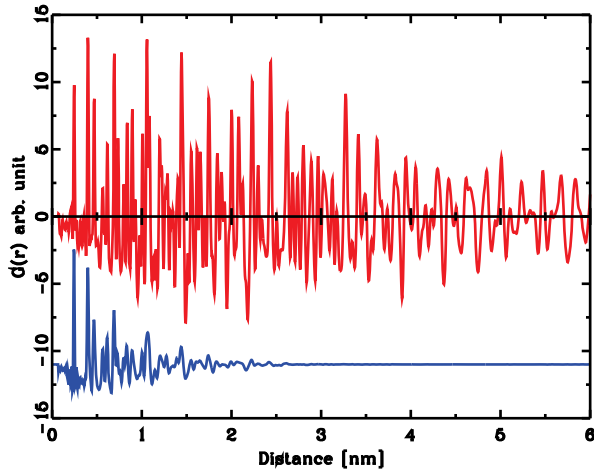


Figure 9: Experimental PDF of nanocrystalline (blue) and crystalline (red) ZnSe. The data were collected at beam line BW5, DESY at 15 K using a wavelength of 0.01 nm. Modified after Neder [33].

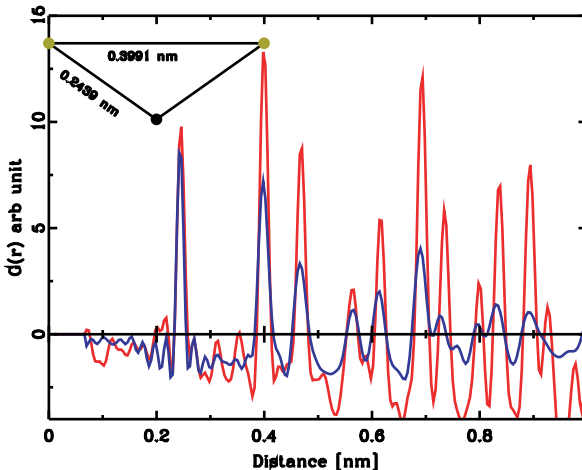


Figure 10: Experimental PDF of nanocrystalline and crystalline ZnSe. Interatomic distance peaks in the first 1 nm. For both samples the peak width increases with increasing distance r . For the crystalline ZnSe it reaches an asymptotic value at low r , whereas the peaks for the nanocrystalline sample become broader over a wider r range. Modified after Neder [33].

around 3.5 nm, whereas those for the crystalline ZnSe extend well beyond 6 nm. This difference points to a diameter of approximately 3.5 nm for the nanocrystalline sample. This diameter agrees with the particle size determined from the powder pattern via the Scherrer equation [1] or from profile analysis (see the contributions by Le Bail and Scardi [34] and references therein). As the PDF is obtained from the diffraction pattern, its information content is identical to that of the diffraction pattern in reciprocal space. This holds for the diameter as well, which, strictly speaking, is the diameter of a structurally coherent domain within the sample. Other techniques such as small angle scattering or transmission electron microscopy (TEM) may observe a different diameter. If the sample consists of individual crystallites whose physical diameter is identical to the coherence length, then all techniques give the same diameter. If, on the other hand, several structurally coherent domains are irregularly intergrown, then the size of the object, as observed in the diffraction pattern or the PDF, does not change, whereas the diameter calculated from the small angle scattering signal indicates a larger size. In the study on ZnSe the TEM data agree with the 3.5 nm size as observed in the powder pattern and the PDF. Bulk ZnSe crystallizes in the zincblende structure (space group $F\bar{4}3m$).

The calculated PDF in Figure 11 is based on an ideal 3.5-nm spherical ZnSe particle with the zincblende structure. The overall agreement confirms the structural model. Significant differences indicate that the model is far from perfect. The nearest neighbor peak is not reproduced well, nor are the significant peaks in the experimental PDF around 2.4 nm.

Under favorable situations, the very local structure of the nanoparticles can be deduced from the PDF data. From Figure 10 we can see that the first two interatomic

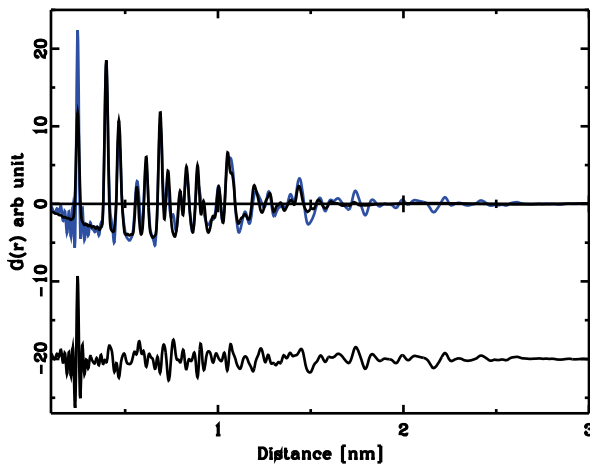


Figure 11: Result of the fit of a spherical ZnSe nanoparticle with perfect zincblende structure to the experimental data. The calculated PDF is in black, the difference curve has been offset for clarity. Modified after Neder [33].

distances in ZnSe are at 0.2439 and 0.3991 nm. With the exception of data collected with anomalous scattering, the PDF determined from an X-ray pattern does not reveal right away with which particular atom pairs a given distance distributions can be associated. Since we have a chemically simple ZnSe compound, chemical experience indicates though that the shortest distance is a Zn–Se bond and that the second distance corresponds to a distance within the coordination shell of the central atom. Figure 10 includes a schematic layout of the first distances in such a binary compound. Within this triangle, all bond distances are known. The resulting bond angle in the central atom is easily calculated to be 109.80° , and this value is in very good agreement with the ideal tetrahedral bond angle of 109.47° . It is reasonable to conclude that the local structure is tetrahedrally coordinated. As the next two distances are also well resolved, their distances at 0.4660 and 0.5640 nm can be used to deduce even more about the structure. We can write these distances as $0.4660 \text{ nm} = 0.2439 \text{ nm} \sqrt{11/3}$ and $0.5640 \text{ nm} = 0.2439 \text{ nm} \sqrt{16/3}$. The multiples of $\sqrt{1/3}$ are typical for a cubic structure, here with lattice parameter 0.5640 nm. Longer distances can be interpreted likewise. The general principle can, however, be applied to more complex crystal structures as well; see Refs. [35–37].

Figure 12 shows the intermediate distance range for both samples. For this particular sample, all peaks in the nanoparticle PDF are shifted to slightly shorter distances compared to that of the bulk structure. This is a straight indication that the interatomic distances of this particular nanocrystalline ZnSe are shortened by a factor of 0.9955. To interpret these subtle differences, the experimental conditions for the two samples had to be exactly the same. This includes the primary wavelength, sample to detector distance, and sample temperature. To derive a more complete structural model, let

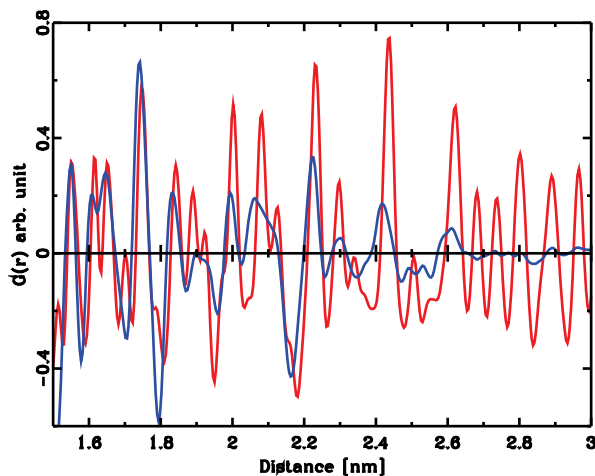


Figure 12: Intermediate distance range. Note the peak width differences in the range 2.0 to 2.2 nm. Modified after Neder [33].

us focus on the different peak widths. The peaks located at 2.0 and at 2.2 nm have almost identical width for both, the nanoparticle and the bulk structure. In contrast, the peaks at distances of approximately 2.1 and 2.3 nm are much wider for the nanoparticle compared to those of the crystalline sample. At first glance, this appears to be a contradictory result. For the nanocrystalline sample, the distance between atom pairs is well defined for pairs separated by both 2.0 and 2.2 nm. The distance at 2.1 nm, which is in between these first two distances, is not well defined at all. We can resolve this contradiction with a proper defect model. The distances in the PDF obtained from a powder diffraction pattern correspond to the projection of all interatomic distances into one dimension. Interatomic vectors of similar distances but very different direction produce peaks at a similar position in the PDF space. Correspondingly, we can resolve the contradiction by assuming that the observed distances are due to interatomic vectors that point into different directions. TEM images of the nanocrystalline sample did not indicate any dislocations and associated strain field. The best model for this sample turned out to be that consisting of a disordered nanocrystalline sample with stacking faults between local Wurtzite–Zincblende-type structures. As the TEM images indicated an ellipsoidal shape, the spherical shape can be replaced by an ellipsoid with rotational symmetry around the hexagonal *c*-axis. This symmetry fits well to the local symmetry of the individual layers stacked along the hexagonal *c*-axis.

The first interatomic distance peak at 0.2439 nm for the samples is significantly narrower than all the following peaks; see Figure 10. This effect is due to a correlated motion of the atoms. Immediate neighbors tend to vibrate in the same direction, whereas atoms at longer distance vibrate completely independently. Thus the time average at these short distances gives a different result compared to the average at longer distances. If all atoms were to vibrate independently from each other, the width of the interatomic distance distribution would be independent of the interatomic distance *r*. Its width would correspond to the convolution of the two probability density functions that describe the time-averaged position of the individual atoms. To correct for the correlated motion, the PDF algorithm allows for a distance-dependent correction of the width.

The final model consists of an ellipsoidally shaped particle with rotational symmetry around the *c*-axis. The final fit is shown in Figure 13, refined parameters are listed in Table 5. The fit is of excellent quality, especially in the distance range above 2 nm, where all features are reproduced. The refined lattice parameters are slightly smaller than the corresponding parameters for crystalline ZnSe at the identical temperature. This is in accordance with the observation that the PDF peaks are shifted to slightly smaller distances. The stacking fault parameter indicates that on average the nanoparticle structure is predominantly a zincblende type, and a perfect zincblende structure can be described by a stacking fault parameter of one. The 30% stacking fault probability is extremely high compared to bulk materials. This value indicates that, for such a very small object, the energy differences between the Zincblende and Wurtzite structure are not significant enough to drive the nanoparticle fully into the

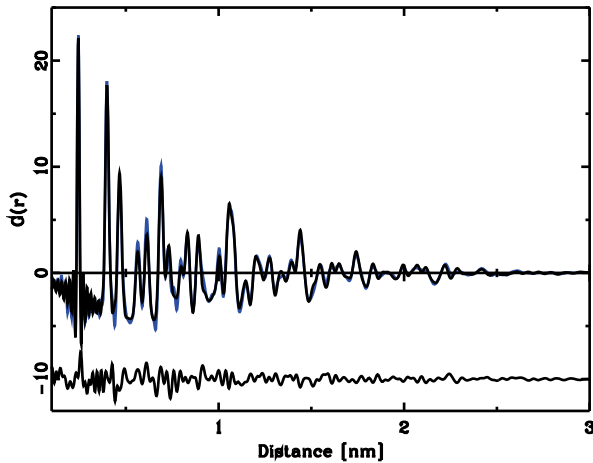


Figure 13: Final result of the refinement of an ellipsoidal model with stacking faults. Modified after Neder [33].

Table 5: Refined ZnSe nanoparticle parameters.

Parameter	Refined value
<i>a</i> -lattice parameter	0.3987 nm
<i>c</i> -lattice parameter	0.6492 nm
<i>z</i> (Zn)	0.3688
ADP	0.0083
Stacking fault probability	0.71
Diameter in <i>a</i> - <i>b</i> plane	2.9 nm
Diameter along [001]	3.9 nm

Zincblende type. Surface effects of the decoration by ligand molecules are the likely reason. The ellipticity agrees well with the TEM images for nanoparticles.

Appendix A. Properties of a Fourier transform

The Fourier transform of a function $f(r)$ is defined as

$$F(S) = \int_{-\infty}^{\infty} f(r) e^{2\pi i S r} dr. \quad (103)$$

The inverse Fourier transform is defined as

$$f(r) = \int_{-\infty}^{\infty} F(S) e^{-2\pi i S r} dS. \quad (104)$$

This simple relationship between the Fourier transform and its inverse holds if the exponent is written with explicit factor 2π . If the factor 2π is combined with the Fourier space variable S as $Q = 2\pi S$, then the constant factor $1/\sqrt{(2\pi)}$ must be included in both equations.

Table 6 summarizes a few basic properties of the Fourier transform, which hold for any real-valued or complex function $f(r)$.

Table 6: Properties of the Fourier transform.

	Real space	Fourier transform space
1	$f(r)$	$F(S)$
2	$F(-r)$	$F(-S)$
3	$f^*(r)$	$F^*(-S)$
4	$f(r - a)$	$e^{2\pi i S a} F(S)$
5	$f(ax)$	$1/a F(S/a)$
6	$f(r) + g(r)$	$F(S) + G(S)$

A.1 Convolution and multiplication theorem

The multiplication theorem states that the Fourier transform of the product of two functions in one space is equal to the convolution of the individual Fourier transforms:

$$F[f(r) \cdot g(r)] = F(S) \otimes G(S). \quad (105)$$

The convolution theorem states that the Fourier transform of a convolution of two functions in one space is equal to the product of the individual Fourier transforms:

$$F[f(r) \otimes g(r)] = F(S) \cdot G(S). \quad (106)$$

A.2 Derivation of the lattice factor

A lattice in one dimension can be written as an infinite sum of delta distributions

$$g(r) = \sum_{j=-\infty}^{\infty} \delta(r - ja). \quad (107)$$

The Fourier transform of a single delta distribution at point ja is calculated from the explicit Fourier integral as

$$F[\delta(r - ja)] = \int_{-\infty}^{\infty} \delta(r - ja) e^{2\pi i S r} dr. \quad (108)$$

With the special properties of the delta distribution, the integrand is zero except when $r = ja$, and thus we can write

$$F[\delta(r - ja)] = e^{2\pi i Sja} \int_{-\infty}^{\infty} \delta(r - ja) dr = e^{2\pi i Sja}. \quad (109)$$

The last equality follows from the basic property of the delta distribution that the integral over the delta distribution is equal to one. For the position $r = 0$, the complex number $e^{2\pi i S0} = 1$.

Since the Fourier transform of a sum of functions is equal to the sum of the individual Fourier transforms, we obtain the Fourier transform of the infinite lattice:

$$F[g(r)] = \sum_{j=-\infty}^{\infty} e^{2\pi i Sja}. \quad (110)$$

For an infinite series of exponentiations, we have the relationship

$$\sum_{j=0}^{\infty} x^j = (1 - x)^{-1}. \quad (111)$$

We can split the sum into two sums from zero to infinity and subtract the one extra term at $j = 0$ to obtain

$$\begin{aligned} F[g(r)] &= \sum_{j=0}^{\infty} [e^{2\pi i Sa}]^j + \sum_{j=0}^{\infty} [e^{-2\pi i Sa}]^j - 1 \\ &= [1 - e^{2\pi i Sa}]^{-1} + [1 - e^{-2\pi i Sa}]^{-1} - 1. \end{aligned} \quad (112)$$

As long as Sa is not an integer number, we can write the last line as

$$\begin{aligned} F[g(r)] &= \frac{1}{[1 - e^{2\pi i Sa}] + [1 - e^{-2\pi i Sa}]} - 1 \\ &= \frac{[1 - e^{-2\pi i Sa}] + [1 - e^{2\pi i Sa}] - [1 - e^{-2\pi i Sa}][1 - e^{2\pi i Sa}]}{[1 - e^{2\pi i Sa}][1 - e^{-2\pi i Sa}]} \\ &= 0 \end{aligned} \quad (113)$$

since the nominator adds up to zero. If Sa is an integer number, then each of the denominators is zero, and the result is infinity. This is the case for all $S = h/a$ where h is an integer number. At each of these regularly spaced points in Fourier space $F(S)$ is infinity and we can write

$$Fg(r) = F(S) = \frac{1}{a} \sum_{h=-\infty}^{\infty} \delta\left(S - \frac{h}{a}\right), \quad (114)$$

where the factor $1/a$ serves to normalize the delta distributions. The Fourier transform of an infinite lattice is also an infinite lattice, spaced at intervals $1/a$. This result can be applied independently to each of the three dimensions of a 3D lattice as well.

A finite lattice can be written either as a finite sum of delta distributions or as an infinite sum of delta distributions multiplied by a step function that equals one within the range of the finite lattice and zero outside:

$$g_{\text{finite}}(r) = \left[\sum_{j=-\infty}^{\infty} \delta(r - ja) \right] \cdot \begin{cases} 1, & r \leq Na/2, \\ 0 & \text{otherwise.} \end{cases} \quad (115)$$

We can now calculate the Fourier transform of this finite lattice by using the multiplication theorem. The Fourier transform of the box function with full width Na and centered at zero is

$$F_{\text{box}}(S) = \frac{\sin(\pi Na \cdot S)}{\pi Na \cdot S}, \quad (116)$$

the so-called sinc function. Thus, as the Fourier transform of the finite lattice, we obtain an infinite lattice in the Fourier space, with each lattice point convoluted by a sinc function:

$$F[g_{\text{finite}}(r)] = \sum_{h=-\infty}^{\infty} \delta(S - h/a) \frac{\sin(\pi Na \cdot S)}{\pi Na \cdot S}. \quad (117)$$

Bibliography

- [1] C. Giacovazzo, H. L. Monaco, G. Artioli, D. Viterbo, M. Milanesio, G. Ferraris, G. Gilli, P. Gilli, G. Zanotti, and M. Catti. *Fundamentals of Crystallography*. Oxford University Press, Oxford, 2011.
- [2] M. M. Julian. *Foundations of Crystallography*. CRC Press Boca Raton, 2008.
- [3] B. K. Vainstein. *Modern Crystallography I, Symmetry of Crystals*. Solid-State Sciences. Springer, Berlin, 1981.
- [4] U. Shmueli (Ed.). *Theories and Techniques of Crystal Structure Determination*. Oxford University Press, Oxford, 2007.
- [5] W. Blake (Ed.). *Crystal Structure Analysis*. Oxford University Press, Oxford, 2009.
- [6] M. F. C. Ladd and R. A. Palmer. *Structure Determination by X-ray Crystallography*. Plenum Press, New York, 1994.
- [7] P. Luger. *Modern X-Ray Analysis on Single Crystals*. Walter de Gruyter, Berlin, 1980.
- [8] G. H. Stout and L. H. Jensen. *X-ray Structure Determination*. Macmillan Publishing, New York, 1968.
- [9] J. Als-Nielsen and D. McMorrow. *Elements of Modern X-ray Physics*. Wiley, New York, 2011.
- [10] A. J. C. Wilson (Ed.). *Mathematical, Physical and Chemical Tables*. International Tables for Crystallography, vol. C, Dordrecht, Holland, 1st edition, 1992.
- [11] B. T. M. Willis and A. W. Pryor. *Thermal Vibrations in Crystallography*. Cambridge University Press, Cambridge, 1975.
- [12] M. T. Dove. *Structure and Dynamics*. Oxford University Press, Oxford, 2003.
- [13] J. M. Cowley. *Diffraction Physics*. North-Holland, Amsterdam, 1981.
- [14] D. Bleiner, J. Costello, F. de Dortan, G. O'Sullivan, L. Pina, and A. Michette (Eds). *Short Wavelength Laboratory Sources*. RSC Publishing, Cambridge, 2015.

- [15] C. G. Darwin. The Theory of X-Ray Reflexion. *Philos. Mag.*, 27:315, 1914.
- [16] C. G. Darwin. The Reflexion of X-Rays from Imperfect Crystals. *Philos. Mag.*, 43:800, 1922.
- [17] T. R. Welberry and T. Weber. 100 years of diffuse scattering. *Crystallogr. Rev.*, 22:2, 2016.
- [18] R. I. Barabash, G. E. Ice, and P. E. A. Turchi (Eds). *Diffuse Scattering and the Fundamental Properties of Materials*. Momentum Press, New York, 2009.
- [19] T. R. Welberry. *Diffuse X-ray Scattering and Models of Disorder*. Oxford University Press, Oxford, 2009.
- [20] V. M. Nield and D. A. Keen. *Diffuse Neutron Scattering from Crystalline Materials*. Oxford University Press, Oxford, 2001.
- [21] T. Michelitsch and A. Wunderlin. On the theory of Huang x-ray scattering caused by point defects in hexagonal crystals. *Phys. Status Solidi B*, 198:615–620, 1996.
- [22] T. Egami and S. J. L. Billinge. *Underneath the Bragg Peaks*. Pergamon, Elmsford, 2003.
- [23] T. Weber and A. Simonov. The three-dimensional pair distribution function analysis of disordered single crystal: basic concepts. *Z. Kristallogr.*, 227:238, 2012.
- [24] F. Zernike and J. A. Prins. Die Beugung von Röntgenstrahlen in Flüssigkeiten als Effekt der Molekülanordnung. *Z. Phys.*, 41:184, 1927.
- [25] P. J. Chupas, X. Qiu, J. C. Hanson, P. L. Lee, C. P. Grey, and S. J. L. Billinge. Rapid-acquisition pair distribution function (RA-PDF) analysis. *J. Appl. Crystallogr.*, 36:1342, 2003.
- [26] J. Becker, M. Bremholm, C. Tyrsted, B. Pauw, K. M. Ø. Jensen, J. Eltzholt, M. Christensen, and B. B. Iversen. Experimental setup for in-situ X-ray SAXS/WAXS/PDF studies of the formation and growth of nanoparticles in near- and supercritical fluids. *J. Appl. Crystallogr.*, 43:729, 2010.
- [27] M. Zobel, A. Windmüller, E. M. Schmidt, K. Götz, T. Milek, D. Zahn, S. A. J. Kimber, J. M. Hudspeth, and R. B. Neder. The evolution of crystalline ordering for ligand-ornamented zinc oxide nanoparticles. *CrystEngComm*, 18:2163, 2016.
- [28] M. Zobel, H. Chatterjee, G. Matveeva, U. Kolb, and R. B. Neder. Room-temperature sol–gel synthesis of organic-capped ZnO nanoparticles. *J. Nanopart. Res.*, 17:200, 2015.
- [29] M. Zobel, R. B. Neder, and S. A. J. Kimber. Universal solvent restructuring induced by colloidal nanoparticles. *Science*, 347:292, 2015.
- [30] J. Kieffer and D. Karkoulis. PyFAL, a versatile library for azimuthal regrouping. *J. Phys. Conf. Ser.*, 425:202012, 2013.
- [31] C. Prescher and V. B. Prakapenka. DIOPTAS: a program for reduction of two-dimensional x-ray diffraction data and data exploration. *High Press. Res.*, 35:223, 2015.
- [32] R. B. Neder, V. I. Korsunskiy, Ch. Chory, G. Müller, A. Hofmann, S. Dembski, Ch. Graf, and E. Rühl. Structural characterization of II–VI semiconductor nanoparticles. *Phys. Status Solidi C*, 4:3221–3233, 2007.
- [33] D. W. Bruce, D. O’Hare, and R. I. Walton (Eds). *Structure from Diffraction Methods*. Wiley, New York, 2014.
- [34] R. E. Dinnebier and S. J. L. Billinge (Eds). *Powder Diffraction*. RSC Publishing, Cambridge, 2008.
- [35] P. Juhas, L. Granlund, P. M. Duxbury, W. F. Punch, and S. J. L. Billinge. The Liga algorithm for ab initio determination of nanostructure. *Acta Crystallogr., Sect. A*, 64:631, 2007.
- [36] M. J. Cliffe and A. Goodwin. Quantification of local geometry and local symmetry in models of disordered materials. *Phys. Status Solidi B*, 250:949, 2013.
- [37] M. J. Cliffe and A. Goodwin. Nanostructure determination from the pair distribution function: a parametric study of the INVERT approach. *J. Phys. Condens. Matter*, 25:454218, 2013.

Karlheinz Schwarz and Peter Blaha

DFT calculations of solids in the ground state

Keywords: DFT, ground state

Introduction

The three-dimensional structure of a solid at the atomic scale and the corresponding electron density is the basis for understanding the electronic structure of such a system. In this chapter, we focus on the ground state of a solid and its fundamental observables. The chapter *TDDFT, Excitations and Spectroscopy* extends such studies to a fourth dimension, namely time. Quantum mechanical calculations play an important role when studying the electronic structure of solids at the length scale of Å or a few nanometers. The main scheme of the theory is the density functional theory (DFT), which strikes a good balance between an accurate quantum mechanical treatment and a sufficiently detailed atomic structure. A real solid is by far too complicated for any theoretical treatment without making proper approximations or idealizations.

In this context, we discuss different aspects such as the atomic structure, the quantum mechanical treatment of the electronic structure, focusing on density functional theory (DFT), and particularly time-independent DFT in this chapter, the computer codes for solving DFT, the parameters that determine the accuracy of the results, and various properties obtainable from DFT calculations. This review introduces these simulation techniques and illustrates, for selected examples, which insights we can gain into structure-property relations.

1 Atomic structure

Let us start with the atomic structure and its idealization. The standard assumption is that a solid is represented by a unit cell, which is repeated (in all three directions) by applying periodic boundary conditions. Accordingly, it is assumed that a solid is perfect, ordered, and infinite. However, a real crystal differs from this ideal situation, for example, due to defects, impurities, surface relaxations, nonstoichiometry, disorder, etc. In crystallography, one averages over a certain domain and focuses on bulk properties to determine the crystal structure in terms of a unit cell, inside which various atoms occupy atomic (Wyckoff) positions. We have discussed these and related aspects in more detail in [1]. We assume knowledge of the basic concepts of solids and their electronic structure. Such topics include the unit cell in the direct or reciprocal space (Brillouin zone), symmetry operations, translations, group theory (space

<https://doi.org/10.1515/9783110433920-003>

group, point group), \mathbf{k} vectors, Bloch theorem, band structures, and the density of states (DOS). The reader can find details about these points, for example, in [2–4]. In most conventional calculations the nuclei are treated as classical particles at $T = 0$. The mass of any nucleus is much higher than that of an electron. Therefore, in most cases, it is justified to make the Born–Oppenheimer approximation, in which the nuclei remain at fixed positions for computing the electronic states by means of quantum mechanics (e.g., DFT). It is assumed that the motion of the nuclei and electrons is independent from each other and no coupling is present, which simplifies calculations. A real strength of theory is that it can calculate artificial model systems irrespective of their existence in nature. We can move, add, or remove atoms and thus can systematically study how such modifications affect properties. In a computer simulation, the atomic structure is defined as an input. However, we must explore whether or not the assumed idealized structure is a good representation of a real material, whose atomic structure we know only approximately from experiment.

2 Quantum mechanics for treating the electronic structure

We need a quantum mechanical treatment to describe the electronic structure of a system of interest and solve a many-particle Schrödinger equation, an intractable task. With the Born–Oppenheimer approximation, we can start with the time-independent Schrödinger equation and describe each electronic state by a many-electron wave function (WF), often labeled ψ . Its modulus $\psi^*\psi$ defines the electron density $\rho(\mathbf{r})$, the probability of finding an electron at position \mathbf{r} . An alternative route to the direct solution of the Schrödinger equation is shifting the focus of the problem from ψ to a fundamental observable of the problem, the density $\rho(\mathbf{r})$. There are two classes of electronic structure methods, wave-function-based and density-based schemes, both of which have their advantages and disadvantages, but there are also methods that combine these two schemes.

2.1 Hartree–Fock and related schemes

In the Hartree–Fock (HF) method, the total electronic wave function of an N -electron system is expressed as a determinant composed of N single-electron WFs, known as the Slater determinant. By construction this determinant has the property that it changes the sign when two electrons are interchanged, i.e., the Pauli exclusion principle. The latter is treated exactly in the HF method and is called the exchange interaction. The corresponding single electronic states are orthogonal to each other, and each electron feels the (time-averaged) electrostatic field created by all other electrons

(and nuclei) in the system. This problem can only be solved iteratively due to the obvious interdependence problem: we need the potential for the WFs but also the WFs for the potential. In simple terms, we need for a selected electron the WFs of all other electrons to compute the corresponding field, but to find each of these WFs, we must know the field. Therefore, we must find the solution in iterating cycles, a procedure called the self-consistent field (SCF), until self-consistency is reached. Instead of solving the intractable N -electron Schrödinger equation, we can solve N one-electron equations in the HF scheme, which makes computation feasible. By taking the time average (for the field) in the HF method we make an approximation, since correlation effects are completely missing. They can be included with post HF schemes such as configuration interaction (CI) or coupled cluster (CC) methods not described here. Such schemes are ab initio methods often used in quantum chemistry, especially for studying molecules. They can be very accurate (almost exact) but quickly become computationally very expensive when the system size increases (for further details, see [1]).

2.2 Density functional theory

In contrast to wave-function-based methods, the fundamental idea of density functional theory (DFT) is to replace the complete many-electron wave function with the much simpler ground-state electron density as the main variable. We start with the statement by Hohenberg and Kohn [5] proposed in 1964. For any system of interacting particles in an external potential $V_{\text{ext}}(\mathbf{r})$, the density is uniquely determined. In this formulation of DFT, they demonstrated a unique one-to-one mapping between the external potential $V_{\text{ext}}(\mathbf{r})$ (from the nuclei) applied to a nondegenerate electronic system and its ground-state density $\rho(\mathbf{r})$, which depends on the position \mathbf{r} , i.e., only three coordinates. This mapping implies that the ground-state energy E of the system is a functional of its ground-state density $\rho(\mathbf{r})$. A universal functional for the energy $E[\rho(\mathbf{r})]$ can be defined in terms of the density. The exact ground state is the global minimum value of this functional:

$$E = T_0[\rho] + \int V_{\text{ext}}\rho(\mathbf{r})d\mathbf{r} + \frac{1}{2} \int \frac{\rho(\mathbf{r})\rho(\mathbf{r}')}{|\mathbf{r}' - \mathbf{r}|} d\mathbf{r}d\mathbf{r}' + E_{\text{xc}}[\rho]. \quad (1)$$

For simplicity, we write equation (1) for an atom with the following terms:

- (i) the kinetic energy T_0 of noninteracting electrons;
- (ii) the Coulomb interaction between the nucleus (with the external potential V_{ext}) and each electron;
- (iii) the Coulomb interaction between the electrons; and
- (iv) the important exchange-correlation energy E_{xc} . The last term includes everything not included in the other terms, namely all quantum mechanical effects, such as exchange, static and dynamic electron–electron correlation, and the difference between the interacting and noninteracting kinetic energies.

In equation (1) we use Hartree atomic units ($\hbar = m_e = e = 1$), where m_e is the rest mass of an electron, and e its charge. The fundamental energy is expressed in terms of Hartree, and the length with respect to the Bohr radius. A Hartree is the ground-state energy of the electron in the hydrogen atom, and the Bohr radius is its average ground-state radius (1 Bohr ≈ 0.529 Å). One commonly uses these units for atoms or molecules. For solids, however, the standard unit for the energy is Rydberg, which differs exactly by a factor of two, i.e., 1 Rydberg = $\frac{1}{2}$ Hartree = ~ 13.605 eV.

In principle, DFT is an exact formulation; however, we do not fully know how to express the interaction between individual electrons. We can only prove that the total energy of the system is a functional of the density whose explicit mathematical form is unknown and thus requires approximations. Mathematics calls this case functional instead of function.

Kohn and Sham [6] (KS) proposed a scheme to make DFT calculations feasible. Their idea relies on mapping the interacting many-body system (the nuclei and electrons) onto a noninteracting system of KS electrons (quasiparticles) that lead to the true density. They introduced orthonormal auxiliary functions Φ_i (Kohn–Sham orbitals), which allow the density to be expressed as

$$\rho(\mathbf{r}) = \sum_i n_i |\Phi_i(\mathbf{r})|^2 \quad (2)$$

with occupation numbers n_i . For such a fictitious system, we write the total wave function as a Slater determinant of these mono-electronic wave functions, the KS orbitals. The latter are obtained by applying the variational method to minimize the total energy, where the number of electrons is constraint to a constant N . This idea introduces the KS equations

$$\left[-\frac{1}{2}\nabla^2 + V_{\text{ext}}(\mathbf{r}) + V_C[\rho(\mathbf{r})] + V_{\text{xc}}[\rho(\mathbf{r})] \right] \Phi_i(\mathbf{r}) = \epsilon_i \Phi_i(\mathbf{r}) \quad (3)$$

with a local one-body potential, the KS potential, mimicking all interelectronic interactions via Hartree and exchange-correlation (XC) contributions. Since this potential is averaged over time, it has been called the mean field approximation (mainly in many-body physics). In equation (3), we have the terms of the kinetic energy, the external potential (from the nuclei), the Coulomb potential V_C , and the important exchange-correlation potential V_{xc} , which formally is the functional derivative of E_{xc} (in equation (1)) with respect to the density ρ . The KS orbitals should be occupied according to the Aufbau principle (defining n_i in equation (2)) and solved self-consistently (as in the Hartree–Fock scheme). Such iteration cycles are necessary, since we need the potential to compute the KS orbitals, from which we obtain the density according to equation (2). Knowing the density, we can compute the potential for the next iteration. If this can be done with integer occupation numbers n_i , then the system is said to be V-representable. This means that the ground-state density can be associated with a Hamiltonian that has an external potential $V(\mathbf{r})$. Levy

[7] and Lieb [8] independently proposed a more general variational routine requiring the density to be only N -representable, which means that it can be derived from an antisymmetric wavefunction. When we express the total energy as in equation (1), approximations are necessary. Writing the density as in equation (2) suggests that we can write the kinetic energy as a sum of kinetic energies of the KS orbitals, but there remains a difference. We can express the kinetic energy as the single-particle kinetic energy plus a correction. In the third term of equation (1) the nominator should be in terms of the two-particle density $\rho^{(2)}(\mathbf{r}, \mathbf{r}')$, which may be interpreted as the probability that an electron exists at point \mathbf{r} given that a second electron exists at point \mathbf{r}' . This term makes the many-particle problem very difficult to solve, forcing us to make an approximation. If the two electrons were completely uncorrelated, then the two-particle density $\rho^{(2)}(\mathbf{r}, \mathbf{r}')$ would be just the product of the one-particle densities (or probabilities) $\rho^{(2)}(\mathbf{r}, \mathbf{r}') = \rho(\mathbf{r})\rho(\mathbf{r}')$ plus a correction. Another problem is the treatment of the Coulomb interaction according to the third term in equation (1). This term contains the Coulomb interaction of an electron with itself (the self-interaction), which is unphysical. In an exact treatment of exchange (as, e.g., in the Hartree–Fock scheme) a complete cancellation of this unphysical term occurs. However, in DFT there often remains a self-interaction error due to the approximations used for E_{xc} . Consequently, the last term in equation (1) must contain all these effects, namely the correction to the kinetic energy, the exchange (Pauli repulsion), and correlation effects (repulsion between electrons), including the self-interaction correction. The specific form of the unknown part of the exchange-correlation functional $E_{xc}[\rho]$ has been the focus of many investigations, leading to a large variety of functionals discussed in literature, e.g., in [9].

2.3 Density functional theory functionals

The real advantage of DFT is that we do not need to know the many-electron WF, which depends for each electron on three position coordinates and the spin and thus on $4N$ variables for N electrons. In principle, this is an enormous simplification, since the density $\rho(\mathbf{r})$ even for very large systems depends only on three coordinates. There is only one system for which these expressions for E_{xc} and V_{xc} can be accurately determined, namely the homogeneous electron gas [10], which is a highly idealized case for describing a simple metal. If we pick out one single electron, then we can express the density of the remaining $N - 1$ electrons by the original total density and an exchange-correlation hole. The exchange hole comes from the Pauli exclusion principle (for electrons with the same spin) and must integrate to -1 , but the correlation hole accounts for the Coulomb repulsion of electrons with opposite spin and contains no charge. The size of this hole depends on the density: for a high (low) density case, the hole is small (big). For any real system, the density is not constant, and thus we must approximate E_{xc} . The choice of DFT functionals is an active field of research.

The reader should look at the newest literature, for example, in the review [1], which covers some aspects. Here we just mention the main categories of the conventional exchange-correlation functionals:

- (i) In the local density approximations (LDA) [6, 10] the concept is the following: the density $\rho(\mathbf{r})$ at a given position \mathbf{r} has a certain value. By assuming that this density is constant throughout space we can use the E_{xc} of the homogeneous electron gas, where E_x is known analytically, and E_c has been calculated numerically by quantum Monte Carlo [10]. In LDA we make this local approximation for each point \mathbf{r} .
- (ii) Since, in practice, the density varies around point \mathbf{r} , we can – as a next step – include a gradient term leading to the generalized gradient approximation (GGA) for which various forms have been parameterized, for example, the one by Perdew–Burke–Ernzerhof (PBE) [11] or a later refinement for solids, called PBEsol [12].
- (iii) The meta-GGAs [13] depend on ρ , $\nabla\rho$, $\nabla^2\rho$, and/or the kinetic energy density τ , respectively. The use of τ allows us to detect regions of space where the density is dominated by orbital overlap or single-electron contributions and even van der Waals regions can be identified. It allows a more flexible construction of functionals. With it, we obtain higher accuracy for more properties (energetics and bonding distances) [14–16], but it leads to a more complicated, nonlocal potential, so that self-consistency is more difficult.
- (iv) Some functionals include an explicit dependence on occupied orbitals (sometimes only for selected orbitals). This allows in principle an exact treatment of exchange, but since exact correlation is unknown and a balanced description of exchange and correlation is very important for obtaining results in agreement with experiment, we should not use exact exchange with some approximate (local) correlation. Here the hybrid functionals [17] should be mentioned, which take only a certain fraction of the Hartree–Fock scheme (with the exact treatment of exchange using KS orbitals) and combine it with a standard GGA to account for correlation. For highly correlated systems, especially for those containing late transition elements (with localized $3d$ electrons) or rare earth atoms (with $4f$ electrons), a Hubbard U is often used, where the parameter U accounts for the energy penalty (repulsion) of occupying $3d$ or $4f$ electrons on the same atom (instead of delocalizing them). The parameter U is defined as $U = E(d^{n+1}) + E(d^{n-1}) - 2E(d^n)$. This leads to schemes like LDA+ U or GGA+ U [18], which are useful in systems where the competition between localized and delocalized (d or f) states determine the property of a solid.

There is a large variety of chemical bonding from insulators to metals and magnetic or van der Waals interactions. Covalent, ionic, or metallic bonds can be well described within DFT, but van der Waals forces are relatively weak (compared to the others), mainly originating from induced dipole moments, but play an important role in intermolecular interactions. They can be included in modern calculations using various

approximations as indicated in [19]. Whereas in particular a semiclassical treatment is possible and computationally very simple, other methods have strong nonlocal character and become increasingly more expensive. The golden standard for van der Waals interactions in quantum chemistry, coupled cluster theory (CCSD(T)), can hardly be applied in solids, and calculations based on the adiabatic-connection fluctuation-dissipation theorem (ACFDT) in the random phase approximation (RPA) are still very expensive [20], and their accuracy is still a matter of debate. Unfortunately, there is not an optimum DFT functional that works well for all cases and properties, making compromises necessary. We refer the reader to a recent paper [21] critically analyzing DFT functionals in terms of accuracy and addressing their differences for molecules and solids. So far, the focus was still on ground-state properties. In the next section, we discuss excitations probing unoccupied states. In the simple one-electron picture, we describe optical excitations from occupied to empty band states, which strictly speaking is not justified. Nevertheless, this one-electron approach is often used and works well for metallic systems. However, for insulators, this scheme leads (e.g., with LDA or GGA) to band gaps that are often too small by 30–50% [22]. A pragmatic way to obtain quite good band gaps is the use of the Tran–Blaha modified Becke–Johnson (TB-mBJ) potential [23]. In this semiempirical scheme the original Becke–Johnson potential, which is a meta-GGA potential designed to reproduce exact exchange potentials in free atoms, was modified using a density-based parameter that can be calculated on the fly for each compound. It yields band gaps comparable to very expensive GW calculations [24], which are considered as golden standard for the calculation of band gaps in solids. We discuss some of these aspects in the next section in connection with excitation.

2.4 Excitations and Koopmans' theorem

Let us consider the ionization process for a simple case such as an atom A (or a molecule). The initial state is the ground state of the neutral A , but in the final state one electron has been removed from the orbital i of the corresponding positive ion A^+ . In the ionization process $A \rightarrow A^+ + e^-$, the total energy difference $E_{\text{exact}}(A) - E_{\text{exact}}(A^+) = \text{IP}$ defines the ionization energy (or called ionization potential IP). In Hartree–Fock theory, this total energy difference equals the orbital energy ϵ_i according to *Koopmans' theorem* [25] but under the assumption that we keep the wave functions from the ground state of the atom also for the ion, as schematically shown in Figure 1. This theorem is the basis for the single-particle description (one-electron picture), in which excitations are interpreted in terms of orbital energies instead of total energy differences, which would be the exact definition.

In an exact treatment, the IP_{exact} is the *total energy difference* between the atom A and the ion A^+ with a separated electron. Koopmans showed that in Hartree–Fock (HF) theory the total energy difference between the atom and the ion equals the *orbital*

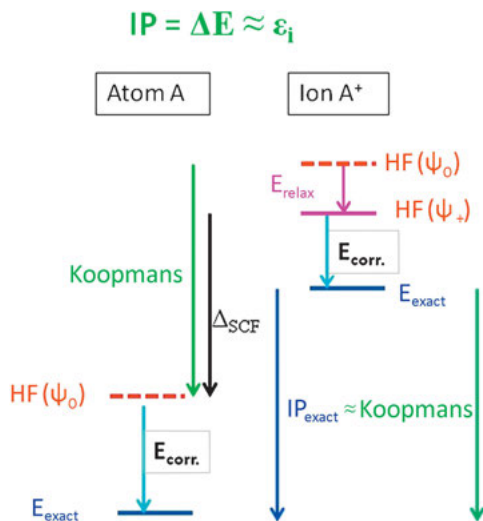


Figure 1: Ionization potential (IP) according to Koopmans' theorem [25] shown in a schematic diagram.

energy ϵ_i when the electron is removed from the orbital i , provided that we keep the ground-state orbitals (labeled Ψ_0). Allowing the orbitals of the ion A^+ to relax (labeled Ψ_+) lowers the HF total energy of the ion by the relaxation energy E_{relax} . This scheme (still within HF) leads to the energy difference $\Delta_{\text{SCF}} = E_{\text{HF}}^A(\Psi_0) - E_{\text{HF}}^{A^+}(\Psi_+)$. It corresponds to the total energy difference taken between the two SCF calculations for the atom and ion. The exact total energies (of both A and A^+) are lower than the HF values by the corresponding correlation energy E_{corr} , since by definition correlation is completely missing in HF. In practice, E_{corr} is often smaller for the ion than for the neutral system, and thus an error cancellation occurs: $E_{\text{corr}}(A) \approx E_{\text{relax}} + E_{\text{corr}}(A^+)$ making Koopmans' IP agree well with the exact one. This is true for many cases, but exceptions occur.

In an atom or ion, we have an integer number of electrons, namely N and $N - 1$, respectively. For large systems, we can expand the total energy in DFT in a power series of continuous occupation numbers (according to equation (2)). In such a representation, the DFT orbital energies ϵ_i are – according to Janak's theorem [26, 27] – the partial derivatives of the total energy with respect to the corresponding fractional occupations numbers n_i :

$$\epsilon_i = \frac{\partial \langle E \rangle}{\partial n_i}. \quad (4)$$

In Koopmans' theorem [25], we have an integer change in electron number, whereas in Janak's theorem [26] a differential change in electron numbers is assumed. One of us has already described this aspect more than forty years ago [28], at that time within the $X\alpha$ and $X\alpha\beta$ method, the early versions of the local density approximation (LDA) and the generalized gradient approximation (GGA). In Figure 2 we show how the energy of the chlorine atom varies with the occupation number n_{3p} of the top valence $3p$

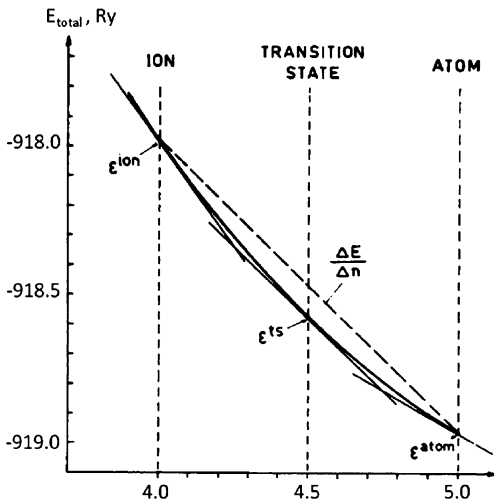


Figure 2: Total energy of the chlorine atom (ion) shown as a function of the (continuous) $3p$ orbital occupation number n_{3p} (taken from Ref. [28]). The secant line $\Delta E/\Delta n$ represents the ionization (in analogy to Koopmans), whereas the tangents to E_{total} correspond to the eigenvalues of the ion Cl^+ (ϵ^{ion}), the transition state (ϵ^{ts}), and the neutral Cl atom (ϵ^{atom}).

electron, i.e., the ionization process. The IP, as the energy difference between atom and ion, corresponds to the secant at the endpoints (with $n_{3p} = 4$ and 5 , respectively).

Formally speaking, the KS eigenvalues are just Lagrange multipliers and thus should have no physical meaning. In practice, many researchers observed that the eigenvalues give a reasonable description for excitations in a form of the band structure in analogy to Koopmans' or Janak's theorem. The main concern is that we need to introduce fractional occupation numbers [29, 30]. Some time ago, Slater introduced the transition state concept [31], in which, for example, half an electron is removed from the $1s$ core state (leading to a configuration $1s^{1.5}$). In such a configuration, this $1s$ orbital energy can be used to estimate the position of core states. Slater's transition state is also used to approximate core level spectra since it is in between the initial and final states and thus includes some relaxations [32]. More recently, the difference between the exact discontinuous behavior and the continuous (inexact) behavior of most functionals was shown for the carbon atom [33] leading to a similar picture as in Figure 2.

Back to the IP of the chlorine atom: In DFT (assuming continuous occupation numbers), a similar slope can be obtained with Slater's transition state, in which half an electron has been removed (with the occupation number 4.5). Geometrically speaking, the tangent at the Slater's transition state agrees with the secant at the ends. From a numerical point of view, the transition state eigenvalue is easier to obtain than computing the total energy difference. However, we cannot use a Slater transition state and keep the N -representability, which requires integer occupation numbers.

For the exact functional E_{xc} , the highest occupied KS eigenvalue is exactly the negative of the ionization potential [29], but this is no longer true for DFT functionals such as LDA or GGA. The fact that total energy differences within LDA are reasonable approximations for the ionization potentials, whereas the eigenvalues are not, suggests that the energy difference benefits from error-cancellation by subtraction (mainly from the self-interaction error).

For insulating solids, the LDA (or GGA) band gap (i.e., from “bare” KS eigenvalues) is too small by 30–50% [22]. The main reason is the discontinuity between the N - and $(N+1)$ -electron systems [30], but it can partly also come from the self-interaction error. Since the value of the band gap is often of fundamental importance for various applications, many attempts have been made to improve the results. Currently, the most accurate and robust first-principles approach to determine the band gap (of weakly correlated insulating materials) is the many-body perturbation theory in the GW approximation [34]. In this scheme, the Green’s function G is multiplied by the screened potential W to account for the excitation process. It is significantly more demanding in terms of computer time than conventional DFT calculations based on LDA or GGA functionals. A simple and pragmatic way to obtain good band gaps is the choice of using the TB-mBJ potential [23], which yields rather accurate gaps for many insulators at a computational cost comparable to GGA.

For correlated systems, the LDA+U or GGA+U schemes [18] can efficiently be used and form a lower and upper Hubbard band approximately separated by U , which must be properly chosen (which makes this method no longer *ab initio*). In simple metals or early transition metals, the valence electrons form a common band and thus are delocalized. However, in a material containing electrons from the $4f$ -shells (or late transition metals), these electrons prefer localized states. This means that these electrons do not want to hop from one atom to the neighboring sites, expressed by a high U value. Such electrons form localized bands, the lower and upper Hubbard bands. In some cases, this band separation causes a gap.

Many-body physics can treat correlation effects more accurately as, for example, in dynamical mean field theory (DMFT), but this often requires properly chosen parameters that are *a priori* not known for a particular system. Recently – in a joint effort – the two fields merged, for example, in schemes such as LDA+DMFT [35]. We start a DFT calculation (e.g., using LDA), transform the Bloch functions of the correlated electrons into maximally localized Wannier functions (see, e.g., [36]), and extract effective tight-binding parameters. With these parameters, we can set up an Andersson impurity model connected to a bath of noninteracting electrons, which can be solved by the DMFT method, as described in a recent review [35].

Presently, Kohn–Sham (KS) density functional theory (DFT) is the state-of-the-art *ab initio* method for studying the electronic properties of materials due to its balance between accuracy and computational efficiency. In quantum chemistry, the term *ab initio* refers to first-principles Hartree–Fock-based theory, excluding DFT. However,

in solid-state theory, we call DFT an *ab initio* method, since it is formally exact. We should keep in mind that, for large systems, every theory must make approximations.

2.5 DFT computer codes

Once we choose a particular exchange-correlation functional, the mathematical problem is completely specified as a set of Kohn–Sham equations, whose solutions yield orbitals and energies from which the total electronic properties can be evaluated. Many groups have developed numerical solution schemes implemented in a variety of computer codes available for solid-state simulations. Recently, a paper on the reproducibility of DFT results was published [37], in which 40 different DFT methods were compared to establish high-precision results for equation-of-state data. Different computer codes should give the same results, provided that they use the same first-principles formalism (e.g., the same DFT functional) carried to full convergence. Although most codes differ vastly in their details of implementation, they agree very well and thus provide reproducibility of DFT predictions. These validation tests have shown that the deviation between accurate codes is often significantly smaller than the typical difference between theory (based on different functionals) and experimental data. In the case a code shows deviations, it should be improved, which has been achieved during recent years. High-precision DFT calculations are essential for developing new improvements, such as new density functionals, which may further increase the predictive power of these simulations. The paper [37] contains many references and details of the various computer codes, and thus we can skip them here. We therefore just summarize the essential steps and start with the atoms, which are the building blocks of a solid.

2.6 Atomic states and basis sets

The electronic configuration of an atom follows the Aufbau principle, which requires us to start with the lowest energy level, the 1s state. It is deep in energy, and the corresponding wave function (or electron density) is near the nucleus, even more so for heavier elements. For the additional electrons, the Pauli principle requires occupation of the next higher levels such as 2s, 2p, and so on till we reach the valence electrons, which are much more delocalized. The wave functions of these electrons must be orthogonal to the core electrons, which do not contribute to chemical bonding. For illustration, we chose a heavy element, such as osmium (with the atomic number $Z = 76$). We surround the Os nucleus by an atomic sphere with a radius of 2.36 Bohr (about 1.25 Å) and characterize the electronic states in three categories:

- (i) *Core electrons* ($1s^2 2s^2 2p^6 3s^2 3p^6 3d^{10} 4s^2 4p^6 4d^{10}$) have low orbital energies varying from $-54\,204$ Ryd (for the 1s state) to about -20.6 Ryd (for the 4d states). Their

wave functions are relatively close to the nucleus with their corresponding electron densities completely confined inside the sphere surrounding the nucleus. We discuss the relativistic aspects in Section 3.2 in connection with Figure 4.

- (ii) *Semicores states* ($5s^2 5p^6 4f^{14}$) are medium in energy (between -7 and -3 Ryd) with more diffuse wave functions. Their densities have a small charge leakage outside this sphere. The principle quantum number of these states is one less than that of the valence electrons (e.g., $5s$ vs. $6s$).
- (iii) *Valence electrons* ($6s^2 5d^6$) are high in energy with delocalized wave functions forming the bonds.

Since the core electrons do not directly contribute to chemical bonding, we try to separate them out. One possibility is to compute their wave functions for an isolated atom but keep them unaltered for the solid description (frozen core approximation). Alternatively, we can obtain them from the spherically symmetric part (within the corresponding atomic sphere) of the actual potential of the solid. The highly localized (or oscillatory) behavior of these core wave functions makes a proper description difficult, especially for methods based on plane-wave expansions. To avoid this difficulty, another approach became popular, that of adding a carefully designed repulsive component to the Kohn–Sham potential, a so-called pseudopotential. We can work with smoother (pseudo)wave functions, which can be well represented and thus lead to a smaller basis set in the so-called pseudopotential schemes (see, e.g., [38]). Alternatively, the projector augmented-plane-wave (PAW) approach defines an explicit transformation between the all-electron and pseudopotential wave functions by means of additional partial-wave basis functions, but their choice is not trivial and thus requires expertise. In contrast to all these approaches, all-electron methods explicitly construct basis functions that are restricted to a specific energy range as, for example, in the linearized-augmented-plane-wave (LAPW) method [39]. It treats core and valence electrons on equal footing (e.g., by using numerical atomic-like orbitals). The electron density from the core electrons may vary (e.g., due to charge transfer in an ionic system) during the SCF cycle. An all-electron treatment has the advantage of being able to include such effects, but this inevitably increases the computation time. More details of the various methods can be found in [38, 40] in terms of concepts and in [37] for their accuracy.

2.7 LAPW method and Wien2k code

One of the all-electron DFT codes for solids based on the LAPW method is the Wien2k code [41], which belongs to the set of most accurate codes, as shown in [37]. During the last 38 years, we have developed this code in collaboration with many others, as summarized in several reviews [39, 42–44]. A recent book chapter [1] describes details

of the method, the underlying formalism, and computational aspects like parallelization or user friendliness. It also gives many references and describes how to calculate properties that depend on the electronic structure of solids with sufficient accuracy. Cottenier has written a book [38], in which he explains in detail DFT and the family of LAPW-methods. Here we just focus on the key concepts.

In the APW method introduced by Slater [45], the unit cell is partitioned into two types of regions: (i) (nonoverlapping) *atomic spheres* centered on the atomic sites and (ii) the remaining *interstitial region* (Figure 3). We can adjust the radii of the spheres (labeled R_{mt}) for the various atoms. Inside each atomic sphere, the wave functions have nearly an atomic character. By taking only the spherical part of the potential inside this sphere, we can express the wave functions as partial waves written as a sum of radial functions u_ℓ times spherical harmonics $Y_{\ell m}$ labeled with the quantum numbers ℓ and m . We use the muffin-tin approximation only for numerically solving the radial functions, which depend on the energies E_ℓ . In the interstitial region, where the potential varies only slowly, we can expand the wave functions in a set of plane waves (PWs) with the vectors \mathbf{K} defined in the reciprocal space. Each PW is augmented (i.e., replaced) by the atomic partial waves inside the atomic sphere, and the two types of basis functions are joined at the sphere boundary so that they agree in value (and slope). Over the years, we have developed three types of augmentation (APW, LAPW, APW+local orbitals), in which the energy dependence of the radial functions is treated differently. The corresponding details can be found in various review papers [1, 38–44], which give a summary of how to run DFT calculations using Wien2k that reach a good convergence while being as efficient as possible. In this context, many details are available from the user's guide (see www.wien2k.at). In contrast to the LCAO approach, where the basis functions are centered at the atomic positions, the APW-based methods represent a spatially confined basis set. A high flexibility of the APW basis functions, due to the numerically solved radial equations and the expansion (Figure 3) in the ℓm series up to $\ell = 8$, are an important reason for a high accuracy of APW-based schemes [37]. The atomic-like representation of these basis

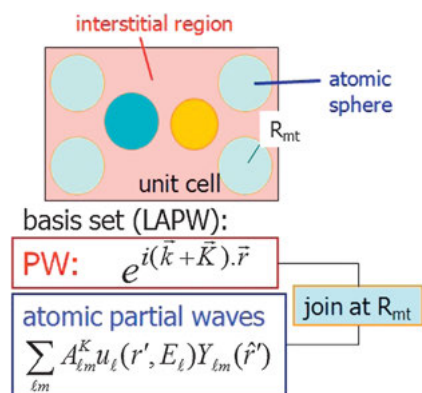


Figure 3: The (linearized-)augmented-plane-wave (LAPW) method: a schematic partitioning of the unit cell into (nonoverlapping) atomic spheres (with a muffin-tin radius R_{mt}) and the corresponding basis sets, namely plane waves (PW) and atomic partial waves in the two types of regions.

functions helps in understanding and interpreting results. In Section 3.5, we show in an example (for BaBiO_3) how a property is affected by details. In our case, we use a full-potential and all-electron method, where we treat the core electrons by solving Dirac's equation, whereas the semicore and valence states are described with the scalar relativistic scheme. When needed, spin-orbit coupling can be included (see Section 3.1). For computational details and aspects like accuracy and full convergence, the reader should refer to the review paper [1].

3 DFT results

In this chapter, we describe some general aspects of DFT calculations and illustrate with a few examples the concepts and results of such calculations. In an old review [46] a rather complete presentation of electronic structure calculations was given for transition metal carbides and nitrides (crystallizing in the simple cubic NaCl structure) illustrating band structure, the SCF cycle, (partial) DOS, chemical bonding (including charge transfer), electron densities, total energy, and x-ray emission spectra (XES). These concepts are still valid. We further present selected and more recent results, but differing in detail.

3.1 Relativistic effects

In a solid that contains heavier elements, relativistic effects become important. The inner electrons of such an element can reach a high velocity (approaching the speed of light) causing a mass enhancement and an orbital contraction. Therefore, we must solve Dirac's equation instead of Schrödinger's equation. The difference is illustrated in Figure 4 for the $1s$ orbital of Os. From a nonrelativistic to a relativistic treatment the $1s$ orbital is significantly lowered in energy by about 468 Ryd to -5420 Ryd. This large shift in energy leads to a contraction of the $1s$ orbital, causing a higher screening of the nuclear charge. This relativistic treatment significantly affects the valence electrons, whose wave functions must be orthogonal to all inner electrons as illustrated in Figure 4 for the $6s$ orbital of Os.

In addition to the mass-velocity term, the Darwin s -shift (Zitterbewegung) affects the orbital energies, and the spin-orbit coupling causes a splitting in $\ell + s$ and $\ell - s$ states as, for example, into the $p_{1/2}$ and $p_{3/2}$ states. Such shifts (with orbital contraction or expansion) combined with spin-orbit splitting are schematically illustrated in Figure 5 for the valence electrons of Os. This spin-orbit term is large for low-lying states but gets smaller for the valence states, for which they can introduce a splitting in the band structure. These orbital energies provide the basis for the three categories of core, semicore, and valence states as discussed in Section 2.2.

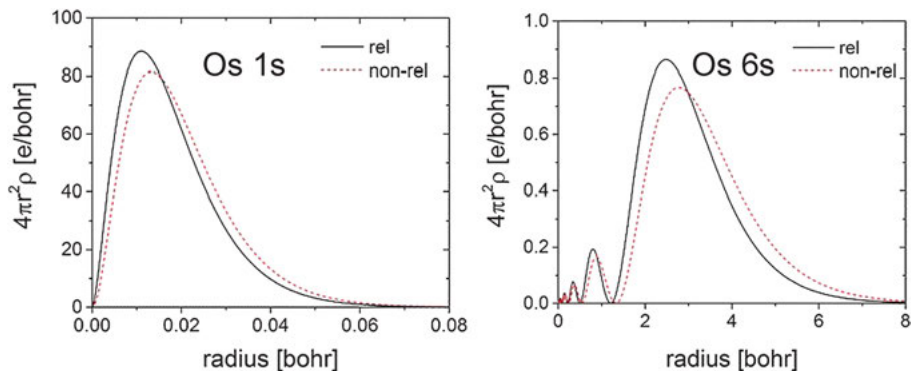


Figure 4: Electron density of the 1s and 6s states in the osmium atom compared between nonrelativistic and relativistic descriptions. Note that the radial scale differs by a factor of one hundred between the two orbitals.

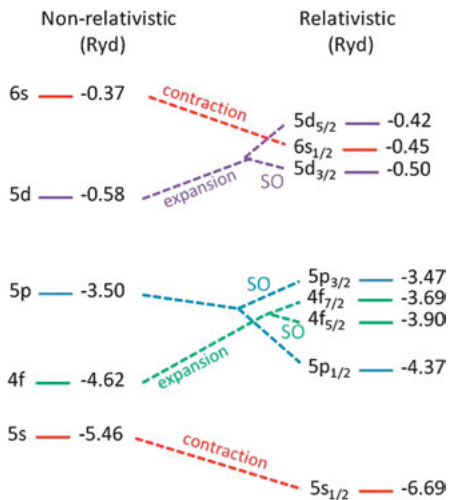


Figure 5: Schematic picture shows how relativity affects the orbital energies of the valence and semicore electrons of osmium, causing a contraction or expansion of the corresponding orbitals and a splitting due to spin-orbit (SO) coupling.

The 5d and 6s states of Au ($Z = 79$) are shifted in a similar way to those of Os ($Z = 76$), causing the *d*-bands to move closer to the Fermi energy. This affects the optical properties, which differ significantly in the 3d – 4d – 5d series of Cu, Ag, Au. The main difference in this series comes from the relativistic effect, as will be discussed in the next section in connection with Figure 7.

3.2 Band structure and density of states

The self-consistent solution of the Kohn–Sham (KS) equations – for a uniform mesh of **k**-points in the irreducible Brillouin zone – yields the KS energies and the correspond-

ing KS orbitals. A plot of these KS energies along high-symmetry lines defines the band structure, a fundamental result of solid-state calculations. Formally, we should not interpret the KS energies as one-particle excitation energies of the system, since they are simply Lagrange multipliers. However, in practice, they are often used to interpret electronic excitations, especially since spectroscopy causes great interest in one-electron energies. Here it helps to label the energy bands in the form of irreducible representations [2]. With this symmetry information, we can distinguish between allowed and forbidden transitions by using, for example, dipole selection rules. In many cases, especially for metallic systems, the band structure works quite well for interpreting excitations, even over a large energy range. There are many examples in the literature illustrating that the calculated energy bands are in close agreement with, for example, angle-resolved photoemission spectra (ARPES), as shown for VSe_2 (for details, see Strocov et al. [47]). There are also exceptions that show significant deviations between this form of theory and experiment.

Here we show (Figure 6) the band structure (including spin-orbit coupling) of the semiconductor InSb using two approximations, namely the GGA functional in the PBE formulation [11] and the TB-mBJ potential [23] (see Section 2.3). Using PBE yields no gap, but with the second choice, TB-mBJ, a small gap opens, and the energies of both the occupied and empty bands agree well with experimental data [48]. Using the TB-mBJ potential is a simple and pragmatic way to obtain good band gaps at a computational cost comparable to GGA, as was shown in [23]. However, TB-mBJ is just an exchange potential but not an energy functional, and thus we cannot use it for the en-

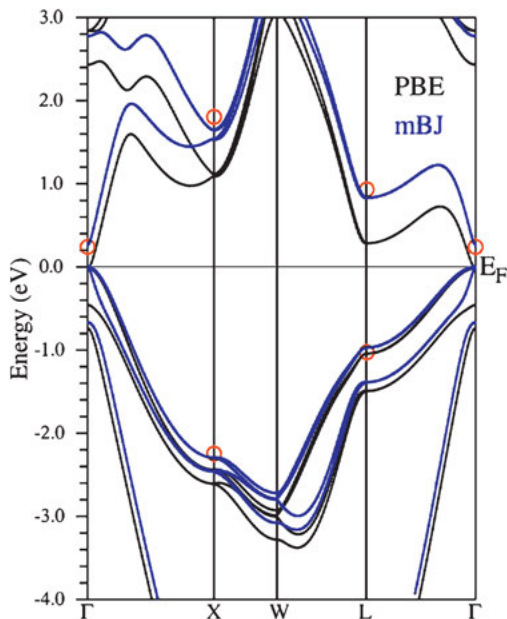


Figure 6: Band structure of InSb for two DFT functionals, namely PBE [11] and TB-mBJ [23]. The experimental (occupied and unoccupied) band states [48] are indicated with red circles.

ergy or the related forces, which we would need for structure optimizations. For each KS eigenvalue $E_n(\mathbf{k})$, the modulus of the corresponding KS orbital leads to an electron density that is normalized in the unit cell. We can decompose this charge by exploiting the LAPW basis set into a contribution q_{out} (from the interstitial region outside the spheres) and those from the atomic regions (labeled by the atom number t):

$$1 = q_{\text{out}} + \sum_{t\ell} q_{t\ell}. \quad (5)$$

The partial atomic charges within each atomic sphere, q_t , can be decomposed further in $q_{t\ell m}$ according to the angular momentum ℓ and sometimes to m (e.g., p_x , p_y , p_z). The wave function contains the complete information of each state, but it is a complex function in three dimensions. The partial charges compress this information to the chemically important part and allow a characterization with a few numbers. This decomposition is very useful especially for analyzing the character of a band. These partial charges depend on the choice of sphere radii and thus should not be over-interpreted, but they are very useful in interpreting chemical bonding (see, e.g., the band-character analysis of the refractory metal compound TiC described in Section 6.2 of [43]). In Section 3.5, we illustrate the usefulness of these partial charges for the perovskite BaBiO₃.

From the KS eigenvalues $E_n(\mathbf{k})$ computed on a sufficiently fine \mathbf{k} -grid in the Brillouin zone (or its irreducible part based on symmetry) we can obtain the density of states (DOS) by counting each state with a weight of one. By using the partial charges (equation (5)) we can decompose the total DOS into partial DOS that specify the chemical character. When a covalent bond originates essentially from two orbitals located at neighboring atoms (A and B), their contributions show up in the corresponding partial DOS in the relevant energy range. Bonding and anti-bonding states between A and

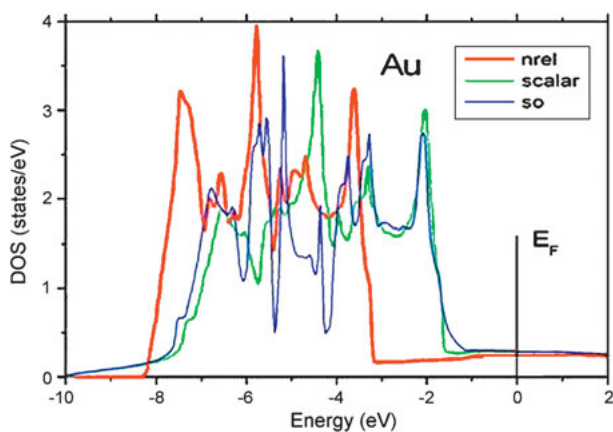


Figure 7: Density of states of gold from a nonrelativistic (nrel) treatment, scalar relativistic (scalar), and additionally including spin-orbit (so) coupling.

B can be visualized by their partial-DOS, where, for example, in the bonding state the A contribution is big, but the one from B is small, whereas the opposite weights are present in the antibonding state.

Relativistic effects influence the energy bands, especially when a solid contains heavy elements as mentioned in Section 3.1 and illustrated in Figure 5 for Os. In the $3d$, $4d$, $5d$ series Cu, Ag, and Au, the relative position of the valence d and s orbitals changes drastically (similar to the Os case of Figure 5) and thus affects the optical properties. The density of states for Au (Figure 7) shows that due to relativistic effects the main peaks, originating from the Au- $5d$ bands, are shifted up in energy (by about 1.7 eV), closer to the Fermi level. The fact that gold has a different absorption than Cu or Ag is mainly due to relativity. In addition, the energy bands also split due to spin-orbit coupling leading to a more peaked DOS.

3.3 Total energy and forces for structure optimization

It is crucial for the total energy to consider how relativity is included in a computation. We illustrate this in Figure 8 for the energy-versus-volume predictions for Os. The equilibrium volume is about 8 percent smaller using a scalar-relativistic [49] versus the nonrelativistic calculation. Including the spin-orbit coupling affects the results by less than half a percent. We performed these calculations with the same functional, namely PBEsol [12], using Wien2k [41]. The equilibrium volume also varies (by a few percent) using different functionals as has been demonstrated in many studies. One of these cases was illustrated for elemental silicon (as one example) presented in Figure 8 of [1], where LDA or GGA were used as the DFT functional to find the equilibrium

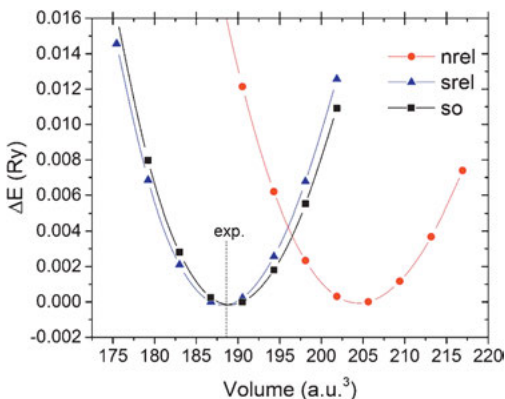


Figure 8: The total energy (with respect to the minimum energy) of hcp osmium ($Z = 76$) is shown as a function of unit cell volume (using PBEsol) for three methods of treating relativistic effects: (i) nonrelativistic (nrel), (ii) scalar relativistic (srel), and (iii) adding the spin-orbit coupling (so) to the srel case. The experimental equilibrium volume was taken from [50].

unit cell. LDA mainly overbinds leading to a volume less than experiment, whereas PBE predicts a too large equilibrium volume. Experiment is often in between. Other functionals can perform better than LDA or GGA, as was shown in [51] for many compounds.

The choice of the DFT functional affects the total energy and especially its minimum, determining the equilibrium volume. We refer the reader to a recent publication [21] critically analyzing DFT functionals in terms of accuracy. We want to mention again the reproducibility study, based on equation-of-state data, comparing 40 different DFT codes as documented in [37]. Here it is appropriate to mention that there are cases where these details matter. For example, when we are close to a phase transition under pressure, predicting a too small equilibrium volume within DFT may induce a phase transition, which does not occur at the real volume. A similar situation can happen near metal–insulator transitions or for a ferroelectric transition. A typical example is the family of perovskites like SrTiO_3 , where Ti is bound to the six neighboring oxygen atoms forming an octahedron. Such corner-shared octahedra can rotate or tilt in a more or less rigid-unit mode. By applying pressure, or changing the cation (corresponding to chemical pressure), phase transitions occur. For many solids, a small volume change does not significantly affect their properties. However, in recent years the focus is much more on such instabilities, because these are often materials of interest for applications (e.g., switching devices). In Section 3.5, we show one example, namely the perovskite BaBiO_3 , for which several aspects will be shown.

For a given atomic structure, DFT allows us to compute not only the total energy but also the forces acting on all the atoms in a unit cell. When atomic (Wyckoff) positions are fixed by symmetry, the corresponding force must be zero, but otherwise a structure relaxation is possible. By moving the atoms according to the forces acting on them we can find the nearest equilibrium geometry where the forces vanish. This structure optimization is an important step, especially in cases where the atomic structure is not well defined or determined by experiment. Structures with impurities, defects, or surfaces are typical examples, where such an optimization is important and where DFT usually yields good results. We illustrate this aspect for the oxygen-deficient double perovskite YBaFe_2O_5 , which shows a phase transition around 308 K between an orthorhombic (space group $Pmma$) and a tetragonal (space group $P4/mmm$) phase. Many references for this compound are given in [52], including DFT results. In both phases, the magnetic moments of the two types of Fe atoms are antiferromagnetically ordered. In the low-temperature phase, a charged ordered (CO) state appears in which Fe^{2+} and Fe^{3+} occupy different atomic positions (as sketched in Figure 9), whereas at high temperatures, a valence-mixed (VM) state exists, in which all Fe atoms are equivalent and have the formal oxidation state $\text{Fe}^{2.5+}$. Such a change between the CO and VM phase is called a Verwey transition. A conventional GGA calculation leads to a metallic behavior, in contrast to experiment, and finds magnetic moments that are too small. GGA+U calculations, however, predict this perovskite to be an insulator with magnetic moments in agreement with experiment. This DFT calculation can

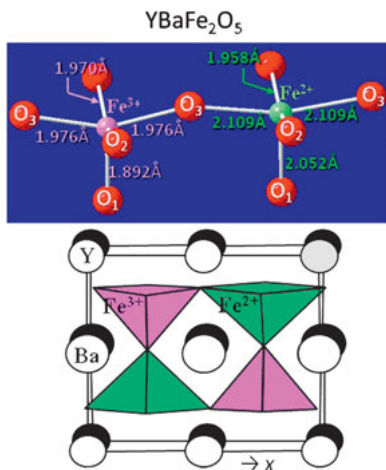


Figure 9: The experimental nearest-neighbor distances (in Å) around the Fe^{2+} and Fe^{3+} in the charged ordered (CO) phase of YBaFe_2O_5 (see Table IV in [52]).

explain all known experimental data. The nearest-neighbor distances (shown in Figure 9) agree well between DFT and experiment and are the crucial quantities between the CO and VM phase. In the CO phase the oxygen between the Fe^{2+} and Fe^{3+} along the x -axis, O_3 , differ significantly in bond length (2.109 Å and 1.976 Å, respectively). A similar effect appears for the O_1 position along the z -axis forming a short bond and a long bond, respectively. However, in the VM phase, all Fe–O distances are close to 2 Å. This structural distortion is mainly responsible for a change between the CO and VM phase and becomes apparent in the electron density (as, e.g., shown in [52] or in Section 6.3 in [1]).

In this example, the authors computed the phonons by the direct method [53]. In a suitable large supercell, a single atom is displaced in a certain direction (x , y , or z), and the forces that appear for all other atoms are computed. From a set of such atomic displacements in all directions and for all the atoms, we can derive force constants in the harmonic approximation yielding the dynamical matrix that allows us to calculate the phonon dispersions. Symmetry helps to reduce this set to independent displacements saving computer time. According to the Born–Oppenheimer approximation, in each of these many DFT calculations the nuclei are at fixed nuclear position and thus assumed to be at rest. However, knowing the forces (or the derived dynamic matrix), we can calculate the phonons. We mention one example, namely $\text{Y}_2\text{Nb}_2\text{O}_7$, which – in the proposed pyrochlore structure – would have imaginary phonon frequencies, indicating an instability (for details, see [54] or Chapter 6.4 in [1]). By following such unstable phonons the authors proposed a relaxed equilibrium structure.

3.4 Electron density, electric field gradients, and magnetism

The fundamental variable in DFT is the electron density, which we can compare with experimental data (for details, see, e.g., [55]). In DFT, it is obtained, as noted in equa-

tion (2), by summing over all occupied states in an atom or solid. We can decompose the total density into contributions from the core, semicore, and valence states. A variety of tools (like XCrystDen [56]) allow us to visualize the (three-dimensional) density. We can even compute the density corresponding to a selected energy window of electronic states to visualize their bonding character. By taking the difference between the crystalline density and a superposition of atomic densities placed at the atomic position of the crystal we obtain a difference density $\Delta\rho = \rho_{\text{cryst}} - \rho_{\text{atoms}}$, which shows chemical bonding effects much more clearly (see discussion of Figure 10 and Section 3.5). This is the real space analog to x-ray diffraction in reciprocal space using atomic structure factors. When we want to compare the computed electron densities with experimental data, we must take into account the motion of the nuclei. In most DFT calculations, the nuclei are assumed to be at rest, whereas in an experiment this motion must be considered, for example, by means of Debye–Waller factors.

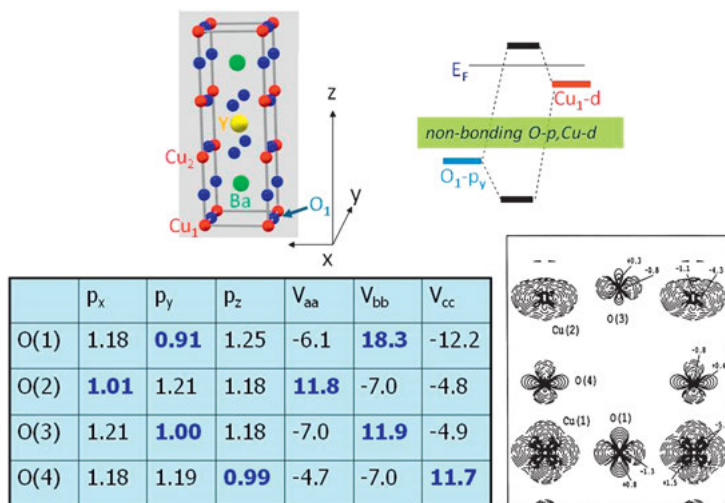


Figure 10: The electric field gradients (EFG) in the high-temperature superconductor $\text{YBa}_2\text{Cu}_3\text{O}_7$ is illustrated with the following: (i) unit cell (top left); (ii) schematic bonding between Cu_1-d and O_1-p_y (top right); (iii) the partial charges $q_{\ell\ell}$ inside the four types of oxygen spheres (decomposed according to the symmetries p_x , p_y , and p_z), and the EFG components V_{aa} , V_{bb} , and V_{cc} (labeled according to the lattice vectors a , b , c in the x , y , z directions); (iv) the difference density $\Delta\rho = \rho_{\text{cryst}} - \rho_{\text{atoms}}$ (bottom right), the crystal density minus the superposed atomic (ionic) densities, in the y – z plane. For further details, see [57].

In a magnetic system, the total density is the sum of the contributions from the spin-up and spin-down electrons, but their difference defines the magnetization density, which determines the magnetic moments. This definition is valid for the special case of collinear magnets such as ferro-, antiferro-, or ferrimagnets. However, there are also noncollinear magnets in which the magnetic moments at different atomic positions

are canted, such as in the case of UO_2 [58]. To find how the magnetic moments are oriented with respect to the crystal structure, spin-orbit interactions must be included. The orientation of the magnetic moments with respect to the crystal axes requires a relativistic treatment. This information is needed, for example, to calculate the magnetic anisotropy energy, which often is a very small quantity but important for applications. In a fully relativistic treatment, the spin is no longer a good quantum number, and thus we must express each state as a combination of two spin states. Another class of solids are the half-metallic ferromagnets, in which the energy bands have metallic character for one spin state but form a gap for the other. This is an important property for spintronic applications. For more details, see, for example, Chapter 4 in [42].

It is a strength of theory to allow various decompositions, which are often useful for interpreting properties, but these may depend on the basis set used in a calculation, for example, when deriving atomic charges. In a linear-combination-of-atomic-orbitals (LCAO) scheme, we take the weights of all atomic orbitals centered at a given atom to determine how much charge corresponds to that atom (Mulliken's population analysis). In an LAPW scheme, the charge inside the related atomic sphere gives an atomic charge, but this value clearly depends on the chosen atomic radius. An alternative, that is, basis-set independent, is the "atoms in molecules" (AIM) procedure by Bader [59], which is based on a topological analysis of the density. It uniquely defines volumes ("atomic basins") that contain exactly one nucleus by enforcing a zero-flux boundary: $\nabla\rho \cdot \mathbf{n} = 0$. Inside such an "atomic basin," this scheme uniquely defines the Bader charge for a given density independent of how this density is obtained (by theory or experiment) [57].

Nuclei with a nuclear quantum number $I \geq 1$ have an electric quadrupole moment Q . One of them is, for example, the most important Mössbauer isotope ^{57}Fe . The nuclear quadrupole interaction is a product of such a moment Q and the electric field gradient (EFG). We can measure this interaction, for example, by experiments like Mössbauer spectroscopy or nuclear magnetic resonance (NMR). The EFG is a ground-state property directly obtainable within DFT. As discussed in Section 6.4 of [43] the EFG originates mainly from the asymmetry of the electron density around the nucleus. This makes the EFG very sensitive to small structural changes, in particular, distortions around the nucleus in question.

The EFG is illustrated in Figure 10 for the high-temperature superconductor $\text{YBa}_2\text{Cu}_3\text{O}_7$, for which the main effects are shown for the oxygen atoms focusing on O_1 , the oxygen between the Cu_1 atoms (along the y direction). The structure consists of the following planes: $\text{Cu}_1\text{-O}_1$, Ba-O , the $\text{Cu}_2\text{-oxygen}$ plane (in which superconductivity occurs), and the Y plane in the center of the unit cell. The EFG is mainly proportional to the asymmetric charge distribution around the given nucleus [57]. In this unit cell, there are four types of oxygen atoms, which have different environments and thus partial charges $q_{t\ell}$ (according to equation (5)) that vary for the directions x , y , and z . Let us focus on the oxygen atom O_1 , which forms strong bonds to the neighboring atoms Cu_1 along the y direction. In a simple and schematic MO picture (Figure 10 top

right), the O_1-p_y orbital forms a strong covalent bond with the Cu_1-d orbital leading to a bonding and antibonding state, where the latter remains partly unoccupied. The other p orbitals (p_x and p_z) have no nearby neighbor and thus form more a nonbonding state, which remains fully occupied. The partial charges consequently differ for the three directions with y being the smallest (see Table in Figure 10). Equal partial charges for p_x , p_y , and p_z would lead to a spherically symmetric charge distribution around oxygen. In the present case, however, we have an asymmetry that becomes apparent in the difference density $\Delta\rho = \rho_{\text{cryst}} - \rho_{\text{atoms}}$ (shown in right bottom of Figure 10). It shows how the superposed (spherically symmetric) atomic (ionic) densities change due to chemical bonding in the SCF cycles to reach the final crystal density ρ_{cryst} . The deviation from spherical symmetry is the main origin for the EFG, a traceless tensor, whose principal component is always found in the same direction where the p -occupation number is smallest (highlighted in blue in the table shown in Figure 10). The calculated EFGs agree well with the experimental data for all oxygen atoms (for further details, see [57]).

3.5 Atomic and electronic structure illustrated for $BaBiO_3$

We illustrate by an example of the perovskite $BaBiO_3$ how various tools can help analyzing the electronic structure. This compound becomes superconducting by partially substituting Ba by K, as studied more than twenty years ago [60]. The undoped material is a semiconductor in which the perovskite structure is unstable with respect to a breathing type distortion (and a tilting of the octahedra). This means that one octahedron (around Bi-1) expands while the neighboring octahedra (around Bi-2) contract. Figure 11 shows how the energy varies (and is lowered) when the oxygen position deviates from the perovskite equilibrium position $x = 0.25$ by a displacement u according to this breathing mode.

In a very simple chemical picture, it is argued that, in this structure, Bi has an oxidation state 4+ but prefers to disproportionate according to the equation $2Bi^{4+} \leftrightarrow Bi^{3+} + Bi^{5+}$ as illustrated in Figure 12. Such a case is called a breathing mode, in which Bi^{3+} (labeled Bi-1) forms a large octahedron, whereas the neighboring Bi^{5+} (labeled Bi-2) forms a small octahedron. The total energy (for the lattice constant of 9.03 Å) is 119 787.261 Ryd. Note that the displacement changes the total energy in the tenth decimal place (a fraction of 1 mRyd), illustrating the high numerical precision necessary for such studies. The barrier height changes drastically as a function of lattice constant (volume). For the large lattice constant of 9.03 Å, the minimum is reached for displacement $u = 0.006$, leading to bond distances between oxygen and Bi-1 and Bi-2 of 2.30 Å and 2.21 Å, respectively (Figure 11). A partial substitution of Ba by K, forming $Ba_{1-x}K_xBiO_3$, shows only a single minimum [60], which is indicative of a strong electron–phonon interaction being responsible for superconductivity.

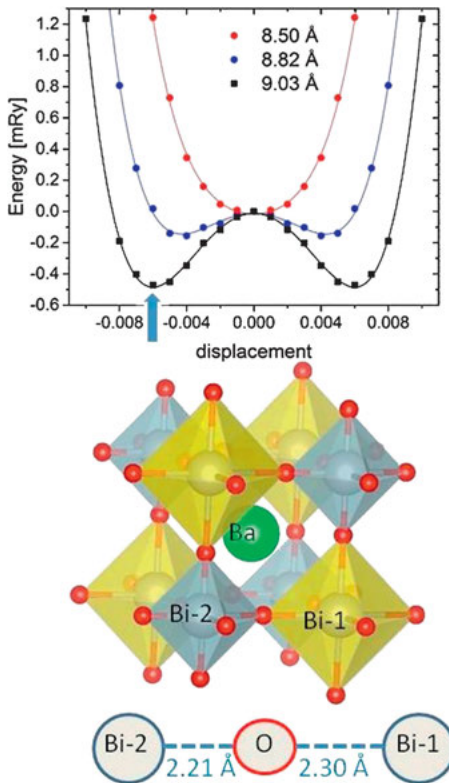


Figure 11: Breathing mode in BaBiO_3 calculated as a frozen phonon (starting from the ideal perovskite with $u = 0$) forming a small Bi-2 (Bi^{5+}) and a neighboring large Bi-1 (Bi^{3+}) octahedron by moving the oxygen atoms (from its position $x = 0.25$) by a displacement u (in fractional coordinates). The barrier for this breathing mode depends on the lattice constant of the crystal, where the blue arrow (in the top figure) indicates the equilibrium state for the large lattice constant 9.03 \AA , for which we show the atomic structure (enlarging the displacement for visibility).

Figure 12 shows the energy bands for the cubic perovskite and the distorted structure, where lower lying bands are not included. The semicore states of Ba- $5p$ form narrow bands around -12 eV below the Fermi energy E_F . The next higher bands between about -11 and -7 eV originate from the Bi- $6s$ states. From about -5 eV to E_F are the oxygen $2p$ bands, which have contributions from the orbitals of neighboring atoms. In the unoccupied bands (in the energy range around $+6 \text{ eV}$), mainly Ba- $6s$ and Bi- $6p$ states contribute. For the breathing distortion, the most important effect is the splitting of the band (between L and W) that crosses E_F . This band originates mainly from O- p_z orbitals interacting with the Bi- $6s$ orbitals. The bond length between the Bi and O atoms differ between 2.21 \AA and 2.30 \AA (Figure 11) and thus affect the bonding.

The difference in bond length becomes apparent, for example, in the difference electron density, a concept we briefly summarize here. We start a DFT calculation by

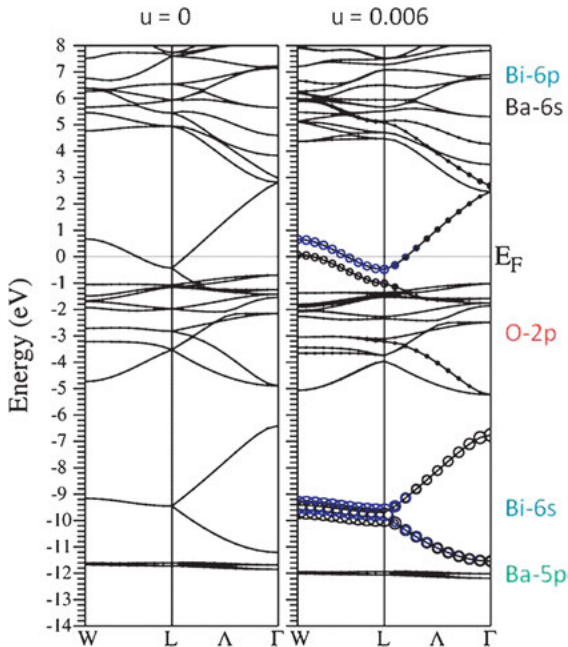


Figure 12: Band structure of BaBiO_3 in the ideal perovskite structure (left) and at the equilibrium (blue arrow in Figure 11) for the breathing mode with a displacement of $u = 0.006$ (right). The circles show the Bi- s character of the bands for Bi-1 (black) and Bi-2 (blue). The labels to the right indicate the main character of the various bands.

putting all the atomic densities at the corresponding positions in the crystal structure and obtain a superposed atomic density ρ_{atoms} , which means that we construct a density without any interaction. After the self-consistent DFT calculation is completed, we obtain the crystal density ρ_{cryst} , which contains all interactions like charge transfer, covalent or metallic bonding, polarization, etc. However, the total crystal density contains so many electrons that bonding effects are hardly visible, especially for Bi (with 83 electrons). By taking the difference $\Delta\rho = \rho_{\text{cryst}} - \rho_{\text{atoms}}$ we focus on the changes caused by chemical bonding. Back to the BaBiO_3 example, in the distorted structure (blue arrow in Figure 11) we show the difference density (Figure 13) which has an asymmetry in the density around the oxygen atoms. Let us take the oxygen on the z -axis where $\Delta\rho$ is negative toward Bi-1 or Bi-2 with a small asymmetry but positive perpendicular (the x - y plane). This deviation from spherical symmetry around the oxygen atom causes a large electric field gradient (EFG), as discussed in [60]. We discuss the chemical origin for this asymmetric charge distribution further (in connection with Figure 14 and Table 1).

Another useful tool is the decomposition of the total density of states (DOS) into partial DOS according to the partial charges defined in equation (5). As mentioned in Section 3.2, for each eigenvalue $E_n(\mathbf{k})$, the modulus of the corresponding orbital leads

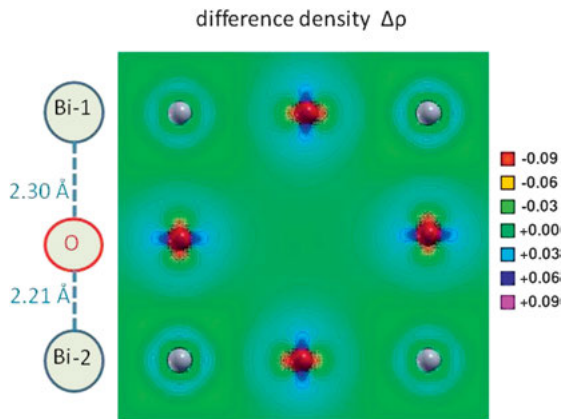


Figure 13: The difference electron density $\Delta\rho = \rho_{\text{cryst}} - \rho_{\text{atoms}}$ is shown for the breathing mode in BaBiO_3 (blue arrow in Figure 11) in the front plane of the crystal. The Bi–O bond distances show the small and large octahedra around Bi-2 and Bi-1, respectively.

to an electron density normalized in the unit cell. In the LAPW method, we can decompose this charge into contributions from all the atomic regions (called q_{ℓ}) and determine how much an angular momentum ℓ (and sometimes m) contributes to this state. Instead of counting each state with a weight of one – leading to the total DOS – we can instead weight it with a q_{ℓ} value leading to a partial DOS. We illustrate the usefulness of these partial DOS for the distorted BaBiO_3 in Figure 14, which clearly shows the main character of the bands. This information allows labeling the bands in Figure 12. Here we just select a few characterizations: the Ba- $5p$ and Bi- $6s$ bands have little contributions from other orbitals, but in the energy range between -6 and $+2$ eV the interaction between Bi and oxygen becomes apparent. The peak in the DOS around -5 eV comes mainly from an interaction between the Bi- $6p$ (Bi- $6s$) and O- p_z orbitals. The O- p_z orbitals strongly interact forming bands with a broad bandwidth (-5.2 to $+1.8$ eV). In contrast to the O- p_z , the O- $(p_x + p_y)$ orbitals interact less and thus have a smaller bandwidth (-3.5 to -0.9 eV). The split bands near E_F originate from an (anti-bonding) interaction between O- p_z orbitals (for the ligand along the z -axis) and Bi $6s$ orbitals (for Bi-1 and Bi-2), as can be seen from the peaks in the partial DOS near E_F and also from the asymmetry in the difference density $\Delta\rho$ (Figure 13).

From the simple ionic picture for Bi^{5+} and Bi^{3+} we would expect a charge density difference of 2 between the two Bi atoms, but in reality this difference is rather small – about 0.03 electrons inside the Bi-atomic spheres (with radius 1.10 \AA) – and thus much smaller than 2 (see Table 1). We want to make some additional comments and focus on the charge distribution around the two Bi atoms (Table 1). We had to choose a relatively small sphere for the Bi atoms to avoid overlapping spheres when we enforce the breathing distortion. Consequently, according to equation (5), a large fraction of the electron density resides outside a Bi sphere and is instead located in the interstitial region or in other atomic spheres (as schematically shown in Figure 3). Bi-1 is at the center of the large octahedron with a Bi-1 oxygen distance of 2.30 \AA , whereas in the small octahedron, Bi-2 has a much shorter Bi–O distance of 2.11 \AA (Figures 11

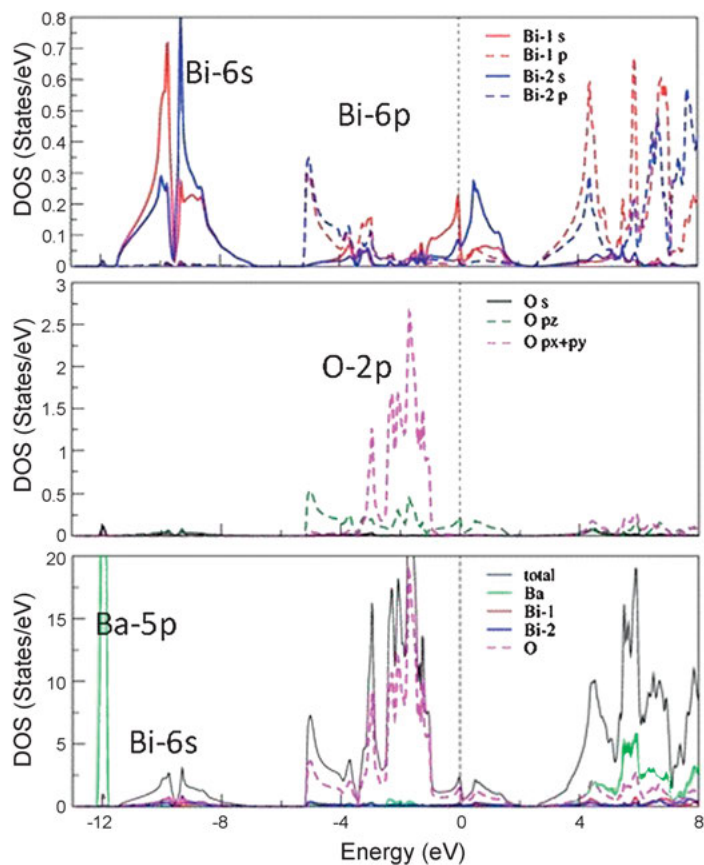


Figure 14: Partial densities of states (DOS) of BaBiO_3 in the breathing mode minimum for atomic contributions of Ba, Bi-1, Bi-2, and O. For oxygen, a further decomposition into s , p_z , and $p_x + p_y$ is given in the second panel, followed (top panel) by a similar decomposition of the DOS for Bi-1 (red) and Bi-2 (blue) into s (solid line) and p (dashed line) contributions. Note the very different scales.

$q_{\ell e}$	Bi-1 (Bi^{3+})	Bi-2 (Bi^{5+})
s	1.042	0.913
p	0.365	0.419
d	9.512	9.542
f	0.026	0.039
total	10.949	10.918

Table 1: Partial charges $q_{\ell e}$ (in electrons) of the semicore and valence electrons of BaBiO_3 for the two Bi atoms Bi-1 and Bi-2. They are computed inside the Bi sphere (with radius 2.08 Bohr $\sim 1.10 \text{ \AA}$) for the equilibrium structure (Figure 11, blue arrow) of the breathing mode $u = 0.006$.

and 13). In the large Bi-1 octahedron, we find about 0.13 e more s -like charge inside the Bi sphere as compared to the smaller Bi-2 octahedron (Table 1). However, the other partial charges – originating from p -, d -, and f -like partial waves (Figure 3) – are larger in the Bi-2 sphere. These off-site contributions originate from the tails of O- $2p$ orbitals,

which are reexpanded in the Bi sphere, and are larger when the Bi–O distance is smaller. This reduces the total charge difference between Bi-1 and Bi-2. In total, there is more density around Bi^{3+} than around Bi^{5+} , as expected, but the integrated charge inside the sphere differs only by 0.03 e, which is much less than expected from an oxidation state description.

There is another surprise that the 6s band of the less oxidized Bi-1 (Bi^{3+}) is lower in energy than that of Bi-2 (Bi^{5+}) for both peaks in the partial DOS (Figure 14) around -10 eV below or near E_F . This is also apparent from Figure 12, which shows the atomic character of these split bands in the same energy regions. In a simple picture, we would argue that the more positively charged states should be lower in energy. The reverse order of the energy positions for the Bi-1 and Bi-2 6s bands must come from electrostatics. The partially negatively charged oxygen ions surround both of these atoms and cause a destabilizing potential, which gets stronger the closer the ions are and thus affects Bi-2 more than Bi-1.

This is just one example illustrating how to get insight into the electronic structure of a solid by analyzing various results: the total energy, the energy bands, and their characters derived from the partial density of states (DOS) or electron densities. Many researchers have used these tools in their DFT calculations for a large variety of studies on solids (from superconductors to heterogeneous catalysts). A small representative list of corresponding references is contained in [1].

3.6 Excitation spectra and optics in the single-electron picture

We mentioned in Sections 3.2 and 3.3 that, formally speaking, we should not interpret the KS energies (in the band structure form) as excitation energies. However, this is often done and works quite well in practice. In optical spectroscopy, direct transitions (conserving \mathbf{k}) are computed from occupied to unoccupied states, where for both states, KS eigenvalues are used [61]. Transition probabilities between these states can be computed and determine the intensity of optical spectra using dipole selection rules, which clearly distinguish between allowed and forbidden transitions. In a metallic solid, an additional Drude term accounts for the free electron contribution. In insulators, for which the DFT gap is often too small when compared to an experimental gap, we can use a “scissor operator.” This sounds complicated, but we can simply rigidly shift the unoccupied DFT bands to adjust the (too small) DFT band gap to the experiment value. However, even after this correction, the theoretical absorption spectrum may differ from experiment, since excitonic features are completely missing in the single-particle picture. These excitonic effects can be small (semiconductors) or very large (insulators), and we need a proper description of the electron–hole interaction, for instance by solving the Bethe–Salpeter equation (BSE) [62]. Nevertheless, angle-resolved photoemission spectra (ARPES), as discussed in connection with Figure 6, illustrate a good agreement with experiment [47]. The electron energy loss spectrum (EELS) can often also be successfully interpreted in a single-electron picture [63].

Another important field is the core-level spectroscopy, which provides atom-specific information, since the involved core states reside near the corresponding nucleus. From a theoretical point of view, this means that the transition probabilities outside the atomic sphere vanish and thus these spectra become atom specific. A good example of this is x-ray emission spectroscopy (XES). Let us take the transition metal carbide or nitride, ZrC or ZrN, which crystallize in the sodium chloride structure. When a core electron is removed, for example, from the 1s state in one carbon (nitrogen) atom, valence electrons can fill this hole emitting an x-ray and yielding the XES. According to the dipole selection rule $\Delta\ell = \pm 1$, we have allowed transitions that are from *p*-like valence states to the 1s-core state. Consequently, the C-1s XES shows the C-*p* partial DOS weighted by the transition probability. Already in 1982, such calculations showed a good agreement with experiment [64] and explained the difference seen between the carbide and nitride. In 1979, von Barth and Grossmann [65] showed that the experimental XES can be well reproduced within a ground-state calculation, rather than with a model including valence band distortions caused by a core hole, a concept later called the “final state rule.”

A similar process occurs in x-ray absorption spectroscopy (XAS) [66], where a core electron is excited to an unoccupied state. In this case, the final state is with a core hole. According to the final state rule mentioned before [65], we should actually represent a situation where the core electron is excited into the conduction band. A simulation of this situation in a solid usually requires creating a supercell with a size of about 32–128 atoms, where a core-hole on only one atom is created. The excited electron can be added to the valence electrons (in cases where the first unoccupied states have predominantly $\ell + 1$ character from the specific atom), or we neutralize the cell by a constant background charge. The electronic structure of the atom with the core hole changes within the self-consistency cycles. The corresponding conduction band states are attracted more strongly due to the less screened nuclear charge and shift down in energy, simulating the effects of an exciton. Partial screening of the core hole can occur by charge transfer from the neighboring atoms. Since we cannot force localization of the excited electron into an orbital of the proper atom, this screening will be incomplete. Therefore, sometimes a simulation with a smaller core hole (“half core hole”) yields a better agreement with experiment [67, 68]. In such a simulation, we calculate the XANES spectrum from the corresponding partial DOS and the radial momentum matrix elements between the core and valence states. In general, a rather good agreement can be obtained for K-edges of light elements (C, N, O) [68], but even L and M edges of heavier elements can be well simulated [69]. Let us mention one exception, namely the $L_{2,3}$ edges of light transition metal compounds, where the simple single-particle approximation breaks down due to the $2p_{1/2}$ and $2p_{3/2}$ states being too close together in energy [66]. The intensity ratio of the L_2 and L_3 peaks strongly deviates from the expected 1:2 ratio. This occurs due to interference effects that change the branching ratio and also to crystal field splitting and even spin-orbit splitting that are not in agreement with experiment.

To properly account for these effects, we have to go a step further and solve the Bethe–Salpeter equations (BSE) [66], with which excitonic effects can be approximated using an effective two-particle (hole and electron) Schrödinger-like equation. The corresponding Hamiltonian contains the energy-difference between the core and conduction band single-electron states and in addition takes into account an attractive screened Coulomb interaction and a repulsive unscreened exchange interaction between the hole and electron. The screening of the Coulomb interaction is considered to be nonlocal (q -dependent) but static ($\omega = 0$). Using such an approach, a very good agreement for the $L_{2,3}$ spectra of compounds such as CaF_2 , TiO_2 , or SrTiO_3 was obtained [66].

4 Going beyond the ground state

Let us summarize the main approximation and assumptions made in running DFT calculations, the Born–Oppenheimer approximation, in which we treat the nuclei as classical particles at fixed atomic positions. We can obtain the Born–Oppenheimer surface from a series of static calculations and compute phonons. For a snapshot in lattice vibrations, the nuclei are not in their equilibrium geometry, but we can study such an atomic arrangement (at a fixed time), which is called frozen phonons. This allows us to find the equilibrium structure of a given system or study its structural phase transitions. The inclusion of pressure is easy for such DFT calculations. Temperature dependence is not included directly but can be included via molecular dynamics simulations or using the free energy obtained from frozen phonon calculations.

Time-independent DFT focuses on ground-state properties, but for excited states, time-dependent DFT (TDDFT) [70, 71] is the formally correct theory. Also in TDDFT, we must make severe approximations by the choice of an approximate XC-kernel, limiting the accuracy of this scheme. In any case, quite often the standard DFT single-particle model describes excitations rather well. A properly chosen scheme (such as a core-hole calculation) allows studying core-excitation spectra. The band gap, an important quantity for semiconductors or insulators, can be calculated using an adjusted DFT functional (such as TB-mBJ [23]). If DFT single-particle theory is not sufficient, then we can use the DFT orbitals as input for many-body perturbation theories, such as the GW approach [34], for better quasiparticle energies or the BSE approach [62, 66] to account for excitonic effects. For highly correlated systems, which need a good description of the localized $3d$ or $4f$ states, inclusion of a Hubbard U may be sufficient (GGA+ U) for a proper description of the electronic structure. However, sometimes we need to go beyond this and use schemes like the dynamical mean field theory (DMFT) [35] to improve the agreement with experiments. Last but not least, the weak but sometimes important van der Waals interactions are usually not well described by standard DFT, requiring more sophisticated schemes to be used [33].

In conclusion, it is appropriate at the end of this chapter to mention that any theoretical approach makes assumptions and must make certain approximations. Let us summarize some already discussed aspects:

- The *atomic structure model*: unit cell, supercell, surface, periodic boundary condition.
- *Quantum mechanics*: time-independent DFT, mean field, many-body theory, DFT functionals, exchange, correlation, Born–Oppenheimer approximation.
- *Accuracy*: basis sets, all-electron treatment, full-potential, convergence (**k**-points), relativistic effects.
- *Ground state vs. excited states*: single-electron picture, excitons, phonons, electron–phonon interaction, $T = 0$ or finite temperature, collective excitations.
- *Time dependence*: time averaging, static, frozen phonons, sudden approximation, fluctuations.

In any theoretical treatment, we must find a good balance between an accurate quantum mechanical treatment and a sufficiently detailed atomic structure. Approximations make simulations feasible and thus are very useful but may neglect aspects that can be essential for certain properties. Time-independent DFT plays an important role in theoretical descriptions, but now the explicit inclusion of time is a new challenge and the topic of this book (for theory, see the next chapter [71]).

Bibliography

- [1] K. Schwarz and P. Blaha. DFT calculations for real solids. In R. Dronskowski, S. Kikkawa, and A. Stein (Eds.), *Handbook of Solid State Chemistry, volume 5*. pages 227–259. Wiley, Weinheim, New York, 2017.
- [2] K. Schwarz. Electrons. In A. Authier (Ed.), *International Tables for Crystallography, Volume D, Physical Properties of Crystals*, pages 294–313. Kluwer Academic Publ., Dordrecht, 2003.
- [3] R. Dronskowski. *Computational Chemistry of Solid State Materials: A Guide for Material Scientists, Chemists, Physicists and Others*. Wiley VCH, New York, 2005.
- [4] R. M. Martin. *Electronic Structure: Basic Theory and Practical Method*. Cambridge University Press, Cambridge, 2008.
- [5] P. Hohenberg and W. Kohn. Inhomogeneous electron gas. *Phys. Rev.*, 136:B864–B871, 1964.
- [6] W. Kohn and L. S. Sham. Self-consistent equations including exchange and correlation effects. *Phys. Rev.*, 140:A1133–A1138, 1965.
- [7] M. Levy. Electron densities in search of Hamiltonians. *Phys. Rev. A*, 26:1200–1208, 1982.
- [8] E. H. Lieb. Density functionals for Coulomb systems. *Int. J. Quant. Chem.*, 24:243–277, 1983.
- [9] A. D. Becke. Perspective: fifty years of density-functional theory in chemical physics. *J. Chem. Phys.*, 140:18A301, 2014.
- [10] D. M. Ceperley and B. J. Alder. Ground state of the electron gas by a stochastic method. *Phys. Rev. Lett.*, 45:566–569, 1980.
- [11] J. P. Perdew, K. Burke, and M. Ernzerhof. Generalized gradient approximation made simple. *Phys. Rev. Lett.*, 77:3865–3868, 1996.

- [12] J. P. Perdew, A. Ruzsinszky, G. I. Csonka, O. A. Vydrov, G. E. Scuseria, L. A. Constantin, X. Zhou, and K. Burke. Restoring the density-gradient expansion for exchange in solids and surfaces. *Phys. Rev. Lett.*, 100:136406, 2008.
- [13] J. P. Perdew, S. Kurth, A. Zupan, and P. Blaha. Accurate density functional with correct formal properties: a step beyond the generalized gradient approximation. *Phys. Rev. Lett.*, 82:2544–2547, 1999.
- [14] F. Tran, J. Stelzl, and P. Blaha. Rungs 1 to 4 of DFT Jacob’s ladder: extensive test on the lattice constant, bulk modulus, and cohesive energy of solids. *J. Chem. Phys.*, 144:204120, 2016.
- [15] J. Sun, A. Ruzsinszky, and J. P. Perdew. Strongly constrained and appropriately normed semilocal density functional. *Phys. Rev. Lett.*, 115:036402, 2015.
- [16] J. Tao and Y. Mo. Accurate semilocal density functional for condensed-matter physics and quantum chemistry. *Phys. Rev. Lett.*, 117:073001, 2016.
- [17] J. P. Perdew, M. Ernzerhof, and K. Burke. Rationale for mixing exact exchange with density functional approximations. *J. Chem. Phys.*, 105:9982, 1996.
- [18] V. I. Anisimov, I. V. Solovyev, M. T. Czyżyk M. A. Korotin, and G. A. Sawatzky. Density-functional theory and NiO photoemission spectra. *Phys. Rev. B*, 48:16929–16934, 1993.
- [19] S. Grimme, A. Hansen, J. G. Brandenburg, and C. Bannwarth. Dispersion-corrected mean-field electronic structure methods. *Chem. Rev.*, 116:5105–5154, 2016.
- [20] F. Mittendorfer, A. Garhofer, J. Redinger, J. Klimes, J. Harl, and G. Kresse. Graphene on Ni(111): strong interaction and weak adsorption. *Phys. Rev. B*, 84:201401, 2011.
- [21] F. Tran, P. Blaha, and K. Schwarz. How close are the Slater and Becke–Roussel potentials in solids? *J. Chem. Theory Comput.*, 11:4717–4726, 2015.
- [22] M. Hybertsen and S. Louie. Self-energy approach to quasiparticle energies using a density functional treatment of dielectric screening. *Adv. Quantum Chem.*, 21:155–174, 1990.
- [23] F. Tran and P. Blaha. Accurate band gaps of semiconductors and insulators with a semilocal exchange-correlation potential. *Phys. Rev. Lett.*, 102:226401, 2009.
- [24] D. Koller, F. Tran, and P. Blaha. Merits and limits of the modified Becke–Johnson exchange potential. *Phys. Rev. B*, 83:195134, 2011.
- [25] T. Koopmans. Über die Zuordnung von Wellenfunktionen und Eigenwerten zu den einzelnen Elektronen eines Atoms. *Physics*, 1:104–113, 1934.
- [26] J. F. Janak. Proof that $\partial E/\partial n_i = \epsilon$ in density-functional theory. *Phys. Rev. B*, 18:7165–7168, 1978.
- [27] J. C. Slater. The self-consistent field for crystals. *Int. J. Quant. Chem.*, 3:727, 1970.
- [28] K. Schwarz. On Slater’s transition state concept for ionization energies. *Chem. Phys.*, 7:100–107, 1975.
- [29] J. P. Perdew, R. G. Parr, M. Levy, and J. L. Balduz. Density-functional theory for fractional particle number: derivative discontinuities of the energy. *Phys. Rev. Lett.*, 49:1691–1695, 1982.
- [30] N. Hadjisavvas and A. Theophilou. Rigorous formulation of Slater’s transition-state theory for excited states. *Phys. Rev. A*, 32:720–724, 1985.
- [31] J. C. Slater, J. B. Mann, T. M. Wilson, and J. H. Wood. Nonintegral occupation numbers in transition atoms in crystals. *Phys. Rev.*, 184:672–694, 1969.
- [32] E. Kablman, P. Blaha, and K. Schwarz. Ab initio study of stabilization of the misfit layer compound $(\text{PbS})_{1,14}\text{TaS}_2$. *Phys. Rev. B*, 82:125308, 2010.
- [33] P. Mori-Sánchez, A. J. Cohen, and W. Yang. Many-electron self-interaction error in approximate density functionals. *J. Chem. Phys.*, 125:201102, 2006.
- [34] H. Jiang and P. Blaha. GW with linearized augmented plane waves extended by high-energy local orbitals. *Phys. Rev. B*, 93:115203, 2016.
- [35] K. Held. Electronic structure calculations using dynamical mean field theory. *Adv. Phys.*, 65:829–926, 2007.

- [36] J. Kunes, R. Arita, P. Wissgott, A. Toschi, H. Ikeda, and K. Held. Wien2wannier: from linearized augmented plane waves to maximally localized Wannier functions. *Comput. Phys. Commun.*, 181:1888–1896, 2010.
- [37] K. Lejaeghere, G. Bihlmayer, T. Björkman, P. Blaha, S. Blügel, V. Blum, D. Caliste, I. E. Castelli, S. J. Clark, A. Dal Corso, S. de Gironcoli, T. Deutsch, J. K. Dewhurst, I. Di Marco, C. Draxl, M. Dułak, O. Eriksson, J. A. Flores-Livas, K. F. Garrity, L. Genovese, P. Giannozzi, M. Giantomassi, S. Goedecker, X. Gonze, O. Grånäs, E. K. U. Gross, A. Gulans, F. Gygi, D. R. Hamann, P. J. Hasnip, N. A. W. Holzwarth, D. Iușan, D. B. Jochym, F. Jollet, D. Jones, G. Kresse, K. Koepnik, E. Küçükbenli, Y. O. Kvashnin, I. L. M. Locht, S. Lubeck, M. Marsman, N. Marzari, U. Nitzsche, L. Nordström, T. Ozaki, L. Paulatto, C. J. Pickard, W. Poelmans, M. I. J. Probert, K. Refson, M. Richter, G.-M. Rignanese, S. Saha, M. Scheffler, M. Schlipf, K. Schwarz, S. Sharma, F. Tavazza, P. Thunström, A. Tkatchenko, M. Torrent, D. Vanderbilt, M. van Setten, V. Van Speybroeck, J.M. Wills, J. R. Yates, G.-X. Zhang, and S. Cottenier. Reproducibility in density-functional theory calculations of solids. *Science*, 351:aad3000, 2016.
- [38] S. Cottenier. *Density Functional Theory and the family of (L)APW-Methods: A Step-by-Step Introduction*. Wiley VCH, New York, 2002–2013. Freely available at <http://www.wien2k.at/reguser/textbooks>.
- [39] G. H. K. Madsen, P. Blaha, K. Schwarz, L. Nordström, and E. Sjöstedt. Efficient linearization of the augmented plane-wave method. *Phys. Rev. B*, 64:195134, 2001.
- [40] D. Singh and L. Nordström. *Plane Waves, Pseudopotentials and the LAPW Method*. Springer, New York, 2006.
- [41] P. Blaha, K. Schwarz, G. K. H. Madsen, D. Kvasnicka, and J. Luitz. *An Augmented Plane Wave Plus Local Orbitals Program for Calculating Crystal Properties*. Vienna University of Technology, Vienna, 2001.
- [42] K. Schwarz and P. Blaha. Solid state calculations using WIEN2k. *Comput. Mater. Sci.*, 28:259, 2003.
- [43] K. Schwarz, P. Blaha, and S. B. Trickey. Efficient linearization of the augmented plane-wave method. *Mol. Phys.*, 108:3147–3166, 2010.
- [44] K. Schwarz. Computation of materials properties at the atomic scale, Chapter 10. In M. R. Pahlavani (Ed.), *Selected Topics in Applications of Quantum Mechanics*, pages 275–310. InTech, Rijeka, 2015, ISBN 978-953-551-2126-8.
- [45] J. C. Slater. Wave functions in a periodic potential. *Phys. Rev.*, 51:846–851, 1937.
- [46] K. Schwarz. Band structure and chemical bonding in transition metal carbides and nitrides. *Crit. Rev. Solid State Mater. Sci.*, 13:211–257, 1987.
- [47] V. N. Strocov, M. Shi, M. Kobayashi, C. Monney, X. Wang, J. Krempasky, T. Schmitt, L. Patthey, H. Berger, and P. Blaha. Three-dimensional electron realm in VSe₂ by soft-x-ray photoelectron spectroscopy: origin of charge-density waves. *Phys. Rev. Lett.*, 109:086401, 2012.
- [48] Y. Kim, M. Marsman, G. Kresse, F. Tran, and P. Blaha. Towards efficient band structure and effective mass calculations for III–V direct band-gap semiconductors. *Phys. Rev. B*, 82:205212, 2010.
- [49] D. D. Koelling and B. N. Harmon. A technique for relativistic spin-polarised calculations. *J. Phys. C, Solid State Phys.*, 10:3107–3114, 1977.
- [50] B. K. Godwal, J. Yan, S. M. Clark, and R. Jeanloz. High-pressure behavior of osmium: an analog for iron in Earth’s core. *J. Appl. Phys.*, 111:112608, 2012.
- [51] P. Haas, F. Tran, and P. Blaha. Calculation of the lattice constant of solids with semilocal functionals. *Phys. Rev. B*, 79:085104, 2009.
- [52] C. Spiel, P. Blaha, and K. Schwarz. Density functional calculations on the charge-ordered and valence-mixed modification of YBaFe₂O₅. *Phys. Rev. B*, 79:115123, 2009.

- [53] K. Parlinski, Z. Q. Li, and Y. Kawazoe. First-principles determination of the soft mode in cubic ZrO_2 . *Phys. Rev. Lett.*, 78:4063–4066, 1997.
- [54] P. Blaha, D. J. Singh, and K. Schwarz. Geometric frustration, electronic instabilities, and charge singlets in $\text{Y}_2\text{Nb}_2\text{O}_7$. *Phys. Rev. Lett.*, 93:216403, 2004.
- [55] P. Coppens. *X-Ray Charge Densities and Chemical Bonding*. Oxford Science Publications, London, 1997.
- [56] A. Kokalj. Xcrysden – a new program for displaying crystalline structures and electron densities. *J. Mol. Graph. Model.*, 17:175, 1999.
- [57] K. Schwarz, C. Ambrosch-Draxl, and P. Blaha. Charge distribution and electric-field gradients in $\text{YBa}_2\text{Cu}_3\text{O}_{7-x}$. *Phys. Rev. B*, 42:2051–2061, 1990.
- [58] R. Laskowski, G. K. H. Madsen, P. Blaha, and K. Schwarz. Magnetic structure and electric-field gradients of uranium dioxide: An ab initio study. *Phys. Rev. B*, 69:140408, 2004.
- [59] R. F. W. Bader. *Atoms In Molecules. A Quantum Theory*. Clarendon Press, Oxford, 1994.
- [60] P. Blaha, K. Schwarz, P. Dufek, G. Vielsack, and W. Weber. The breathing mode of BaBiO_3 : Electric field gradient and total energy calculations. *Z. Naturforsch. A*, 49:129–132, 1994.
- [61] C. Ambrosch-Draxl and J. Sofo. Linear optical properties of solids within the full-potential linearized augmented plane-wave method. *Comput. Phys. Commun.*, 175:1–14, 2006.
- [62] W. Hetaba, P. Blaha, F. Tran, and P. Schattschneider. Calculating energy loss spectra of NiO: advantages of the modified Becke–Johnson potential. *Phys. Rev. B*, 85:205108, 2012.
- [63] F. Karsai, F. P. Tiwald, R. Laskowski, F. Tran, D. Koller, S. Gräfe, J. Burgdörfer, L. Wirtz, and P. Blaha. F center in lithium fluoride revisited: comparison of solid-state physics and quantum-chemistry approaches. *Phys. Rev. B*, 89:12542, 2014.
- [64] K. Schwarz, H. Ripplinger, and A. Neckel. Energy band structure and x-ray emission spectra of ZrC and ZrN. *Z. Phys. B*, 48:79–87, 1982.
- [65] U. von Barth and G. Grossmann. Effect of the core hole on x-ray-emission spectra in simple metals. *Solid State Commun.*, 32:645–649, 1979.
- [66] R. Laskowski and P. Blaha. Understanding the $L_{2,3}$ x-ray absorption spectra of early 3d transition elements. *Phys. Rev. B*, 82:205104, 2010.
- [67] J. Luitz, M. Maier, C. Hebert, P. Schattschneider, P. Blaha, K. Schwarz, and B. Jouffrey. Partial core hole screening in the Cu L_3 edge. *Eur. Phys. J. B*, 21:363, 2001.
- [68] T. Mizoguchi, I. Tanaka, S. Yoshioka, M. Kunisu, T. Yamamoto, and W. Y. Ching. First-principles calculations of ELNES and XANES of selected wide-gap materials: dependence on crystal structure and orientation. *Phys. Rev. B*, 70:045103, 2004.
- [69] M. W. Murphy, Y. M. Yiu, M. J. Ward, L. Liu, Y. Hu, J. A. Zapien, Y. Liu, and T. K. Sham. Electronic structure and optical properties of $\text{Cd}_x\text{Se}_{1-x}$ solid solution nanostructures from x-ray absorption near edge structure, x-ray excited optical luminescence, and density functional theory investigations. *J. Appl. Phys.*, 116:193709, 2014.
- [70] E. Runge and E. K. U. Gross. Density-functional theory for time-dependent systems. *Phys. Rev. Lett.*, 52:997–1000, 1984.
- [71] V. Olevano. TDDFT, excitations and spectroscopy. In T. Woike and D. Schaniel (Eds.), *Structure Analysis on Different Time Scales*. DeGruyter, Berlin, 2017.

Valerio Olevano

TDDFT, excitations, and spectroscopy

Applications to optical, electron and X-ray spectroscopy

Keywords: TDDFT, time-dependent, TDLDA, electronic excitations, spectroscopy, EELS, IXSS, optical absorption

Introduction

Density-functional theory (DFT) is the today condensed matter reference to calculate from first principles ground-state properties, in particular the static atomic structure. Time-dependent density-functional theory (TDDFT) is an extension of DFT to address excited-state properties, dynamics, and spectroscopy. TDDFT is in principle exact theory to calculate ab initio electronic neutral excitations, as sampled in optical or energy-loss spectra. However, like in DFT, the exchange-correlation functional, a fundamental ingredient of the theory, is unknown. We must resort to approximations, and the local-density approximation (LDA) has less validity than in DFT, in particular on optical spectra in insulators. We here provide a simplified review of the fundamental aspects of the theory, theorems, frameworks, basic equations, and standard approximations, referring to the literature for more in-depth analysis. The main focus is rather on the applications where TDDFT revealed more successful: excitations and time-dependent electronic and ionic dynamics in atoms and molecules, optical absorption, electron energy-loss spectroscopy (EELS), and inelastic X-ray scattering (IXSS) in solids and nanosystems. Thanks to a continuous comparison with the experiment, the review critically assesses TDDFT standard approximations, advantages, and drawbacks, reporting on some recent progresses and current challenges. TDDFT has achieved an overall good agreement with the experiment, allowing, on one hand, the interpretation of experimental spectra in terms of elementary excitations and the comprehension of the mechanisms driving physical, chemical, and even biological processes; on the other hand, ab initio TDDFT can today predict spectroscopic and dielectric properties with interesting returns in materials science.

1 From DFT to TDDFT: electronic excitations

In the previous chapter, we have seen how the formidable many-body problem in condensed matter, can be very efficiently tackled by density-functional theory (DFT) [1, 2]. The electronic density $\rho(\mathbf{r})$ is the minimal degree of freedom needed to fully deter-

<https://doi.org/10.1515/9783110433920-004>

mine any static property of a condensed matter system. DFT is in principle exact theory to calculate all ground-state properties, e.g., the atomic structure, the total energy, etc., with an accuracy that depends on the approximation done on the exchange-correlation functional.

Although a very successful theory, DFT has its limits. Static DFT and the static ground-state density $\rho(\mathbf{r})$ is not sufficient to describe the dynamics and the excitation of a system in response to an applied external time-dependent perturbation $\delta v(\mathbf{r}, t)$. For example, in an energy-loss experiment, where electrons of charge $q = -e$ are shot at velocity \mathbf{v} to a condensed matter system, the perturbation is the time-dependent external Coulomb potential

$$\delta v(\mathbf{r}, t) = \frac{q}{|\mathbf{r} - \mathbf{v}t|}.$$

In an optical experiment, the time-dependent external perturbation can be a laser pulse or any generic transverse electromagnetic wave in the optical limit,

$$\delta v(\mathbf{r}, t) = (\mathbf{e} \cdot \mathbf{r}) D_0 f(t) \sin(\omega t),$$

where ω is the light frequency, \mathbf{e} is its polarization, D_0 is the amplitude, and $f(t)$ is the laser pulse envelope. (Unless not evident from the context, we will omit in what follows vectorial bold notation like, e.g., in \mathbf{r} .) These and other possible time-dependent perturbations cannot be accounted by DFT.

Time-dependent density-functional theory (TDDFT) is an extension of DFT that allows us to describe excited state properties, excitations, and spectroscopy. The exceedingly difficult task of calculating the wavefunction $\Psi(r_1, \dots, r_N, t)$ of many interacting particles by direct solution of the many-body time-dependent Schrödinger equation

$$i\partial_t \Psi(r_1, \dots, r_N, t) = H(r_1, \dots, r_N, t) \Psi(r_1, \dots, r_N, t) \quad (1)$$

is replaced by the simpler problem of calculating the time-dependent electronic density $\rho(r, t)$, a function of only one space variable r , with evident reduction of the degrees of freedom. The time-dependent density alone,

$$\rho(r, t) = \int dr_2 \dots dr_N |\Psi(r, r_2, \dots, r_N, t)|^2, \quad (2)$$

is a sufficient degree of freedom to fully describe the response of a system to the time-dependent perturbation. This is the thesis of the Runge–Gross theorem [3] (Section 2), an extension of the DFT Hohenberg–Kohn theorem to the time-dependent case.

In parallel to DFT, it is also possible to solve TDDFT by introduction of a fictitious auxiliary noninteracting Kohn–Sham system, constructed to provide the exact density of the real system. The density and all other observables can be calculated by solving the time-dependent independent-particle Kohn–Sham equations [4] (Section 3). The

original system-size exponential scaling of the full many-body Schrödinger equation is replaced in TDDFT by a much more favorable scaling. TDDFT can in principle access the same system sizes as DFT, solids, molecules, up to nano- and biological systems, complementing ground-state with excited-state studies.

Whenever the applied time-dependent external perturbation is small with respect to the external static potential, e.g., due to the nuclei, perturbation theory can be applied on top of DFT. The system undergoes a little depart from ground state and equilibrium, and TDDFT can be formulated in linear response from static DFT (Section 4). This is the situation occurring in the most spread experimental techniques, probing the response of a system to a perturbation like electron beams (electron energy-loss spectroscopy or EELS), light or weak lasers (optical absorption spectroscopy, ellipsometry, etc.), or X-rays (X-ray absorption, inelastic X-ray scattering spectroscopy, or IXSS). This is also the situation addressed by the vast majority of TDDFT applications, aiming at the calculation of excitation energies and spectra. Here TDDFT has provided the most impressive successes, achieving almost quantitative accuracies on, for example, EELS and IXSS spectroscopies already at the lowest levels of approximation.

The development of more intense laser sources, together with the possibility to study the evolution of a system out of equilibrium in pump-and-probe geometries, has opened promising applications of TDDFT beyond the linear response regime. Here, in parallel to experimental challenges, theory has in front the challenge of developing approximations more suitable to the nonperturbative regime; the challenge of developing more complete formalisms, for example, allowing the access to coupled electron–ion dynamics for applications to photo-explosion or photo-chemistry, as those illustrated in the next chapter on time-resolved X-ray diffraction (TRXRD); or a TDDFT formalism to address electronic quantum transport in nano- and molecular electronics devices [5].

2 The Runge–Gross theorem

The DFT Hohenberg–Kohn theorem proves a one-to-one correspondence between a static external potential $v(r)$, for instance, the Coulomb potential of nuclei, and the static ground-state density $\rho(r)$,

$$v(r) \Leftrightarrow \rho(r). \quad (3)$$

This is sufficient if we are only interested in the ground state, but not sufficient if we want to study the excitation, the response of the system to an external perturbation, such as an incident electromagnetic wave switched on at an initial time t_0 . The extra complication is that the external perturbation is in general represented by a time-dependent external potential $\delta v(r, t)$. The total external potential acting on the system,

which is the sum of the static external potential due to the nuclei and the external perturbation,

$$v(r, t) = v(r) + \delta v(r, t), \quad (4)$$

depends on time. Since the Hohenberg–Kohn theorem, equation (3), only holds between static potentials and densities, DFT does not apply. To describe the system excitation, we should go beyond DFT, toward the formulation of a time-dependent theory.

The rigorous foundation of time-dependent density-functional theory is the Runge–Gross theorem [3], an extension of the Hohenberg–Kohn theorem to the time-dependent case. The Runge–Gross theorem states a one-to-one correspondence between the external time-dependent potential $v(r, t)$ and the *time-dependent* density $\rho(r, t)$. However, the formulation of the theorem is not as straightforward as the Hohenberg–Kohn theorem, equation (3). First, the density is in a one-to-one correspondence with the class of external potentials given by $v(r, t) + \alpha(t)$ with an arbitrary merely time-dependent function $\alpha(t)$. This issue is not peculiar to TDDFT. The addition of a pure time-dependent function $\alpha(t)$ to the external potential and to the total Hamiltonian in the full time-dependent Schrödinger equation (1) reflects in an uninfluential merely time-dependent phase factor on the full wavefunction, $\Psi(t) \rightarrow \Psi'(t) = e^{-i\alpha(t)}\Psi(t)$. Observables do not depend on the wavefunction time-dependent phase factor $e^{-i\alpha(t)}$. Second, the time-dependent external potential is in one-to-one correspondence with the time-dependent density *and* a fixed initial state $\Psi_0 = \Psi(t_0)$. The initial state is a boundary condition necessary also to fix the solution to the original first-degree differential Schrödinger equation (1). The Runge–Gross theorem can be finally mathematically formulated as

$$v(r, t) + \alpha(t) \xleftrightarrow{\Psi_0} \rho(r, t). \quad (5)$$

For a given system, say of N electrons with their fixed form of kinetic and many-body interaction Hamiltonians, the external potential is the only remaining degree of freedom. Once fixed the external potential and the initial state, every observable O is determined. Thanks to the stated one-to-one correspondence, the Runge–Gross theorem has the important corollary that every observable is a *unique functional* of the time-dependent density (and of the initial state):

$$O(t) = O[\rho, \Psi_0](t). \quad (6)$$

So, knowledge of the time-evolution of the density $\rho(r, t)$ can give access to the value of an observable, provided that its functional form is known, without passing by the complex many-body wavefunction and the solution of the full time-dependent Schrödinger equation (1).

Relying on the Runge–Gross theorem, it becomes possible to build a time-dependent density-functional theory in analogy to static DFT based on the Hohenberg–Kohn

theorem. The variational principle, which holds in DFT for the energy functional $E[\rho] = \langle \Psi | H | \Psi \rangle$ whose minimum, $\delta E[\rho] / \delta \rho(r, t) = 0$, occurs at the ground-state density, can be extended also to TDDFT. Since TDDFT is a time-dependent theory, instead of focussing on the energy, we need to introduce the action

$$A[\rho] = \int_{t_0}^{t_1} dt \langle \Psi(t) | i\partial_t - H(t) | \Psi(t) \rangle.$$

The stationary points of the action, $\delta A[\rho] / \delta \rho(r, t) = 0$, provide the exact time-dependent density $\rho(r, t)$. A possible resolution scheme for TDDFT can rely on the variational principle: by varying the action and searching for the stationary points we can get the exact time-dependent density of the system.

At this point, we should mention some difficulties with the Runge–Gross theorem.

Dependence on the initial state: the dependence on the initial state Ψ_0 is a remarkable complication with respect to static DFT, where observables are functionals of the density alone. This dependence implies that we still have to deal with many-body wavefunctions $\Psi_0(r_1, \dots, r_N)$ and at least with the solution of the time-independent Schrödinger equation at the initial time, although just only to fix a boundary condition. However, supposing to start from the ground state as initial state and in systems presenting a nondegenerate ground-state, the latter is a unique functional of the static ground-state density alone, $\Psi_0 = \Psi_0[\rho_0]$, by the classical Hohenberg–Kohn theorem. Observables are in this case functionals of the density alone even in the time-dependent evolution. On the other hand, an initial state not chosen to be the ground state would allow us to describe the sudden switch-on of the perturbation, which otherwise could not be covered by the Runge–Gross theorem, and this constitutes the second problem.

Limits of the Runge–Gross theorem: the Runge–Gross theorem has been demonstrated for a much more restricted domain of validity than the Hohenberg–Kohn theorem. The original Runge–Gross demonstration relies on the hypothesis that the external potential $v(r, t)$ is analytic at the initial time t_0 , that is, all time derivatives $\partial^n v / \partial t^n$ exist at t_0 , so that $v(r, t)$ admits a Taylor expansion in t_0 . This excludes many possibilities, among them the adiabatical switch-on. However, though a general proof of the Runge–Gross theorem for arbitrary time-dependent potentials $v(r, t)$ does not exist [6], the theorem has been extended in the following years to other classes of potentials, so that we may hope that it is more general than actually demonstrated. In particular, the validity of the theorem has been extended significantly for small perturbations [7, 8] in the linear response regime, the most important for TDDFT applications.

v-representability problem: like in DFT and for the Hohenberg–Kohn theorem, the Runge–Gross theorem states the uniqueness of the potential corresponding to a density. However, it does not state its existence. There can exist densities that do not correspond to any potential [9]. This can be a problem when varying functionals with

respect to arbitrary densities. It can become more critical for the existence of a Kohn–Sham system, as we will see in the next section.

3 Time-dependent Kohn–Sham equations

The Runge–Gross theorem states that any observable is a unique functional of the density. However, like in DFT, finding an explicit form of functionals can be rather difficult. This is in particular true for the kinetic energy functional and motivates the introduction of a Kohn–Sham scheme also in TDDFT.

The proof of the Runge–Gross theorem is independent from the form of the many-body interaction between the particles. In particular, the theorem is also valid in the case of noninteracting particles. Provided that the density is *noninteracting v -representable*, there exists an unique potential associated with it. Thus we can solve TDDFT by a Kohn–Sham scheme like in DFT. A Kohn–Sham fictitious noninteracting system is introduced such that, by construction, it provides exactly the same density $\rho(r, t)$ of the real interacting system. The potential associated with this system is called the Kohn–Sham potential $v^{\text{KS}}(r, t)[\rho]$, and it is a functional of the density (and of the noninteracting system initial state $\Phi_0 = \Phi(t = 0)$). We can solve the Kohn–Sham system by solving an easier single-particle Schrödinger equation. With respect to static DFT, the TDDFT Kohn–Sham equation is a time-dependent Schrödinger-like equation

$$i\partial_t\phi_i^{\text{KS}}(r, t) = \left[-\frac{1}{2}\partial_r^2 + v^{\text{KS}}(r, t) \right] \phi_i^{\text{KS}}(r, t), \quad (7)$$

where $\phi_i^{\text{KS}}(r, t)$ are the Kohn–Sham wavefunctions. The density can be calculated by a sum over Kohn–Sham wavefunctions of all occupied states:

$$\rho(r, t) = \sum_i^{\text{occ}} |\phi_i^{\text{KS}}(r, t)|^2. \quad (8)$$

As in the static DFT case, it is convenient to split the Kohn–Sham potential into three terms:

$$v^{\text{KS}}[\rho](r, t) = v(r, t) + v_{\text{H}}[\rho](r, t) + v_{\text{xc}}[\rho](r, t) \quad (9)$$

with an external potential v , a Hartree potential

$$v_{\text{H}}[\rho](r, t) = \int dr' \frac{\rho(r', t)}{|r - r'|}, \quad (10)$$

and an exchange-correlation potential

$$v_{\text{xc}}[\rho](r, t) = \frac{\delta A_{\text{xc}}[\rho]}{\delta \rho(r, t)} \quad (11)$$

related to the exchange-correlation action $A_{xc}[\rho]$. Like in DFT, the latter is unknown and needs to be approximated.

When following the Kohn–Sham scheme, we run into further difficulties.

Noninteracting v-representability problem: as already mentioned, the v-representability becomes a more serious problem within the Kohn–Sham scheme. A real density ρ corresponding to a real external potential v may not be noninteracting v-representable, i.e., it may be that this density ρ is not a solution of a noninteracting system and does not correspond to some Kohn–Sham potential v^{KS} . In this case, the Kohn–Sham system does not exist, and the Kohn–Sham resolution scheme is not viable. The question of the noninteracting and interacting v-representabilities has been analyzed extensively [10, 11, 6, 12] but still keeps open.

Symmetry-causality paradox: the response function $\delta v_{xc}[\rho](r, t)/\delta\rho(r', t')$, called the exchange-correlation kernel and denoted $f_{xc}[\rho](r, t, r', t')$, as we will see in Section 4, must be *causal*, that is, $f_{xc}(t, t') = 0$ for all $t' > t$, implying that the density changes $\delta\rho(t')$ at later times $t' > t$ cannot affect the exchange-correlation potential at earlier times. But from equation (11) we could write $f_{xc}[\rho](r, t, r', t') = \delta^2 A_{xc}[\rho]/\delta\rho(r, t)\delta\rho(r', t')$, which is *symmetric* in t and t' in contrast to its causality. This is the so called symmetry-causality paradox. The paradox is related to the fact that TDDFT is inherently an out-of-equilibrium theory. The application of a time-dependent perturbation inevitably brings the system out of equilibrium. Formulation of TDDFT as a truly out-of-equilibrium theory within a Keldysh formalism [13] solves the paradox.

4 TDDFT in linear response

An important simplification of the theory is achieved when working in the linear response regime [4, 14–18]. Suppose that we can split the time-dependent external potential into a purely static term (to be identified, as usual, with the potential generated by the positive nuclei or ions) and a time-dependent perturbation term, as in equation (4):

$$v(r, t) = v(r) + \delta v(r, t)$$

with a time-dependent perturbation term, which is off before an initial time t_0 , $\delta v(r, t) = 0$ for all $t < t_0$, and which is in particular much smaller than the static term,

$$\delta v(r, t) \ll v(r). \quad (12)$$

Then the theory can be factorized into an ordinary static density-functional theory plus a linear response theory to the small time-dependent perturbation. In this case

the Hohenberg–Kohn and Runge–Gross theorems together state that the linear response time-dependent variation to the density is one-to-one with the time-dependent perturbation to the external potential,

$$\delta\rho(r, t) \Leftrightarrow \delta v(r, t).$$

Condition (12) is usually satisfied when considering normal situations referring to condensed matter systems submitted to small excitation. This is the case in optical spectroscopy using ordinary light, energy-loss spectroscopy, or X-ray spectroscopies. On the other hand, for spectroscopies implying strong electromagnetic fields, intense lasers, etc., condition (12) does not hold anymore, and the situation cannot be described by linear-response TDDFT.

A linear-response TDDFT (LR-TDDFT) calculation is a two-step procedure: starting from the static ionic external potential $v(r)$, we perform an ordinary static DFT calculation of the Kohn–Sham energies ϵ_i^{KS} and wavefunctions $\phi_i^{\text{KS}}(r)$, and so of the ground-state electronic density $\rho(r)$; then we do a linear-response TDDFT calculation of the density variation $\delta\rho(r, t)$ corresponding to the external time-dependent perturbation $\delta v(r, t)$. From $\delta\rho(r, t)$ we can then calculate the *polarizability* χ of the system defined as the linear response proportionality coefficient $\delta\rho = \chi\delta v$ of the density with respect to the external potential

$$\delta\rho(x_1) = \int dx_2 \chi(x_1, x_2) \delta v(x_2), \quad (13)$$

where we have used the notation x for the space and time variables, $x = \{r, t\}$, possibly including also the spin index, $x = \{r, t, \sigma\}$. For the remainder of the chapter, when it will be clear from context, we will simplify the notation omitting convolution products $\int dx$ as in equation (13).

It is possible to follow a Kohn–Sham scheme also in linear-response TDDFT. A fictitious noninteracting Kohn–Sham (KS) system is introduced under the hypothesis that its density response $\delta\rho^{\text{KS}}$ is equal to the density response of the real system, $\delta\rho = \delta\rho^{\text{KS}}$, but in response to an effective (Kohn–Sham) perturbation,

$$\delta v^{\text{KS}}(x) = \delta v(x) + \delta v_{\text{H}}(x) + \delta v_{\text{xc}}(x), \quad (14)$$

composed of the real external perturbation $\delta v(x)$ plus the Hartree term

$$\delta v_{\text{H}}(x_1) = \int dx_2 w(x_1, x_2) \delta\rho(x_2) \quad (15)$$

and the exchange-correlation term

$$\delta v_{\text{xc}}(x_1) = \int dx_2 f_{\text{xc}}[\rho](x_1, x_2) \delta\rho(x_2) \quad (16)$$

with the instantaneous static Coulomb interaction

$$w(x_1, x_2) = \frac{1}{|r_2 - r_1|} \delta(t_1, t_2)$$

and

$$f_{xc}[\rho](x_1, x_2) = \frac{\delta v_{xc}[\rho](x_1)}{\delta \rho(x_2)},$$

which is called the *exchange-correlation kernel* and is the fundamental quantity in linear-response TDDFT and, at the same time, the big unknown of the theory. We will consider it again all over the rest of this chapter and in particular in Sections 6, 13, and 14 to provide approximations to it, evaluate their performances and drawbacks, and study possible improvements.

For the fictitious KS independent particle system, we can introduce the corresponding *Kohn–Sham polarizability* χ^{KS} by

$$\delta \rho(x_1) = \int dx_2 \chi^{\text{KS}}(x_1, x_2) \delta v^{\text{KS}}(x_2), \quad (17)$$

that is, the polarizability of the independent-particle system that responds to the external perturbation δv^{KS} by the density variation $\delta \rho$. By applying perturbation theory to the Kohn–Sham equation (7) it can be shown that the Kohn–Sham polarizability is provided by the Adler–Wiser [19, 20] analytic expression

$$\chi^{\text{KS}}(r_1, r_2, \omega) = \sum_{ij} (f_i^{\text{KS}} - f_j^{\text{KS}}) \frac{\phi_j^{\text{KS}}(r_1) \phi_i^{\text{KS}*}(r_1) \phi_i^{\text{KS}}(r_2) \phi_j^{\text{KS}*}(r_2)}{\omega - (\epsilon_j^{\text{KS}} - \epsilon_i^{\text{KS}}) + i\eta}, \quad (18)$$

where ϵ_i^{KS} are the DFT Kohn–Sham energies, $\phi_i^{\text{KS}}(r)$ are the respective wavefunctions, and f_i^{KS} are their occupation numbers (η is an infinitesimal introduced to have well-defined Fourier transforms, $\chi(\tau = t_2 - t_1) \rightarrow \chi(\omega)$, for polarizabilities and other response functions). The Kohn–Sham polarizability can hence be calculated once we have solved the static DFT Kohn–Sham problem. By combining equations (13), (17), and (14) we can express the polarizability χ of the real system in a Dyson-like form

$$\chi = \chi^{\text{KS}} + \chi^{\text{KS}}(w + f_{xc})\chi \quad (19)$$

or also in an explicit form

$$\chi = (1 - \chi^{\text{KS}}w - \chi^{\text{KS}}f_{xc})^{-1} \chi^{\text{KS}} \quad (20)$$

in terms of the Kohn–Sham polarizability χ^{KS} and of the unknown exchange-correlation kernel f_{xc} . So, once we have an expression for the kernel, it is relatively easy to calculate, within LR-TDDFT, the full polarizability χ of the real system.

The polarizability χ is a fundamental quantity of any condensed matter system. It directly contains the excitation energies of the system, as we will see in Section 5. In Section 7, we will see that χ is directly related to the dielectric function and so to optical spectroscopy, EELS, and other experimental observables and spectra. The macroscopic dielectric function also enters into Maxwell equations in matter. So, knowledge of the polarizability or, equivalently, of the dielectric function fully determines the di-

electric properties of a condensed matter system. In nonmagnetic systems, the dielectric polarizability is alone sufficient to fully determine the behavior of matter under electromagnetic fields.

5 Excitation energies

To study excitations or to have direct access to spectroscopy, it is convenient to pass from the time space to the frequency ω -space. After the Fourier transform, all the convolution products in the time space, like the definition of the polarizability equation (13), become direct products in the frequency space,

$$\delta\rho(\omega) = \chi(\omega)\delta v(\omega).$$

From the latter expression we can see that the frequencies ω_l where the polarizability χ diverges correspond to the resonances, self-sustained modes of the system. These frequencies are the excitation energies of the system and can be extracted from the analytic structure of the polarizability by looking for the poles ω_l of the full polarizability χ . These are different from the poles of the zeroth-order Kohn–Sham polarizability χ^{KS} , which, as we can see from equation (18), correspond to the differences between the static DFT Kohn–Sham eigenvalues, $\omega_l^{\text{KS}} = \epsilon_j^{\text{KS}} - \epsilon_i^{\text{KS}}$. By introducing a compact Hartree plus exchange-correlation kernel $f_{\text{Hxc}} = w + f_{\text{xc}}$ in equation (20),

$$\chi = (1 - \chi^{\text{KS}} f_{\text{Hxc}})^{-1} \chi^{\text{KS}}, \quad (21)$$

we can see that the inverse operator $(1 - \chi^{\text{KS}} f_{\text{Hxc}})^{-1}$ has the task to bring the poles of its right operand χ^{KS} , that is, the excitations of the Kohn–Sham fictitious noninteracting system, to the poles of the full polarizability χ , that is, the excitations of the real system. Rewriting equation (21) as

$$[1 - \chi^{\text{KS}}(\omega) f_{\text{Hxc}}(\omega)] \chi(\omega) = \chi^{\text{KS}}(\omega) \quad (22)$$

and neglecting its real space r, r' structure, we can see that the poles ω_l of $\chi(\omega)$ must correspond to the zeros of the term $[1 - \chi^{\text{KS}}(\omega) f_{\text{Hxc}}(\omega)]$ for the right-hand side of the equation, $\chi^{\text{KS}}(\omega)$, to remain finite at ω_l . More rigorously, the true excitation energies ω_l are precisely those frequencies where the eigenvalues of the integral operator $[1 - \chi^{\text{KS}}(\omega) f_{\text{Hxc}}(\omega)]$ vanish. Therefore, the search for the excitation energies of the real system can be recast into an eigensystem problem. After some algebra, the true excitation energies can be calculated as the eigenvalues ω_l of the matrix equation

$$\begin{pmatrix} A & B \\ B^* & A^* \end{pmatrix} \begin{pmatrix} X \\ Y \end{pmatrix} = \omega_l \begin{pmatrix} 1 & 0 \\ 0 & -1 \end{pmatrix} \begin{pmatrix} X \\ Y \end{pmatrix}, \quad (23)$$

where

$$\begin{aligned} A_{tt'} &= \omega_t^{\text{KS}} \delta_{tt'} + 2 \int dr dr' \rho_t^{\text{KS}*}(r) f_{\text{Hxc}}(r, r') \rho_{t'}^{\text{KS}}(r'), \\ B_{tt'} &= 2 \int dr dr' \rho_t^{\text{KS}*}(r) f_{\text{Hxc}}(r, r') \rho_{-t'}^{\text{KS}}(r'), \\ \omega_t^{\text{KS}} &= \epsilon_j^{\text{KS}} - \epsilon_i^{\text{KS}}, \\ \rho_t^{\text{KS}}(r) &= \phi_i^{\text{KS}*}(r) \phi_j^{\text{KS}}(r). \end{aligned}$$

We can also consider a quadratic form of equation (23),

$$MF_l = \omega_l^2 F_l, \quad (24)$$

or can also consider an approximation, known as the Tamm–Dancoff approximation (TDA), consisting in the neglect of the coupling B matrix, $B = 0$.

Equations (23) and (24), known in chemistry as the Casida equations [21–24] allow us to directly calculate the excitation energies ω_l of a finite system, like a molecule or an atom. We will see in Section 9 an application of these equations to the calculation of the excitations in the helium atom. On this system, in Figure 1, we will compare the starting DFT Kohn–Sham energy differences ω_t^{KS} and the final TDDFT excitation energies ω_l obtained as solutions of equation (23) or (24), to the exact excitation energies obtained by an exact Hylleraas-like calculation [25] or measured with high-accuracy experiments in helium.

We can also calculate the oscillator strength associated with the excitation ω_l from the eigenvector F_l or $(X Y)$. Physically, an oscillator strength can be interpreted as the probability for the system to make the transition to the excited state, exactly like the Einstein coefficients of time-dependent perturbation theory and Fermi’s golden rule in noninteracting systems, e.g., the hydrogen atom. An oscillator strength equal to zero indicates a forbidden transition.

6 RPA and ALDA exchange-correlation kernel approximations

As we anticipated in Section 4, TDDFT would be an exact theory if we knew the exact density-functional form of the exchange-correlation term. Like in DFT, this term has to be approximated. The most common approximations for the exchange-correlation kernel f_{xc} are the *random-phase approximation* (RPA) and the *adiabatic local-density approximation* (indicated as ALDA or TDLDA). In the RPA approximation the exchange-correlation kernel is set to zero, $f_{\text{xc}} = 0$, and exchange-correlation effects are neglected. This is not such a crude approximation as we might think. Indeed, exchange-correlation effects are neglected only in the linear response to the external

perturbation, but not in the previous static DFT calculation, where they were taken into account by choosing an appropriate exchange-correlation potential v_{xc} in LDA or GGA for example. Later we will see examples of the validity of this approximation.

In the adiabatic local-density approximation, the kernel is taken to be

$$f_{xc}^{\text{ALDA}}(x_1, x_2) = \frac{\delta v_{xc}^{\text{LDA}}[\rho](x_1)}{\delta \rho(x_2)} = \delta(x_1, x_2) f_{xc}^{\text{HEG}}(\rho(r)), \quad (25)$$

where $f_{xc}^{\text{HEG}}(\rho)$ is the exchange-correlation kernel of the homogeneous electron gas or jellium model. The ALDA kernel is a local and ω -independent static (instantaneous) approximation. As we will show, TDLDA is a good approximation to calculate EELS or IXSS and even CIXS spectra. RPA and TDLDA are however unsatisfactory for optical spectra in semiconductors and insulators, i.e., spectra where electron-hole (e - h) interaction effects, giving rise to bound excitons or excitonic effects, are important. To provide new good approximations for the exchange-correlation kernel beyond ALDA and to make TDDFT work also on optical properties was the motivation of the last ten-year research efforts. This is presented in the last part of this chapter.

7 Dielectric function and experimental spectra

From the polarizability we can calculate the *microscopic dielectric function* $\varepsilon(x_1, x_2)$,

$$\varepsilon^{-1} = 1 + w\chi. \quad (26)$$

Observable quantities and spectra are related to the *macroscopic dielectric function* ε_{M} obtained from the microscopic ε by spatially averaging over a distance large enough with respect to the microscopic structure of the system (e.g., an elementary cell in periodic crystalline solids):

$$\varepsilon_{\text{M}}(r, r', \omega) = \overline{\varepsilon(r, r', \omega)}. \quad (27)$$

It can be shown that in solids the operation of averaging corresponds to the reciprocal space expression

$$\varepsilon_{\text{M}}(q, \omega) = \frac{1}{\varepsilon_{G=0, G'=0}^{-1}(q, \omega)}, \quad (28)$$

that is, the macroscopic ε_{M} is the inverse of the $G = G' = 0$ element (G and G' are reciprocal-space vectors) of the reciprocal-space *inverse* microscopic dielectric matrix ε^{-1} . This does not correspond to the $G = G' = 0$ element of the *direct* microscopic dielectric matrix ε ,

$$\varepsilon_{\text{M}}^{\text{NLF}}(q, \omega) = \varepsilon_{G=0, G'=0}(q, \omega), \quad (29)$$

if the microscopic dielectric matrix contains off-diagonal terms. Expression (29) is an *approximation* (NLF) to the exact macroscopic dielectric function. By this approximation the so-called crystal *local-field* effects are neglected (no local-field effects, NLF). We can see that the two expressions (28) and (29) coincide for the homogeneous electron gas or jellium model. Local-field effects are absent in the homogeneous electron gas and marginal in weakly inhomogeneous systems (e.g., silicon). They become important in systems presenting strong inhomogeneities in the electronic density, such as reduced dimensionality systems (2D surfaces/graphene, 1D nanotubes/wires, 0D clusters, etc.).

The macroscopic dielectric function ϵ_M is the key quantity to calculate observables and spectra. For example, the *dielectric constant* is given by

$$\epsilon_\infty = \lim_{q \rightarrow 0} \epsilon_M(q, \omega = 0). \quad (30)$$

The ordinary *optical absorption*, as measured, e.g., in ellipsometry, is directly related to the imaginary part of the macroscopic dielectric function:

$$\text{ABS}(\omega) = \mathbb{J}\epsilon_M(q \rightarrow 0, \omega). \quad (31)$$

Finally, the *energy-loss function*, as measured in EELS or IXSS, is related to minus the imaginary part of the inverse macroscopic dielectric function:

$$\text{ELF}(q, \omega) = -\mathbb{J}\epsilon_M^{-1}(q, \omega). \quad (32)$$

8 TDDFT implementations and codes

The equations presented in the previous sections are implemented in several TDDFT codes, though not so many like in the case of DFT. TDDFT codes differ by the used basis set, e.g., plane waves (PW), linearized augmented plane waves (LAPW), Gaussians, etc., like in DFT. Most importantly, there are implementations in the real time-space and in the frequency-reciprocal space.

The DP code [26] is a linear-response TDDFT pseudopotential code on a plane-wave basis set working in the frequency-reciprocal space, although some quantities are calculated in the frequency-real space. The code allows us to calculate dielectric and optical spectra, such as optical absorption, reflectivity, refraction indices, EELS, IXSS, and CIXS spectra. It uses periodic boundary conditions and works both on bulk 3D systems and also, by using supercells containing vacuum, on 2D surfaces, 1D nanotubes/wires, and 0D clusters and molecules. It can deal with both insulating or metallic systems. Several approximations to the exchange-correlation kernel are implemented, and local-field effects can be switched on and off.

The DP code relies on a previous DFT calculation of the KS energies and wavefunctions, provided by another PW code like, for example, ABINIT [27]. The first task

is to back Fourier transform the KS wavefunctions, $\phi_i^{\text{KS}}(G) \rightarrow \phi_i^{\text{KS}}(r)$, from the reciprocal to the real space. Then DP calculates in the real space the optical matrix elements $\rho_{ij}^{\text{KS}}(r) = \phi_i^{\text{KS}*}(r)\phi_j^{\text{KS}}(r)$, which are Fourier transformed, $\rho_{ij}^{\text{KS}}(r) \rightarrow \rho_{ij}^{\text{KS}}(G)$, to the reciprocal space. The next step is the calculation of the Kohn–Sham polarizability

$$\chi_{G_1 G_2}^{\text{KS}}(q, \omega) = \sum_{i,j \neq i} (f_i^{\text{KS}} - f_j^{\text{KS}}) \frac{\rho_{ij}^{\text{KS}}(G_1, q) \rho_{ij}^{\text{KS}*}(G_2, q)}{\epsilon_i^{\text{KS}} - \epsilon_j^{\text{KS}} - \omega - i\eta}. \quad (33)$$

At this point the RPA dielectric function and spectra in the NLF approximation are already available via $\epsilon_M^{\text{RPA-NLF}}(q, \omega) = 1 - w\chi_{00}^{\text{KS}}(q, \omega)$. For approximations beyond, DP first calculates the polarizability χ by equation (20). The ALDA exchange-correlation f_{xc} is calculated in the real space and then Fourier transformed in the reciprocal space. At the end, DP calculates the dielectric function ϵ (equation (26)) and finally the observable macroscopic dielectric function $\epsilon_M(q, \omega)$ (equation (28)), including local-field effects. The function $\epsilon_M(q, \omega)$ is provided in an output file, both in the real and imaginary parts, as a function of ω (the BZ vector q is fixed and specified as an input parameter to the DP code). The most time-consuming steps are the calculation of χ^{KS} , where Fourier transforms are carried out using FFT (scaling $O(N \log N)$ instead of $O(N^2)$), and the matrix inversion to calculate χ (equation (20)), which is however replaced by the resolution of a linear system of equations (scaling $O(N^2)$ instead of $O(N^3)$).

An example of a linear-response TDDFT code on a LAPW basis set is Elk [28]. The Elk code works in the frequency-reciprocal space and allows us to perform all-electron full-potential nonpseudopotential calculations.

A real space-time implementation of TDDFT is the Octopus code [29]. The real space implementation makes it particularly well suited to isolated systems (atoms, molecules, clusters, etc.), though of course with limitations on periodic systems. However, its most important feature is that it can go beyond the linear-response TDDFT, thanks to the explicit evaluation of the time evolution of the density.

9 TDDFT on the simplest example: He atom

The simplest many-body interacting system in nature is the helium atom. Here many-body means just only two electrons. For this system, there are both very accurate experimental measures and theoretical calculations for the ground and excited states. It looks a toy model, but, contrary to other widespread many-body models, it is a real system with a real long-range Coulomb many-body interaction among electrons. So, it represents an important workbench model for theory because, instead of comparing directly with the experience, we can compare different many-body theories at the same nonrelativistic level of physics, e.g., switching off relativistic and finite nuclear mass effects, QED radiative corrections, etc. TDDFT is in principle an exact theory to calculate excited states, and so exact TDDFT should work also on the helium atom.

A different issue is whether a given approximation within TDDFT, e.g., RPA or adiabatic LDA (TDLDA), is going to provide accurate results, or at least good enough to reproduce with an acceptable approximation, or just only qualitatively, the right physics of a system.

The helium atom is a good example to show how TDDFT works in practice and what are the typical results we can get out. In the example we report here, the first step is a DFT calculation of the ground-state density and the Kohn–Sham electronic structure, both energies ϵ_i^{KS} and wavefunctions $\phi_i^{\text{KS}}(r)$. Then a linear-response TDDFT calculation (equations (23) and (24)) is performed on top of DFT to get the neutral excitation energies, to be compared with the transition energies observed in an optical absorption experiment, and optionally also the oscillator strengths. The quality of a TDDFT calculation is affected by both steps. In particular, it is affected by both the approximation for the static exchange–correlation potential $v_{\text{xc}}(r)$, used in the ground-state DFT calculation, and also by the approximation for the exchange–correlation kernel $f_{\text{xc}}(r, r', \omega)$, used in the following linear-response TDDFT calculation. Of course, it is preferable to coherently use the same level of approximation in both steps, e.g., LDA in DFT and ALDA in TDDFT, but this is not necessary. As we will see in this and following examples, the quality of a given approximation, e.g., LDA, not necessarily is the same in DFT and TDDFT. This depends on the system typology (e.g., isolated, extended, 2D, etc.) and on the studied properties. We will rediscuss this point.

In Figure 1 we show both a table and a diagram presenting the excitation energies of the helium atom for the lowest excited states $n^{2S+1}L$, both the singlet $S = 0$ and the triplet $S = 1$ series. The excitation energies are measured from the ground state 1^1S , which is hence set as the zero of the energies, whereas the continuum of first ionization, $\text{He}^+(1s) + e^-$, lies at 0.9037 Ha. The result indicated in the table and in the graph as “exact” is the accurate variational nonrelativistic calculation of Ref. [25]. It coincides with the experiment within the quoted 10^{-4} Ha accuracy. This is to be compared with the DFT and TDDFT results, the first two columns in the table and in the graph.

The helium atom is a fortunate case where the exact DFT static Kohn–Sham potential is known [30]. This is possible since we know from very accurate variational calculations [30] the full many-body wavefunction and the density of the ground state, from which we can derive the Kohn–Sham doubly occupied wavefunction, and invert the Kohn–Sham equation to get the exact Kohn–Sham potential. We can then solve the Kohn–Sham equations to find the exact Kohn–Sham energies and wavefunctions, so to have the best starting point to perform the following linear-response TDDFT calculation. In Figure 1 we present the results of such calculation [14], done using the exact Kohn–Sham potential for the static DFT calculation and the TDLDA approximation for the linear-response TDDFT last step. These results will faithfully represent the performances of TDDFT and the TDLDA approximation, without being affected by approximations in the DFT first step. We first report the DFT Kohn–Sham energy differences $\omega_{ij}^{\text{KS}} = \epsilon_j^{\text{KS}} - \epsilon_i^{\text{KS}}$ calculated using the unapproximated exact Kohn–Sham

DFT Exact KS	TDDFT ALDA	Exact (EXP)	State
0.8836	0.8838	0.8838	5^1P
	0.8832	0.8832	5^3P
0.8819	0.8835	0.8825	5^1S
	0.8815	0.8811	5^3S
0.8722	0.8726	0.8727	4^1P
	0.8715	0.8714	4^3P
0.8688	0.8719	0.8701	4^1S
	0.8679	0.8672	4^3S
0.8476	0.8483	0.8486	3^1P
	0.8457	0.8456	3^3P
0.8392	0.8461	0.8425	3^1S
	0.8368	0.8350	3^3S
0.7772	0.7764	0.7799	2^1P
	0.7698	0.7706	2^3P
0.7460	0.7678	0.7578	2^1S
	0.7351	0.7285	2^3S

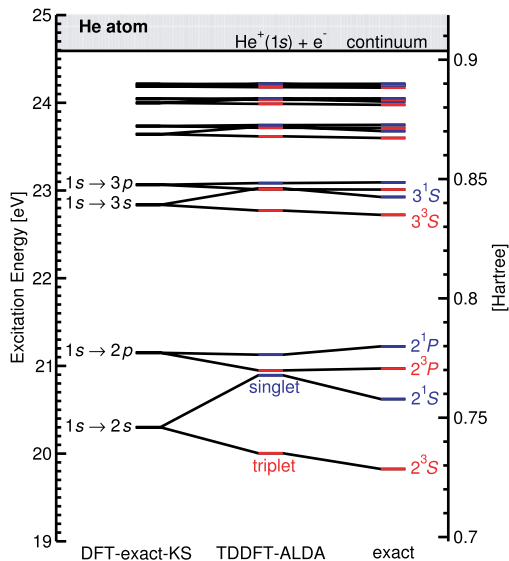


Figure 1: Helium atom excitation energies for the lowest states $n^{2S+1}L$ with $n = 2 \rightarrow 5$, $L = S, P$, both the singlet $S = 0$ and the triplet $S = 1$ series. The 0 of the energy is set to the ground state 1^1S , so that the continuum $\text{He}^+(1s) + e^-$ is set to the ionization potential 0.9037 Ha. Left: DFT Kohn–Sham energy differences from the exact Kohn–Sham potential [30]; middle: TDDFT in the ALDA approximation [31]; right: exact nonrelativistic result [25], which, within the quoted 10^{-4} Ha accuracy, also coincides with the experiment.

potential. Once again, we stress that the DFT Kohn–Sham eigenvalues are the energies of a fictitious noninteracting system, and so they are unphysical. They cannot be interpreted as the true quasiparticle charged (addition or removal of an electron) excitation energies of the many-body interacting system, nor their difference can be interpreted as the neutral excitation energies. Nevertheless, we remark that, at least in the case of He atom, the Kohn–Sham energy differences are already surprisingly close to the exact neutral excitation energies of the system. They lie in the middle between the singlet and triplet energies, and they are a very good starting point for the next linear-response TDDFT correction. Finally, we remark that TDDFT in the adiabatic LDA reveals a very good approximation for the singlet–triplet splitting. This is a surprisingly good result also in consideration of the simplicity of the TDLDA approximation. For the highest excited states, TDLDA is in perfect quantitative agreement with the exact result. However, this is the easiest part of the spectrum for TDDFT to reproduce to. Indeed, here the singlet–triplet exchange split is small, and so the validity of the final result is above all due to the exact DFT KS starting point. The accuracy of the DFT-TDDFT result deteriorates when going toward the lowest energy states, and here we see the limits of the ALDA approximation. In some cases, TDLDA inverts the order of states, like in the case of 3^1S and 3^3P .

We mention however that if the same LDA approximation were applied also to the first step static DFT calculation, the Kohn–Sham energy differences (starting point for the TDDFT calculation) would result much worse. Apart from only the first occupied state, the rest of the Kohn–Sham LDA energy spectrum is unbound, raised in the continuum. There is no Rydberg series in DFT Kohn–Sham LDA (or also GGA) atoms. This is due to the wrong exponential e^{-r} , instead of $1/r$, asymptotical decay of the LDA (and GGA) potential. This is a very difficult starting point for the TDDFT approximated kernel to correct. So, the surprisingly good result reproduced in Figure 1 is just only thanks to our knowledge of the exact DFT KS potential in this system. Unfortunately, exact DFT results are only known for a few systems, mainly simple atoms.

10 TDDFT electron and ion dynamics versus TRXRD

The direct solution of the time-dependent Kohn–Sham equation (7) in real space-time allows us to follow the evolution of a system electronic density $\rho(r, t)$ after excitation by an external potential $\delta v(r, t)$. In this way, we can access the full (beyond linear) response of a system submitted to a strong perturbation and have a time-resolved study of phenomena, like the ionization of a molecule, or the breaking or the formation of chemical bonds, etc. This is a kind of studies that become more and more available from the experiment, thanks to the advent of ultrashort, femtosecond and below, laser pulses and pump-and-probe experimental setups.

Figure 2 presents a real space-time TDLDA calculation [32] on an acetylene molecule excited by a short laser pulse. The figure presents snapshots of the time-dependent electron localization function [32, 34], a quantity related to the electron density, current, and kinetic energy density and more suited to put into evidence chemical bondings. The molecule is initially in its ground state (Figure 2(a)), characterized by two blobs around the hydrogen atoms and the torus typical for a triple bond between the two carbon atoms. With the raising of the laser pulse, the electron cloud starts to oscillate until the system ionizes, as it is evident from two blobs of electrons that leave the system toward the left (Figure 2(b)) and the right (Figure 2(c)), with wave-packets that spread with time. Later, the central torus widens (Figure 2(d)) until it breaks into two separate tori (Figure 2(e)) around the two carbon atoms: this can be interpreted as the transition from the bonding π state to the antibonding π^* state. The system is left into the excited state.

In the previous example the ions are kept fixed at their molecular ground-state equilibrium position, and only electronic degrees of freedom are let evolve along the time-dependent TDDFT dynamics. This is valid when the perturbation is small with respect to the ionic potential and so does not cause a rearrangement of the atomic structure, a chemical reaction, or the fragmentation of the molecule. However, we can

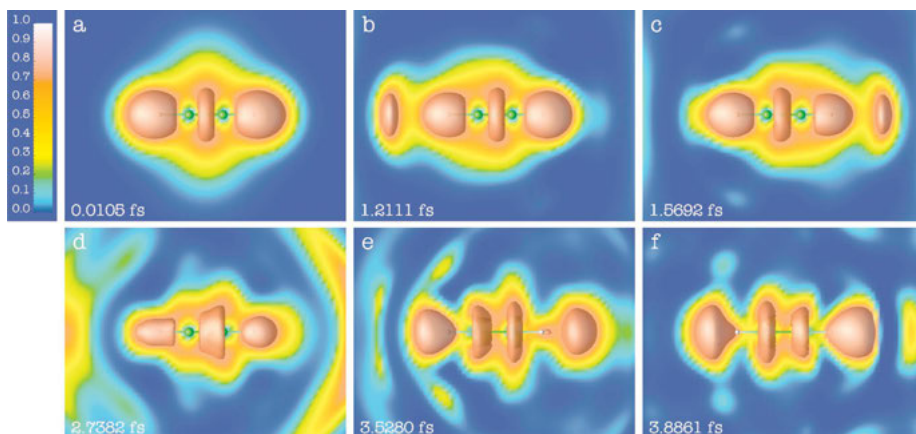


Figure 2: Snapshots of the time-dependent electron localization (TD-ELF) for the excitation of acetylene (C_2H_2) by a laser pulse polarized along the molecular axis at frequency $\omega = 17.5$ eV, intensity $I = 1.2 \cdot 10^{14}$ W cm^{-2} , pulse duration 7 fs (Reprinted with permission from Ref. [32]. Copyright (2005) by the American Physical Society.). The molecule is along the longitudinal axis, with the carbon atoms represented by green and the hydrogens by white balls. The sequence shows first the ionization of the molecule and then the transition from the bonding state π to the antibonding state π^* . The full movie can be watched at [33].

also relax the constraint on the ion positions and perform a full electron and ion time-dependent TDDFT dynamics. Figure 3 presents a real-space TDLDA dynamics [32] on an ethene molecule shot by a fast nonrelativistic proton. Figure 3 (a) shows the initial configuration with the proton (bottom white sphere) shot against the leftmost carbon atom (green sphere) of the molecule. While approaching the molecule, the proton is seen to dress some electronic charge (Figure 3 (b)). Then it is scattered and leaves the system bringing part of the electronic charge (Figure 3 (c)). The molecule is left into a perturbed excited state. In Figure 3 (d) the leftmost carbon has already broken the bonds with the two hydrogens (which are going to form a hydrogen molecule), and in Figure 3 (e), we can see the formation of a lone pair above it. Finally, in Figure 3 (f) the molecule is completely exploded into a H_2 molecule (left) and two CH fragments, each with a characteristic lone pair near the C atom.

This kind of theoretical studies can be of real benefit in the interpretation of experiments and a valuable complement of time-resolved X-ray diffraction (TRXRD) studies, as treated in the next chapter. By TRXRD we can follow the dynamics of nuclei under the effect of an external perturbation. In the next chapter, we present an example of a TRXRD study on the photodissociation of the I_3^- ion following excitation by light pulses of different wavelengths. Ab initio static DFT calculated data are already used to make an energetic balance of each possible reaction pathway from the reactant to the different possible solute species and to interpret TRXRD data. A more complete study of the full dynamics of the I_3^- photodissociation by TDDFT can be done in a way similar to the examples we have presented on acetylene under laser excitation and on

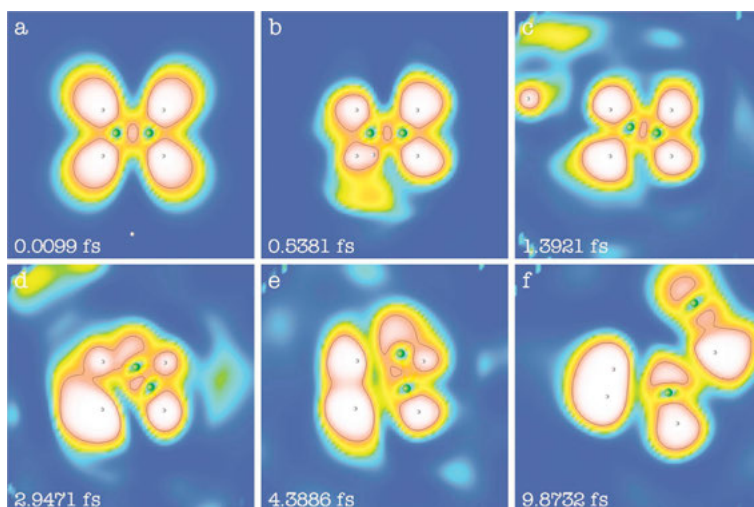


Figure 3: Snapshots of the time-dependent electron localization (TD-ELF) for the scattering of a proton of energy $E_{\text{kin}} \approx 2$ keV by an ethene molecule (C_2H_4 , reprinted with permission from Ref. [32]. Copyright (2005) by the American Physical Society.). Same color scheme as in Figure 2. The sequence shows the breaking of bonds and subsequent creation of lone pairs, leading to the fragmentation of the molecule into several pieces (H_2 and two CH). The full movie can be watched at [35].

the dynamics of ethene dissociation. This is already possible at the today computing power, although care is required when dealing with atomic elements well beyond the first rows of the periodic table.

Full TDDFT dynamics of the reaction paths in more complex molecules, like the photoactive yellow protein (PYP) also presented in the next chapter, are still out of reach. However, first TDDFT studies restricted only to the active regions of a protein, like chromophores into photoactive proteins, and to its electronic degrees of freedom were already possible, for example, on the green fluorescent protein (GFP) and its blue mutant (BFP) [36]. Although without a full ionic and electronic dynamics, we can supplement TRXRD studies by sampling a reaction path with electronic-only TDDFT calculations of excitations [36]. Along this line, one serious drawback is represented by the noncorrect representation of the so-called *conical intersections* (CIs) [37, 38] between potential energy surfaces of the ground and excited states (see Figure 4). CIs play a fundamental role in photochemistry as the critical points that allow a given chemical reaction path from the reactants to the products. The identification of the CIs is already an important step forward in the study of photochemical reactions. Unfortunately, CIs are points where the traditional Born–Oppenheimer approximation breakdowns, and coupling between ionic and electronic degrees of freedom must be explicitly taken into account [39]. This is an active domain of research with many efforts also in the direction of evaluating the crossed validity of exchange–correlation and/or the Tamm–Dancoff approximations for a correct description of CIs.

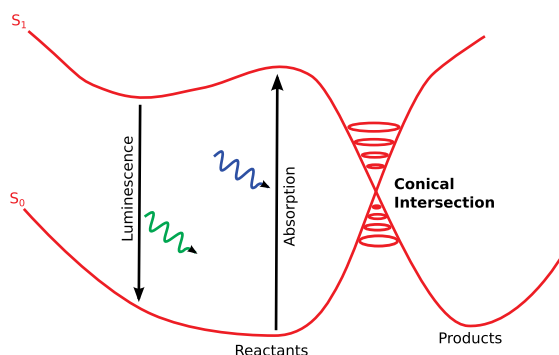


Figure 4: Conical intersection (CI) between ground and excited states potential energy surfaces, allowing a radiationless decay in a photochemistry reaction.

The examples presented in this section can give an idea of what TDDFT is going to achieve in the nearest future with increasing computer power and improved code algorithms, both in the direction of more involved studies and more complex systems. Indeed, with respect to other many-body approaches, TDDFT keeps at a reasonable computational cost and scaling ($O(N^4)$ with N the number of atoms in the molecule or periodic solid elementary cell), whereas TDDFT reliability is directly related to the limits of validity of the chosen approximation. For instance, TDLDA is expected to overestimate ionization rates due to its incorrect long-range behavior. Most of the present theoretical work goes in the direction of improving standard approximations to correct this and other known drawbacks, like the mentioned problem of conical intersections.

11 TDDFT on EELS: local-field effects

We will now show examples of typical TDDFT results using the RPA and TDLDA approximations on electron energy-loss spectra (EELS) of a prototypical system like bulk silicon. Figure 5 shows the EELS experimental spectrum measured [40] at $q \sim 0$, that is, almost zero-momentum transfer (red dots). The spectrum presents a single peak at 16.7 eV, corresponding to the plasmon resonance collective excitation of bulk silicon. We then show the energy-loss function calculated [41] by the DP code in the RPA NLF (without local-field effects), the RPA (with local-field effects), and TDLDA approximations. We remark an overall agreement of TDLDA with the experiment. Both the position and strength of the plasmon resonance are correctly reproduced by the TDLDA approximation. We can also conclude that in this $q \sim 0$ case, the RPA result is not that bad and at least qualitatively in agreement. The plasmon energy is already well reproduced at the level of the RPA without local-field effects. Local-field effects improve on the resonance height.

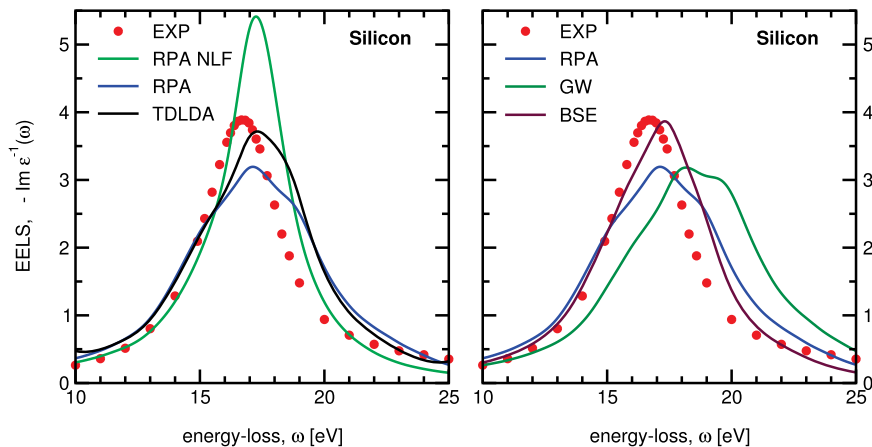


Figure 5: Energy-loss spectra (EELS) in silicon at $q \approx 0$ momentum transfer. Left (reproducing Figure 3 of Ref. [42]): Energy-loss function in the RPA without (NLF, light green dot-dashed line) and with local-field effects (blue dashed line), TDLDA (black continuous line), EELS experiment (red dots from Ref. [40]). Right (reproducing Figure 2 of Ref. [43]): Energy-loss function in the RPA (blue dashed line), GW-RPA (green dashed line), Bethe–Salpeter approach (BSE brown continuous line), EELS experiment (red dots from Ref. [40]).

This surprising result can be explained when looking at Figure 5 (right panel), where we present the bulk silicon EELS calculated [43] by solving the Bethe–Salpeter equation (BSE) in the GW approximation within the framework of ab initio many-body quantum field theory. The latter is an approach relying on second quantization of fields and the electronic propagator or Green function $G(x_1, x_2)$ as fundamental degree of freedom, instead of the (time-dependent) density $\rho(x)$ of DFT and TDDFT. Ab initio many-body Green function theory is an alternative to DFT and TDDFT, with the important advantage that approximations within the theory are more easily to find by physical intuition. For example, the GW approximation to the self-energy can be seen as an evolution of the Hartree–Fock method by replacing the bare Fock exchange with a screened exchange, thus introducing some correlations in the form of screening. The disadvantage of two-point Green functions $G(x_1, x_2)$ is that they are much heavier to calculate with respect to single-point densities $\rho(x)$ as in DFT and TDDFT. The scaling of Green function methods with the number of electrons is more unfavorable than in DFT and TDDFT, so that GW and BSE calculations are restricted to much simpler systems. Bulk silicon is still an affordable system for Green function methods, so that the GW and BSE results here can represent not only a comparison term for TDDFT, but also an invaluable tool to understand the physics at bench thanks to their more intuitive physical meaning. For instance, the GW approximation on the self-energy introduces electron–electron (e – e) interaction self-energy effects on top of the RPA approximation. In Figure 5 we remark that the introduction of these effects (GW-RPA curve) surprisingly worsens the result. GW shifts the plasmon position to the highest energies

and faraway from the experiment. On the other hand, introduction of electron–hole ($e-h$) interaction effects on top of GW, as by resolution of the Bethe–Salpeter equation (BSE curve), restores a good agreement with the experiment by shifting back again the plasmon resonance. To a large extent, $e-e$ and $e-h$ interaction effects compensate each other in EELS. As a consequence, the RPA lowest level of approximation, which neglects both effects, is already a good approximation. To improve upon RPA, we cannot introduce only one of them and should take into account both. This seems to be the case of the ALDA kernel, at least for EELS spectra.

We now discuss local-field effects and their importance. As introduced in Section 7, local-field effects are directly related to density inhomogeneities of the system. They enter into play with the departure from homogeneity and become increasingly important with the increase of density inhomogeneity. To illustrate these points, we take the example of graphite [44, 45], which is a system of intermediate 3D/2D character: it is in fact a 3D bulk solid, but its carbon atoms are arranged in 2D flat planes of graphene, weakly bounded and stacked one on top of the other. As a consequence of this particular atomic structure, the system looks homogeneous in the xy -direction, whereas it appears to be inhomogeneous along the z -direction. This can be appreciated in EELS by varying the direction of the momentum q transferred to the sample with respect to the system crystal axes. In Figure 6, we report EELS spectra taken [44, 45] for graphite at almost zero-momentum transfer, $q \approx 0$, but oriented along several directions: from the in-plane direction (q parallel to the graphene planes) to the out-of-plane direction (q perpendicular to the graphene planes and parallel to the z axis). The red dots are the spectra measured at the indicated experimental setup angles θ with respect to the z axis. We then report RPA spectra calculated with and without local-field effects (respectively LF and NLF). For momentum transfer in the in-plane direction, where EELS samples a homogeneous system, we cannot notice any appreciable difference between the RPA-NLF and RPA-LF spectra. Along this direction, local-field effects are negligible, and the RPA-NLF is a good approximation. Differences between spectra start to appear for q departing from the in-plane direction. Local-field effects become more and more important by going toward the out-of-plane direction. Inclusion of them neatly improves the result: the RPA-LF result is in very good, quantitative agreement with the experiment at all sampled directions. Only the $\theta = 30^\circ$ direction shows a small difference between the RPA-LF curve and the experiment, which is probably due to a small difference between the calculated and experimental angle collections [44]. For this direction, we also show the TDLDA spectrum, which does not show any appreciable difference with respect to RPA-LF. Exchange-correlation effects, as accounted by the ALDA approximation, are small also in all other directions at almost zero, $q \approx 0$, transferred momentum. Graphite is a good example to show the importance of local-field effects and their relation to density inhomogeneities.

Graphite is also a good example to show the fundamental contribution of ab initio theory to a correct interpretation of experimental findings. In Figure 6, right, we report the in-plane RPA NLF graphite EELS spectrum, which we have already seen to be in

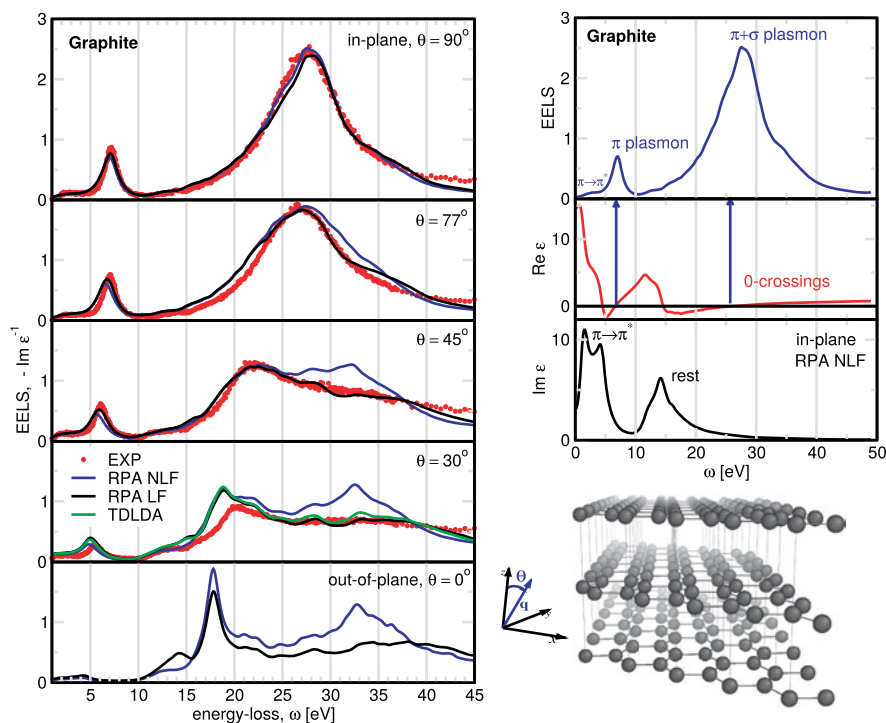


Figure 6: EELS spectra of graphite (from Ref. [44, 45]) for small q transferred momentum at several directions, from in plane (top) to out-of-plane (bottom). Red dots: experiment; blue dashed line: RPA without LF effects; black solid line: RPA with LF; green dot-dashed line: TDLDA.

quantitative agreement with the experiment. We also show in comparison the RPA NLF real ($\Re\epsilon$) and imaginary ($\Im\epsilon$) parts of the macroscopic dielectric function. This comparison allows us to provide an unambiguous interpretation of EELS spectra and excitations. EELS peaks can be associated with either single-particle or collective excitations. Single-particle excitations are associated with electron–hole “optical” transitions, for example, the excitation of one electron from a valence to a conduction band as by a photon. They appear as peaks in the imaginary part of the dielectric function, which is directly related to the optical absorption (Section 7). EELS peaks that have a direct correspondence in the imaginary part of the dielectric function are to be classified as single-particle excitations. On the other hand, collective excitations are associated with the collective motion of the plasma of electrons, e.g., plasmons. A plasmon resonance is by definition in direct correspondence to the zeros of the real part of the dielectric function: indeed, at the frequencies where $\epsilon(\omega) = 0$, the system supports self-sustained modes $E(\omega) = D(\omega)/\epsilon(\omega)$ without the presence of an external field D . In graphite (Figure 6, right) the only visible structure in the EELS that can be associated with a single-particle excitation is the low-energy shoulder from 0 to 6 eV, directly corresponding to the main peak in $\Im\epsilon$, which is due to transitions from π to π^*

states. The two main EELS peaks at 7 and 28 eV are both associated with zeros of $\Re\epsilon$: therefore they are both bulk plasmon collective excitations. We can go further with the interpretation. The real and imaginary parts of the dielectric function are related by Kramers–Kronig relations, so that a peak in the imaginary part is followed by a characteristic s-shaped feature in the real part, occasionally producing a crossing to zero. In graphite the imaginary part presents two main absorption peaks: a low-energy peak (0–6 eV) due to single-particle excitations involving only transitions from π to π^* states, the closest to the Fermi energy, and a highest energy peak (14 eV), involving transitions also from σ and to σ^* states. This can be verified in an ab initio calculation (not in an experiment) by selectively removing those states from the calculation. In between the two main peaks the optical absorption falls almost to zero, so that also in the real part, there is a separation between the two characteristic Kramers–Kronig features and the zero-crossings. The plasmon arising from the first low-energy 0-crossing is to be associated with the collective motion of only π electrons, whereas it is the collective motion of all (valence) electrons that gives rise to the highest energy plasmon. This justifies the interpretation of the two main graphite excitations as π -plasmon and total plasmon, respectively.

We conclude this section by discussing local-field effects under reduction of the system dimensionality, from 3D graphite to 2D graphene. In Figure 7, we show the

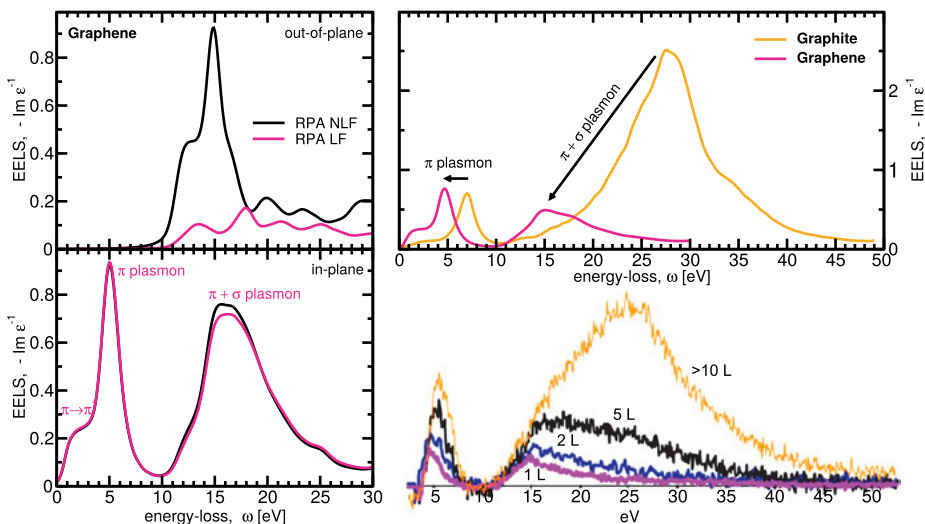


Figure 7: Graphene vs graphite electron energy-loss spectra (EELS). Left: TDDFT RPA approximation calculation of graphene energy-loss function at $q \approx 0$ for both out-of-plane (top) and in-plane (bottom) momentum transfer directions, with (magenta continuous lines) and without (dashed black lines) local-field effects. Right: TDDFT RPA LF energy-loss functions (top) of graphite (yellow dot-dashed line) and graphene (magenta continuous line) as compared to the EELS experiment by Eberlein et al. [46] (bottom) for a single graphene monolayer (pink curve), two layers of graphene (blue), five (black) and more than ten layers of graphene (yellow). Reprinted with permission from Ref. [46]. Copyright (2008) by the American Physical Society.

energy-loss function of graphene for the in-plane and the out-of-plane momentum transfer directions in the RPA with and without local-field effects. Like in graphite, local-field effects are negligible in the in-plane direction, where the electron density is homogeneous. On the other hand, local-fields are responsible for a strong suppression, a depolarization effect in the out-of-plane z direction along which the density goes to zero in the vacuum. The same effect can also be observed in 1D nanotubes or nanowires [47, 48] along directions orthogonal to the tube/wire axis. In Figure 7, left, we show the in-plane EELS spectra calculated by TDDFT in the RPA LF approximation for both graphite and graphene. In the same figure, right, we also show the experimental [46] EELS spectra taken for one graphene monolayer, and up to ten layers of graphene that, from a dielectric point of view, can already be considered bulk graphite. The TDDFT calculation [49, 50] predicted the correct shift of both plasmons in going from graphite to graphene (shifts emphasized by the black arrows in the top-left panel of Figure 7), although with an overestimation of the oscillator strength of the π plasmon.

12 TDDFT on IXSS: exchange-correlation effects

We have seen that in EELS spectra at almost zero-momentum transfer, $q \approx 0$, exchange-correlation effects as accounted by the adiabatic LDA approximation are small, and the RPA approximation is already in a very good agreement with the experiment. This is not the case for finite momentum transfer. Exchange-correlation effects become more important when going to the largest q . Although it is possible to acquire energy-loss spectra at small though finite q , an experimental technique that allows us to access the range of very large q (up to several Brillouin zones) is inelastic X-ray scattering spectroscopy (IXSS). IXSS requires to use intense synchrotron radiation X-rays as primary beam and detects the scattered photons at given angle related to the momentum transfer. IXSS measures the dynamic structure factor $S(q, \omega)$, which is related to the macroscopic dielectric function $\varepsilon_M(q, \omega)$ by

$$S(q, \omega) = \frac{q^2}{4\pi^2\rho} (-\Im\varepsilon_M^{-1}(q, \omega)),$$

where ρ is the electron density. We see that the dynamic structure factor is directly proportional to the energy-loss function $-\Im\varepsilon_M^{-1}$, so that EELS and IXSS measure in practice the same observable, though with different resolution at different regimes.

Again for the prototypical bulk silicon, we show in Figure 8 the experimental dynamic structure factor [51] at different transferred momenta along the [111] direction. Once again, we compare the experiment to the TDDFT results in the RPA with local-field (LF) effects and the TDLDA approximations. At the smallest q the two approximations provide almost no different results, like we have already seen for $q \approx 0$ at the

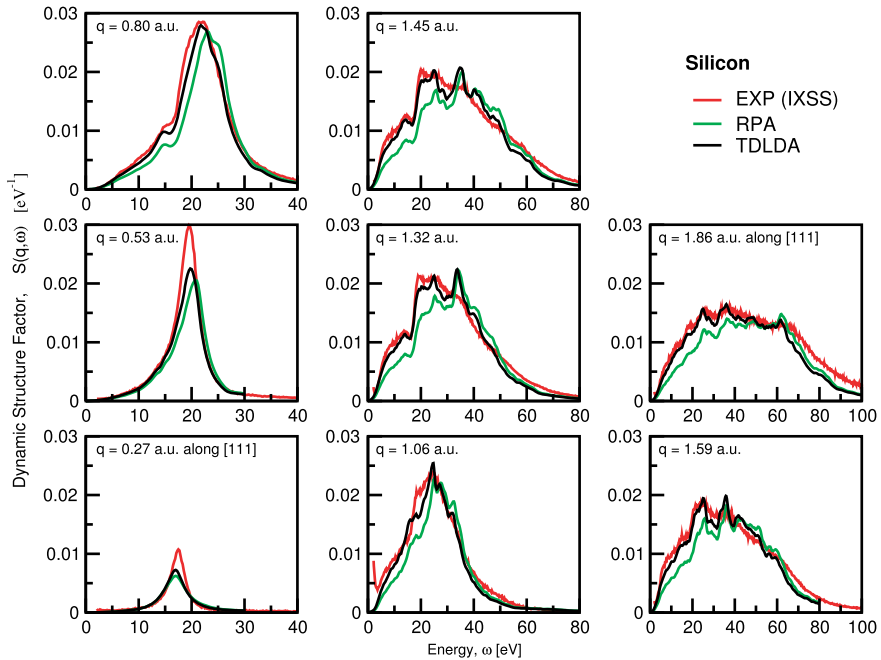


Figure 8: Silicon dynamic structure factor $S(q, \omega)$ for different transferred momenta q along the [111] direction (from Ref. [51]). Red lines: experimental inelastic X-ray spectrum (IXSS) taken at the European synchrotron radiation facility (ESRF); green dashed lines: TDDFT in the RPA with local-field effects approximation; black lines: TDDFT in the ALDA approximation.

example of graphite (Figure 6). Exchange and correlation effects, as accounted by the adiabatic LDA exchange-correlation kernel, are negligible at the lowest q but become more important with increasing q . At $q = 0.80$ a.u., we observe an already marked difference of TDLDA with respect to RPA in the direction of an improved agreement with the experiment. At the largest q , TDLDA and RPA present large differences, especially in the low-energy spectral range where TDLDA is in an almost quantitative agreement with the experiment. Two conclusions can be drawn: (1) in the energy-loss function, exchange and correlation effects are important at the largest transferred momenta; (2) adiabatic LDA is a good approximation to the TDDFT exchange-correlation kernel at least on the energy-loss function low-energy range.

In Figure 9, we focus on the $q = 1.32$ a.u. to provide an analysis with more details. The effect of local fields can be appreciated as nonnegligible by comparing RPA LF and NLF spectra. Local-fields have the effect to push spectral weight from low to high energies. Surprisingly, the RPA NLF result appears closest to the experiment. Inclusion of exchange-correlation effects on top restores a good result, as if there were a compensation between LF and xc effects. However, a more careful analysis shows that the RPA NLF result cannot even qualitatively capture important aspects. At 17 eV the ex-

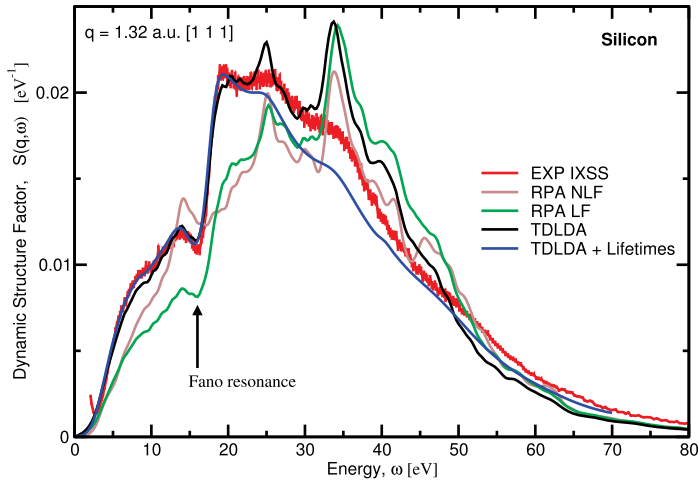


Figure 9: Silicon dynamic structure factor at $q = 1.32$ a.u. along the $[111]$ direction (from Figure 4 of Ref. [42] and Figure 1 of Ref. [51]). Red line: IXSS experiment [52, 51]; short-dashed brown line: TDDFT in the RPA without local-field effects (NLF) approximation; long-dashed green line: TDDFT in the RPA with local-field (LF) effects; black continuous line: TDDFT in the ALDA approximation (TDLDA); blue dot-dashed line: TDLDA plus lifetime effects.

periment presents a characteristic asymmetric feature (small peak/shoulder followed by a steep rise) typical for a Fano resonance [53]. This is the interpretation given by Schülke et al. [54] by using a model. The Fano resonance would result from the interaction of the silicon plasmon ~ 17 eV discrete excitation (see the $q \approx 0$ EELS in Figure 5) with the continuum of electron–hole excitations. In Figure 9 we can see that TDLDA is in a quantitative agreement with the experiment in the low-energy range and up to 22 eV. The 17 eV asymmetric feature is perfectly reproduced by TDLDA. This is also the case for the RPA LF result, apart from an underestimation of the spectral intensity. On the other hand, we observe a peak at 17 eV in the RPA NLF result, but we do not observe the characteristic asymmetry with the following steep rise. We can see that local-fields related to nondiagonal elements of the microscopic dielectric matrix play an important role in the Fano mechanism.

Finally, we observe that the TDLDA result starts to present deviations from the experiment beyond 22 eV. We observe well-defined peaks, which are however in correspondence to perceptible structures in the experiment. This disagreement has been attributed to lifetime effects [51] that in principle are accounted by the exact exchange–correlation kernel f_{xc} of TDDFT but not by the TDLDA approximation. An approximative inclusion of such effects, as by introducing a Fermi-liquid imaginary part to the single-particle energies or by adding an equivalent non-Hermitian kernel f_{xc}^{LF} [51], would produce a better result like the TDLDA + Lifetime spectrum of Figure 9. From the present example we can conclude that the adiabatic LDA approximation can al-

ready bring an important part of exchange-correlation effects but of course presents its limits. One of them is certainly the lack of lifetime effects.

We can think that the very good performances of TDDFT on the energy-loss function and related observables we have shown so far are restricted only to particularly simple systems, like silicon, graphite, and graphene. We may wonder about the limits and a breakdown of TDDFT on a more complex system, like, for example, strongly-correlated systems. In reality, TDDFT is in principle an exact theory to calculate *neutral* excitation and optical/energy-loss spectra. This is granted by the Runge–Gross theorem and all the formal developments of the theory. So exact, nonapproximated TDDFT is able to describe energy-loss spectra no matter the condensed matter system. However, we might ask about the limits of the adiabatic LDA approximation and a breakdown of TDLDA on more complex systems. High-temperature superconductors cuprates can certainly be considered a severe workbench to check the validity of TDLDA. The cuprate pairing mechanism allowing such high critical temperatures is so far unknown, albeit 30 years of theoretical efforts. A large part of the scientific community believes that the pairing mechanism and superconductivity are related to a strong correlation physics. They certainly show a nonconventional, not yet explained physics. Checking the validity of TDLDA on the energy-loss function of cuprates can represent a severe workbench for the ALDA approximation. The energy-loss function is in particular related to the screening of the system and so also to antiscreening ranges where the pairing is going to occur. So, study of the energy-loss function and of the screening is not even a marginal one for the purpose of understanding superconductivity mechanisms.

In Figure 10, we report the dynamic structure factor $S(q, \omega)$ of YBCO ($\text{YBa}_2\text{Cu}_3\text{O}_7$) as a function of exchanged energy and momentum [55]. The experimental $S(q, \omega)$ has been measured by an IXSS experiment at the European Synchrotron Radiation Facility (ESRF) on a YBCO sample in the normal phase. The theoretical spectra are TDDFT calculations in the RPA with local field effects and ALDA (TDLDA) approximations. Already at a first look, the complexity and the physical richness of this system are immediately evident. We cannot enter into the detailed interpretation of all the excitations in YBCO, like we did for graphite, and their effect on the dielectric screening. This can be found in the original reference [55]. Here we just only report that even in YBCO the TDLDA approximation does not breakdown and is perfectly able to describe and interpret almost all excitations together with their dispersion in the experimental dynamic structure factor (apart from the energy region D+E in the figure, for which a discussion is provided in [55]). Although the spectra reported here and in Ref. [55] refer to the normal, nonsuperconducting phase of YBCO, it can nevertheless be considered a success of TDDFT. Manifestations of a nonconventional physics are indeed already present in the normal phase, and the whole phase diagram of cuprates still awaits for a coherent explanation.

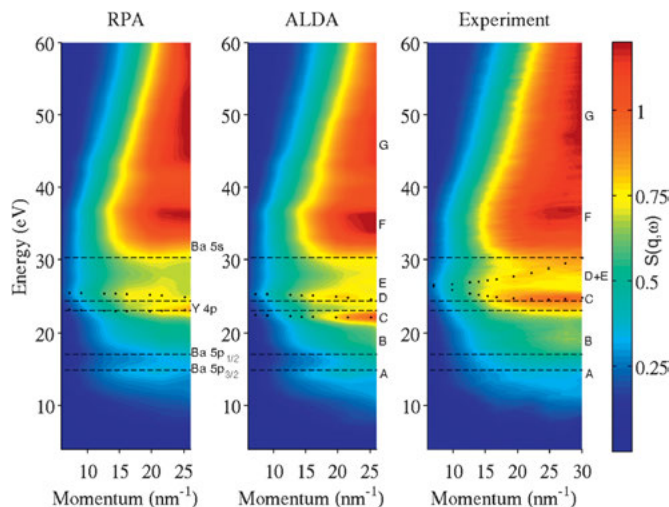


Figure 10: Inelastic X-ray scattering spectra (IXSS) in YBCO (Ref. [51]). The dynamic structure factor $S(q, \omega)$ is plot in false colors (rightmost bar) as a function of exchanged momentum and energy. The first two panels refer to TDDFT calculations of $S(q, \omega)$ in the RPA (with local field effects) and ALDA (TDLDA) approximations, whereas the third is the IXSS experiment taken at the European synchrotron radiation facility (ESRF). The most prominent spectral features are labeled A-G on the ALDA and experimental plots. The nominal core-electron excitation energies are marked with dashed lines and labeled in the RPA plot. The dispersion of features C and D are marked with dots as a guide for the eye.

13 Optical spectroscopy: TDLDA drawbacks

We begin this section by presenting an example of application to the study of optical properties where TDDFT and theory brought an important contribution: the study of the optical visual degradation of Leonardo Da Vinci's iconic self-portrait (Figure 11, [56, 57]). Diagnostic studies of the state of conservation and degradation causes and rates of artworks are an invaluable information for conservators and restorers to establish the best conditions for their public enjoy, if suitable, or to plan possible restorations. Access to the most precious or most degraded artistic heritage by intrusive and destructive experimental techniques is very often refused by art critics and operators. This was the case of the Leonardo Da Vinci's self-portrait, red chalk on paper, nowadays not anymore exposed to public and external agents. For a diagnostic study of its conservation state, the acquisition of optical spectra by only reflection under exposure to ordinary (nonintense and noncoherent) light were solely agreed. Without the possibility of an ordinary chemical analysis of a small piece of the artwork or other experimental manipulations, resort to theory was the only possibility to characterize the state of degradation of the masterpiece.

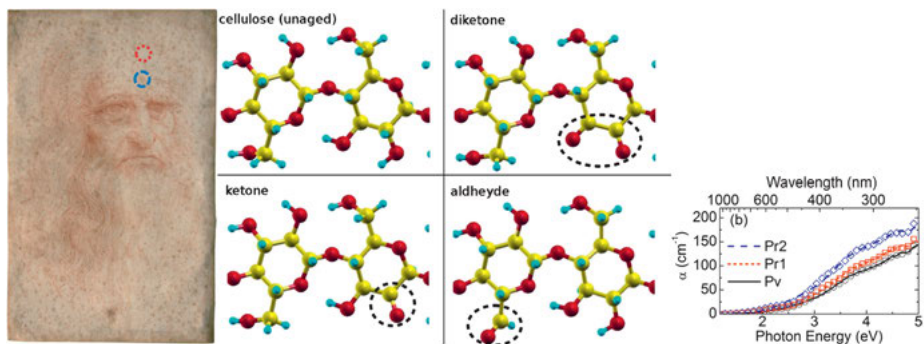


Figure 11: Experimental (lines) and TDDFT theoretical (symbols) optical absorption spectra (right) of three spots on Leonardo Da Vinci's iconic self-portrait (left, Pr2 in blue, Pr1 in red, Pv in black and taken on the back side of the portrait). The atomic structure of pristine cellulose and three representative oxidized groups (evidenced by dashed circles) of aged cellulose, diketone, ketone, and aldehyde is shown in the middle panel. Reproduced from Figures 1, 2, and 3 of [56] with the permission of AIP Publishing.

TDDFT optical spectra calculations by the DP code were carried out for pristine cellulose, main component of paper, and several products of cellulose ageing, oxidized groups such as diketone, ketone, and aldehyde (some of them shown in Figure 11) that act as chromophores and are responsible for the yellowing of cellulose. Theoretical TDDFT spectra were calculated and then used as a reference to characterize experimental spectra measured at different spots on the artwork, chosen to explore the largest range of its conservation state, from the best conserved to the most degraded points (indicated on the portrait in Figure 11). A linear combination of TDDFT spectra corresponding to single oxidized groups was determined by a best fit with the experimental spectra. The linear coefficients of the fit provided an estimate of the concentration of chromophores responsible for paper ageing and made it possible to obtain chemical information of the artwork by nondestructive and nonintrusive optical measures. This has allowed us to establish the present status of the masterpiece – to be compared with future analysis for a measure of the degradation rate – and the main causes of degradation along the artwork history, e.g., moisture, to be carefully avoided in any future conservation program.

The very good match between TDDFT and measured spectra in Figure 11 is effective, i.e., we cannot obtain it by simply adjusting the fitting coefficients in a linear combination of spectra of other chromophores or completely different materials that are certainly absent from the artwork [56, 57]. We can be surprised by the accuracy of TDDFT calculations that were carried out using the adiabatic local-density approximation (ALDA or TDLDA). As we will illustrate in the following, TDLDA present severe drawbacks on optical spectra of infinite bulk solids, like, for example, an underestimation of the optical absorption onset. For instance, the TDLDA gap of bulk cellulose was found to be 5.15 eV, whereas cellulose does not absorb light above 200 nm (below

6 eV). However, the yellow color seen in aged paper is mainly due to oxidized cellulose chromophores, absorbing below 5 eV and in the highest energy band of visible light, violet and blue, and continuing to scatter lowest energy yellow and red photons. These absorption peaks are due to transitions between electronic states that are localized around the oxidized groups, in practice to be considered as defects of the cellulose bulk crystal. So, the orbitals involved in this range of the optical spectrum and in these transitions are very much localized on the chromophore defects and do not mix with delocalized periodic Bloch states. A local exchange-correlation approximation can be expected to work reasonably well in these situations, and this explains the good results obtained by Refs. [56, 57]. So, on optical spectra of defects, like also in isolated systems as atoms or molecules, TDLDA works reasonably well and much better than in periodic solids, as we will see in the next example.

TDDFT is an in principle exact theory to calculate all neutral excitations and so also optical spectra. The question is whether the most common TDDFT approximations RPA and TDLDA are good enough to capture the physics of excitations of, e.g., optical absorption. Figure 12 presents the experimental imaginary part of the macroscopic dielectric function $\Im\epsilon(\omega)$ (red dots), directly related to the optical absorption, measured by the ellipsometry experiment of Ref. [58] in bulk silicon. In the same figure, we show TDDFT calculations, as by the DP code [41], of the RPA with and without LF effects and TDLDA spectra. We remark “some” qualitative agreement of TDDFT with the experiment: we observe in the experiment three peaks, at 3.5, 4.3, and 5.3 eV, which

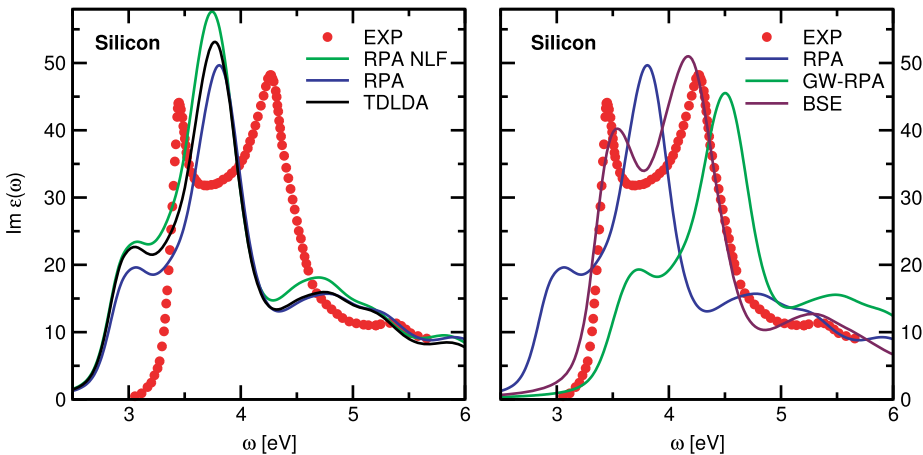


Figure 12: Optical absorption in silicon. Left (reproducing Figure 2 of Ref. [42]): Imaginary part of the macroscopic dielectric function in the RPA without (NLF, green dot-dashed line) and with local-field effects (blue dashed line), TDLDA (black continuous line), ellipsometry experiment (red dots from Ref. [58]). Right (reproducing Figure 1 of Ref. [59]): Imaginary part of the macroscopic dielectric function in the RPA (blue dashed line), GW-RPA (green dot-dashed line), Bethe–Salpeter equation approach (BSE, brown continuous line), ellipsometry experiment (red dots from Ref. [58]).

are more or less reproduced by three structures in the theory, whether in the RPA or TDLDA approximation. Comparing RPA curves with LF and without them (NLF), local-field effects seem to have the same weight as exchange-correlation effects. We also remark that there is no improvement in going from the RPA to the TDLDA approximation. The agreement with the experiment is unsatisfactory for two reasons:

- (1) The TDLDA (or RPA) optical onset appears red-shifted by ~ 0.6 eV with respect to the experiment. Not only the onset, but also the whole spectrum seems rigidly red-shifted with respect to the experiment by those 0.6 eV.
- (2) The height of the first lowest energy peak seems underestimated by the theory with respect to the experiment. Both in RPA and TDLDA, this peak appears like a shoulder of the main peak, whereas in the experiment, it is of almost the same height. Nevertheless, we remark some agreement between theory and experiment on the height of the second and third highest energy peaks.

The cause of the first problem seems quite easy to trace. Indeed, 0.6 eV is exactly the band gap underestimation of the DFT-LDA Kohn–Sham electronic structure with respect to the true, quasiparticle electronic structure in silicon. A quasiparticle self-energy calculation, as in the GW approximation [60, 61] within the framework of many-body perturbation theory, takes into account in a satisfactory way correlation electron–electron (e – e) interaction effects and corrects the DFT band gap underestimation. A GW-RPA spectrum, calculated using an RPA approximation on top of a GW electronic structure, appears blue-shifted with respect to the KS-RPA spectrum by a 0.6 eV (see the GW-RPA curve in Figure 12, right). GW-RPA improves on the position of the optical onset and all other structures. The remaining discrepancies with the experiment, in particular the underestimation of the first low-energy peak, have to be ascribed to electron–hole (e – h) interaction effects still missing in the GW-RPA approximation to the polarizability. Inclusion of e – h interaction diagrams to the polarizability (vertex corrections), as by solution of the Bethe–Salpeter equation (BSE) within the framework of many-body perturbation theory, fully captures all the physics involved in optical spectroscopy. This is demonstrated by a BSE calculation [59] of the silicon optical absorption. The BSE curve (Figure 12, right) corrects the underestimation of the first peak and is in good agreement with the experiment.

Apparently, BSE seems also to slightly blue-shift the GW-RPA spectrum. However, accurate verification of results [59] has shown that in silicon there is negligible (<0.1 eV) BSE correction to GW excitation energies. The first absorption peak in silicon is not really a bound exciton, i.e., an electron–hole bound state. Nevertheless, its strength is strongly determined by electron–hole interaction (excitonic) effects. So the reshape of the spectrum from GW-RPA (without e – h) to BSE (with e – h interaction effect) is just only a redistribution of oscillator strength from high to low energies. This transfer of oscillator strength from high to low energy is the typical e – h interaction *excitonic effect* in small band-gap semiconductors. In these systems the screening is intermediate between metals and insulators.

The effect of e - h interactions is much more spectacular in large band-gap insulators, where interactions are almost unscreened. An electron promoted by a photon into a conduction state interacts strongly with the hole left in the valence band, so that they can be bound into an *exciton* at an energy level lower than a pair of free electron and hole. In the optical absorption spectrum, excitons appear as discrete peaks at an energy lower than the band-gap, which corresponds to the onset of the continuum of electron-hole pairs. This is particularly evident in solids of rare gas elements.

In Figure 13, we report the experimental [62] optical absorption spectrum (red dots) of solid argon. The band-gap in solid argon is 14.2 eV, and the dielectric constant is very close to 1. At a low energy, we observe discrete peaks, which are available optical excitations of the system within the band-gap: this is a whole series of bound excitons due to e - h interaction effects. The energy difference between the band-gap/onset of the continuum and the exciton is defined as the *exciton binding energy*. In solid argon the binding energy of the first exciton is up to 2 eV, among the largest exciton binding energies. In Figure 13, we present also TDDFT spectra. Both the RPA and the TD-LDA approximations miss completely the excitons and produce an unsatisfactory result, unlike silicon far to be even qualitative. Within many-body perturbation theory the GW-RPA approximation corrects the onset of the continuum, aligning it to the band-gap energy, but still misses the excitons. Only the Bethe-Salpeter equation introduces the right physics to capture excitons. In the optical absorption of solid argon the BSE correction to GW-RPA is spectacular.

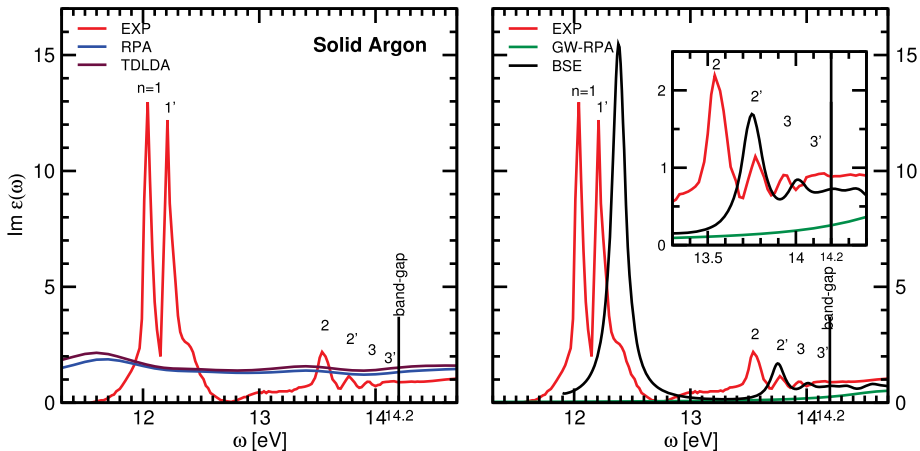


Figure 13: Optical absorption in solid argon (from Ref. [63]). Left: red line, experiment; blue dashed line, RPA; brown continuous line, TD-LDA. Right: red line, experiment; dot-dashed green line, GW-RPA; black continuous line, Bethe-Salpeter equation result. There are two exciton series, the spin triplet n and the singlet n' . Nonspin-polarized calculations are supposed to reproduce only the spin singlet n' series. The band-gap is 14.2 eV in argon.

Within many-body perturbation theory, the Bethe–Salpeter equation on top of the GW approximation proved to contain the right many-body physics to describe optical properties of condensed matter systems. On the other hand, within TDDFT, the RPA and also the ALDA approximations do not contain such many-body physics. Note that this is a drawback of the approximations, not of TDDFT, which is in principle an exact theory for optical excitations. The problem is that the ALDA approximation is missing some important characteristics of the *exact* xc kernel directly related to e – h interaction effects.

14 Beyond TDLDA: long-range contribution (LRC) kernel and developments

Both in solid argon and in silicon (Figures 12 and 13), we have seen that the TDLDA optical absorption is almost coincident with the RPA. A local kernel like ALDA has in practice no effect. This can be explained by the following argument [41]: the xc kernel appears in equation (19) only in a term $\chi^{\text{KS}} f_{\text{xc}}$, where it is coupled to the Kohn–Sham polarizability χ^{KS} . In the optical limit as $q \rightarrow 0$, the Kohn–Sham polarizability goes to zero as $\lim_{q \rightarrow 0} \chi^{\text{KS}}(q) \sim q^2 \rightarrow 0$, as it can be seen from equation (33) and from the fact that $\rho_{ij}^{\text{KS}}(q) \sim q \rightarrow 0$. A local kernel like ALDA behaves as a constant as $q \rightarrow 0$, $\lim_{q \rightarrow 0} f_{\text{xc}}^{\text{ALDA}} = \text{const}$, so that the term $\lim_{q \rightarrow 0} \chi^{\text{KS}} f_{\text{xc}}^{\text{ALDA}} = 0$ goes to zero in the optical limit. This explains why ALDA results cannot differ from taking *tout court* $f_{\text{xc}} = 0$, like in RPA. To depart from RPA, we have to consider xc kernels containing nonlocal contributions. First attempts having introduced semilocal or short-range nonlocality [42, 41] proved to be still not sufficient. The true exact kernel of insulators and semiconductors must contain an *ultranonlocal*, long-range $1/q^2$ Coulomb-like contribution. In the optical limit an ultranonlocal kernel diverges, $\lim_{q \rightarrow 0} f_{\text{xc}} = \infty$, in such a way to have a finite contribution from the $\chi^{\text{KS}} f_{\text{xc}}$ term. This is the only way for an xc kernel to produce in the optical limit a departure from the RPA $f_{\text{xc}} = 0$ approximation [64].

A first step toward the solution of TDLDA drawbacks on optical excitations in semiconductors and insulators was the introduction of the so-called long-range contribution (LRC) only, also dubbed α/q^2 kernel for its mathematical shape in reciprocal space [41, 65],

$$f_{\text{xc}}^{\text{LRC}}(q) = \frac{\alpha}{q^2}. \quad (34)$$

Here α is a material-dependent parameter that should reduce to zero in metals and in jellium (homogeneous electron gas) model, which is known not to present an LRC contribution in its kernel. From its real space expression

$$f_{\text{xc}}^{\text{LRC}}(r, r') = \frac{\alpha}{4\pi|r - r'|}, \quad (35)$$

it can be seen that this kernel contains an ultranlocal, i.e., a long-range Coulomb-like contribution. This is an important difference with respect to the local ALDA kernel (25), but also with respect to nonlocal or semilocal kernels [42]. As we will see, this is the characteristics that must be owned by the true exact xc kernel of insulators and semiconductors to properly account for $e-h$ interaction and, more generally, many-body effects.

When introducing a kernel of the form α/q^2 [64], the optical absorption (TDDFT KS-LRC curve in Figure 14) finally starts to differ appreciably from RPA and TDLDA. We observe a redistribution of spectral weight from low to large energies when taking a positive LRC ($\alpha > 0$). At increasing α , the first peak is more and more damped, until we can achieve a situation where the optical onset arises at larger energies, thus correcting the Kohn–Sham band-gap underestimation. However, for a kernel of the simple only one-parameter form α/q^2 , it is difficult to correct both RPA drawbacks, i.e., the underestimation of the optical onset (lack of $e-e$ interaction effects) and the underestimation of the low-energy spectral weight (lack of $e-h$ excitonic effects). Of course, the true exact kernel should correct the Kohn–Sham independent particle polarizability χ^{KS} for *both* effects. In general the kernel can always be split into two components:

$$f_{\text{xc}} = f_{\text{xc}}^{e-e} + f_{\text{xc}}^{e-h}. \quad (36)$$

The first component introduces $e-e$ self-energy effects and brings the Kohn–Sham polarizability χ^{KS} to a quasiparticle GW-RPA polarizability χ^{QP} :

$$\chi^{\text{QP}} = \chi^{\text{KS}} + \chi^{\text{KS}} f_{\text{xc}}^{e-e} \chi^{\text{QP}}, \quad (37)$$

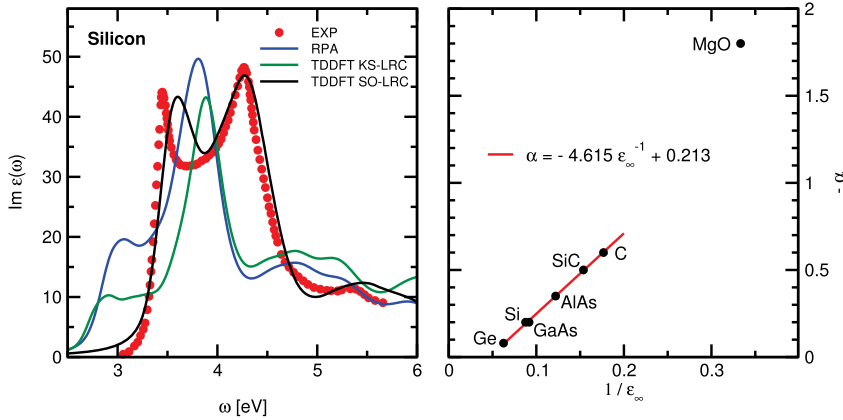


Figure 14: Optical absorption in silicon. Imaginary part of the macroscopic dielectric function in the LRC on top of χ^{KS} (green dot-dashed line, reproducing with higher convergence solid line of Figure 6.5 in Ref. [41]), LRC on top of χ^{QP} (black continuous line, reproducing Figure 1 of Ref. [65]), TDDFT RPA (blue dashed line), and ellipsometry experiment (red dots from Ref. [58]). Right: Relationship $|\alpha|$ parameter (y-axis) dielectric constant ϵ_∞^{-1} (x-axis) (reproducing Figure 12 of Ref. [67]) for several materials.

whereas the second term introduces e - h excitonic effects and leads to the final full polarizability χ :

$$\chi = \chi^{\text{QP}} + \chi^{\text{QP}}(w + f_{\text{xc}}^{e-h})\chi. \quad (38)$$

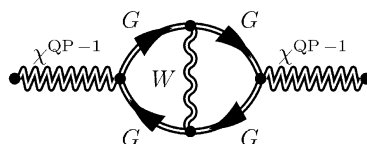
In practice [65], we can skip the first step and directly calculate χ^{QP} by the Adler–Wiser formula (18), using a rigid *scissor operator* (SO) correction of Kohn–Sham conduction energies with respect to valence. The SO correction can be adjusted to the ab initio GW band-gap correction, which is in a good agreement with experimentally measured band-gaps. This should provide a result close to the GW-RPA spectrum of Figure 12. The remaining task of introducing e - h excitonic effects is then taken by an $f_{\text{xc}}^{e-h} = f_{\text{xc}}^{\text{LRC}} = \alpha/q^2$ long-range contribution kernel. This term has the task to transfer oscillator strength in the backward direction, from high to low energies, exactly like BSE on top of GW (Figure 12). This is done by a negative divergence, $\alpha < 0$.

The result of this TDDFT SO-LRC approach [65] is presented for silicon in Figure 14. The TDDFT SO-LRC is in practice as good as the Bethe–Salpeter result with respect to the experiment, but at a much cheaper computational cost. The BSE and LRC kernels seem to reproduce the same physics, i.e., the transfer of spectral weight from high to low energy, characteristic of excitonic effects in intermediate screening semiconductors. The amplitude of the transfer is modulated by the parameter α , and the direction is due to its negative sign. The strength α of the divergency should be inversely proportional to the screening in the system. The smaller the screening (large band-gap insulators), the larger α . α is expected to be 0 for metals (e - h interaction fully screened). In fact, it can be found that an α provided by the linear expression

$$\alpha = -4.615\varepsilon_{\infty}^{-1} + 0.213 \quad (39)$$

(see also Figure 14), where ε_{∞} is the dielectric constant of the material, either experimental or RPA (with some correction to the coefficients), can provide results close to the BSE approach and in a good agreement with the experiment. For silicon, we have $\alpha \simeq -0.2$.

This approximation provides a good result for semiconductors and small bandgap insulators like diamond, but it breaks down for large band-gap insulators (e.g., MgO) and in particular in systems presenting more than one bound exciton. We can further complicate the LRC expression, introducing more than one parameter or a frequency dependence [68, 69] and have some improvement but at the cost of more and more empirical expressions. Following a less empirical route and by reverse engineering from the Bethe–Salpeter equation, we can derive an expression of the TDDFT xc kernel related to the BSE kernel $\Xi = W$, where $W = \varepsilon^{-1}w$ is the screened Coulomb interaction. This kernel, the dubbed *Nanoquanta kernel* (NQ) [65, 66, 70–75] can be written in a diagrammatic condensed form as

$$f_{xc} = \chi^{QP-1} G G W G G \chi^{QP-1} =$$


where G is the Green function, i.e., the electron (forward) or the hole (backward arrow) propagator. This kernel is rooted into the Bethe–Salpeter kernel $\Xi = W$, which introduces an interaction between the electron and the hole (the wiggly line between the electron and hole propagators). When plugged into the TDDFT equation (19), the NQ kernel must provide by construction the same result as the Bethe–Salpeter equation.

The Nanoquanta kernel result [63] for solid argon is presented in Figure 15. Like the Bethe–Salpeter kernel (Figure 13), the NQ kernel is able to reproduce the complete series of three peaks associated with bound excitons in argon, whereas RPA, TDLD, and GW-RPA fail. Note that this Nanoquanta approach has addressed also the other xc kernel f_{xc}^{e-e} term responsible for the $e-e$ interaction self-energy effects. This has demonstrated that a full TDDFT kernel, able to account for both $e-e$ and $e-h$, exists and can be calculated, though with a computational effort not much cheaper than the many-body GW and BSE approaches.

More recent developments have tried to improve upon the Nanoquanta and LRC kernels by following self-consistent approaches [76], by relying on beyond LDA, e.g., meta-GGA functionals within pure TDDFT [77, 78], and finally, relying on approxima-

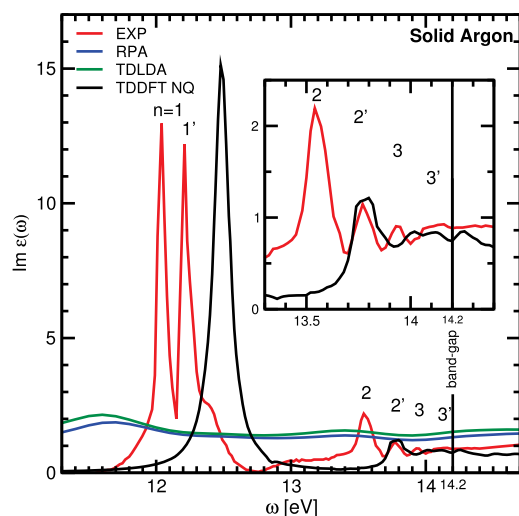


Figure 15: Optical absorption in solid argon (from Ref. [63]). Red line: experiment; blue dashed line: RPA; green dot-dashed line: TDLD; black continuous line: Nanoquanta (NQ) kernel. There are two exciton series, the spin triplet n and the singlet n' . Nonspin-polarized calculations are supposed to reproduce only the spin singlet n' series. The band-gap is 14.2 eV in argon.

tions beyond LDA and not routed anymore into the jellium model, toward, e.g., the jellium-with-gap model [79].

15 Outlook and conclusions

We have provided a simple but necessarily incomplete introduction to TDDFT, reviewing just only the main issues and some of the problems still awaiting for a solution. Among the main challenges still in front, we can mention: the description of the Rydberg series in atoms (Section 9); double excitations in molecules [80], where two electrons are promoted to excited states, which questions the validity of the adiabatic approximation; charge-transfer excitations in organic molecules, that is, excitations where the electron and hole wavefunctions have small or no overlap; conical intersections in photochemistry reaction paths (Section 10), where the Born–Oppenheimer approximation is under question; memory effects in the electron and ion dynamics (Section 10); many-body effects in optical spectra of solids (Section 14). All these are problems of the approximations to the exchange-correlation functional, not of TDDFT theory itself. As illustrated at the example of optical spectra, developments beyond standard approximations (e.g., adiabatic LDA, GGA, etc.) have the potentiality to cure or alleviate these problems. For more complete reviews of TDDFT problems, challenges, developments, and perspectives, we refer to Refs. [81, 82] and references therein.

We have provided only a few examples where the vast majority of TDDFT applications mainly lie, excitations and spectroscopy in the linear response regime, and where also standard approximations work better. We have also shown some examples of beyond-linear electron and even ion dynamics (Section 10), out of the few nonlinear TDDFT applications available in the literature. We would like to mention here very recent applications of TDDFT to nonlinear optics [83, 84], allowing the access to multiple photon excitations by intense lasers, second harmonic generation, and providing spectra in a good agreement with experiments. Next years experimental developments going in the direction to have more intense and coherent laser and X-ray sources (like the XFEL facility in Hamburg), with improved spatial resolution and with pump and probe setups allowing the study of the time evolution with a resolution achieving the femtosecond and below, will certainly stimulate TDDFT developments and applications in the same direction. The dynamics of the fragmentation of the ethene molecule (Section 10) is today an isolated but promising example of what TDDFT can do in the next years to supplement future experiments, understand mechanisms beyond physical, chemical, and even biological processes, and finally achieve the power of prediction toward the engineering of new materials, for example, in photovoltaics.

Bibliography

- [1] P. Hohenberg and W. Kohn. Inhomogeneous electron gas. *Phys. Rev.*, 136:B864, 1964.
- [2] W. Kohn and L. J. Sham. Self-consistent equations including exchange and correlation effects. *Phys. Rev.*, 140:A1133, 1965.
- [3] E. Runge and E. K. U. Gross. Density-functional theory for time-dependent systems. *Phys. Rev. Lett.*, 52:997, 1984.
- [4] E. K. U. Gross and W. Kohn. Local density-functional theory of frequency-dependent linear response. *Phys. Rev. Lett.*, 55:2850, 1985.
- [5] S. Kurth, G. Stefanucci, C.-O. Almbladh, A. Rubio, and E. K. U. Gross. Time-dependent quantum transport: a practical scheme using density functional theory. *Phys. Rev. B*, 72:035308, 2005.
- [6] N. T. Maitra, T. N. Todorov, C. Woodward, and K. Burke. Density-potential mapping in time-dependent density-functional theory. *Phys. Rev. A*, 81:042525, 2010.
- [7] T. K. Ng and K. S. Singwi. Time-dependent density-functional theory in the linear-response regime. *Phys. Rev. Lett.*, 59:2627, 1987.
- [8] R. van Leeuwen. Key concepts in time-dependent density-functional theory. *Int. J. Mod. Phys. B*, 15:1969, 2001.
- [9] M. Levy. Electron densities in search of Hamiltonians. *Phys. Rev. A*, 26:1200, 1982.
- [10] H. Kohl and R. M. Dreizler. Time-dependent density-functional theory: conceptual and practical aspects. *Phys. Rev. Lett.*, 56:1993, 1986.
- [11] S. K. Ghosh and A. K. Dhara. Density-functional theory of many-electron systems subjected to time-dependent electric and magnetic fields. *Phys. Rev. A*, 38:1149, 1988.
- [12] M Ruggenthaler, M. Penz, and R. van Leeuwen. Existence, uniqueness, and construction of the density-potential mapping in time-dependent density-functional theory. *J. Phys. Condens. Matter*, 27:203202, 2015.
- [13] R. van Leeuwen. Causality and symmetry in time-dependent density-functional theory. *Phys. Rev. Lett.*, 80:1280, 1998.
- [14] M. Petersilka, U. J. Gossmann, and E. K. U. Gross. Excitation energies from time-dependent density-functional theory. *Phys. Rev. Lett.*, 76:1212, 1996.
- [15] T. Ando. Inter-subband optical-absorption in space-charge layers on semiconductor surfaces. *Z. Phys. B*, 26:263, 1977.
- [16] T. Ando. Inter-subband optical-transitions in a surface space-charge layer. *Solid State Commun.*, 21:133, 1977.
- [17] A. Zangwill and P. Soven. Density-functional approach to local-field effects in finite systems: photoabsorption in the rare gases. *Phys. Rev. A*, 21:1561, 1980.
- [18] A. Zangwill and P. Soven. Resonant photoemission in barium and cerium. *Phys. Rev. Lett.*, 45:204, 1980.
- [19] S. L. Adler. Quantum theory of the dielectric constant in real solids. *Phys. Rev.*, 126:413, 1962.
- [20] N. Wiser. Dielectric constant with local field effects included. *Phys. Rev.*, 129:62, 1963.
- [21] D. J. Thouless. Vibrational states of nuclei in random phase approximation. *Nucl. Phys.*, 22:78, 1961.
- [22] D. J. Rowe. Equations-of-motion method and the extended shell model. *Rev. Mod. Phys.*, 40:153, 1968.
- [23] M. E. Casida. Time-dependent density functional response theory for molecules. In D. E. Chong (Ed.), *Recent Advances in Density Functional Methods*. Recent Advances in Computational Chemistry, volume 1, page 155. World Scientific, Singapore, 1995.
- [24] M. E. Casida. Time-dependent density functional response theory of molecular systems: theory, computational methods, and functionals. In J. M. Seminario (Ed.), *Recent Developments and Application of Modern Density Functional Theory*, page 391. Elsevier, Amsterdam, 1996.

- [25] A. Kono and S. Hattori. Accurate oscillator strengths for neutral helium. *Phys. Rev. A*, 29:2981, 1984.
- [26] V. Olevano et al. <http://www.dp-code.org>, 2005–2017.
- [27] X. Gonze et al. <http://www.abinit.org>, 1998–2017.
- [28] J. K. Dewurst, S. Sharma, et al. <http://elk.sourceforge.net/>, 2017.
- [29] M. A. L. Marques, A. Castro, G. F. Bertsch, and A. Rubio. Octopus: a first-principles tool for excited electron-ion dynamics. *Comput. Phys. Commun.* 151:60, 2003.
- [30] C. J. Umrigar and X. Gonze. Accurate exchange-correlation potentials and total-energy components for the helium isoelectronic series. *Phys. Rev. A*, 50:3827, 1994.
- [31] M. Petersilka, E. K. U. Gross, and K. Burke. Excitation energies from time-dependent density-functional theory using exact and approximate potentials. *Int. J. Quant. Chem.*, 80:534, 2000.
- [32] T. Burnus, M. A. L. Marques, and E. K. U. Gross. Time-dependent electron localization function. *Phys. Rev. A*, 71:010501, 2005.
- [33] T. Burnus, M. A. L. Marques, and E. K. U. Gross. Time-dependent quantum transport: a practical scheme using density functional theory. *Phys. Rev. A*, 71:010501, 2005. Acetylene molecule excitation movie, Supplemental Material, <http://journals.aps.org/pr/supplemental/10.1103/PhysRevA.71.010501/C2H2.mpeg>.
- [34] A. D. Becke and K. E. Edgecombe. A simple measure of electron localization in atomic and molecular systems. *J. Chem. Phys.*, 92:5397, 1990.
- [35] T. Burnus, M. A. L. Marques, and E. K. U. Gross. Time-dependent electron localization function. *Phys. Rev. A*, 71:010501, 2005. Ethene molecule fragmentation movie, Supplemental Material, <http://journals.aps.org/pr/supplemental/10.1103/PhysRevA.71.010501/C2H4.mpeg>.
- [36] A. Castro, M. A. L. Marques, D. Varsano, F. Sottile, and A. Rubio. The challenge of predicting optical properties of biomolecules: what can we learn from time-dependent density-functional theory? *C. R. Phys.*, 10:469, 2009.
- [37] D. R. Yarkony. Diabological conical intersections. *Rev. Mod. Phys.*, 68:985, 1996.
- [38] W. Domcke, D. R. Yarkony, and H. K. Noppel, editors. *Conical Intersections: Electronic Structure, Dynamics and Spectroscopy*. World Scientific, Singapore, 2004.
- [39] L. Cederbaum. Born-oppenheimer approximation and beyond. In W. Domcke, D. R. Yarkony, and H. K. Noppel (Eds.), *Conical Intersections: Electronic Structure, Dynamics and Spectroscopy*, page 3. World Scientific, Singapore, 2004.
- [40] J. Stiebling. Optical properties of mono-crystalline silicon by electron energy-loss measurements. *Z. Phys. B*, 31:355, 1978.
- [41] V. Olevano. *Proprietà Dielettriche di Semiconduttori oltre l'Approssimazione di Densità Locale*. PhD thesis, Università di Roma “Tor Vergata”, Rome, 1999.
- [42] V. Olevano, M. Palummo, G. Onida, and R. Del Sole. Exchange and correlation effects beyond the LDA on the dielectric function of silicon. *Phys. Rev. B*, 60:14224, 1999.
- [43] V. Olevano and L. Reining. Excitonic effects on the silicon plasmon resonance. *Phys. Rev. Lett.*, 86:5962, 2001.
- [44] A. G. Marinopoulos, L. Reining, V. Olevano, A. Rubio, T. Pichler, X. Liu, M. Knupfer, and J. Fink. Anisotropy and interplane interactions in the dielectric response of graphite. *Phys. Rev. Lett.*, 89:076402, 2002.
- [45] A. G. Marinopoulos, L. Reining, A. Rubio, and V. Olevano. Ab initio study of the optical absorption and wave-vector-dependent dielectric response of graphite. *Phys. Rev. B*, 69:245419, 2004.
- [46] T. Eberlein, U. Bangert, R. R. Nair, R. Jones, M. Gass, A. L. Bleloch, K. S. Novoselov, A. Geim, and P. R. Briddon. Plasmon spectroscopy of free-standing graphene films. *Phys. Rev. B*, 77:233406, 2008.

- [47] A. G. Marinopoulos, L. Wirtz, A. Marini, V. Olevano, A. Rubio, and L. Reining. Optical absorption and electron energy loss spectra of carbon and boron nitride nanotubes: a first principles approach. *Appl. Phys. A*, 78:1157, 2004.
- [48] M. Bruno, M. Palumbo, A. Marini, R. Del Sole, V. Olevano, A. N. Kholod, and S. Ossicini. Excitons in germanium nanowires: quantum confinement, orientation, and anisotropy effects within a first-principles approach. *Phys. Rev. B*, 72:153310, 2005.
- [49] P. E. Trevisanutto, C. Giorgetti, L. Reining, M. Ladisa, and V. Olevano. Ab initio GW many-body effects in graphene. *Phys. Rev. Lett.*, 101:226405, 2008.
- [50] C. Kramberger, R. Hambach, C. Giorgetti, M. H. Rummeli, M. Knupfer, J. Fink, B. Büchner, L. Reining, E. Einarsson, S. Maruyama, F. Sottile, K. Hannewald, V. Olevano, A. G. Marinopoulos, and T. Pichler. Linear plasmon dispersion in single-wall carbon nanotubes and the collective excitation spectrum of graphene. *Phys. Rev. Lett.*, 100:196803, 2008.
- [51] H. C. Weissker, J. Serrano, S. Huotari, F. Bruneval, F. Sottile, G. Monaco, M. Krisch, V. Olevano, and L. Reining. Signatures of short-range many-body effects in the dielectric function of silicon for finite momentum transfer. *Phys. Rev. Lett.*, 97:237602, 2006.
- [52] K. Sturm, W. Schülke, and J. R. Schmitz. Plasmon-fano resonance inside the particle-hole excitation spectrum of simple metals and semiconductors. *Phys. Rev. Lett.*, 68:228, 1992.
- [53] U. Fano. Effects of configuration interaction on intensities and phase shifts. *Phys. Rev.*, 124:1866, 1961.
- [54] W. Schülke, J. R. Schmitz, H. Schulte-Schrepping, and A. Kaprolat. Dynamic and static structure factor of electrons in Si: inelastic x-ray scattering results. *Phys. Rev. B*, 52:11721, 1995.
- [55] S. Huotari, J. A. Soininen, G. Vankó, G. Monaco, and V. Olevano. Screening in YBCO at large wave vectors. *Phys. Rev. B*, 82:064514, 2010.
- [56] A. Mosca Conte, O. Pulci, M. C. Misiti, J. Lojewska, L. Teodonio, C. Violante, and M. Missori. Visual degradation in Leonardo da Vinci's iconic self-portrait: a nanoscale study. *Appl. Phys. Lett.*, 104:224101, 2014.
- [57] M. Missori, O. Pulci, L. Teodonio, C. Violante, M. C. Misiti, I. Kupchak, J. Bagniuk, J. Lojewska, and A. Mosca Conte. Optical response of strongly absorbing inhomogeneous materials: application to paper degradation. *Phys. Rev. B*, 89:054201, 2014.
- [58] P. Lautenschlager, M. Garriga, L. Viña, and M. Cardona. Temperature dependence of the dielectric function and interband critical points in silicon. *Phys. Rev. B*, 36:4821, 1987.
- [59] S. Albrecht, L. Reining, R. Del Sole, and G. Onida. Ab initio calculation of excitonic effects in the optical spectra of semiconductors. *Phys. Rev. Lett.*, 80:4510, 1998.
- [60] M. S. Hybertsen and S. G. Louie. First-principles theory of quasiparticles: calculation of band gaps in semiconductors and insulators. *Phys. Rev. Lett.*, 55:1418, 1985.
- [61] R. W. Godby, M. Schlüter, and L. J. Sham. Quasiparticle energies in GaAs and AlAs. *Phys. Rev. B*, 35:4170, 1987.
- [62] V. Saile, M. Skibowski, W. Steinmann, P. Gürtler, E. E. Koch, and A. Kozevnikov. Observation of surface excitons in rare-gas solids. *Phys. Rev. Lett.*, 37:305, 1976.
- [63] F. Sottile, M. Marsili, V. Olevano, and L. Reining. Efficient ab initio calculations of bound and continuum excitons in the absorption spectra of semiconductors and insulators. *Phys. Rev. B*, 76:161103(R), 2007.
- [64] V. Olevano. *Proprietà Dielettriche di Semiconduttori oltre l'Approssimazione di Densità Locale*. PhD thesis, Università di Roma "Tor Vergata", Rome, 1999, pp. 101 and 107.
- [65] L. Reining, V. Olevano, A. Rubio, and G. Onida. Excitonic effects in solids described by time-dependent density functional theory. *Phys. Rev. Lett.*, 88:066404, 2002.
- [66] F. Sottile, V. Olevano, and L. Reining. Parameter-free calculation of response functions in time-dependent density-functional theory. *Phys. Rev. Lett.*, 91:056402, 2003.

- [67] S. Botti, F. Sottile, N. Vast, V. Olevano, H. C. Weissker, L. Reining, A. Rubio, G. Onida, R. Del Sole, and R. W. Godby. Long-range contribution to the exchange-correlation kernel of time-dependent density-functional theory. *Phys. Rev. B*, 69:155112, 2004.
- [68] S. Botti, A. Fourreau, F. Nguyen, Y.-O. Renault, F. Sottile, and L. Reining. Energy dependence of the exchange-correlation kernel of time-dependent density functional theory: a simple model for solids. *Phys. Rev. B*, 72:125203, 2005.
- [69] R. Del Sole, G. Adragna, V. Olevano, and L. Reining. Long-range behavior and frequency dependence of exchange-correlation kernels in solids. *Phys. Rev. B*, 67:045207, 2003.
- [70] G. Adragna. *Ab initio calculation of the TDDFT exchange-correlation kernel for semiconductors and insulators*. PhD thesis, Università di Roma "Tor Vergata", Rome, 2002.
- [71] G. Adragna, R. Del Sole, and A. Marini. Ab initio calculation of the exchange-correlation kernel in extended systems. *Phys. Rev. B*, 68:165108, 2003.
- [72] I. V. Tokatly and O. Pankratov. Many-body diagrammatic expansion in a Kohn–Sham basis: implications for time-dependent density functional theory of excited states. *Phys. Rev. Lett.*, 86:2078, 2001.
- [73] U. von Barth, N. E. Dahlen, R. van Leeuwen, and G. Stefanucci. Conserving approximations in time-dependent density functional theory. *Phys. Rev. B*, 72:235109, 2005.
- [74] F. Bruneval, F. Sottile, V. Olevano, R. Del Sole, and L. Reining. Many-body perturbation theory using the density-functional concept: beyond the GW approximation. *Phys. Rev. Lett.*, 94:186402, 2005.
- [75] M. Gatti, V. Olevano, L. Reining, and I. V. Tokatly. Transforming nonlocality into a frequency dependence: a shortcut to spectroscopy. *Phys. Rev. Lett.*, 99:057401, 2007.
- [76] S. Sharma, J. K. Dewhurst, A. Sanna, and E. K. U. Gross. Bootstrap approximation for the exchange-correlation kernel of time-dependent density-functional theory. *Phys. Rev. Lett.*, 107:186401, 2011.
- [77] V. U. Nazarov and G. Vignale. Optics of semiconductors from meta-generalized-gradient-approximation-based time-dependent density-functional theory. *Phys. Rev. Lett.*, 107:216402, 2011.
- [78] V. U. Nazarov, G. Vignale, and Y.-C. Chang. Exact dynamical exchange-correlation kernel of a weakly inhomogeneous electron gas. *Phys. Rev. Lett.*, 102:113001, 2009.
- [79] P. E. Trevisanuto, A. Terentjevs, L. A. Constantin, V. Olevano, and F. Della Sala. Optical spectra of solids obtained by time-dependent density functional theory with the jellium-with-gap-model exchange-correlation kernel. *Phys. Rev. B*, 87:205143, 2013.
- [80] P. Elliott, S. Goldson, C. Canahui, and N. T. Maitra. Perspectives on double-excitations in TDDFT. *Chem. Phys.*, 391:110, 2011.
- [81] N. T. Maitra. Perspective: fundamental aspects of time-dependent density functional theory. *J. Chem. Phys.*, 144:220901, 2016.
- [82] K. Burke, J. Werschnik, and E. K. U. Gross. Time-dependent density functional theory: past, present, and future. *J. Chem. Phys.*, 123:062206, 2005.
- [83] E. Luppi, H. Hübener, and V. Vénier. Ab initio second-order nonlinear optics in solids: second-harmonic generation spectroscopy from time-dependent density-functional theory. *Phys. Rev. B*, 82:235201, 2010.
- [84] M. Grüning, D. Sangalli, and C. Attaccalite. Dielectrics in a time-dependent electric field: a real-time approach based on density-polarization functional theory. *Phys. Rev. B*, 94:035149, 2016.

Sébastien Pillet

Time-resolved structural analysis: probing condensed matter in motion

Keywords: time-resolved X-ray scattering

Introduction

Without any doubt, one of the most fundamental properties of a solid is its crystallographic structure. A thorough understanding of the physical properties of condensed matter requires a detailed mapping of the atomic structure and its dynamics over multiple length scales and different time scales. Several methods may provide a detailed description of the structural organization of matter, such as elastic scattering/diffraction of X-rays, neutrons or electrons, X-ray absorption spectroscopies (EXAFS and XANES), and magnetic resonance spectroscopies (NMR, NQR). X-ray diffraction is nowadays routinely applied through laboratory diffractometer setups run by X-ray tube or rotating anode sources, whereas synchrotron radiation facilities, owing to their wavelength tunability and high spatial and temporal coherence, afford additional possibilities of unique experiments such as resonant X-ray diffraction or coherent scattering.

In broad areas of physics, chemistry, and biology, there is a strong demand for a precise characterization of the geometric structure and its evolution in time with respect to the processes governed by this evolution. For instance, the reactivity and function of molecules and biomolecules are determined by the interplay between their electronic and geometric structures. Much of today's condensed matter physics is dominated by understanding and controlling the interplay between electrons, spins, and the underlying lattice, giving rise to various ordered/disordered states with remarkable physical properties. Imaging the dynamics of these three degrees of freedom at the molecular level is mandatory if a deep theoretical understanding of materials is to be achieved. As far as atomic configurations are concerned, the femtosecond vibration of molecular bonds sets a fundamental limit between different regimes. The structural dynamics of complex systems built from many atoms involve intermediates and transition states on a multidimensional energy landscape. In the solid state, the whole processes may cover 15 orders of magnitude in time (from femtoseconds to seconds) and more than seven orders of magnitude in space (from subangstroms to micrometers). Detailed information on the dynamic behavior of such systems may be provided by various time-resolved techniques that employ a pump-probe scheme in a very general sense. The pump is used to perturb the system from its equilibrium state, whereas the probe monitors the subsequent response of struc-

<https://doi.org/10.1515/9783110433920-005>

tural, electronic, or spin degrees of freedom. Depending on which degree of freedom is to be monitored, various time-resolved techniques have been developed over the last few decades. Time-resolved photoelectron spectroscopy allows for a mapping of the transient energy distribution of the electrons. Time-resolved optical spectroscopy (transmission, reflectivity, second harmonic generation) probes an optical response that is sensitive to carrier distribution, i.e., the electronic response of the solid after perturbation. Time-resolved vibrational spectroscopy (infrared or Raman) explores the potential energy landscape of the ground or excited states. Besides these techniques, time-resolved X-ray and electron scattering have the potential to monitor directly the atomic positions in real time and provide direct evidence for the atomic displacements as a function of time.

Figure 1 gives the time scales of a range of chemical and physical phenomena occurring in solution or in the crystalline phase. Electronic motions, exchange interactions between electronic spins, are the fastest processes in the femtosecond and sub-femtosecond regimes. Atomic motions and molecular vibrations occur on a slightly slower time scale (femtosecond to picosecond); for instance, the stretching vibration frequency of a carbonyl C=O chemical bond is of order 52 THz ($\sim 1720 \text{ cm}^{-1}$), so that it takes nearly 19 fs for completing one vibration period. Optical and acoustic phonons (lattice vibration), as well as vibrational cooling, occur on the picosecond time scale. Heat diffusion and thermal transfers in crystalline solids happen on the microsecond to millisecond time scale.

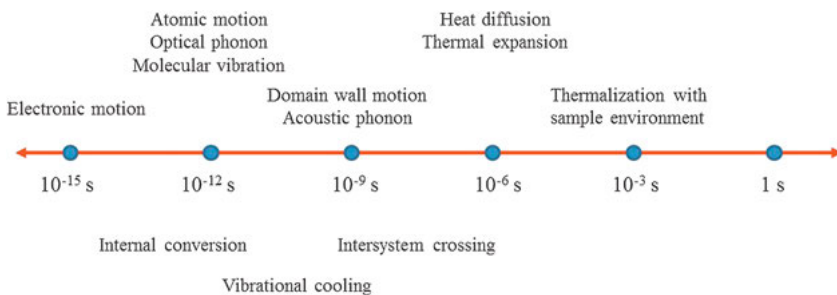


Figure 1: Timescales of various chemical and physical processes in solution and crystalline solids.

Crystalline materials correspond to a very special case characterized by a regular structural organization, periodic in space (translational invariance) and highly symmetric. The physical properties of crystals are defined by relations between measurable quantities, which for most of them (except mass and volume) have to be specified in direction and magnitude: crystals are intrinsically anisotropic, and their physical properties are described by tensors.

The central concern of this chapter may be formulated as follows: we are interested in the structural response of a solid while it is driven by an applied time-

dependent force that modifies its properties. By studying the response of the system, that is, how it evolves irreversibly toward a final state or recovers reversibly to the equilibrium state, we can learn important information on the system itself.

Figure 2 describes a very simple illustration of structural perturbation of a molecular crystalline solid built from diarylethene molecules, which exhibit an open-ring molecular conformation transformed to a closed-ring conformation upon ultraviolet ($\lambda = 365 \text{ nm}$) laser irradiation. This process has a purely molecular origin, but the photoinduced structural change triggers a microscopic local distortion of the crystal packing, which in turn transforms to a macroscopic single-crystal deformation: a square crystal with corner angles of 88° and 92° reversibly changes to a lozenge shape with corner angles of 82° and 98° . In parallel, the optical absorption change turns the crystal from transparent to blue.

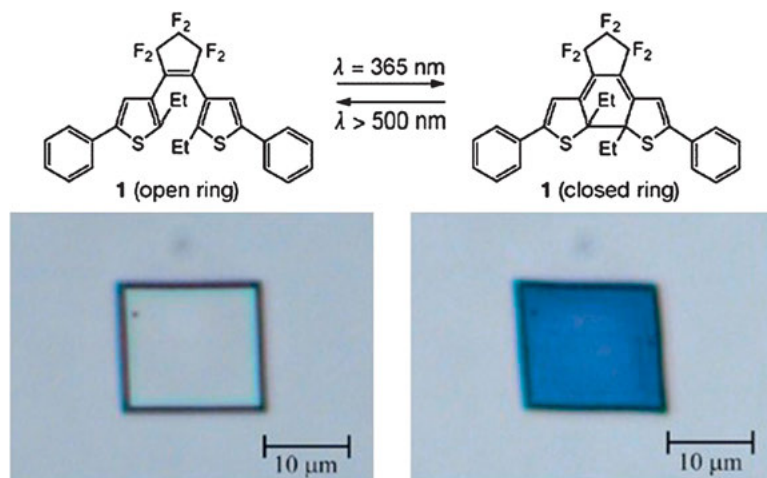


Figure 2: Modification of macroscopic physical properties associated to a photoinduced molecular structural change. The change from the open- to the closed-ring conformation of the 1,2-bis(2-ethyl-5-phenyl-3-thienyl)perfluorocyclopentene molecules in crystals upon ultraviolet laser irradiation triggers modifications of crystal shape and optical absorption [1]. Reprinted by permission from Macmillan Publishers Ltd, copyright (2007).

In this chapter, we describe the approaches developed to determine the evolution of the structural organization of matter in the time domain. We present the methods, instruments, and applications from various disciplines (physics, chemistry, biology) and perspectives. Hereafter, we restrict ourselves to X-ray scattering methods applied to crystalline and noncrystalline materials. X-rays are highly appropriate for probing the structural dynamics of matter for several reasons: (i) their short wavelength (nearly 1 \AA and below) is compatible with interatomic distances allowing a high spatial resolution to be achieved, (ii) they present high penetration depth in matter, and (iii) pulsed X-ray sources are readily available (synchrotron radiation and X-ray Free-

Electron Laser facilities). Progress in time-resolved X-ray scattering has closely followed the advances in X-ray sources and techniques over the years. The development of optical laser sources was certainly the very first breakthrough for fast time-resolved experiments. Over the last decades, the advent of third-generation synchrotron radiation facilities provided the brightest source of tunable X-rays, with pulse durations of the order of tens to hundreds of picoseconds. The setting up of table-top laser plasma sources in the late nineties delivered a real revolution opening the field to femtosecond time resolution, albeit with rather limited flux. More recently, the advent of X-ray Free-Electron Laser (XFEL) sources and slicing modes at synchrotrons already push the frontier of temporal and spatial resolution, with fantastic beam characteristics in terms of peak brightness, spatial coherence, and pulse duration, clearly opening a new area of ultrafast time-resolved X-ray scattering.

Structural dynamics is still at its infancy; many new open questions related to chemical, physical, or biological processes are still to be solved, facing important scientific and technological challenges. Time-resolved structural studies hold the promise of brilliant scientific advances in the time domain down to attoseconds for the near future.

This chapter is organized as follows. In Section 1, we introduce time in the general formalism of X-ray scattering of noncrystalline and crystalline systems. Experimental methods are detailed in Section 2. Selected examples of structural dynamics in solvated molecules, nanoparticles, and crystalline solids probed by time-resolved X-ray scattering techniques are described in Section 3.

1 Time-resolved X-ray scattering formalism for a driven sample

In this section, we derive general equations for time-resolved X-ray scattering. The formalism should be general enough to cover crystal, nanocrystal, or solution scattering with time resolution from femtosecond to second.

In a very general case (see the chapter *Static structural analysis of condensed matter*), X-rays are scattered by the electron density distribution of the sample, which is simply the sum of all the contributions of the N_{at} atoms at position \mathbf{r}_i constituting the entire probed sample:

$$\rho(\mathbf{r}) = \sum_{i=1}^{N_{\text{at}}} \rho_i(\mathbf{r} - \mathbf{r}_i). \quad (1)$$

In a first approximation, called the Independent Atom Model (IAM), the atomic electron density distribution $\rho_i(\mathbf{r} - \mathbf{r}_i)$ is considered spherical and unperturbed by the formation of interatomic chemical bonds (independent atoms). This approximation is

valid for most of the cases, especially if we are interested only in the structural analysis. More specific formalisms based on a multipolar expansion of the atomic electron density have been developed in the literature to go beyond this approximation; the reader is referred to the more specialized literature for further information on that topic [2]. The total electron density $\rho(\mathbf{r})$ introduced here from the experimental point of view is the fundamental observable of DFT-based calculations discussed in the chapter *DFT calculations of solids in the ground state*.

When an incident X-ray beam interacts with a complex system built from a large collection of atoms, whether it is a liquid, a small cluster, or a crystalline solid, the complex amplitude of the scattered wave in a general direction is described in electron units by

$$A(\mathbf{S}) = \sum_{i=1}^{N_{\text{at}}} f_i e^{2i\pi\mathbf{S}\cdot\mathbf{r}_i}, \quad (2)$$

where f_i is the atomic form factor for an atom i situated at the position \mathbf{r}_i , f_i is the Fourier transform of the corresponding spherical atomic electron density $\rho_i(\mathbf{r} - \mathbf{r}_i)$, \mathbf{S} is the scattering vector defined by $(\mathbf{s} - \mathbf{s}_0)/\lambda$, where \mathbf{s}_0 and \mathbf{s} are unit vectors in the directions of the incident and diffracted beams, and λ is the X-ray wavelength. The scattered intensity is obtained as

$$I(\mathbf{S}) = A(\mathbf{S}) \times A^*(\mathbf{S}) = \sum_{i=1}^{N_{\text{at}}} \sum_{j=1}^{N_{\text{at}}} f_i f_j e^{2i\pi\mathbf{S}\cdot(\mathbf{r}_i - \mathbf{r}_j)}. \quad (3)$$

According to equation (3), it is important to note that the X-ray scattered signal does not provide any information on the instantaneous atomic positions, but rather on the pairwise interatomic vectors $\mathbf{r}_i - \mathbf{r}_j$. This equation can be indistinctly applied to any kind of sample, whether it is crystalline or noncrystalline. Even at absolute zero temperature, the atoms are vibrating around their equilibrium positions, which we can simply describe in a first approximation by a harmonic behavior. The corresponding function describing the nuclear configurations is the probability density function $P(u)$. The dynamic atomic electron density is simply the convolution of the static (“frozen” lattice approximation) electron density by the probability density function:

$$\rho_{\text{dynamic}}(\mathbf{r}) = \rho_{\text{static}} \otimes P(\mathbf{r}) = \int_V \rho_{\text{static}}(\mathbf{r} - \mathbf{u}) \times P(\mathbf{u}) d\mathbf{u}. \quad (4)$$

This leads by Fourier transform to the atomic form factor being the product of the static atomic form factor with the Fourier transform of the probability density function:

$$f(\mathbf{S}) = f_{\text{static}}(\mathbf{S}) \times T(\mathbf{S}). \quad (5)$$

In the isotropic harmonic approximation, the probability distribution $P(\mathbf{u})$ averaged over all populated energy levels takes a Gaussian form $P(u) = \frac{1}{\sqrt{2\pi U}} e^{-\frac{u^2}{2U}}$, where $U = \langle u^2 \rangle$

is the mean square displacement of the atoms around their equilibrium position r_{eq} due to thermal vibrations (Figure 3). Following this, we have

$$T(\mathbf{S}) = e^{-2\pi^2 U S^2} = e^{-8\pi^2 U \frac{\sin^2 \theta}{\lambda^2}} = e^{-B \frac{\sin^2 \theta}{\lambda^2}}, \quad (6)$$

where $T(\mathbf{S})$ is called the Debye–Waller factor. It describes the attenuation of X-ray scattering or coherent neutron scattering caused by thermal motion; it depends on the scattering vector \mathbf{S} (or the scattering angle θ in the isotropic approximation).

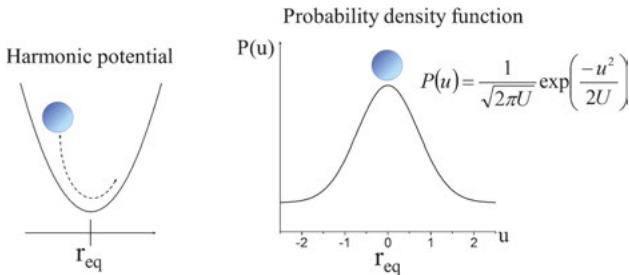


Figure 3: Scheme of harmonic potential (left) and associated probability density function due to atomic displacements (right), where u is the displacement of the atom around its equilibrium position r_{eq} , and U is the atomic mean square displacement.

During a conventional X-ray scattering experiment, the duration of the X-ray fundamental interaction with matter is of the order of a few femtoseconds, whereas the whole experiment may last several hours. As a consequence, during the scattering process, the X-rays “see” the atoms of the crystal as frozen at their instantaneous position spatially distributed in the crystal according to their probability distribution function around the equilibrium position. The factor $T(\mathbf{S})$ corresponds therefore to a spatial and temporal average of the atomic positions.

Consider now the time-resolved case. When the system is subject to a perturbation, its electron density is modified, and so is the potential energy hypersurface, which induces forces on the nucleus. As a response, the structure evolves as a function of time spanning the complete time scales from fs to s. We have thus to consider the total electron density as a time-dependent quantity $\rho(\mathbf{r}, t)$ that interacts with the incident X-ray pulse whose temporal shape is defined by $X(t)$: this is the semiclassical approximation. Equation (3) becomes

$$I(\mathbf{S}, t) = \int_0^\infty X(t) \sum_{i=1}^{N_{\text{at}}} \sum_{j=1}^{N_{\text{at}}} f_i f_j e^{2i\pi\mathbf{S} \cdot (\mathbf{r}_i(t) - \mathbf{r}_j(t))} dt. \quad (7)$$

The goal here is to derive the transient electron density as a function of time and build a comprehensive time-dependent structural model. The very general experiment is depicted in Figure 4. It consists in (1) pump the sample with an appropriate pertur-

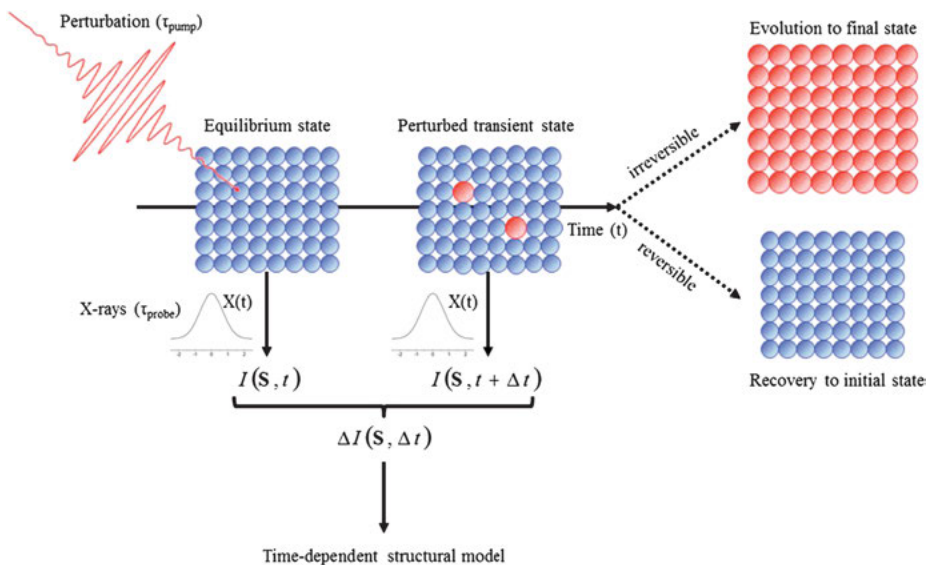


Figure 4: General scheme of a time-resolved experiment. The measured signal $I(\mathbf{S}, t + \Delta t)$ is used to model the time-dependent structural response to the perturbation. The dynamical process to be studied may be reversible or irreversible.

bation of duration τ_{pump} , (2) probe the sample using X-ray scattering and acquire the scattered signal $I(\mathbf{S}, t)$ during a period τ_{probe} , and (3) build a structural model out of the time-dependent scattered signal.

Equation (7) states that the dynamic electron density distribution, which is probed in a time-resolved experiment, is the average electron density integrated over the X-ray probe pulse. In this case, depending on the time resolution of the scattering experiment τ_{probe} and on the time resolution of the pump perturbation τ_{pump} , different situations may be considered. For a time resolution longer than the characteristic time of atomic vibrations (few tens of femtoseconds to picoseconds), the probability density function can describe appropriately the atomic vibrational behavior just like a conventional nontime-resolved experiment. For ultrafast measurements, two situations have to be considered. When the atoms are perturbed and displaced from their equilibrium positions in a noncoherent manner, the time average approximation is not valid anymore, whereas the spatial average still holds. Accordingly, the system is simply seen during τ_{probe} in a static configuration with atoms displaced from their equilibrium positions, as illustrated in Figure 5 (a); the probability density function is still a good approximation. When a coherent perturbation is produced, leading to a coherent displacement of the atoms, neither the temporal nor the spatial average holds (Figure 5 (b)).

Depending on the sample considered, crystalline solid or solution, this time-resolved scattering formalism has to be adapted. It is worth noting that in the solution

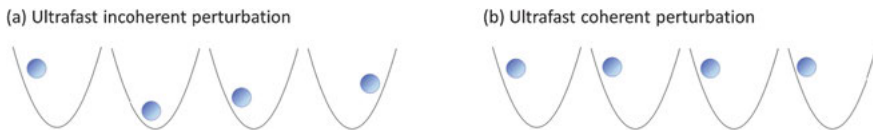


Figure 5: Instantaneous displacement of neighboring atoms during an (a) ultrafast incoherent and (b) ultrafast coherent perturbations.

scattering scientific community, the scattering vector is denoted \mathbf{q} , whereas \mathbf{H} is used in the crystallographic community. For consistency with the corresponding literature, we use these two definitions appropriately.

1.1 Time-resolved scattering of noncrystalline samples

A noncrystalline sample such as a solution (solute molecules diluted in a solvent) is constituted from a statistical ensemble of subsystems (molecules) randomly oriented, where only short-range ordering can develop. A solution is considered as an isotropic statistically homogeneous sample. We are thus interested in finding the average scattered intensity from equation (3) when the constituting molecules are allowed to take with equal probability all orientations in space. In terms of $q = (4\pi \sin \theta)/\lambda$, the average for each exponential term is given by

$$\langle e^{2\pi i \mathbf{S} \cdot \mathbf{r}_{ij}} \rangle = \frac{1}{4\pi r_{ij}^2} \int_{\phi=0}^{\pi} e^{i q r_{ij} \cos \phi} 2\pi r_{ij}^2 \sin \phi d\phi = \frac{\sin q r_{ij}}{q r_{ij}}, \quad (8)$$

where $r_{ij} = |\mathbf{r}_i - \mathbf{r}_j|$. The scattered intensity is thus simply given by

$$I(q) = S(q) = \sum_{i=1}^{N_{\text{at}}} f_i^2 + \sum_{i=1}^{N_{\text{at}}} \sum_{j \neq i=1}^{N_{\text{at}}} f_i f_j \frac{\sin q r_{ij}}{q r_{ij}}, \quad (9)$$

which is also called the *Debye scattering* equation. It is important to note that owing to the spherical average, only the magnitudes of the interatomic distances are involved in equation (9), contrary to the more general equation (3). For practical modeling, the scattering can be decomposed into three contributions (Figure 6): a solute-only term (yellow arrows), a solvent only term (blue arrows), and a solute–solvent cross correlation term (green arrows):

$$S(q) = S(q)_{\text{solute}} + S(q)_{\text{solute-solvent}} + S(q)_{\text{solvent}}. \quad (10)$$

The schematic of a pump–probe time-resolved X-ray solution scattering experiment is given in Figure 7. The sample is contained in a capillary and consists of protein molecules that are periodically excited by a pulsed laser and then probed by pulsed X-rays. The time-dependent scattering signal is accumulated at various time delays t on a bidimensional detector.

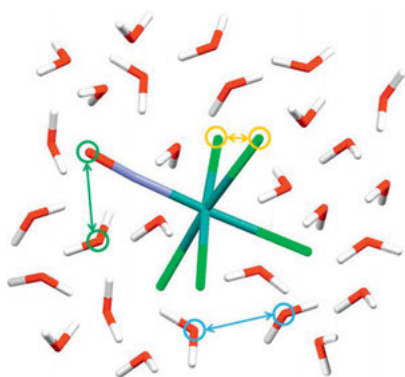


Figure 6: Schematic representation of the three contributions to the scattered signal of a molecule dissolved in water. Yellow arrows depict atomic pairs of the solute only, blue arrows depict atomic pairs of the solvent, and green arrows correspond to solute–solvent atomic pairs.

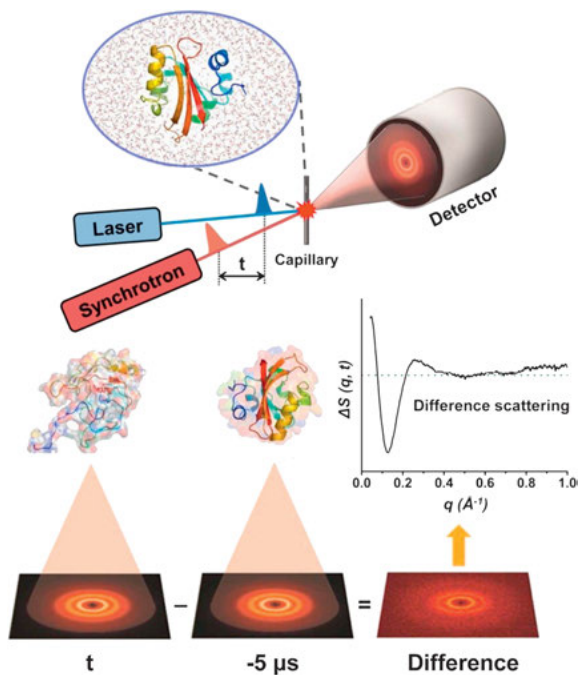


Figure 7: Schematic of a time-resolved X-ray solution scattering experiment. The solution is contained in a capillary or flowed through a liquid jet, which is irradiated by an optical laser pump pulse. X-ray pulses generated by a synchrotron are selected after a time delay t using a combination of high-speed choppers and shutters and sent to the sample. The reference scattering data recorded before the laser pulse are subtracted from the positive time delay data to provide the difference net scattering signal $\Delta S(q, t)$ [3–7]. Reprinted from [4] with permission from ACS (<http://pubs.acs.org/doi/10.1021/acs.accounts.5b00198>).

In a highly diluted solution, the total scattering signal contains a large background scattering from the solvent, so that the net signal on the photoinduced structural reorganization within the sample is derived in a pump–probe sequence from the difference in the pre- and post-pump scattered intensity $\Delta S(q, t)$ at a pump–probe time delay t . It may be decomposed as

$$\Delta S(q, t) = \Delta S(q, t)_{\text{solute}} + \Delta S(q, t)_{\text{solute-solvent}} + \Delta S(q, t)_{\text{solvent}}. \quad (11)$$

The term $\Delta S(q, t)_{\text{solvent}}$ is very sensitive to the thermodynamic variables of the solvent, such as temperature, pressure, and density. These variables are modified due to the energy transfer from light-absorbing solute molecules to the surrounding solvent molecules. The change in the solvent scattering at a given time delay t may be described by two hydrodynamic variables as [8]

$$\Delta S(q, t)_{\text{solvent}} = \left(\frac{\partial S}{\partial T} \right)_{\rho} \Delta T(t) + \left(\frac{\partial S}{\partial \rho} \right)_{T} \Delta \rho(t), \quad (12)$$

where $\Delta T(t)$ and $\Delta \rho(t)$ represent the temperature and density changes of the solvent after the laser pulse. Building a structural model out of the difference in the scattered signal $\Delta S(q, t)$ requires first to define all the k different species involved in the complete transformation, equilibrium species, and transient species and to define their characteristic individual scattering functions $S_k(q)$. The time evolution is encoded in kinetic functions $c_k(t)$ defining the respective time-dependent concentration of the k species. Accordingly, equation (11) is rewritten as

$$\begin{aligned} \Delta S(q, t) &= \Delta S(q, t)_{\text{solute-related}} + \Delta S(q, t)_{\text{solvent only}}, \\ \Delta S(q, t) &= \left[\sum_k c_k(t) S_k(q) - S_g(q) \sum_k c_k(0) \right] + \left(\frac{\partial S}{\partial T} \right)_{\rho} \Delta T(t) + \left(\frac{\partial S}{\partial \rho} \right)_{T} \Delta \rho(t), \end{aligned} \quad (13)$$

where $S_g(q)$ is the scattering intensity related to the reactants. The structural model is built by starting from an atomic configuration and calculating the corresponding scattering signal using the partial Debye formula:

$$S_k(q) = \sum_{i=1}^{N_{\text{at}}^k} f_i f_i + \sum_{i=1}^{N_{\text{at}}^k} \sum_{j \neq i=1}^{N_{\text{at}}^k} f_i f_j \frac{\sin qr_{ij}}{qr_{ij}}, \quad (14)$$

where the sum runs over all the N_{at}^k atoms of the k th molecule. The calculation of the Debye equation is highly time and resource consuming due to the large possible combinations over i and j indices. In practice, the Debye formula can be expressed in terms of the radial distribution functions $g_{ij}(r)$ (available, for instance, from molecular dynamic simulations) [5]:

$$S_k(q) = \sum_{i=1}^{N_{\text{at}}^k} f_i^2 + \sum_{i=1}^{N_{\text{at}}^k} \sum_{j \neq i=1}^{N_{\text{at}}^k} f_i f_j \int_0^{\infty} (g_{ij}(r) - 1) \frac{\sin qr}{qr} 4\pi r^2 dr. \quad (15)$$

1.2 Time-resolved scattering of crystalline materials

In the case of crystalline materials, the periodic long-range ordering of the constituting atoms in the crystal leads to important modifications of equations (1) and (3). For a crystal, the total electron density defined in equation (1) can be simplified noticeably by considering translational invariance and symmetry properties of the crystal. We can consider the N_{at} atoms arranged in N identical unit cells containing n atoms each. The atomic position vector \mathbf{r}_i can be replaced by $\mathbf{r}_i = \mathbf{R}_N + \mathbf{r}_{i0}$, where \mathbf{R}_N defines the position of the N th unit cell, and \mathbf{r}_{i0} is the local atomic position in that unit cell:

$$\rho(\mathbf{r}) = \sum_{i=1}^{N_{\text{at}}} \rho_i(\mathbf{r} - \mathbf{r}_i) = \left[\sum_N \delta(\mathbf{r} - \mathbf{R}_N) \right] \otimes \left[\sum_{j=1}^n \rho_j(\mathbf{r}_{j0}) \right]. \quad (16)$$

The first term on the right-hand side takes nonzero values only at the origin of the unit cells of the crystal, whereas the second term is the superposition of the atomic electron densities (j runs from 1 to n) within a reference unit cell placed at the origin of the crystal.

The Fourier transform of the crystal total electron density given by equation (16) leads to the structure factor of the crystal (constituted from $n_a \times n_b \times n_c$ unit cells):

$$\begin{aligned} F_{\text{crystal}}(\mathbf{H}) &= \sum_N e^{2i\pi\mathbf{H}\cdot\mathbf{R}_N} \times \sum_{j=1}^n f_j e^{2i\pi\mathbf{H}\cdot\mathbf{r}_{j0}} \\ &= \Gamma(\mathbf{H}) \times F(\mathbf{H}), \end{aligned} \quad (17)$$

where $\Gamma(\mathbf{H})$ is the interference function, and $F(\mathbf{H})$ is the unit cell scattering factor. These two functions contain very important information on the structural organization in the crystal. The interference function represents the long-range structural coherence, whereas the structure factor determines the scattering of a unit cell. For a crystalline solid, equation (3) is therefore given by

$$I(\mathbf{S}) = I(\mathbf{H}) = \sum_N \sum_{N'} e^{2i\pi\mathbf{H}\cdot(\mathbf{r}_N - \mathbf{r}_{N'})} \times \sum_{i=1}^n \sum_{j=1}^n f_i f_j e^{2i\pi\mathbf{H}\cdot(\mathbf{r}_{i0} - \mathbf{r}_{j0})}. \quad (18)$$

By comparison with solution scattering discussed in the previous section the fundamental periodicity of a crystal leads to a fantastic enhancement of the X-ray scattered signal at specific regular positions $\mathbf{S} = \mathbf{H}$ in the reciprocal space defined by the scattering vector $\mathbf{H} = h\mathbf{a}^* + k\mathbf{b}^* + l\mathbf{c}^*$ with h, k, l taking only integer values and corresponding to the nodes of the reciprocal lattice.

A perturbation of the crystal may modify the two functions $\Gamma(\mathbf{H})$ and $F(\mathbf{H})$ in different ways, so that the outcome of a time-resolved X-ray scattering experiment for a crystalline sample is a complete description of the temporal evolution of the interference function and the scattering factor. As will be described further, the signature of several important structural distortions of the crystal may be obvious on the diffrac-

tion pattern of a crystal under perturbation. As a consequence, X-ray diffraction is a powerful technique to investigate the physical mechanisms by which the crystal responds to the external perturbation. Figures 8 and 9 illustrate the major cases of crystal distortions and the corresponding diffraction patterns, on which we will base our discussions of selected examples of time-resolved structural studies from the literature later on in this chapter (Section 3).

Case (a) illustrated in Figure 8 corresponds to a regular 2D crystal in equilibrium ground state (GS) with one atom at the origin of the unit cell with perfect translational symmetry given by the interference function $\Gamma(\mathbf{H})$. The atoms are distributed around their mean position with amplitudes given by the atomic displacement parameter (or Debye–Waller parameter B). The corresponding Bragg peaks in reciprocal space are regularly spaced with low-intensity oscillations owing to finite-size effects in the calculation of the Fourier transform (calculation for a crystal of 50×50 unit cells).

In case (b), the scattering power of 10% of the atoms randomly distributed over the entire crystal has been modified to simulate a random distribution of 10% photoexcited species. The perfect periodicity is preserved in terms of unit cell shape, and, as a consequence, the position of the Bragg peaks is not modified in the reciprocal space (Figure 8 (b), middle and right). On the contrary, the structure factor of the unit cell is modified, and so is the respective intensity of each Bragg peak with respect to the regular crystal of case (a). In that case, X-ray diffraction provides a spatial average of the crystal structure. The structure factor for such a random distribution (RD) with a fraction p of excited state (ES) and $(1 - p)$ ground state (GS) species may be approximated by

$$\begin{aligned} F_{\text{RD}}(\mathbf{H}) &= (1 - p) \times \sum_{j=1}^n f_j^{\text{GS}} e^{2i\pi\mathbf{H}\cdot\mathbf{r}_{j0}} + p \times \sum_{j=1}^n f_j^{\text{ES}} e^{2i\pi\mathbf{H}\cdot\mathbf{r}_{j0}} \\ &= (1 - p) \times F_{\text{GS}}(\mathbf{H}) + p \times F_{\text{ES}}(\mathbf{H}), \end{aligned} \quad (19)$$

and therefore the Bragg intensity is proportional to

$$\begin{aligned} F_{\text{RD}}^2(\mathbf{H}) &= (1 - p)^2 \times |F_{\text{GS}}(\mathbf{H})|^2 + p^2 \times |F_{\text{ES}}(\mathbf{H})|^2 \\ &\quad + p(1 - p) \times (F_{\text{GS}}(\mathbf{H})F_{\text{ES}}^*(\mathbf{H}) + F_{\text{ES}}(\mathbf{H})F_{\text{GS}}^*(\mathbf{H})). \end{aligned} \quad (20)$$

Note that this random distribution is reflected by a high background incoherently scattered signal in Figure 8 (b), center. In case (c), the photoexcited species are clustered at the center of the crystal. The position of the Bragg peaks is not modified, but the respective intensities are modified. In the cluster model (CM), the Bragg intensity is proportional to

$$F_{\text{CM}}^2(\mathbf{H}) = (1 - p) \times |F_{\text{GS}}(\mathbf{H})|^2 + p \times |F_{\text{ES}}(\mathbf{H})|^2. \quad (21)$$

One important aspect is that although 10% of the molecules have been switched to the photoexcited state as for case (b), the intensity of the Bragg reflections is different from

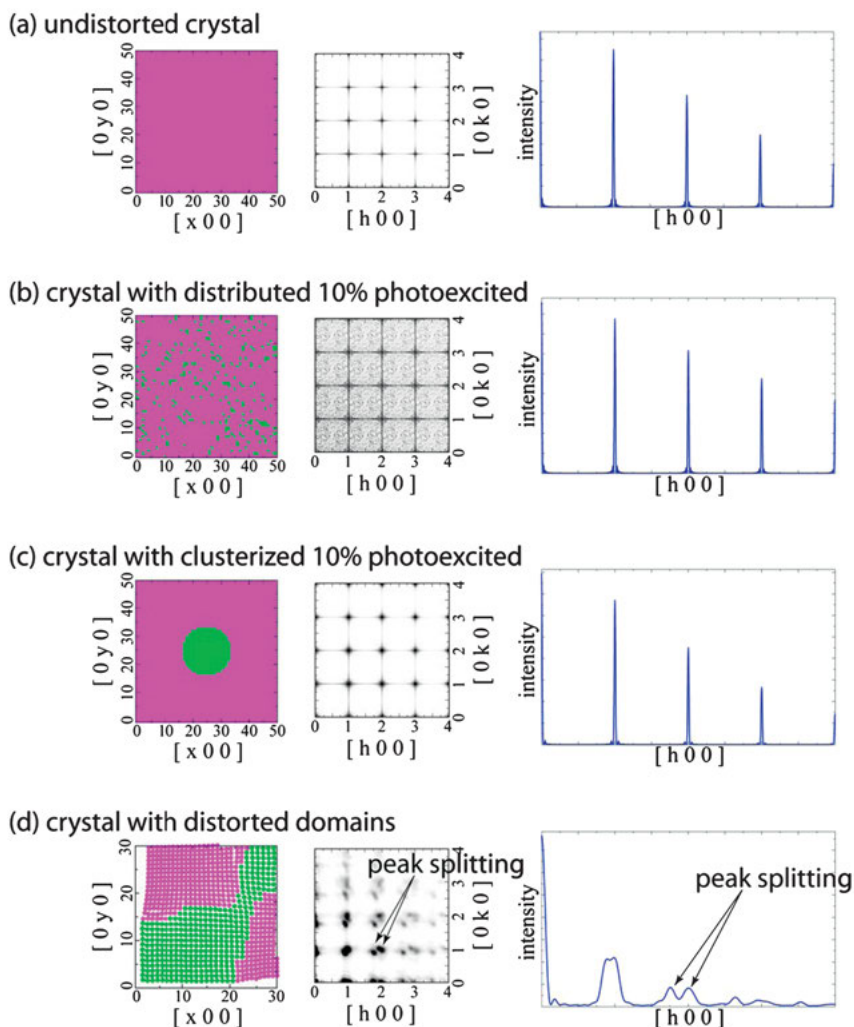


Figure 8: Diffraction patterns of selected model cases of distortions of a regular initial 50×50 crystal structure (30×30 for case d). In each diagram, left: the representation of a 2D crystal. Pink dots represent unperturbed initial species (for instance, ground-state molecules); green dots represent perturbed species (for instance, excited-state molecules). Middle: the corresponding 2D $[hk0]$ diffraction pattern computed from the direct Fourier transform of the crystal configuration. Right: the intensity along the $[h00]$ section of the diffraction pattern. (a) A regular undistorted crystal. (b) A crystal with 10% excited-state species randomly distributed. (c) 10% excited-state species forming a cluster (domain model). (d) A crystal with a large excited-state cluster accompanied with structural relaxations.

case (b). In a real experiment, the careful analysis of the Bragg intensities therefore allows us to distinguish between the two extreme situations and decide whether the photoexcited species are randomly distributed or clustered in the crystal [9].

In the last case, depicted in Figure 8 (d), a lattice distortion accompanies the clusterization of the atomic or molecular species. Long-range order is lost, and the crystal is in a heterogeneous configuration. The photoexcited state exhibits lattice constants larger than those of the ground state, leading to important structural relaxation at the domain boundary to preserve the continuity of the crystal. The corresponding diffraction pattern therefore exhibits a splitting of the Bragg peaks in two contributions, one for each lattice constant.

We have seen in the previous section that the atoms in any structure are subject to internal and external vibrational modes. This has important consequences in a crystalline solid and modifies strongly the diffraction pattern. Different situations are depicted in Figure 9.

Collective modulations of the crystal structure induce very systematic and very characteristic features. The activation of a single coherent acoustic phonon generates a collective and concerted oscillation of the atoms around their equilibrium positions, which manifests as weak sidebands in the vicinity of the Bragg peaks (case (e) in Figure 9). The activation of multiple thermal phonons reduces the global intensity of Bragg peaks, as shown in Figure 9 (f), a phenomenon summarized in the well-known Debye–Waller factor. This thermal vibration effect causes decoherence in the diffraction phenomenon (loss of spatial and temporal phase relationship); the observed attenuation in diffracted intensity is given by equation (5). Static incoherent atomic displacement induces similar attenuation on the Bragg peak intensities (Figure 9 (g)) and as such is indistinguishable from dynamic atomic displacements from a single temperature diffraction experiment (Figure 9 (f)). A static periodic modulation of the structure is shown in Figure 9 (h), which could correspond, for instance, to a Peierls-type lattice distortion. The modulation induces here a dimerization of the structure and correspondingly a doubling of the unit cell parameter in the x direction. This doubling corresponds to the appearance of weak superlattice reflections in the reciprocal space. Monitoring the intensity of superlattice reflections gives direct insights on the amplitude of atomic displacement under dimerization. For a nondimerized structure, the intensity of the superlattice reflections is null.

In the context of time-resolved X-ray diffraction studies on externally perturbed systems, any of these model cases may be detected and therefore qualitatively interpreted in terms of perturbation of the corresponding crystal structure. The quantitative monitoring of the temporal evolution of the intensity distribution over the entire reciprocal space provides detailed information on the kinetics of the physical processes under investigation. For instance, the temporal evolution of the intensity of superlattice reflections provides details on the photoinduced melting of charge and orbital order in manganites (see examples detailed in Section 3.7). The fitting of the evolution of Bragg intensities during photoexcitation in spin crossover molecular complexes allowed the determination of kinetic parameters of metastable state domain nucleation and growth [10]. The intensity of acoustic phonon sidebands has also been monitored after ultrafast photoexcitation [11–14].

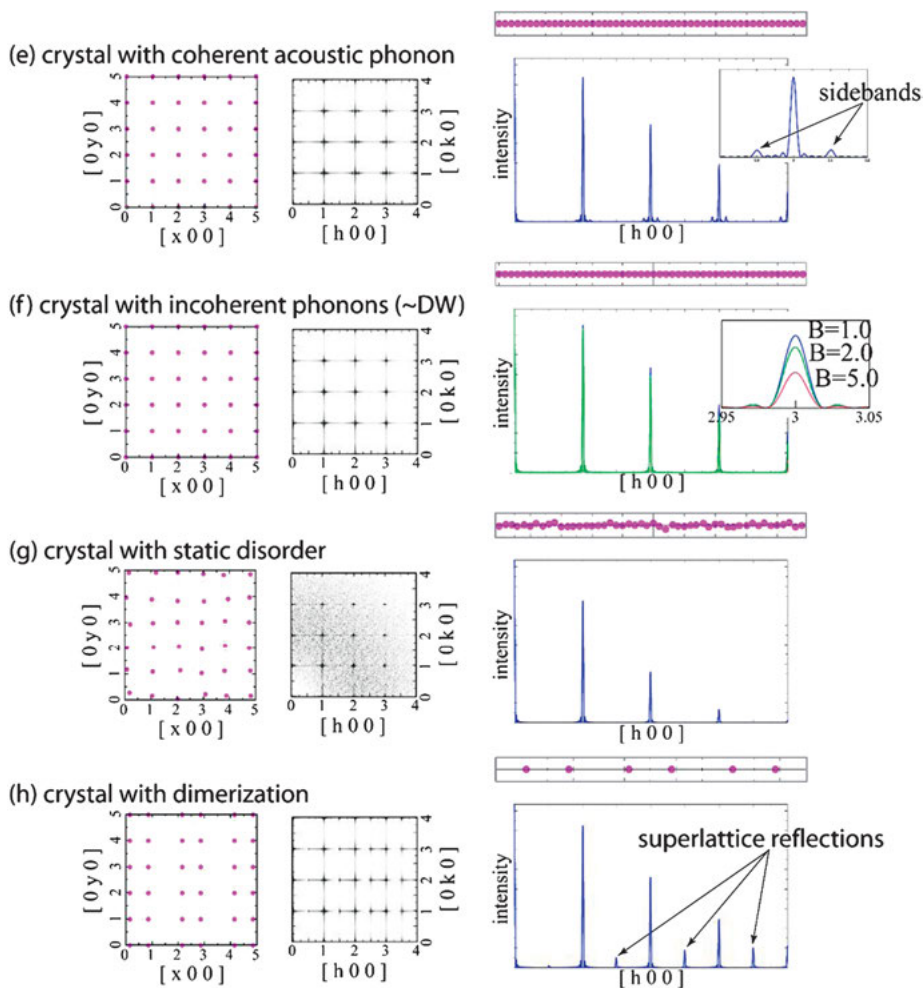


Figure 9: Diffraction patterns of selected model cases of coherent and incoherent distortions of a regular initial 50×50 crystal structure. Left of each diagram: the representation of a 6×6 zoom of the 2D crystal. Middle: the corresponding 2D $[hk0]$ diffraction pattern computed from the direct Fourier transform of the crystal configuration. Right: the intensity along the $[h00]$ section of the diffraction pattern and a section of the crystal along the x axis. (e) A crystal whose atoms are displaced by a coherent acoustic phonon propagating along the x direction. (f) A crystal whose atoms are displaced by incoherent phonons that could be approximated by a Debye–Waller (DW) factor. Right: three different values of B (defined in equation (6)) have been used for comparison purposes. (g) A crystal with static atomic disorder. (h) A crystal with a dimerization along the x direction.

As illustrated in Figure 9 (e, f), the impact of an ultrafast laser on a crystal may generate incoherent or coherent phonons whose influence on the Bragg intensities may be fundamentally different. For instance, laser excitation of Ge below the nonthermal melting threshold results in the transfer of electronic energy to incoherent lat-

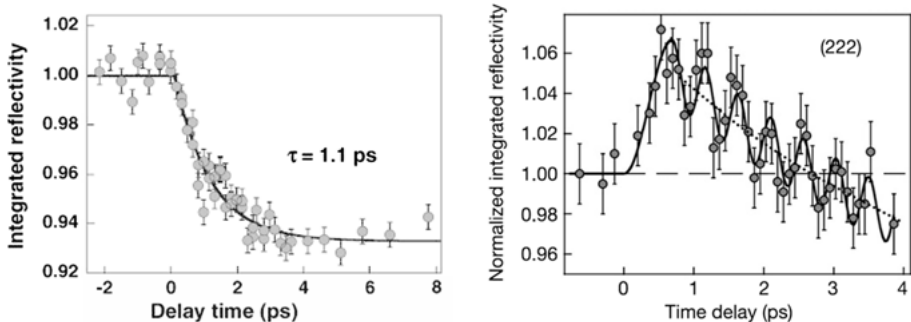


Figure 10: Left: X-ray diffraction intensity from the (400) peak of germanium for weak laser excitation. Republished with permission of IOP Publishing Ltd, from [15]; permission conveyed through Copyright Clearance Center, Inc. Right: Bragg intensity of the (222) reflection in bismuth as a function of time delay between the optical pump pulse and the X-ray probe pulse [16]. Reprinted by permission from Macmillan Publishers Ltd, copyright (2003).

tice vibrations increasing the temperature of the material. In that case, a global decrease in intensity of Bragg peaks is observed (see Figure 10, left) [15], corresponding to a transient and time-dependent increase in the Debye–Waller parameter $B(t)$ (Figure 9 (f, g)). On the contrary, the excitation of coherent lattice vibrations using an ultrafast laser leads to a strongly coherent displacive excitation in the crystal. The induced atomic motion was detected by measuring the weak oscillations in the optical reflectivity and X-ray Bragg peak intensity at the phonon frequency that are produced by the lattice vibrations (Figure 10, right) [16]. In this situation, the instantaneous positions of the atoms in the crystal are strongly correlated, introducing coherence.

Following case Figure 9 (f), the expression of the Debye–Waller factor given in equation (6) may be used to estimate lattice heating in crystals following a laser pulse from the systematic decrease in Bragg peak intensities. Assuming in a rough approximation that the Debye–Waller factor is identical for all the atoms of the structure, the structure factor may be written as

$$\begin{aligned} F(\mathbf{H}) &= \sum_{j=1}^n f_j e^{2i\pi\mathbf{H}\cdot\mathbf{r}_{j0}} e^{-B_j \frac{\sin^2\theta}{\lambda^2}} \\ &= e^{-B \frac{\sin^2\theta}{\lambda^2}} \sum_{j=1}^n f_j e^{2i\pi\mathbf{H}\cdot\mathbf{r}_{j0}}, \end{aligned} \quad (22)$$

and the corresponding scattered intensity is approximated by

$$I(\mathbf{H}) \approx e^{-2B \frac{\sin^2\theta}{\lambda^2}} \sum_{i=1}^n \sum_{j=1}^n f_i f_j e^{2i\pi\mathbf{H}\cdot(\mathbf{r}_{i0} - \mathbf{r}_{j0})}. \quad (23)$$

The logarithm of the ratio of the Bragg intensities with laser on and laser off is then simply

$$\ln(R) = \ln \left[\frac{I_{\text{on}}(\mathbf{H})}{I_{\text{off}}(\mathbf{H})} \right] = -2\Delta B \frac{\sin^2\theta}{\lambda^2} + K. \quad (24)$$

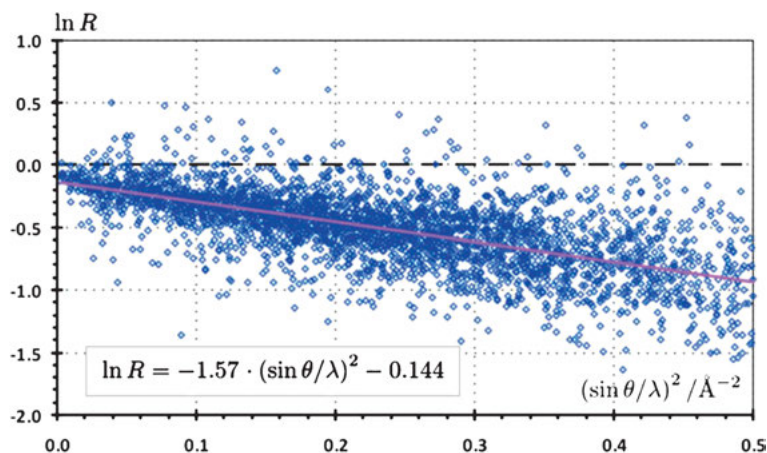


Figure 11: Example of photo-Wilson plot $\ln(R) = \ln \left[\frac{I_{\text{on}}(\mathbf{H})}{I_{\text{off}}(\mathbf{H})} \right]$ as a function of $\frac{\sin^2 \theta}{\lambda^2}$. The slope of the fitted line is $-2\Delta B$ [17]. Reproduced with permission of the International Union of Crystallography.

By plotting the ratio $\ln(R) = \ln \left[\frac{I_{\text{on}}(\mathbf{H})}{I_{\text{off}}(\mathbf{H})} \right]$ as a function of $\frac{\sin^2 \theta}{\lambda^2}$ we can directly estimate the increase in average of the Debye–Waller parameter ΔB due to laser lattice heating. An illustration of this approach, called a photo-Wilson plot, is given in Figure 11.

2 Time-resolved X-ray scattering experimental methods

The advent of ultrafast spectroscopy and pump–probe techniques in the 1960s made possible the observation and identification in real time of the optical and vibrational signatures of transient events, metastable species, and excited states up to femtosecond resolution. The extension of this approach to keV hard X-ray and electron ultrafast scattering provided a way to study the structural dynamics of matter in real time with subpicosecond and subangstrom resolutions. We discuss in this section the typical experimental methods of time-resolved X-ray scattering that have been developed so far.

2.1 Instrumental considerations

For time-resolved structural studies, the choice of X-ray technique and X-ray source, especially in terms of achievable time resolution, is defined by the nature and the temporal evolution of the dynamical phenomenon. Depending on the reversibility or irreversibility of the dynamical process, a repetitive (stroboscopic) or single shot experiment is carried out (see Figure 4).

2.1.1 The pump–probe approach

The most efficient and used method to perform time-resolved experiments is to use the so-called pump–probe approach. In a typical pump–probe experiment, a dynamical process is initiated by applying a pump perturbation $S(t)$ to a sample (a short laser pulse, a pressure pulse, a periodic electric field, etc.) whose response is detected after a tunable time delay Δt through an X-ray probe pulse $X(t)$. The time-dependent evolution of the nonequilibrium atomic structure of the sample can be monitored by measuring the X-ray scattered signal as a function of Δt . Different schemes may be used to achieve time resolution in a pump–probe experiment:

- (1) Using an intrinsically pulsed X-ray source such as a synchrotron or an X-ray Free-Electron Laser (XFEL) or a mechanically chopped X-ray source. This corresponds to the first case in Figure 12. The time resolution is provided by the characteristics of the pump pulse $S(t)$ and the probe X-ray pulse $X(t)$ and our ability to adjust precisely the time delay Δt .

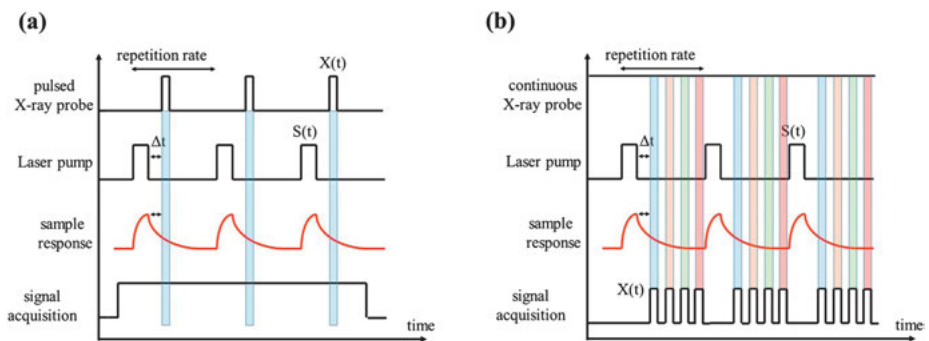


Figure 12: Principle of time-resolved X-ray scattering pump–probe measurement with (a) an intrinsically pulsed X-ray beam provided by a synchrotron or an XFEL and (b) a quasi-continuous X-ray beam with a scattered signal sampled by a fast gated detector. The scattered signal is recorded during four different time windows in this example.

- (2) Using a continuous X-ray source (laboratory X-ray tube) or quasi-continuous X-ray beam (synchrotron when its temporal structure is not used) and sampling the scattered signal at the pump–probe rate by a fast gated detector such as hybrid pixel detectors or streak cameras. In addition to the previous criteria, time resolution depends on the gating characteristics of the detector as well.

The overall time resolution is given by

$$\tau = (\tau_{\text{pump}}^2 + \tau_{\text{probe}}^2 + \tau_{\text{mismatch}}^2 + \tau_{\text{jitter}}^2 + \tau_{\text{detector}}^2)^{1/2}, \quad (25)$$

where τ_{pump} and τ_{probe} are the pump and probe pulse widths, respectively, τ_{mismatch} is the mismatch in the temporal overlap between the pump and probe pulses, τ_{jitter}

is the timing jitter between the pump and probe pulses, and τ_{detector} is the opening window of the gated detector if used.

2.1.2 X-ray sources

The choice of X-ray source for time-resolved X-ray scattering experiments depends critically on several factors such as the projected time regime and the required characteristics of the X-ray beam in terms of monochromaticity, energy, coherence, and intensity [18].

Experiments may be conducted with conventional laboratory X-ray diffraction setups equipped with X-ray tubes or rotating anodes, delivering a continuous X-ray beam. Time resolution is provided in two ways. In the first approach, a sequence of repetitive X-ray pulses is generated from the continuous X-ray beam using a fast optical chopper, which is a multislit blade rotating at a very high rotating speed, delivering X-ray pulses of a few μs length at frequencies up to 100 kHz. The X-ray detector used in this configuration may be a conventional CCD or image-plate system [19]. Using this kind of instrument, the time resolution that can be achieved is limited by the duration of the X-ray probe pulse generated by the rotating chopper and therefore by the width of the blade slots and rotation speed. This method corresponds to case (a) depicted in Figure 12. The second approach uses a fast gated X-ray detector (hybrid pixel array detector or streak camera) synchronized with the application of the pump pulse. The detector accumulates the desired scattered signal only during chosen time windows as depicted in case (b) of Figure 12. The maximum time resolution in that case is given by the response time of the electronics of the X-ray detector (typically, in the nanosecond range at present for hybrid pixel array detector and subpicosecond for streak camera). The major drawback of laboratory-based time-resolved instruments, which limit their application, is the very modest X-ray flux during each measurement cycle.

Owing to the increased sophistication, stability, and brightness of the now available third-generation synchrotron radiation sources, time-resolved diffraction techniques have evolved drastically over the last decade [20]. Intense hard X-ray pulses ($\sim 10^{12}$ ph/s) are generated by synchrotrons such as Spring-8 (Japan), European Synchrotron Radiation Facility (ESRF, France), Advanced Photon Source (APS, USA), SOLEIL (France), PETRA III (Germany), or Swiss Light Source (SLS, Switzerland). In a synchrotron, the radiofrequency cavity compensates the energy loss due to synchrotron emission and compresses the pulse duration of the electron bunch to typically 100 ps. Of major importance for time-resolved experiments is the fact that synchrotron storage rings can be run in different modes, corresponding to different filling patterns (distribution of the electron bunches cycling in the ring) such as the uniform filling mode, 4-bunch mode, and 16-bunch mode (equidistant bunch filling modes), hybrid modes with a single pulse opposite to multibunch. A train of short

X-ray pulses with different temporal structures (pulse width and pulse separation) may be generated. For instance, for the ESRF storage ring in the 16-bunch mode, X-ray pulses of nearly 100 ps duration are separated by 176 ns at an orbit frequency of approximately 355 kHz. A combination of heat-load chopper and high-speed chopper is conveniently used to select and isolate a short sequence of pulses, or even a single pulse, out of the pulse train of the synchrotron [21–23]. The frequency of the choppers is phase-locked to the temporal structure of the storage ring. The ultimate time resolution that can be achieved is limited by the width of the synchrotron pulse, typically in the range 60–100 ps. It is important to recognize that for such experiments, most of the X-rays generated by the ring are blocked by the chopper to isolate short pulses. As a consequence, the effective flux in the selected pulse is very limited, which requires an initial ultrabright synchrotron. For pump–probe experiments, an additional perturbation pump (for instance, pulsed laser) is synchronized with the X-ray pulses. A typical experimental scheme is given in Figure 13.

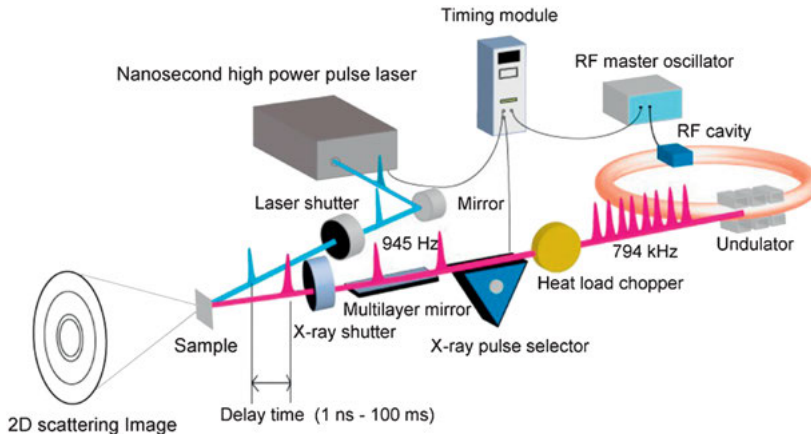


Figure 13: Schematic of a pump–probe time-resolved X-ray diffraction experiment using the temporal structure of a synchrotron. Adapted from [7] in accordance with the Creative Commons Attribution (CC BY) license.

Ultrashort pulses with duration down to 100 fs may be produced and selected in a synchrotron storage ring by several techniques [20], such as the low- α mode (using specific optics in the storage ring to shorten the electron bunch) or the laser-slicing method. In this latter case, an intense femtosecond infrared laser is locked with the radiofrequency clock of the synchrotron and aligned with the accelerated electron bunches in an undulator. The interaction between the high electric field of the ultrashort laser light pulse and the relativistic electrons results in an energy modulation of a thin slice of the electron bunch, which leads to a transverse spatial separation from the main bunch. Pulses of synchrotron radiation from the offset electrons occur with

the same duration as the duration of the laser light pulse [24, 25]. This technique is, for instance, implemented at the synchrotron SLS [26] and BESSY II [27].

Laser-driven plasma table-top sources offer an attractive alternative to accelerator-based sources [28–32]. Monochromatic X-ray pulses are generated by focusing very intense (10^{15} – 10^{16} W/cm²) femtosecond optical pulses onto a metallic target (Cu or Ti). First, hot electrons are generated by ionization of the atoms of the target through a thin plasma layer. The hot electrons interact with the incident laser pulse and are further accelerated back toward the solid target atoms with a net energy gain. The hot electrons excite K-shell electrons from atoms in the bulk of the metal target. The K-shell holes are filled by recombination of electrons from higher shells, emitting the characteristic $K\alpha$ hard X-ray lines. The principle of radiation is therefore similar to that in a conventional X-ray tube or rotating anode. The duration of the $K\alpha$ emission is governed by the thermalization time of the electrons in the target and by the duration of the laser pulse near 100 fs. These sources have been used to study the structural dynamics of nonthermal melting or, for instance, acoustic and optical coherent phonons in semiconductors [31]. A schematic illustration of a laser plasma X-ray source synchronized with a pump laser for time-resolved crystallography is shown in Figure 14. Such a scheme is very convenient for pump–probe photo-induced experiments, since the optical pulses of the laser system are used at the same time to generate the X-rays by focusing on the metal target and as the pump excitation of the sample. The delay between the pump and probe pulses is easily adjusted by changing the optical path length in a delay stage.

The XFELs are the most recent pulsed X-ray sources, which are characterized by high brightness (higher than 10^{10} ph/pulse), high coherence ($\sim 100\%$ transverse, $\sim 1\%$ longitudinal), and short pulse duration (~ 100 fs) with a repetition rate of ~ 100 Hz. The XFEL radiation is achieved by the self-amplification of spontaneous emission of high-

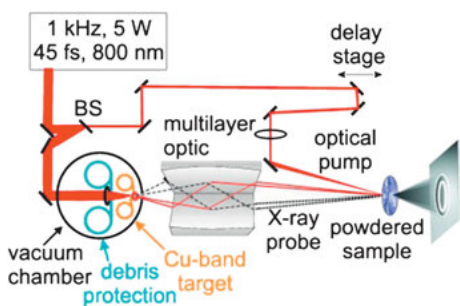


Figure 14: Schematic of a table-top X-ray diffraction instrument with ultrafast plasma X-ray source. 800-nm laser pulses are generated by an ultrafast Ti:sapphire laser producing 45-fs pulses of 5-mJ energy. The output of the laser is separated by a beam splitter to pump the sample and generate probe X-ray pulses at the characteristic Cu $K\alpha$ photon energy of 8.05 keV (wavelength 0.154 nm) by focusing on a Cu target. The delay between pump and probe is adjusted through a delay stage. The diffracted signal is collected on a large-area X-ray CCD detector. Reprinted with permission from [29].

energy high-peak current and ultrashort pulsed electron bunches in long-aligned undulators. The fundamental principles of XFEL radiation and technical details of the instrument are given in the chapter *Ultrafast Science*.

2.1.3 Detectors for time-resolved X-ray scattering

Depending on the time-resolved experiment, several types of detectors may be used. When the X-ray beam is either pulsed or chopped, a conventional integrating detector such as an image-plate (IP) or a CCD detector may be efficient. When a selection within a sequence of X-ray pulses is needed, for instance, for selecting a single X-ray bunch out of a multibunch mode of a synchrotron, a fast detector is required. For that purpose, a silicon avalanche photodiode (APD) or an X-ray streak camera with temporal responses in the nanosecond and subpicosecond regime, respectively, are appropriate [33, 34].

The recent development of gated single-photon-counting pixel area detectors (PAD) has opened new possibilities in the area of pump–probe time-resolved X-ray experiments [35–37]. These detectors can be gated with resolution in the nanosecond regime, which is faster than the separation between individual X-ray bunches at synchrotron radiation sources; X-ray choppers are not needed anymore to select single X-ray pulses. For slower time-resolved experiments (millisecond to microsecond), the detector can be gated to enable the measurement of the X-ray signal in tunable acquisition windows, allowing time-resolved measurements to be conducted with X-ray tubes on laboratory instruments [36] without the need for an X-ray beam chopper (Figure 12 (b)). One limitation of such detectors is their read-out time, which should be sufficiently short to enable sampling at the pump–probe repetition rate (for a 100 Hz repetition rate, the read-out time should be, for instance, less than 10 ms).

2.2 The perturbation

Most of the half a million crystal structures determined through single crystal or powder X-ray or neutron diffraction experiments have been conducted at ambient conditions (i.e., at 298 K and 0.1 MPa). Detailed structural information can be provided by investigating systems out of equilibrium and monitoring the return to equilibrium as a function of time. For that purpose, we need a way to perturb the system by acting on one of its degrees of freedom while probing the structural degrees of freedom. The physical properties of crystalline materials may be altered by applying various kinds of external stimulus, such as electric field, light irradiation, temperature, pressure, and chemical environment. All these perturbation means have to be classified depending on whether they induce a change of potential energy surface (optical excitation)

or simply disturb the system on the ground-state potential energy surface (pressure jump, acoustic pulses, temperature jump, electric field).

2.2.1 Optical excitation

When a molecule or a solid absorbs an optical photon with energy ranging from ultraviolet to near-infrared, an electronic transition may occur, characterized by an ultrafast redistribution of the electron density while the nuclei retain the same configuration as the ground state. Such a primary excited state is referred as the Franck–Condon state (Figure 15). This process is ultrafast, within a few fs, much faster than half the intramolecular vibrations. The initial electronic excitation is followed by several types of secondary processes. The redistributed electron density induces forces on the nucleus that define the initial direction of the subsequent structural trajectories on the excited potential energy surface. The Franck–Condon state being unstable, the nuclei structurally relax within tens of femtoseconds to a few picoseconds: the excited state is equilibrated to a new structure with structural coordinates (q_{ES1}) different from the ground state (q_{GS}). This equilibrated excited state ES1 can relax directly to the ground state or further evolve to a series of secondary excited states (ES2, ...) through internal conversion (electronic transitions without change of spin multiplicity) or intersystem crossing (electronic transitions with change of spin multiplicity). Relaxations from these secondary excited states proceed by emission of photons (fluorescence or phosphorescence processes) or through radiationless transitions.

From the primary populated Franck–Condon state, different situations may happen to relax the excess of energy depending on the time-scale of the reaction dynamics. Slow processes (characteristic times in the ns–s range) are activated, governed by

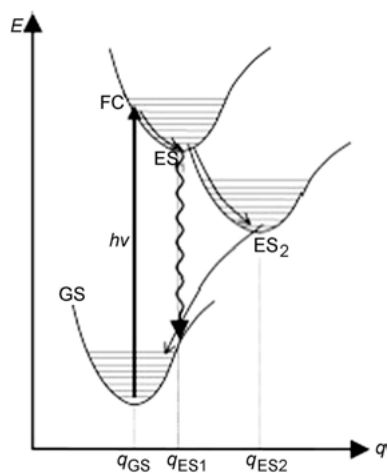


Figure 15: Schematic of the interaction of light with a molecule in the ground state (GS) and subsequent processes. q is a generalized molecular coordinate. FC is the Franck–Condon short-lived excited state, ES1 and ES2 are the first and second thermally equilibrated excited states. Reprinted from [38] by permission from John Wiley & Sons, Inc.

random diffusion of atoms and molecules, the intermediate conformations being dispersed through a Boltzmann distribution on the potential energy surface of ES1: relaxation occurs incoherently (heat generation and diffusion). For ultrafast dynamics (in the femto- to picosecond regime), the atoms and molecules can move on the potential energy surface without dephasing, and relaxation occurs through electron–phonon coupling by emission of coherent phonons.

The complete photophysical properties of a system are usually determined using time-resolved transient optical absorption and emission experiments at visible and ultraviolet frequencies, often completed by time-resolved vibrational spectroscopy, which has a structural sensitivity. The dynamics and spectral signatures of the various intermediate excited states are thus precisely defined, reflecting the specific electronic, vibrational, and rotational states. These techniques alone can, however, provide only limited information on the exact structural coordinates associated with the dynamical process. Combining optical pump excitation with X-ray scattering probe techniques, the structural changes of rapidly evolving systems can be resolved with atomic resolution down to the ultrafast time scale.

In the context of structural dynamics, optical transitions are conveniently triggered using fast lasers as optical pump sources, easily available over the ns to fs time scale, and covering the entire UV to IR spectral range. The complete response of the sample depends on the individual absorption cross-section of the photoactive atoms or molecules and the quantum yield of the different photoinduced processes. Accordingly, in practice, only a fraction of the photoactive elements are effectively in the desired excited state while probed by X-ray scattering techniques. A quite intense pump laser and a very accurate X-ray scattering experiment are necessary.

2.2.2 Electric field

There have been considerable efforts and significant achievements in X-ray crystallography under an applied external electric field. Piezoelectric crystals are characterized by the appearance of a dielectric polarization in response to an applied mechanical stress (direct piezoelectricity) or development of a macroscopic deformation or strain in response to an applied electric field (inverse piezoelectricity). Ferroelectric materials possess a macroscopic electric polarization P_S , which can be reversed by an external electric field. This process, called polarization switching, is usually described as the nucleation and growth of domains with a switched spontaneous polarization parallel to the electric field. This ferroelectric transition may be coupled to other properties of the material such as strain or magnetic order, leading to multiferroicity. The complete mechanism is depicted in Figure 16 as a typical P – E hysteresis loop, starting from a crystal initially in a multidomain state. When the positive electric field is applied, polarization switching occurs, leading to the appearance of intrinsic lattice

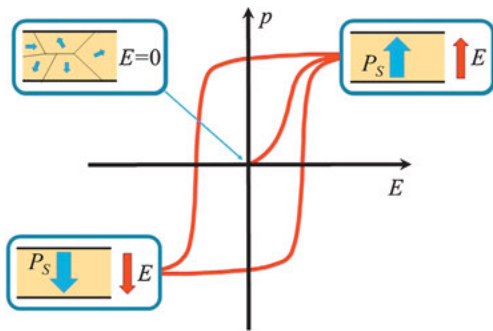


Figure 16: Polarization switching (P - E hysteresis loop) in ferroelectrics under applied electric fields.

strain. Reversing the electric field induces polarization switching with nucleation and growth of so-called 180° -domains.

The structural response of a crystal to an applied external electric field involves different spatial lengths from atomic and bond length distortions to mesoscopic domain nucleation and growth and domain wall motions. The entire response of the crystal spans several decades of time from the purely ultrafast elemental electron density redistribution under the electric field to the domain wall motion limited by the speed of sound ($\sim 1\text{--}4\,000\text{ ms}^{-1}$) and depends on the sample geometry (single crystal, thin film, or thin-film ceramic) and mechanism [39–41]. Quite slow domain wall velocities of a few meters per second correspond to short switching characteristic times (e.g., nanoseconds) for thin crystalline films of a few hundred nanometers thickness. Domain nucleation occurs in the submicrosecond time scale. Lattice deformations and interatomic bond distortions are subtle effects, which require very accurate and extremely stable experiments. The deformation of the unit cell (lattice strain) related to polarization switching may be followed accurately using X-ray diffraction under a unipolar applied static electric field. The deformation of the unit cell (or strain $[\epsilon_{ij}]$) is related to the electric field through the piezoelectric tensor $[d_{ijk}]$ of rank three: $\epsilon_{ij} = d_{ijk}E_k$, where d_{ijk} are the coefficients of linear electrostriction (converse piezoelectric effect). Due to the crystal symmetry, the elements d_{ijk} are not independent.

Applications of such methodologies have focused on piezoelectric (quartz, GaAsO_4) and ferroelectric materials (BaTiO_3 , $\text{PbZr}_{1-x}\text{Ti}_x\text{O}_4$ (PZT) ceramics), covering dynamics of ferroelectric or ferroelastic domains, propagation of elastic deformation in solids, dynamics of texture in piezoelectric ceramics, using experiments developed at synchrotron radiation facilities or dedicated laboratory diffraction instruments.

2.2.3 Pressure pulses

During the last decades, high-pressure crystallography has evolved into a very mature approach, which can be regularly applied in laboratories and dedicated synchrotron

facilities [42]. Structural analysis in nonambient conditions under variable high pressure extends the understanding of the solid state, allowing the determination of phase diagrams, the exploration of polymorphism, phase transitions, solid state cohesion forces, and structure-property relationships in a more general perspective. Using various pressure cells (e.g. diamond-anvil cell), high pressures of several tens of giga-Pascals (GPa) may be routinely applied on single crystals and powder samples. These cells use a pressure medium to impose hydrostatic conditions (i.e., the applied pressure is isotropic on the sample).

In the time domain, dedicated pressure cells have been developed to generate pressure jumps in the range 0.1–500 MPa on the millisecond time scale [43]. Application area covers soft condensed matter and biomolecular phase transformations. The most efficient method to generate much faster and much higher pressure pulses, which can be further synchronized with X-ray diffraction experiments, is using a powerful pulsed laser [44]. Focusing a laser pulse of short duration (subnanosecond) and high intensity on the surface of a sample create a plasma, which expands outward and drives a shock wave in the sample. The induced shock pressure is related to the characteristics of the laser and target; pressures up to nearly 15 GPa have been produced in the context of time-resolved diffraction experiments. Using this method, only uniaxial pressures may be applied. Reported investigations concern strain propagation in silicon [32, 45, 46], bismuth [47, 48], or the bcc(α)-to-hcp(ϵ) phase transition in shock-compressed iron [49] with time resolutions of nanosecond to picosecond. It has been shown that the propagation of the shock wave in the crystalline sample changes the interplanar distances, leading to a shift and broadening of the Bragg peaks. Time-resolved monitoring of the rocking curve evolution provides direct insight into the lattice response with respect to the transient strain propagation. Typical velocities of the propagating front were estimated to be a few $\text{km}\cdot\text{s}^{-1}$, which correspond to time domains of a few nanoseconds, setting the required time resolution of the diffraction experiment to subnanosecond. Quite recently, elastic shock waves in diamond have been imaged using X-ray phase contrast imaging at an XFEL source [50].

2.2.4 Fast solution mixing

Many important technology production processes take place on heterogeneous reaction systems. Improvement of these processes requires techniques and experimental setups yielding detailed structural information during the reaction process in real time. Specific reaction cells, called stopped-flow cells, have been designed for mixing the reactants of the reaction with high speed and enabling X-ray diffraction measurements to be performed in situ as the reaction proceeds [51]. Measurements are performed at a delay Δt after mixing the reactants. The specificity of these experiments is their irreversible nature, preventing any stroboscopic procedure to be applied. The basic idea is to continuously refresh the sample by a continuous flow. This technique

has recently evolved dramatically in view of XFEL experiments: mixing jet systems have been designed, enabling time resolution of 250 μs [52].

2.2.5 Mode-selective vibrational excitation

We have discussed before the process by which absorption of an optical photon can electronically excite the system and bring it to the excited potential energy surface. Optical excitation can also be used to probe the dynamics of the electronic ground state of the system through selective excitation of vibration modes using mid-infrared pulsed laser light. These intense femtosecond pulses in the mid-infrared can be tuned into resonance with infrared-active crystal lattice modes (phonons) of the solid [53–59]. Driven by the pulsed field, the atoms oscillate about their equilibrium positions along the normal coordinate of the considered mode. This concept has been clearly demonstrated for rhombohedrally distorted perovskite $\text{La}_{0.7}\text{Sr}_{0.3}\text{MnO}_3$, for which the resonant excitation of the infrared-active phonon mode at 605 cm^{-1} (20 THz) corresponding to the Mn–O stretching mode induces the excitation of a Raman-active mode (at 1.2 THz) corresponding to the rotation of oxygen octahedral around the Mn cations. The intensity modulation of relevant X-ray Bragg peaks, resulting from atomic motions along the phonon coordinate, was followed using time-resolved ultrafast X-ray diffraction and adjusted to a model of driven damped harmonic oscillator [59].

3 Time-resolved structural analysis: model case studies

In the previous section, we have described in detail all the instruments and methods typically used to derive dynamic structural information from time-resolved X-ray scattering experiments. We present in this section a representative selection of experiments and results published in the literature on very different sample types, from solvated molecules in liquid phase to the behavior of individual molecules in a crystal and to cooperative effects in crystalline solids. These chosen examples can be identified according to the model cases illustrated in Figures 8 and 9.

3.1 Static relaxed metastable states and photostationary states

The methods of X-ray crystallography have been extended to derive the structure of photosensitive molecules in an out-of-equilibrium metastable state with extended lifetime; this approach is termed *photocrystallography*. Single crystals containing

the desired photosensitive entity are illuminated with a laser of appropriate wavelength in well-chosen temperature conditions to populate a high concentration of metastable state molecules in the crystal, and the corresponding crystal structure is determined to extract the structural configuration of the species in the metastable state. Representative examples are photoinduced metastable states of molecular coordination complexes with spin state change, photoinduced linkage isomerism (e.g., nitrosyl complexes), photoinduced *cis-trans* isomerism of organic molecules. In most of these cases, the photoinduced process has a purely molecular origin, modulated by the environment in the crystal packing. We can take one representative example of this family to illustrate the methods and concepts of structural determination of out-of-equilibrium states.

$[\text{RuCl}(\text{NO})_2(\text{PPh}_3)_2]\text{BF}_4$ is a photoswitchable dinitrosyl pentacoordinated compound [60]. Infrared spectroscopy analysis has shown that photoexcitation with light of appropriate wavelength (405 nm) results in a strong modification of the symmetrically $\nu_s(\text{NO})$ and asymmetrically $\nu_{\text{as}}(\text{NO})$ coupled NO stretching vibrations, which are measured in the ground state (GS) at 1866 cm^{-1} and 1686 cm^{-1} , respectively (Figure 17). After photoexcitation at 10 K, the appearance of two new vibrational bands at 1871 cm^{-1} and 1653 cm^{-1} indicates a conformation change of the nitrosyl groups toward a photogenerated metastable state (ES) assigned to a photoinduced linkage isomer. Variable-temperature infrared kinetic measurements in the range 80–114 K showed that the photoisomer decay follows a thermally activated Arrhenius behavior with an activation energy of 0.22 eV.

The infrared analysis allows defining the appropriate experimental conditions for the photocrystallographic investigation. According to the Arrhenius behavior, the ES to GS relaxation is temperature dependent in a well-predictable and tunable manner.

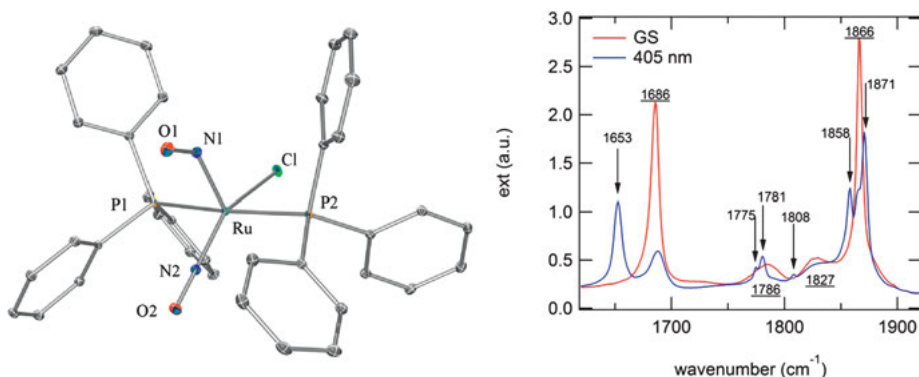


Figure 17: Left: Molecular structure of the $[\text{RuCl}(\text{NO})_2(\text{PPh}_3)_2]^+$ cationic complex in the ground state. Right: Infrared spectra (range $1620\text{--}1920\text{ cm}^{-1}$) of $[\text{RuCl}(\text{NO})_2(\text{PPh}_3)_2]\text{BF}_4$ at 10 K. Arrows indicate new lines arising upon illumination with light of the wavelength 405 nm. Underlined numbers refer to positions of ground state (GS) bands [60]. Reproduced with permission of the International Union of Crystallography.

Under continuous laser excitation, the kinetics of the population $n(t)$ of the metastable state results from a competition between the GS to ES photoexcitation and the ES to GS relaxation with rate constants k_1 and k_{-1} , respectively. The evolution equation of the excitation process is given by

$$\Phi_{\text{photoexcitation}} = \frac{dn(t)}{dt} = (1 - n(t))k_1. \quad (26)$$

The concentration of excited molecules grows exponentially:

$$n(t) = 1 - e^{-k_1 t}. \quad (27)$$

Similarly, the evolution equation of the relaxation process is given by

$$\Phi_{\text{relaxation}} = \frac{dn(t)}{dt} = -n(t)k_{-1}. \quad (28)$$

The whole process may be described by the following equation:

$$\frac{dn(t)}{dt} = \Phi_{\text{photoexcitation}} - \Phi_{\text{relaxation}} = (1 - n(t))k_1 - n(t)k_{-1}. \quad (29)$$

Solution of equation (29) gives the temporal evolution of the metastable state population:

$$n(t) = 1 - \frac{1 + n_{\text{stat}}(e^{(k_1+k_{-1})t} - 1)}{e^{(k_1+k_{-1})t}} \quad (30)$$

with $n_{\text{stat}} = \frac{k_1}{k_1+k_{-1}}$. The final population reached as $t \rightarrow \infty$ is called the photostationary state n_{stat} and is illustrated in Figure 18 for different values of the rate constants.

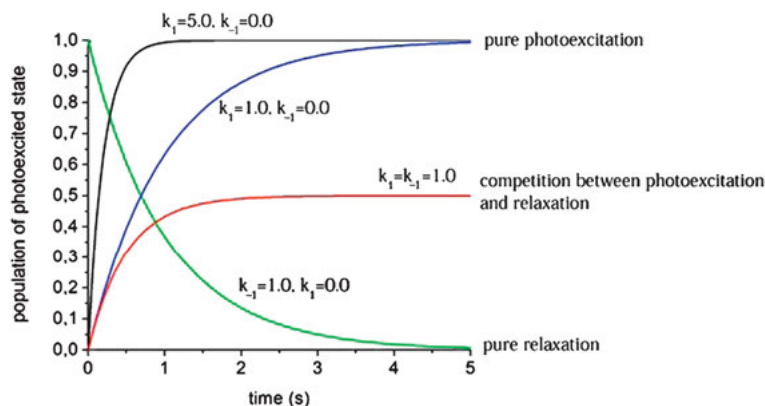


Figure 18: Evolution of the population of metastable state $n(t)$ as a function of the initial conditions ($n(0) = 0$ or $n(0) = 1$) and photoexcitation and relaxation rate constants (k_1, k_{-1}).

In addition to this kinetic competition, a limited photoconversion may also result from an overlap between absorption bands of the ground state and metastable state, leading to an additional competition between photoinduced ground state to metastable state and photoinduced metastable state to ground-state conversion.

In the case of $[\text{RuCl}(\text{NO})_2(\text{PPh}_3)_2]\text{BF}_4$, X-ray diffraction experiments were conducted at very low temperature to minimize the metastable state to ground state relaxation effect and therefore to reach a high photostationary population n_{stat} . First indications of the structural reorganization are provided by the so-called *photodifference map*, which is the Fourier transform of the difference between the photoexcited and ground-state structure factors. The phases of the structure factors are required to compute this electron density map but are not accessible experimentally. As a first approximation, the phases of the ground-state and photoirradiated states are considered to be equal to those of the ground state calculated from the ground-state structural model. This approximation is of better validity in the case of centrosymmetric structures:

$$\begin{aligned} \Delta\rho(\mathbf{r}) &= \rho_{\text{ES}}(\mathbf{r}) - \rho_{\text{GS}}(\mathbf{r}) \\ &= \frac{1}{V} \sum_{hkl} [|F_{\text{ES}}^{\text{obs}}(\mathbf{H})| - |F_{\text{GS}}^{\text{obs}}(\mathbf{H})|] e^{i\varphi_{\text{GS}}^{\text{calc}}} e^{-2i\pi\mathbf{H}\cdot\mathbf{r}}. \end{aligned} \quad (31)$$

This Fourier summation requires completeness of the Bragg peak intensity measurements to avoid any bias or artefacts in the map. The corresponding photodifference map for $[\text{RuCl}(\text{NO})_2(\text{PPh}_3)_2]\text{BF}_4$ is given in Figure 19.

The X-ray diffraction experiment was conducted on a single crystal in the photostationary state, which therefore contains at the same time molecules in the ground state

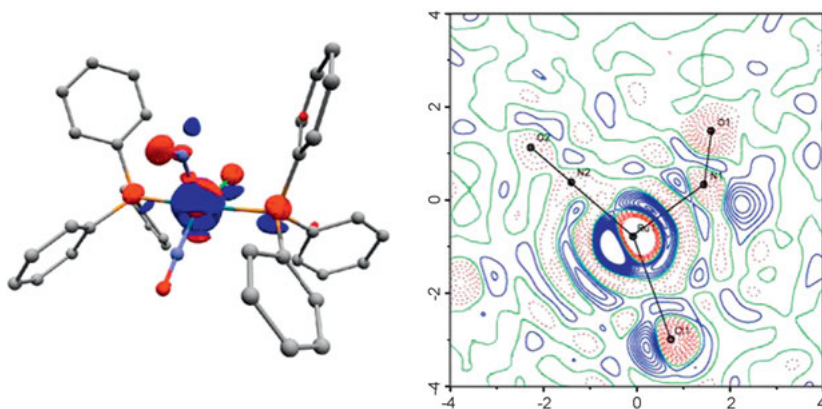


Figure 19: Left: 3D photodifference map with isosurface of $\pm 4.0 \text{ e}\text{\AA}^{-3}$ (red, negative; blue, positive) at 10 K after irradiation with 405 nm. The map is based on 8 634 independent measured reflections. Right: Section of the photodifference map in the RuN1N2 plane with isocontour of $\pm 1.0 \text{ e}\text{\AA}^{-3}$ (red, negative; blue, positive) [60]. Reproduced with permission of the International Union of Crystallography.

and molecules in the metastable state, which are spatially randomly distributed in the sample. This corresponds to the situation (b) in Figure 8 discussed before. The total electron density of the crystal at any instant t during the photoexcitation is given by

$$\rho(\mathbf{r}, t) = \sum_{i=1}^2 c_i(t) \rho_i(\mathbf{r}), \quad (32)$$

which for only two species (GS and photoexcited ES) at the photostationary state reduces to

$$\rho(\mathbf{r}, t = \infty) = c_{\text{GS}} \rho_{\text{GS}}(\mathbf{r}) + c_{\text{ES}} \rho_{\text{ES}}(\mathbf{r}). \quad (33)$$

Accordingly, the diffracted Bragg intensities are given by equation (20). From this, a structural model of the photogenerated metastable state was built and refined by least-square methods against the experimentally measured data. The result is given in Figure 20. It shows a rotation of one of the two nitrosyl groups.

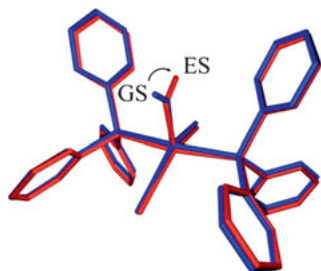


Figure 20: Structural reorganization upon photoexcitation (ground state GS in blue, photoexcited state in red) [60]. Reproduced with permission of the International Union of Crystallography.

This example illustrates the efficiency of photocrystallography to derive the atomic positions of photoinduced molecular metastable states. In the present example, the population of the metastable state in the crystal was estimated to 52(1)%, which means that the measured crystal contained almost half of the molecules in the ground-state structural configuration, and half in the photogenerated metastable state configuration with a random spatial distribution. As is shown in Figure 21, the information about the structural contrast between photoexcited state and ground state evaluated as $(I_{\text{ES}}(\mathbf{H}) - I_{\text{GS}}(\mathbf{H})) / I_{\text{GS}}(\mathbf{H})$ is quite large in the structure factor amplitude with 52% population. This contrast would be significantly reduced at a photostationary state with a metastable state population of only 10%.

3.2 Time-resolved X-ray solution scattering to study molecular photodynamics: photodissociation of I_3^- in methanol

Using the photocrystallographic approach described in the previous example, the molecular structure of out-of-equilibrium photoexcited states can be derived accu-

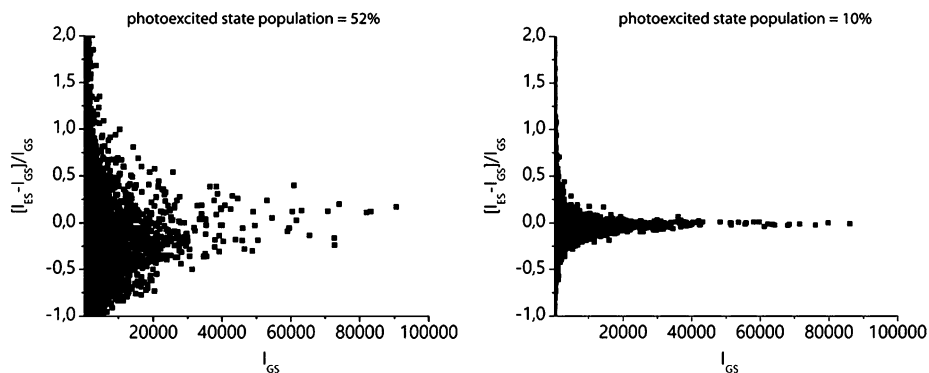


Figure 21: Contrast in Bragg peak intensities between the photoexcited state ($I_{ES}(\mathbf{H})$) and the ground state ($I_{GS}(\mathbf{H})$) for two different populations of the photogenerated metastable state at the photostationary state.

rately with atomic resolution in a quasi-static situation in a crystal. At the photostationary state ($t \rightarrow \infty$ in Figure 18), the system is not evolving as a function of time during the X-ray diffraction experiment.

Time-resolved X-ray solution scattering has been developed at synchrotron radiation sources to investigate the dynamics of chemical reactions in real time. Solutions are much simpler to handle than crystals and much less demanding in terms of sample requirements, but more demanding in terms of brightness of the X-ray beam. Unfortunately, solution scattering is much less informative than crystal diffraction. Only average isotropic information can be obtained due to the homogeneity and orientation randomness of the sample, with the exception of coherent scattering techniques (see the chapter *Ultrafast Science*).

In a solution, the dynamics are not only determined by the potential energy surface of the reactant–product species, but the surrounding solvent also plays a crucial role in modifying the energies of all species and defining the reaction pathway.

One of the simplest photoinduced chemical reactions studied by X-ray time-resolved solution scattering is the photodissociation of the triiodide ion I_3^- [61, 3]. This study followed a pump–probe approach and is illustrative of the potential of such experiments, aiming at deriving the reaction pathways and identifying the structural signature of various intermediate species and their respective time-dependent concentration changes. Such processes may be simulated by theoretical calculation as well (see the chapter *TDDFT, Excitation and Spectroscopy*). The changes in the nuclear coordinates in real time were directly recorded by varying the time delay between the laser pulse and the X-ray probe pulse. As shown in Figure 22, I_3^- may undergo three different possible dissociation pathways: two-body dissociation ($I_2^- + I$), three-body dissociation ($I^- + I + I$), and I_2 formation ($I_2 + I^-$). Time-resolved X-ray solution scattering has, at the same time, the potential to discriminate between these three

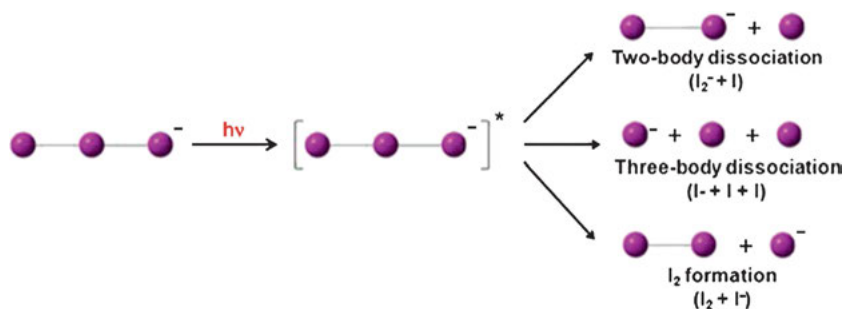


Figure 22: Candidate reaction pathways for the photodissociation of I_3^- in solution, involving two-body and three-body dissociations [61, 3]. Adapted from [3] in accordance with the Creative Commons Attribution (CC BY) license.

possibilities by detecting the presence of every intermediate species and to derive their precise molecular structure.

Time-resolved X-ray solution scattering experiments were conducted using the laser pump–probe scheme at the beamline NW14A at KEK. Laser pulses of 2-ps duration and 400-nm wavelength (second harmonic generation of the output pulses from an amplified Ti:Sapphire laser system) were focused by a lens to a spot of 300 μm on a 10-mM solution of I_3^- ions in methanol, which was circulated to refresh continuously the measured sample. 100-ps X-ray pulses with 3×10^8 photons per pulse were focused on the sample to perfectly overlap spatially with the pump laser pulses. The scattering signal was acquired with an area detector at various time delays: 100 ps, 300 ps, 1 ns, 3 ns, 10 ns, 30 ns, 50 ns, 100 ns, 300 ns, 1 μs , and 3 μs . The corresponding experimental difference scattering curves $q\Delta S(q, t)$ are shown in Figure 23 (a, b).

Detailed information of the structural dynamics can be retrieved from a global fitting procedure of the full set of difference scattering curves using equation (13). In practice, atom–atom pair distribution functions (PDF) $g_R(r)$ are calculated for the different chemical species (reactant, intermediate, product, and solvent) from molecular dynamic simulations combined with quantum chemical calculations for instance (see the chapter *Static structural analysis of condensed matter* in this book for the general scheme). Then the corresponding scattering curves $S_k(q)$ for the solute-only and solute–solvent cross terms are computed from the sine Fourier transform of $g_R(r)$. The solvent term is then derived using a separate solvent-heating time-resolved X-ray solution scattering experiment, where the pure solvent is vibrationally excited by near-infrared light [8]. The theoretical difference scattering curves are finally calculated from all these contributions. The experimental $\Delta S(q, t)$ curves at various time delays are related to each other through reaction kinetics, *i.e.* the time-dependent concentration change of all the solute species ($c_k(t)$ in equation (13)). The global fitting procedure therefore aims at retrieving the individual scattering curves $S_k(q)$ of all the chemical species and their respective concentration change $c_k(t)$. For the photodissociation of I_3^- , the time-resolved X-ray solution scattering data were analyzed by considering

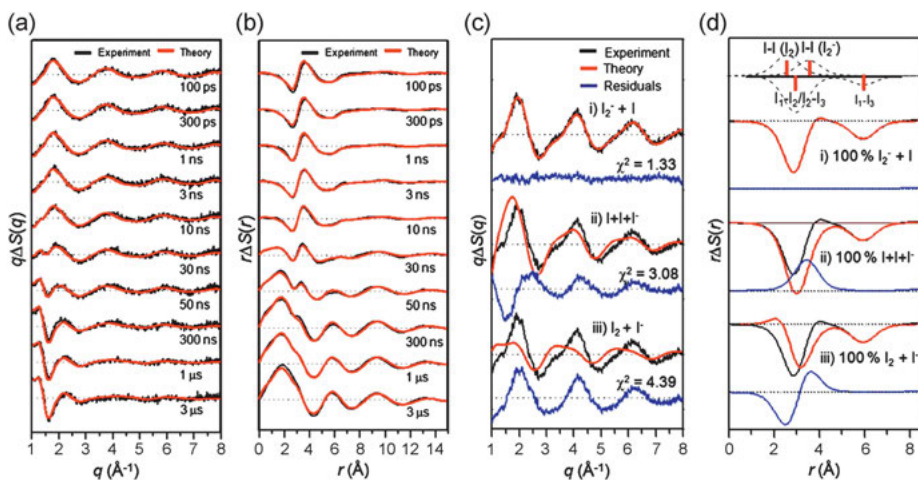


Figure 23: (a) Time-resolved difference X-ray scattering curves $q\Delta S(q, t)$ for the photodissociation of I_3^- : experimental curve in black, and theoretical fit in red. (b) Corresponding difference radial distribution functions $r\Delta S(r, t)$, calculated by the sine-Fourier transform of $q\Delta S(q, t)$. (c) Experimental and theoretical difference scattering curves and (d) radial distribution function at time delay of 100 ps using the three dynamic models given in Figure 22. Adapted from [3] in accordance with the Creative Commons Attribution (CC BY) license.

the three candidate reaction pathways; Figure 23 (c, d) show the results for the 100-ps delay data. The model employing a two-body pathway gives a much better fit than the model employing the three-body dissociation or the I_2 formation pathway. The radial distribution function $r\Delta S(r, t)$ provides a more intuitive real space view of the results. Bond lengths of various I–I atomic pairs are given in the top panel of Figure 23 (d), which help identifying the structure of the different species. The negative peak near 6 \AA indicates the depletion of the I_1 – I_3 distance in the parent I_3^- ions. The broad feature around 3–4 \AA is a combination of the depletion of the I_1 – I_2 and I_2 – I_3 distances in the parent I_3^- ions, and the formation of the I–I bond in the I_2^- ions.

From the global analysis over the entire time range from 100 ps to 3 μ s, the reaction dynamics of the different species involved may be retrieved, as illustrated in Figure 24. After 400 nm laser photoexcitation, excited I_3^- ions dissociate into I_2^- and I within less than 100 ps, which is the time resolution of the experiment. The ions I_2^- and I then recombine in approximately 80 ns. To extract more quantitative information on the structure of the ground I_3^- and intermediate I_2^- species, maximum likelihood methods have been developed for fitting the experimental scattering curves. Quite accurate I–I bond distances of 3.03(4) and 2.94(3) \AA were calculated for I_3^- , and 3.59(4) \AA for I_2^- .

This typical photodissociation study shows that by combining the structural sensitivity of X-ray scattering to the current nearly 100 ps time resolution achievable at third generation synchrotron radiation sources, the structural dynamics in solution may be elucidated in detail and in a quantitative manner. Other examples

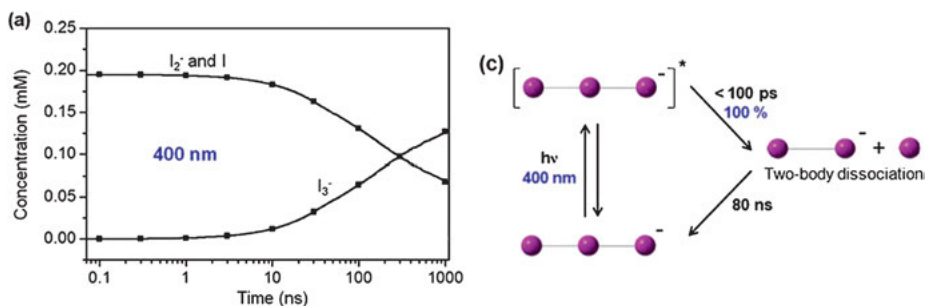


Figure 24: (a) Time-dependent concentration changes of the different transient solute species after photodissociation of I_3^- in methanol. (c) Reaction mechanism deduced from the global fitting to the scattering curves [61, 3]. Adapted from [3] in accordance with the Creative Commons Attribution (CC BY) license.

of time-resolved X-ray solution scattering studies cover the photochemistry of small molecules (CHI_3 , HgI_2 , $HgBr_2$, I_2 , Br_2) and more complex transition metal photosensitive molecules ($Ru_3(CO)_{12}$, $[Pt_2(P_2O_5H_2)_4]^{4-}$ or $cis-[Ru(bpy)_2(py)_2]^{2+}$) [62–70].

Due to the time resolution limitation at synchrotron radiation facilities, faster phenomena such as bond breaking and bond formation are out of reach. The very first direct observation of bond formation in solution has been carried out using XFEL radiation with a time resolution of nearly 500 fs in the gold trimer $[Au(CN)^{2-}]_3$ [71]. Owing to the faster time resolution, femtosecond X-ray pulses generated from XFEL sources may also provide new knowledge on the ultrashort time scale dynamics, such as coherent vibrational relaxation (periodic oscillations along the reaction coordinate) of the transient species on the hot ground-state potential or of the excited reactant species on the excited-state potential.

3.3 Molecular response: kinetic and chemical mechanisms of the bacterial blue light receptor PYP (photoactive yellow protein) from femtoseconds to seconds from solution and crystal X-ray scattering

The bacterial blue light photoreceptor PYP (photoactive yellow protein) has been for a long time used as a prototype system to develop time-resolved X-ray scattering methods covering nearly ten decades of time resolution. This is therefore an excellent example from the literature to illustrate to which extent a combination of different time-resolved small-angle and wide-angle scattering techniques performed in solution or single crystal can provide a unified view of a complex sequence of structural modifications triggered by an initial photoinduced reaction.

All biological and chemical reactions involve a motion of atoms that proceeds via a series of transient intermediate states with lifetimes spanning a wide time range from femtoseconds to seconds. Watching a protein function in real time with atomic reso-

lution is a definite goal in molecular biophysics. The relationship between a protein function and its structure is controlled by its dynamical properties, where molecular motions play a crucial role in various processes such as bond breaking, side-chain rotation, helix motion, etc. A complete understanding of protein function requires specific experiments capable of tracking both its structure and its dynamics. A fantastic breakthrough in protein structural science was achieved in the mid-1990s by the group led by K. Moffat and M. Wulff. It has developed the first time-resolved X-ray crystallography approach to catch transient three-dimensional structures of a protein (myoglobin) as it changes in response to ligand (carbon monoxide, CO) dissociation and rebinding [72, 73]. This polychromatic (Laue) X-ray diffraction experiment on single crystal was a real technological challenge; the very intense 150 ps X-ray pulses at the European Synchrotron Radiation Facility opened the way to understand the kinetics and dynamics of protein functions with atomic resolution. The focus of time-resolved structural analysis in this context is the following:

- (i) Dynamics: identify the 3D detailed atomic and molecular rearrangements between the different k intermediate species (k is a priori unknown).
- (ii) Kinetics: derive the associated time-dependent concentration profiles $c_k(t)$ and transition rates.

These scattering results provide a structural foundation to time-resolved spectroscopic investigations in solution and molecular dynamics simulations.

The typical experiment consists in photolysis of the crystal with a short visible laser pulse to initiate the biological reaction and monitoring the subsequent structural changes by collecting X-ray diffraction data at various time delays. Difference Fourier electron density maps (so-called photodifference maps) are then calculated at each time delay, and a structural model is built from the electron density maps, revealing the difference between the average structure at a time delay t with the ground-state structure.

PYP is a small photoreceptor protein that has served as a useful model system for understanding the photoreception and the subsequent signal transduction at a molecular level; the structure of the protein is given in Figure 25. This representative example is a success story, which followed the instrumental evolution from the pioneering Moffat's experiment at third-generation synchrotron (ESRF) in 1996 to recent ultrafast XFEL measurements, accompanying the continuous improvement in analysis methods and time resolution of the diffraction experiments. It served as a particular challenging test to explore the limitation and improvements of time-resolved X-ray scattering methods.

The chromophore in PYP is *p*-coumaric acid (pCA, 4-hydroxycinnamic acid); it is located in an inner binding pocket of the protein, attached covalently, and experiencing a network of hydrogen bonds with the residues of the pocket. Upon absorption of a blue photon ($\lambda_{\max} \sim 446$ nm) by the pCA chromophore, PYP enters a completely reversible photocycle illustrated in Figure 25, which has been revealed by transient

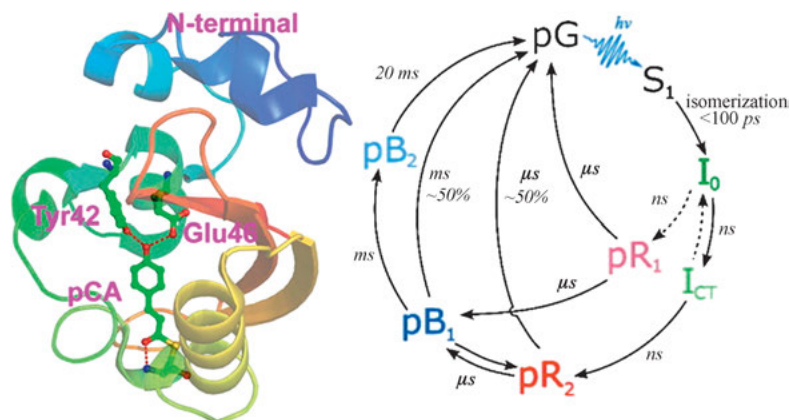


Figure 25: Simplified photocycle of photoactive yellow protein, which shows the different intermediates and the time scale between the formation of each. The dark state pG is activated by absorption of a blue photon (450 nm) that initiates the whole reversible cycle [4, 74]. Reprinted from [74] Copyright (2016), with permission from Elsevier and from [4] with permission from ACS (<http://pubs.acs.org/doi/10.1021/acs.accounts.5b00198>).

visible absorption spectroscopy. The protein is photoexcited from the pG ground state to an electronically excited state pG*, from which pCA undergoes a very fast *trans*-to-*cis* isomerization, followed by thermal relaxations to red-shifted intermediates (pR1, pR2, $\lambda_{\text{max}} \sim 465 \text{ nm}$), to blue-shifted intermediates (pB1, pB2, $\lambda_{\text{max}} \sim 355 \text{ nm}$). Spontaneous return to pG by a relatively slow process completes the cycle. Along the complete reaction path, hydrogen bonds are continuously modified, which couple to protein rearrangements, resulting in changes in shape and electrostatic potential at the protein surface, likely at the origin of the signal transduction. The long lifetime of the pB states (ms) allows a recognition of the signal by the organism.

3.3.1 Time-resolved X-ray crystallography from 100 ps to 1 s

The very first experiment aimed at structurally characterizing the important long-lived signaling pB state and was carried out at the National Synchrotron Light Source (NSLS at Brookhaven National Laboratory) [75]. The PYP single crystal was exposed to continuous laser illumination at 496.5 nm for 200 ms until the photostationary state was produced. The laser was then turned off, and the crystal was exposed to a 10 ms polychromatic X-ray pulse. This sequence was repeated 10 to 16 times to improve the signal statistics. The procedure was then repeated for each rotation position of the crystal to measure the complete diffraction sphere. The experiment provided a set of dark and light-on Bragg peak intensities, from which the corresponding dark $|F_{\text{GS}}(\mathbf{H})|$ and light-on $|F_{\text{ES}}(\mathbf{H})|$ structure factor moduli were calculated. The photodifference $|F_{\text{ES}}(\mathbf{H})| -$

$|F_{\text{GS}}(\mathbf{H})|$ electron density maps were computed, from which the structure of the photo-stationary state was refined, revealing significant structural modifications, including *trans*-to-*cis* isomerization of the pCA chromophore.

Earlier intermediates in the photocycle (pR states) were detected in a similar way, using the specific time structure of the ESRF synchrotron [76]. Here, a shorter time delay of 1 ns was used, synchronizing a 7-ns laser pulse with the X-ray pulse of 150-ps duration of the synchrotron operating in a single-bunch mode. The *trans*-to-*cis* isomerization was observed as complete within the time delay 1 ns.

In those two pioneering experiments, although a pump–probe scheme was used, the structural information that can be obtained is rather obscured by the fact that a single time delay is analyzed as a single point in a rather conventional structural refinement. In the general case, each time delay Δt corresponds to a mixture of structural configurations. Deconvolution of the structure of the individual intermediates is therefore quite difficult. A major breakthrough in terms of methodology was introduced by a global structural refinement of many diffraction data sets measured at many time delays. More than 40 time delays covering 10 decades from 100 ps to 1 s were measured at the Advanced Photon Source (APS) and ESRF and combined [77, 78]. The complete determination of the kinetic mechanism and identification of the intermediates was carried out using a mathematical procedure called Singular Value Decomposition (SVD), which we briefly describe here.

The experimental pump–probe procedure consists in measuring X-ray diffraction data at fixed time delays Δt after pump laser pulses. The negative time point (for instance, -20 ns) corresponds to a situation in which the X-ray pulse arrives in advance of the laser pulse, which provides the dark ground state pG. For each time delay Δt , the 3D difference electron density map $\Delta\rho(\mathbf{r}, \Delta t)$ is computed from the Fourier transform of the difference between photoexcited and dark structure factor moduli $\Delta F(hkl, \Delta t)$. Figure 26 shows the difference in electron density for PYP at $\Delta t = 100$ ps.

The method of SVD allows extracting time-independent difference electron densities for relevant intermediates from the mixture of time-dependent densities at each time point. First, an $M \times N$ data matrix A is constructed by arranging M grid points of $\Delta\rho(\mathbf{r}, \Delta t)$ at N time points. SVD decomposes this time- and real-space-dependent data matrix A into three matrices: the matrix U of left singular vectors corresponding to time-independent difference electron density maps, the matrix V^T (transpose of a matrix V) of right singular vectors containing the time dependence of the corresponding left singular vectors, and the matrix S whose diagonal elements (the singular values) represent the degree to which the left and right singular vectors contribute to the data matrix. In a mathematical form, $A = USV^T$.

Using an SVD and global data analysis methodology, accurate structures of all the intermediates and the rate parameters for interconversion between them were recovered. Four intermediates, denoted pR0, pR1, pR2, and pB0, were required to account for the time-dependent difference density maps. Figure 27 shows the results in different forms: time-dependent population of each intermediate in the photocycle

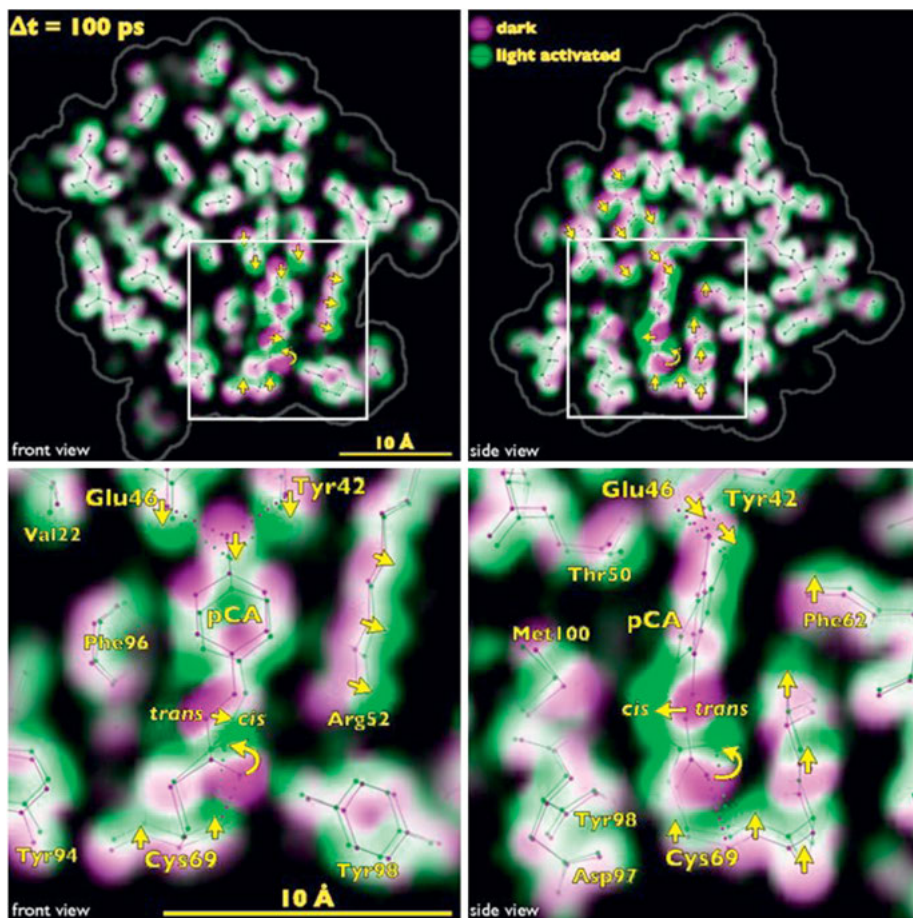


Figure 26: Superposition of the ground state (magenta) and 100-ps (green) electron density maps of PYP, together with corresponding structural changes. Large amplitude atomic displacements are depicted as yellow arrows [78].

(Figure 27 (B)) and structures of the four intermediates overlaid with corresponding electron density maps (Figure 27 (C–F)).

3.3.2 Time-resolved solution scattering from 100 ps to 1 s

Such a study illustrates the detailed structural kinetic information that can be retrieved at atomic-scale resolution from time-resolved X-ray diffraction experiments on crystals. Time-resolved crystallography effectively probes the dynamical structure with high spatial and temporal resolution. However, we may wonder whether the crystal environment may restrict large structural changes due to inherent crystal contacts. This is important in the case of PYP since time-resolved spectroscopic studies in so-

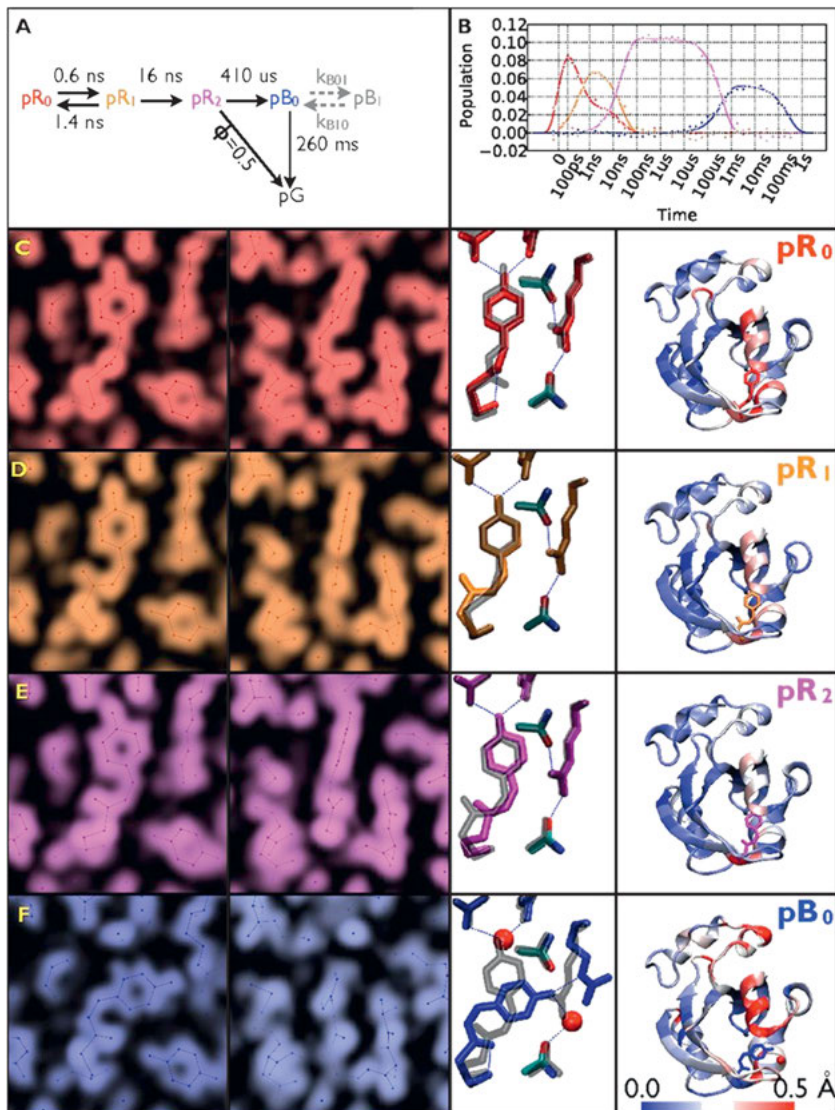


Figure 27: Results of the kinetic global structural analysis. (A) Kinetic model. (B) Time-dependent populations of each intermediate in the PYP photocycle. (C–F) Electron density maps and structure of the different intermediates [78].

lution and crystalline phases suggest that the reaction pathways depend on the sample phase. The reaction path visualized by time-resolved X-ray crystallography may not represent the kinetic mechanism applicable in solution. In this situation, pump-probe X-ray solution scattering methods have been employed with the same temporal resolution as the crystallographic investigations, i.e., from picoseconds to milliseconds [4, 79, 80]. The goal of solution scattering measurements is to investigate the

molecular mechanism by which pCA photoisomerization drives the protein conformational changes that lead to the PYP signaling state. In that sense, it is perfectly complementary to time-resolved X-ray crystallography, probing a different spatial scale.

The first measurement was performed at the ESRF in the 16-bunch filling mode (16 equally spaced intense bunches). The photoreaction was initiated with laser pulses at 460 nm and sent to a capillary containing the solution sample. X-ray pulses at $-50 \mu\text{s}$ and at 21 time delays from $3.16 \mu\text{s}$ to 300 ms probed the sample. The corresponding time-resolved difference scattering curves $q\Delta S(q, t)$ are given in Figure 28. The complete set of data curves was analyzed using an SVD scheme to provide (i) the individual time-independent difference scattering curves for the four major components assigned to the pR1, pR2, pB1, and pB2 intermediates (corresponding to the photocycle illustrated in Figure 25) and (ii) the associated time-dependent populations. Those populations compare quite well with the time-resolved crystallographic results.

The molecular shape was reconstructed from the individual scattering curves of each intermediate. Let us recall that solution scattering corresponds to an orientation averaging of the scattered signal due to the random orientation of the solute molecules in the solvent at the probed time scale (μs –ms). To get relevant structural informa-

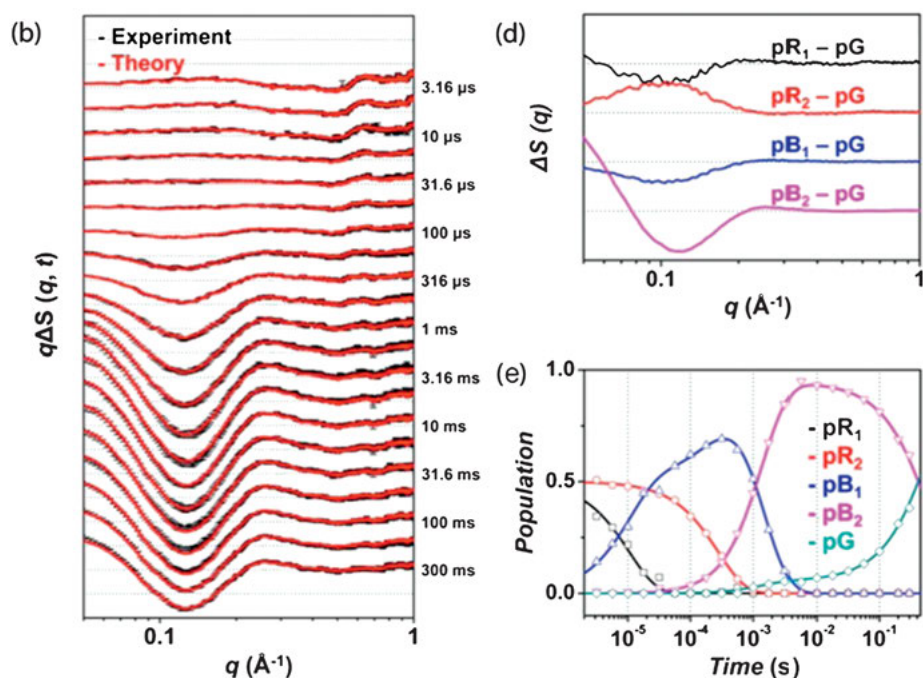


Figure 28: (b) Time-resolved difference scattering curves $q\Delta S(q, t)$ of PYP in solution and model curves calculated from the kinetic analysis (in red). (d) Difference scattering curves of the different intermediates. (e) Population changes of the different intermediates as a function of time. Reprinted from [4] with permission from ACS (<http://pubs.acs.org/doi/10.1021/acs.accounts.5b00198>).

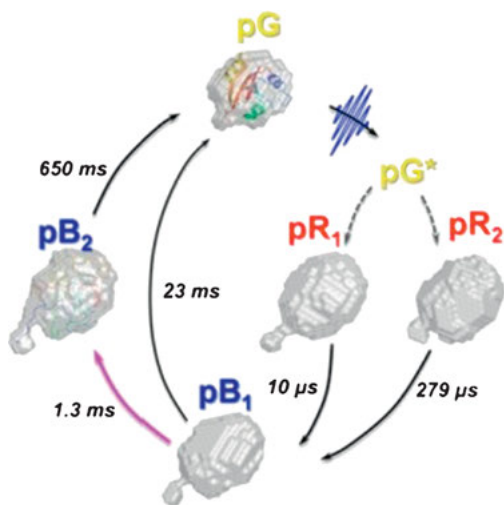


Figure 29: Global molecular shapes of the protein intermediates in solution obtained from the shape reconstruction method of solution scattering data. Reprinted from [4] with permission from ACS (<http://pubs.acs.org/doi/10.1021/acs.accounts.5b00198>).

tion from the orientation average curve, a specific Monte Carlo modeling procedure was used as detailed in [4]. The results are given in Figure 29. It shows large conformational changes of the protein, especially a protrusion of the *N*-terminal domain in the signaling pB1 and pB2 states, which proves that the photoinduced reorganization propagates from the inner chromophore to the entire protein along the photocycle. The protein volume gradually increases and becomes maximal in the final intermediate. In addition, the data reveal that a common kinetic mechanism is applicable to both crystalline and solution phases.

A separate time-resolved X-ray solution scattering experiment was performed with a much shorter ~ 150 ps time resolution [80]. Solution scattering data were measured at the APS running in the hybrid filling mode (a single bunch isolated from the remaining bunches). The solution was contained in a silica capillary, which was translated along a direction orthogonal to the X-ray and laser beams to refresh the sample between each pump–probe cycle. The originality of this measurement is that the time resolution is much shorter than the rotational diffusion of the solution. For PYP in solution, the absorption probability of the pCA chromophore depends on the angle between the laser polarization vector and the transition dipole moment for pCA, which is nominally aligned along the pCA long axis. Photoisomerization of pCA triggers the protein contraction as identified in the photocrystallographic experiments detailed above. Accordingly, photoactivation of PYP produces an anisotropic orientational distribution of photoexcited pR0 states that favors PYP whose pCA is aligned with the laser polarization axis. Scattering from an anisotropic orientational distribution of pR0 intermediates can produce an anisotropic X-ray scattering pattern, which was recorded in a time-resolved manner in this experiment.

The difference scattering signal was analyzed using an SVD scheme. The results are given in Figure 30. We can see that the derived time-dependent population of the

pR0 and pR1,2 states matches perfectly the longer evolution of the previous experiment (Figure 28). The small angle part of the scattering curves (shaded area in Figure 30 (A)) was integrated and divided by the ground-state amplitude to compute the relative change (Figure 30 (B)). The nearly 1.8% increase in integrated small angle X-ray scattering (SAXS) signal corresponds to a volume change of -0.25% , reflecting a global contraction of the protein.

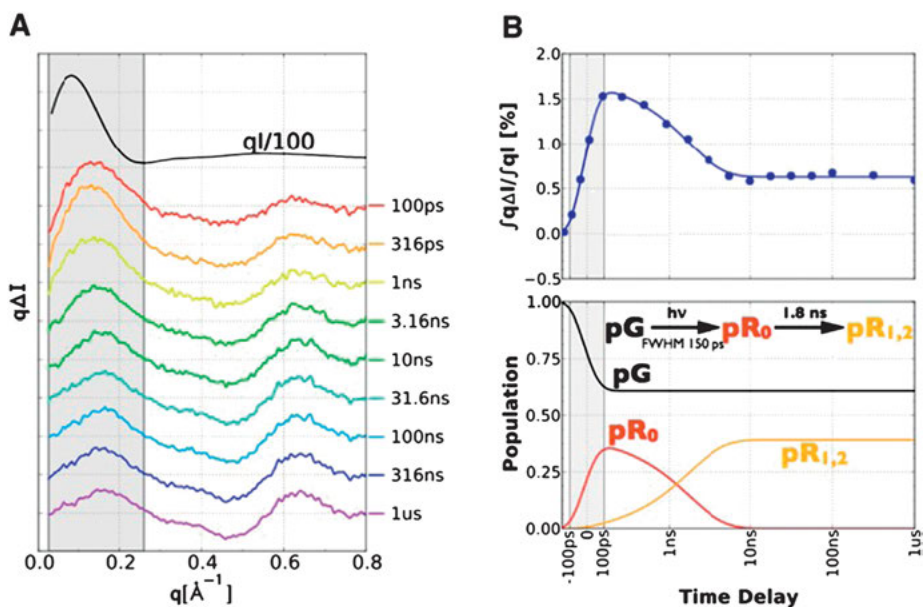


Figure 30: (A) Time-resolved Small Angle X-ray Scattering (SAXS) data recorded as a function of pump–probe time delay. (B) (top) Time dependence of the integrated SAXS intensity (integration over the shaded region of figure A). (bottom) Time-dependent population of the different intermediates. Reprinted with permission from [80]. Copyright (2013) American Chemical Society.

3.3.3 Serial crystallography at XFEL facilities

The crystal and solution scattering experiments detailed in the previous sections were all based on a pump–probe measurement scheme, which is applicable to reversible photoactivated processes only. This was the case of the reversible photocycle of PYP. For nonreversible processes, an alternative measurement strategy has to be employed, such as time-resolved serial crystallography [81–84]. Synchrotron-based diffraction experiments are currently restricted to strongly scattering, relatively large crystals due to the X-ray beam brilliance. The time resolution is at the moment limited to about 100 ps (extended to 100 fs in slicing modes as presented in Section 2) by the duration of the probe X-ray pulse. As shown in Figure 25, the very earliest events of the photocycle of PYP, the photoisomerization of the pCA chromophore occurs on ultrafast

time scales and therefore could not be resolved with the synchrotron experiments described before. The method of serial femtosecond crystallography at XFEL sources has opened new possibilities for structural crystallography. In a typical experiment, a stream of nano- or microcrystals suspended in mother liquor, which could be close to the physiological conditions, is delivered by a liquid jet injector to the laser interaction region. The jet is further illuminated by very intense X-ray pulses from a free-electron laser X-ray source. A massive X-ray dose is delivered to the sample by the femtosecond X-ray pulse, leading to a destruction of the crystal, but only after the diffraction signal has been recorded (see the description and Figure 1 in the chapter *Ultrafast science*). Using such an approach, each crystal is illuminated only once by the laser and X-ray pulse before the next crystal arrives. Using this measurement protocol, much smaller crystals may be measured, but more importantly, irreversible photoinduced processes can be measured. The very first serial femtosecond crystallography experiment conducted on PYP was performed at the LCLS (Linac Coherent Light Source, Stanford) [83]. By comparison with the previous Laue synchrotron experiments, the difference electron density maps have shown a nice similarity, establishing the importance of the methods for challenging studies at much shorter time scales in the fs to ps range [84]. Through this high temporal resolution experiment, the structural dynamics of the *trans-to-cis* photoisomerization reaction of pCA has been monitored.

3.4 From the molecular to the macroscopic crystal response: successive steps of the dynamical process of photoinduced spin transitions

In the previous example, the molecules were considered as noninteracting entities in a crystal, whose photoexcitation may be considered as a spatially random unimolecular process. The structure of the transient excited states could be derived through time-resolved X-ray crystallography. In cooperative crystals, for which the constituting elements (atoms/ions/molecules) interact through various kinds of interactions, the unimolecular approximation may not be valid, the photoinduced events being not independent anymore. In such cases, we may expect not only the rates, but also the mechanisms to depend on the environment. In the following, we consider iron coordination complexes as representative examples of cooperative solids; their structural dynamics have been quite extensively studied.

The molecular switching phenomenon in Fe-coordination complexes (Fe(II) and Fe(III) complexes), especially those with FeN_6 coordination environment exhibiting the so-called spin-crossover phenomenon, is quite well understood and documented. The electron configuration of Fe(II) ions consists of six electrons distributed within $3d$ atomic orbitals. In perfect octahedral O_h coordination, five d orbitals are split into two subsets, namely d_{xy} , d_{xz} , d_{yz} , which are the basis of the t_{2g} irreducible representation, and d_{z^2} and $d_{x^2-y^2}$, which are the basis of the e_g irreducible representation. The t_{2g}

orbitals are nonbonding, whereas the e_g orbitals are antibonding, so that the transfer of one electron from a t_{2g} orbital to a e_g orbital is accompanied by an elongation of the Fe–N bond distance, which may be taken as the reaction coordinate. For Fe(II) complexes, the bond length typically increases by 0.20 Å. As a consequence, the Fe–N bond stretching frequency shows a marked difference between the high-spin (HS) and the low-spin (LS) states, lying around 390–430 cm^{-1} in the LS state and 210–250 cm^{-1} in the HS state, associated with a softer potential owing to the more antibonding character in the HS state.

As an illustrative example of Fe(II)-based complexes, Figure 31 shows the potential energy diagram (Djablonski diagram) of $[\text{Fe}^{\text{II}}(\text{bpy})_3]^{2+}$ in water. The energy diagram shows that the ${}^1A_1(t_{2g}^6)$ electronic state is the LS ground state, ${}^5T_2(t_{2g}^4e_g^2)$ is the HS lowest excited state. Higher in energy are several higher excited singlet, triplet, and quintet states (ligand field or metal centered states), and low lying metal–ligand charge transfer (MLCT) states. The dynamics of the switching in spin-crossover and LS Fe-complexes has been explored extensively through transient optical absorption spectroscopy and X-ray absorption spectroscopy experiments performed in solution [85]. These measurements allow drawing a general scheme for the fundamental molecular processes. Fe(II) molecular complexes undergo an LS to HS molecular photoinduced spin state switching on a sub-ps time scale. More specifically, electrons from the 1A_1 -singlet ground state are excited optically in the higher lying MLCT bands, from which the electronic population relaxes to the 5T_2 state via intersystem crossing. The photoexcited HS state can last from ns to days and has been extensively characterized for many systems through very-low-temperature measurements, as well as ns transient optical measurements at more elevated temperatures (typically at 100–250 K). The exact pathway by which the MLCT state relaxes to the 5T_2 state is system dependent and is still a matter of debate in the literature, especially whether a triplet 3T_1 state is involved.

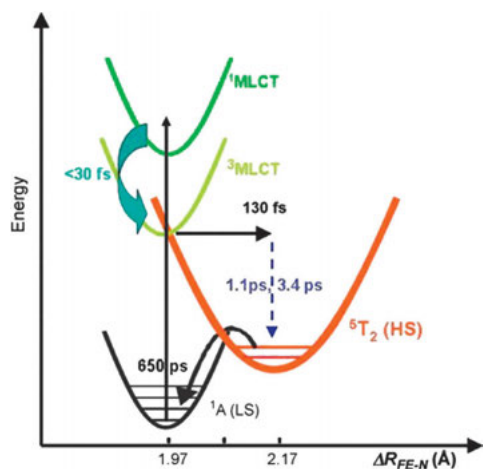


Figure 31: Potential energy diagram of $[\text{Fe}^{\text{II}}(\text{bpy})_3]^{2+}$ in water. Reprinted from [85], Copyright (2010), with permission from Elsevier.

In the solid state, the photoactive Fe(II) (or Fe(III)) molecules are confined in a crystalline matrix of other molecules with which they interact, rendering the mechanisms more complex. We may expect that the photoinduced dynamics follow a complex pathway from the molecular switching extending to the macroscopic scale through a sequence of different processes spanning almost ten decades in time. This mechanism has been studied on a prototype Fe(III) spin-crossover complex [(TPA)Fe(III)(TCC)]PF₆ (TPA denotes tris(2-pyridylmethyl)amine, and TCC denotes 3,4,5,6-tetrachlorocatecholate) whose molecular structure is shown in Figure 32. For this complex, the ⟨Fe–N⟩ bond length varies from ⟨Fe–N⟩_{LS} = 1.967(3) Å to ⟨Fe–N⟩_{HS} = 2.127(3) Å determined from X-ray crystallography and structural refinement at thermal equilibrium (at 400 K in the complete HS state and at 80 K in the complete LS state). In a crystal containing a fraction X_{HS} of HS molecule and $(1 - X_{\text{HS}})$ LS molecules, the spatially averaged bond distance is given by

$$\langle \text{Fe-N} \rangle = X_{\text{HS}} \langle \text{Fe-N} \rangle_{\text{HS}} + (1 - X_{\text{HS}}) \langle \text{Fe-N} \rangle_{\text{LS}}. \quad (34)$$

Pump–probe time-resolved optical and X-ray spectroscopy measurements have shown that the out-of-equilibrium transformation dynamics in Fe(II)-based complexes triggered by a femtosecond laser pulse exhibits a succession of consecutive steps, spanning sub-ps to μs time scale [85]. The variation in intensity of the transmitted probe light ($\Delta I/I$) measured at 600 nm on a single crystal of [(TPA)Fe(III)(TCC)]PF₆ after femtosecond excitation at 800 nm is given in Figure 32. First, the absorption of light locally switches a small fraction $\Delta X_{\text{HS}}^{hv} \approx 1\%$ of molecules from LS to HS in the sub-ps time scale. This is called the photoinduced step. The absorption is then constant until 1–10 ns, and no further molecular switching occurs. During this interval, photoexcited molecules release heat through electron–phonon coupling and phonon–phonon relaxation processes. Fifty ns after photoexcitation, the fraction of HS molecules increases during a second step, and finally a third step is identified by a further increase of the HS population on the microsecond regime.

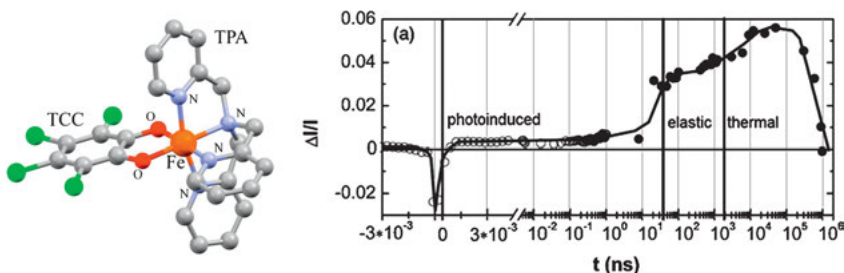


Figure 32: Left: Molecular structure of [(TPA)Fe(III)(TCC)]PF₆ (TPA denotes tris(2-pyridylmethyl)amine, and TCC denotes 3,4,5,6-tetrachlorocatecholate). Right: Differential intensity of transmitted probe light ($\Delta I/I$) measured on a single crystal of [(TPA)Fe(III)(TCC)]PF₆ after femtosecond excitation at 800 nm at 200 K probed at 600 nm [86–89]. Reprinted from [88], Copyright (2010), with permission from Elsevier.

To draw a complete structural dynamics picture, time-resolved X-ray diffraction experiments have been performed with 100 ps resolution at X-ray synchrotron radiation facilities. The results are given in Figure 33. From the structural analysis, the time-dependent unit cell parameter $a(t)$ and $\langle\text{Fe-N}\rangle(t)$ bond distances have been retrieved with high accuracy. From $\langle\text{Fe-N}\rangle(t)$ the time evolution of the HS fraction may be computed and compared to the visible absorption spectroscopy results as

$$\langle\text{Fe-N}\rangle(t) = X_{\text{HS}}(t)\langle\text{Fe-N}\rangle_{\text{HS}} + (1 - X_{\text{HS}}(t))\langle\text{Fe-N}\rangle_{\text{LS}} \quad (35)$$

and

$$X_{\text{HS}}(t) = \frac{\langle\text{Fe-N}\rangle(t) - \langle\text{Fe-N}\rangle_{\text{LS}}}{\langle\text{Fe-N}\rangle_{\text{HS}} - \langle\text{Fe-N}\rangle_{\text{LS}}}. \quad (36)$$

Although collective effects are at the origin of the observed physical properties, this crystallographic treatment follows case (b) of Figure 8, assuming a random distribution of photoexcited species. In addition, oscillation of Bragg peak intensity reveals the presence of ultrafast acoustic phonons after laser pulse excitation (case (e) of Figure 9). In some particular cases, a clear time-resolved evolution of the width of the Bragg peaks is observed and attributed to strain and inhomogeneities development in the crystal (this corresponds therefore to case (d) of Figure 8). The evolution of all these parameters parallels the visible transient absorption behavior nicely and allows defining the complete transformation mechanism covering time scales from femtoseconds to seconds (Figure 33, right). During the three successive steps, the HS molecule

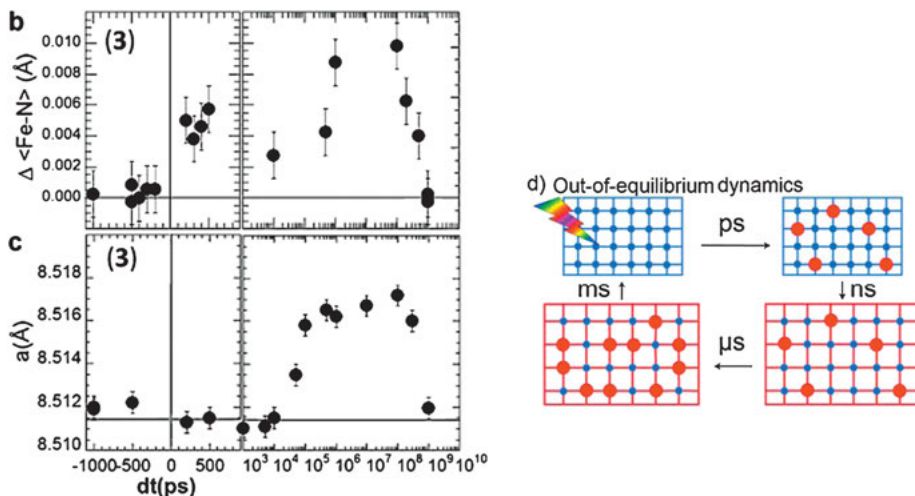


Figure 33: Time-dependent structural changes: (b) evolution of the average Fe-N bond distance $\Delta\langle\text{Fe-N}\rangle$, (c) evolution of the unit cell parameter a , (d) schematic drawing of the complete dynamics. Reprinted with permission from [89]. Copyright (2009) by the American Physical Society.

population $X_{\text{HS}}(t)$ is revealed by the temporal evolution of the $\langle \text{Fe-N} \rangle(t)$ average bond length evolution. A nearly 3% instantaneous increase of HS-state molecules occurs just after the pump laser pulse during the 100 ps of the phototransformation, which is the time resolution of the diffraction experiment. Faster processes are not resolved with this experimental configuration. The molecular structure is unchanged in the 1–10 ns range. During this time, the unit cell volume remains constant. Volume expansion involves propagation of cell deformation, limited by the speed of sound, and therefore occurs at slower time scale. This first step is therefore a unimolecular process. Volume expansion occurs in a few tens of nanoseconds owing to combined expansion of phototransformed HS molecules and local heating by nonradiative energy dissipation of relaxing higher lying charge transfer states. The HS population increases from 3% to 6% in the microsecond time scale associated with a thermally activated process resulting from the heating. Ultimately, the crystal recovers thermal equilibrium in the millisecond time scale. It is worth noting that steps 2 and 3 rely on elastic wave propagation and heat diffusion processes and, as such, are expected to depend strongly on the size and shape of the probed samples, owing to different available degrees of freedom for energy redistribution.

The crystal structure of the monoclinic form of $[(\text{TPA})\text{Fe}(\text{III})(\text{TCC})]\text{PF}_6$ was evaluated at two delays, 500 ps and 50 μs , from accurate time-resolved X-ray diffraction measurements performed at the Advanced Photon Source (APS, BioCARS beamline). The corresponding photodifference maps are given in Figure 34. These two maps show significant electron density redistribution upon excitation. At 500 ps, a shift of electron density around Fe1 toward O1 is observed, even more pronounced at 50 μs . A structural refinement based on the intensity ratios has been performed to derive the complete molecular geometry change. A systematic Fe–N and Fe–O bond elongation has been characterized.

The example of $[(\text{TPA})\text{Fe}(\text{III})(\text{TCC})]\text{PF}_6$ described in this section highlights that time-resolved X-ray scattering methods on single crystals have the potential to resolve the structural dynamics over different time scales and different length scales. As a

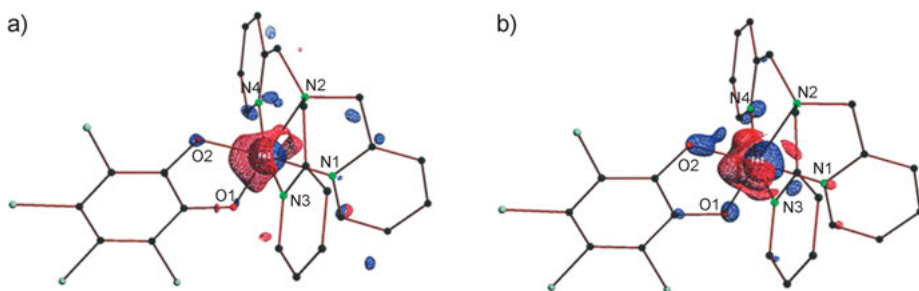


Figure 34: Photodifference maps of the monoclinic form of $[(\text{TPA})\text{Fe}(\text{III})(\text{TCC})]\text{PF}_6$ for (a) the 500 ps data and (b) the 50 μs data with isosurfaces (red positive, blue negative) of $\pm 0.14 \text{ e}\text{\AA}^{-3}$, and $\pm 0.46 \text{ e}\text{\AA}^{-3}$, respectively. Reproduced from Ref. [86] with permission from the PCCP Owner Societies.

matter of fact, the transient displacement of Bragg peaks allowed deriving the temporal evolution of the unit cell (volume expansion and distortion). Altered dynamics are expected to happen for nanoparticles or low-dimensional systems. Indeed, the time scale for processes (ii) and (iii) have been reported much faster in nanoparticles of the SCO system $[\text{Fe}(\text{pz})\text{Pt}(\text{CN})_4]$. For that purpose, appropriate methods for the time-resolved structural analysis of nanoscale objects are required; this is the subject of the next section.

3.5 Time-resolved total X-ray scattering: dynamic behavior of nanoscale systems

Total X-ray scattering coupled to Debye function analysis in reciprocal space, or pair distribution function (PDF) analysis in the real space has revolutionized the structural determination of disordered and nanoscale materials (see the chapter *Static structural analysis of condensed matter*). This nanocrystallographic approach has expanded much recently owing to the growing accessibility to high-flux X-ray beamlines at third-generation synchrotron sources. The advances in terms of beam stability, flux, and X-ray detector technologies render possible the time-resolved or time-dependent extension of the method. This has enabled the in situ studies of materials as functions of temperature, pressure, or reaction coordinate.

One of the first time-resolved PDF analyses was performed at the Advanced Photon Source, using a fast-readout (30 Hz) silicon detector [90]. The study focused on the reduction of $\text{Pt}^{\text{IV}}\text{O}_2$ to metallic Pt^0 under hydrogen gas at elevated temperature. The complete measurement took ~ 6 s for 200 consecutive $G(r)$ measurements. The process is irreversible, and therefore, no stroboscopic technique was used. The intensity of the peaks corresponding to Pt–O and Pt···Pt distances was followed as a function of time to detect the appearance of Pt^0 (Figure 35). The PDF of the final product was successfully refined as the face-centered cubic structure of metallic Pt^0 .

Catalytic processes have been investigated measuring total X-ray scattering of ~ 2 nm size Pt nanoparticles while changing periodically every 30 s the external environment between stoichiometric (*stoic*; $2\text{CO}:\text{O}_2$) and oxidizing (*ox*; $\text{CO}:\text{O}_2$) conditions, total X-ray scattering data being collected every 1 s [91]. The temporal resolution of the experiment was therefore 1 second. Structural changes have been detected in the PDF, which indicated that the nanoparticles adapt rapidly and reversibly to the modulated chemical environment.

The mechanisms of formation of nanoparticles for various materials, such as WO_3 , TiO_2 , Pt, Pt_3Gd , and maghemite ($\gamma\text{-Fe}_2\text{O}_3$), has been followed by in situ time-resolved total X-ray scattering coupled to pair distribution function analysis using a specifically designed reactor for hydrothermal synthesis [92–96]. The precursor solution was inserted and heated monitoring the scattering signal during the reaction progress with a resolution of nearly 1 second. The analysis provided in real-time direct information

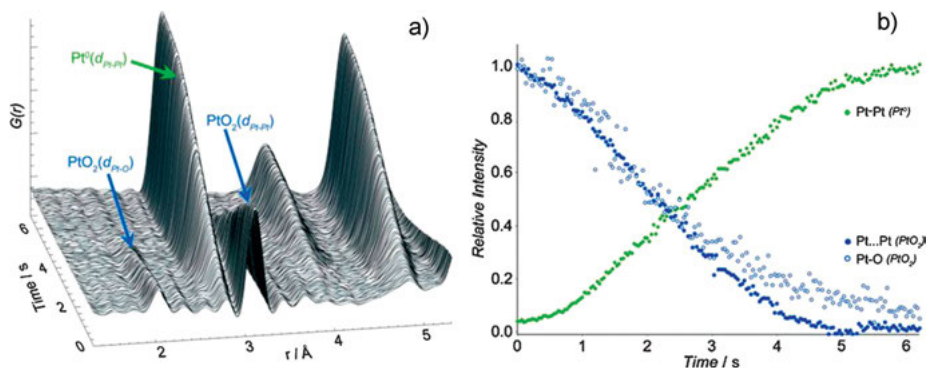


Figure 35: (a) Series of 200 PDFs collected over ~ 6 s for the in situ reduction of $\text{Pt}^{\text{IV}}\text{O}_2$ to metallic Pt^0 under hydrogen gas. (b) Relative peak intensity corresponding to the $\text{Pt}\cdots\text{Pt}$ and Pt-O bond lengths during the reaction [90]. Reproduced with permission of the International Union of Crystallography.

on the buildup of local structure (first-neighbor interatomic bond formation, polyhedral transformation) and cluster growth through the damping of the correlations in the PDF at longer distances. The presence of transient structural species may also be detected. The data can be further fit to kinetic models such as the Avrami model of nucleation and growth.

The evolution of the atomic structure during maghemite ($\gamma\text{-Fe}_2\text{O}_3$) nanoparticle formation provides a very illustrative experiment [95]. The goal was to understand how tetrahedral and octahedral iron oxide units link to form crystalline maghemite nanoparticles. The precursor solution contained ammonium iron(III) citrate. The experimental PDF of the precursor solution presents sharp peaks, characteristic of Fe-O , C-C , and C-O bonds, which have been modeled as octahedrally coordinated Fe(III) [FeO_6] complexes, which most probably form coordination polymers [$\text{Fe}(\text{H}_2\text{cit})(\text{H}_2\text{O})_n$] in solution. The formation of maghemite was followed at temperatures ranging from 270 to 370 $^\circ\text{C}$ and at 250 bar using the hydrothermal synthesis setup. The corresponding time-dependent PDFs obtained at 320 $^\circ$ are given in Figure 36. As can be seen, just after initiation of the reaction, the precursor peaks in the range 2.5–5.5 \AA decrease in intensity, corresponding to a change of Fe coordination. This relates to a decomposition of the citrate ions in CO , CO_2 , and H_2O . Simultaneous peaks at 3.2 \AA and 3.5 \AA appear, indicating the formation of Fe-Fe and Fe-O correlations. The final structure agrees with the crystalline spinel form $\gamma\text{-Fe}_2\text{O}_3$. After 10–20 s, the peaks detected in the range 2.9–3.5 \AA indicate that the octahedral and tetrahedral Fe environments (Fe_O , Fe_T) may be distinguished in the nanoclusters (Figure 36). The appearance of the $\text{Fe}_\text{O}-\text{Fe}_\text{T}$ correlation peak in the PDF is delayed, which demonstrates that the primary clusters in the solution consist exclusively of edge-sharing [FeO_6] units with very short-range order. After ~ 10 s, the presence of a peak at 3.5 \AA corresponds to the disordered maghemite-like assembly of tetrahedrally (corner sharing) and octahedrally (edge-

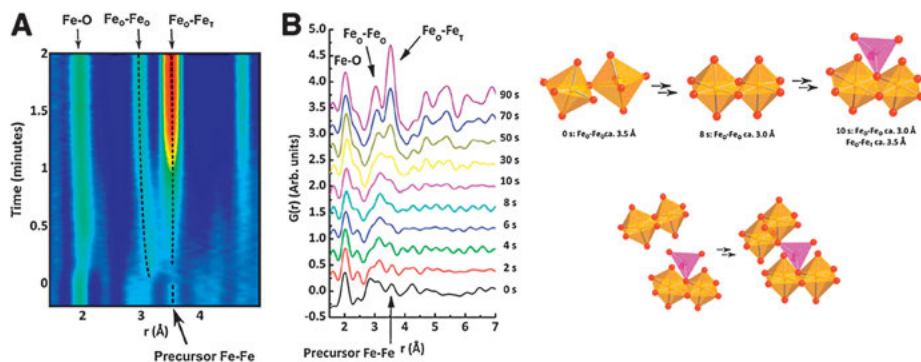


Figure 36: Left: (A) Contour plot of the low r -range PDFs obtained at 320° and (B) selected PDFs at the initial stages during maghemite formation. Right: Proposed structural model for the mechanism of formation and growth of maghemite $\gamma\text{-Fe}_2\text{O}_3$ nanoparticles: initial formation of octahedrally coordinated iron to edge-sharing cluster and condensation through tetrahedrally coordinated iron atoms. Adapted with permission from [95]. Copyright (2014) American Chemical Society.

sharing) coordinated iron atoms. The complete process proposed by the authors is depicted on the right panel in Figure 36.

3.6 Time-resolved crystallography under external applied electric field

The structural response of piezoelectric and ferroelectric materials has been studied through quasi-static and time-resolved X-ray diffraction methods on single crystals and ceramics. This provides nice illustrative examples of case (d) of Figure 8. BaTiO_3 is a model ferroelectric system, which has been studied in detail. It has a cubic perovskite-type structure (space group $Pm\bar{3}m$) in the high-temperature phase and undergoes a first-order ferroelectric phase transition to a tetragonal phase (space group $P4mm$) at $T_c = 400$ K. In the tetragonal phase, Ti is displaced in the crystallographic c direction, resulting in a spontaneous polarization along the c -axis (Figure 37). Six polarization orientations are possible in the crystal in the tetragonal phase, forming 90° -domains and 180° -domains due to the cubic to tetragonal symmetry reduction. In tetragonal BaTiO_3 , the application of an electric field results in a displacement of the Ti atom along the electric field direction, giving rise to a lattice distortion as shown in Figure 37 (b). When the electric field is applied along the direction of spontaneous polarization, the c -axis of the lattice elongates, whereas in contrast, the a -axis shrinks. The components d_{33} and d_{31} of the piezoelectric tensor may be derived from this unit cell deformation as given in Figure 37.

X-ray diffraction measurements have been performed using the BL-1A beamline of the Photon Factory of the high-energy accelerator research organization (KEK) in Japan [97]. The X-ray beam was incident on the c -face and a -face of a monodomain BaTiO_3 single crystal, applying the static electric field in the direction of spontaneous

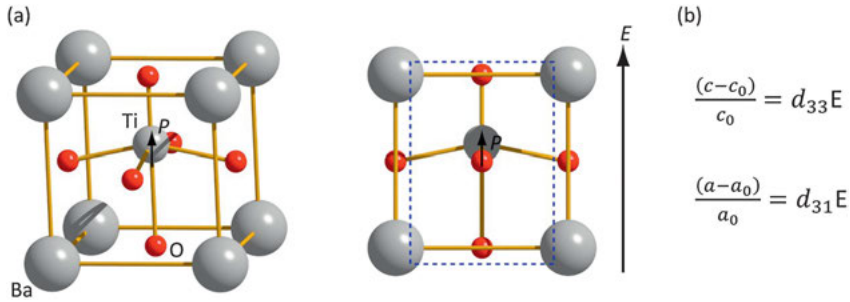


Figure 37: (a) Tetragonal structure of BaTiO₃ perovskite. (b) Piezoelectric effect. The Ti atom is displaced along the direction of the applied electric field leading to a lattice distortion depicted as blue dotted lines. When an electric field is applied along the direction of spontaneous polarization, the *c*-axis elongates giving a positive value of d_{33} , whereas the *a*-axis contracts giving a negative value of d_{31} .

polarization along the *c*-axis direction. The amplitude of the electric field was at least ten times larger than the coercitive field ($\sim 1 \text{ kV cm}^{-1}$) necessary for domain switching. The measurements were first performed for the positive ($E+$) direction and then changed to the negative direction ($E-$). A linear expansion of the *c*-axis and linear contraction of the *a*-axis was observed (Figure 38), corresponding to estimated values of $149(54) \text{ pm V}^{-1}$ and $-82(61) \text{ pm V}^{-1}$ of the piezoelectric coefficients d_{33} and d_{31} , respectively.

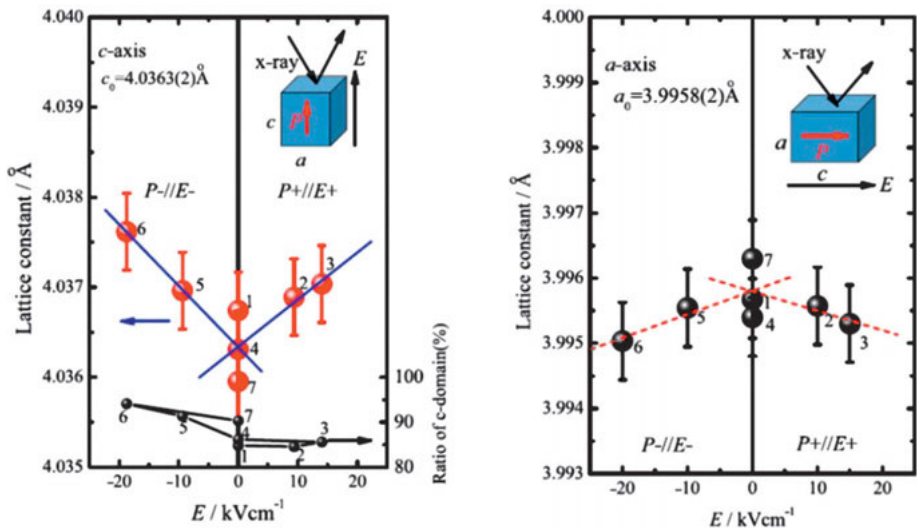


Figure 38: Left: Elongation of the *c*-axis of BaTiO₃ versus electric field E applied along the direction of the spontaneous polarization P . Right: Contraction of the *a*-axis versus electric field E applied perpendicularly to the spontaneous polarization P . Republished with permission of IOP Publishing Ltd, from [97]; permission conveyed through Copyright Clearance Center, Inc.

The dynamics of polarization switching was further investigated using a weaker periodic electric field of ± 22 V across a 1-mm thick single crystal of BaTiO_3 [98]. An alternating sine wave electric field with a frequency of 250 kHz was applied along the c -axis direction. The diffraction experiment was conducted on the SCD beamline of the ANKA synchrotron. The diffraction signal was recorded using an avalanche photodiode synchronized to the period of the external electric field. The position and intensity of the (400) Bragg peak was followed in a time-resolved manner to probe the lattice deformation (related to the peak position $\Delta d/d$) and position of the titanium relative to the symmetry position in the unit cell (related to the intensity of the peak $\Delta I/I$). A periodic angular shift of the Bragg peak was detected (Figure 39, left), which described a hysteresis loop of the lattice strain $\Delta d/d$ (upper panel of Figure 39, right), as also schematized in Figure 8 (d). Since the electric field was weak compared to the coercive field, the change in integrated intensity can entirely be attributed to the change of the structure factor (lower panel of Figure 39, right) and therefore atomic displacement within the unit cell (equation (18)).

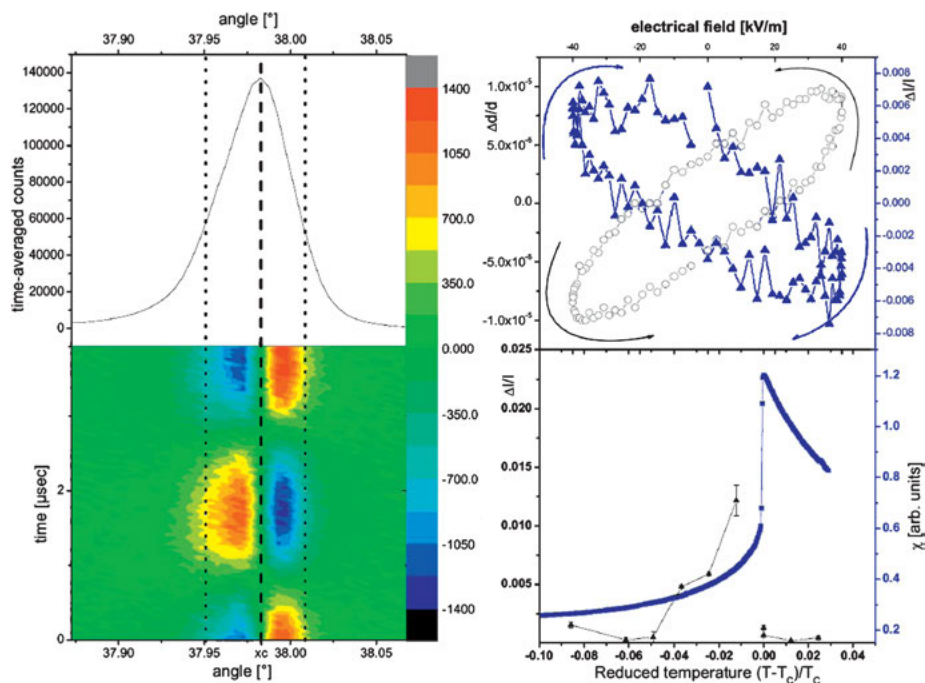


Figure 39: Left: Time-average and time-resolved displacement of the (400) Bragg peak under periodic electric field. Upper right: Hysteresis loops of the change of the intensity $\Delta I/I$ (triangles) and strain $\Delta d/d$ (circles) of the (400) peaks as a function of applied electric field. Lower right: Change in Bragg peak intensity as a function of temperature (triangles) and dielectric response of the crystal (squares). Reprinted with permission from [98].

A similar experiment with a much higher electric field was conducted using the BL02B1 beamline at Spring-8 to follow the lattice strain response during and after polarization reversal. A sequence of X-ray pulses of $4\text{-}\mu\text{s}$ width was isolated from the 508 MHz frequency of the synchrotron, which defined the time resolution of the experiment. A cyclic bipolar square wave electric voltage $V_{\text{ext}}(t)$ with 600 Hz frequency, matching the X-ray pulse frequency, was applied to a single crystal of BaTiO_3 . The delay Δt was controlled. The schematic of the experiment is given in Figure 40.

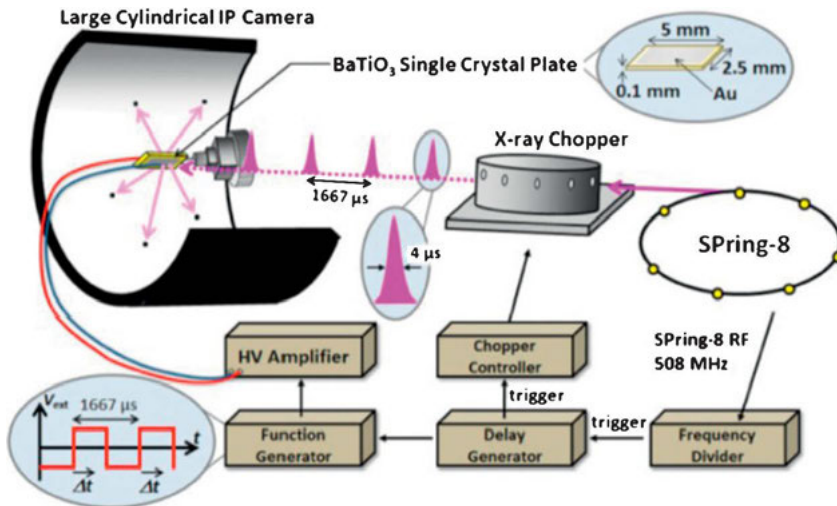


Figure 40: Schematics of the experimental setup for time-resolved X-ray diffraction under electric field at Spring-8 BL02B1. X-rays out of the synchrotron are selected by an X-ray chopper. The bipolar square wave external electric field $V_{\text{ext}}(t)$ with amplitude 125 V and period $1667\text{ }\mu\text{s}$ is applied on the sample [99]. Copyright 2011 The Japan Society of Applied Physics.

The measured voltage $V(t)$ on the crystal is given in Figure 41. It shows the polarity switching and periodicity of the external square wave voltage $V_{\text{ext}}(t)$ with additional oscillations, defining six regimes schematized in Figure 41 (labeled I, ..., VI). The corresponding tetragonality c/a measured through time-resolved X-ray diffraction is given in parallel. In region I, the crystal is in a monodomain state with tetragonality $c/a = 1.0110$. When V_{ext} becomes positive, polarization reversal occurs and is completed at $\Delta t \sim 50\text{ }\mu\text{s}$. The sample should be in a multidomain state in this time region. In region II, c/a decreases because the electric field is opposite to the spontaneous polarization of the sample. 180° -domains are forming and growing. In region III, c/a increases to a value of 1.0114 . Then both $V(t)$ and $c/a(t)$ behave with damped oscil-

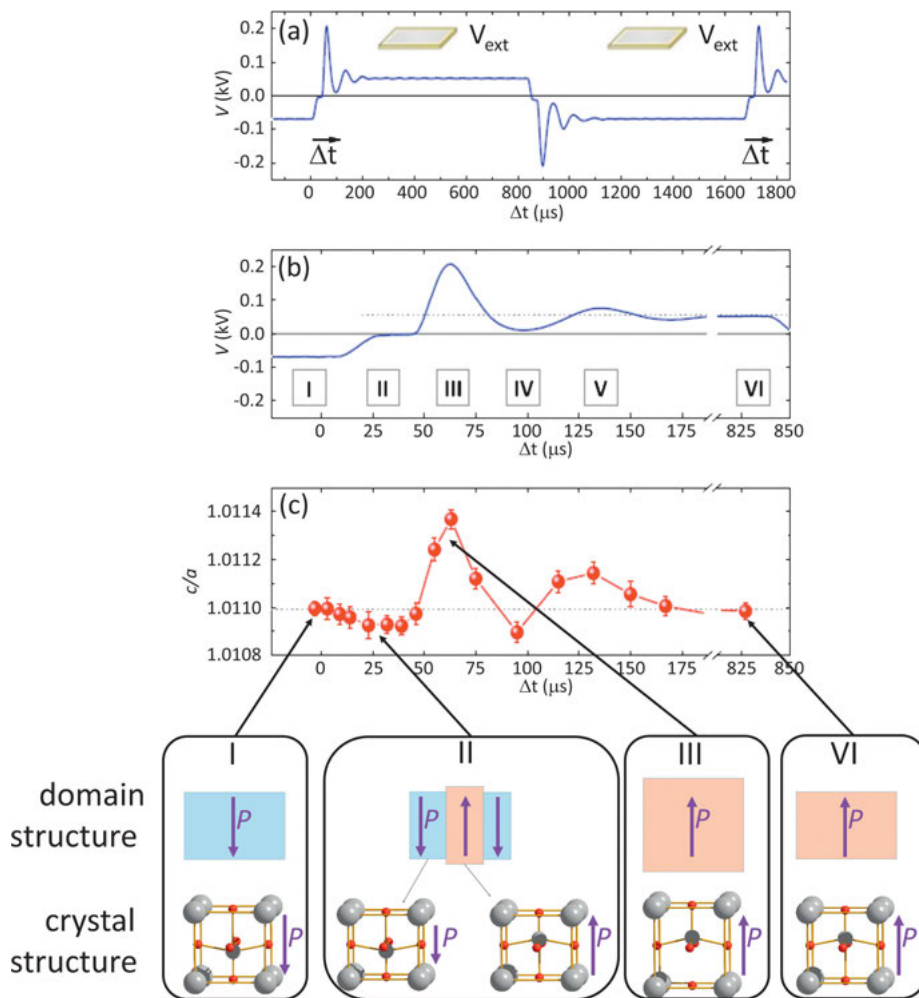


Figure 41: Top: (a) Time dependence of the effective electric voltage $V(t)$ applied to BaTiO₃ single crystal plate for a bipolar square wave driving electric voltage. (b) Enlarged $V(\Delta t)$ showing the six time periods (labeled I, ..., VI). (c) Tetragonality c/a as a function of Δt . Bottom: Schematic of the ferroelectric domain structure and crystal structure expected in each time region. Adapted from [99] and [100]. Copyright 2011 The Japan Society of Applied Physics.

lation in regions IV and V and finally diminish at $\Delta t \sim 800 \mu\text{s}$. This is attributed to piezoelectric vibration corresponding to a vibration of the lattice strain.

From these experiments we can conclude that a domain motion in ferroelectric crystals occurs in the μs time scale. The domain wall dynamics in the model system Pb(Zr_xTi_{1-x})O₃ (PZT) has been specifically investigated using time-resolved X-ray and neutron diffraction experiments to follow the transient and cooperative motions dur-

ing polarization switching. It has been observed that at progressive higher electric field, the speed of polarization switching scales with the magnitude of the electric field but is limited by the propagation velocity of elastic deformations in the crystal, which is several km/s. Time-resolved diffraction experiments have been conducted at the Advanced Photon Source using a focused X-ray beam to a 115-nm spot using Fresnel zone plate optics [101]. In PZT crystals, the (002) and (00 $\bar{2}$) Bragg reflections of the tetragonal phase correspond to opposite polarization states and can differ in intensity by 30% or more, resulting from the noncentrosymmetric unit cell. Probing the peak position and intensity of the (002) reflection gives insights on the lattice strain and domain switching, respectively. X-ray bunches of 100 ps separated in time by 153 ns were used from the synchrotron. Bipolar electric field cycles of 18 V pulses ($E+$ and $E-$) were applied to the sample with a repetition rate of 10 kHz. The amplitude of the electric field (18 V) is higher than the coercive field, and polarization switching occurred during the electric pulses. At the onset of the electric field, the (002) Bragg peak shifted to a higher angular 2θ value, corresponding to a shrinking of the PZT lattice along the c -axis (Figure 42). Hundreds of nanoseconds later, the (002) peak shifted to a lower 2θ value, and in parallel, the intensity decreased. Two points denoted **a** and **b** were defined on the intensity curve $I(t)$ and assigned to the beginning and end of the scattering signature of the reversal of the piezoelectric response.

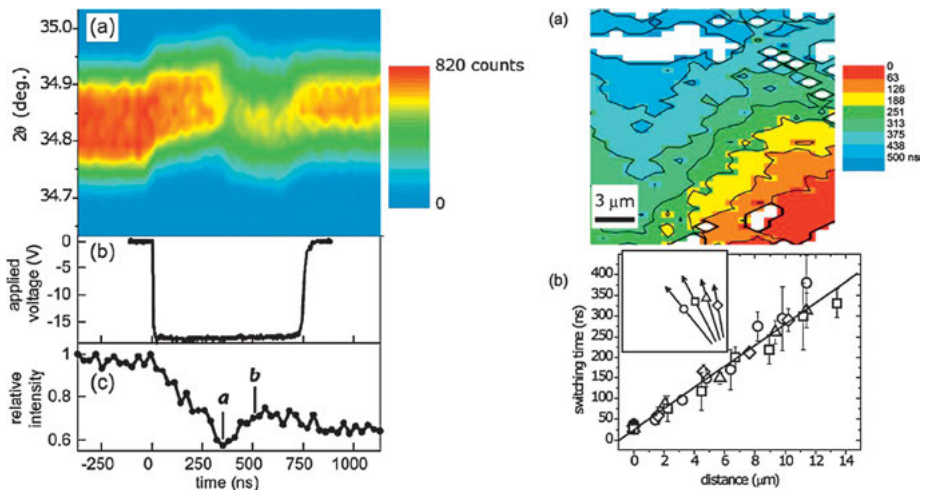


Figure 42: Left: Intensity and 2θ position of the PZT (002) Bragg reflection during the switching of the remnant polarization by a -18 V pulse. Right top: Polarization switching time in a $20 \times 20 \mu\text{m}^2$ area. Right bottom: polarization switching time as a function of distance along the arrows depicted in the inset. Reprinted with permission from [101]. Copyright (2006) by the American Physical Society.

One important specificity of this experiment was the focusing of the X-ray beam to 115 nm, which was used to map spatially the response of the PZT sample to the electric field, so that the domain wall displacement can be directly imaged in the time domain. The position in time of the midpoint $\mathbf{a} - \mathbf{b}$ was monitored as a function of the position of the beam on the sample. This midpoint was associated with the switching time at each spatial position; it corresponds to the time needed for a polarization domain wall to travel from the nucleation site to the measurement position. The corresponding map is given in Figure 42, right. It shows the nucleation site, domain growth direction, and domain wall velocity. The distribution of nucleation sites is limited to a single nucleus in the bottom right corner. The linear plot of the switching time as a function of position gives an average domain wall velocity of 40 ms^{-1} for 18 V electric pulses, which is below the limit set by elastic deformation.

The experiments detailed above focused on the time evolution of only a few relevant Bragg peaks to probe the macroscopic domain switching and lattice strain during polarization switching. Understanding the mechanisms of polarization switching requires a characterization of the crystal structure at subangstrom resolution as a function of time under an external applied electric field. This requires measuring with high accuracy the intensity change of all Bragg reflections up to subatomic resolution (high reciprocal space coverage). Such experiments have been conducted on the model piezoelectric system quartz using a quasi-static electric field [102, 103]. α -quartz is a piezoelectric material whose structure is formed by corner-sharing SiO_4 tetrahedra; it crystallizes in the trigonal $P3_121$ (or $P3_221$) space group ($a_p = 4.91 \text{ \AA}$, $c_p = 5.40 \text{ \AA}$). For a long time, the origin of piezoelectricity of α -quartz was attributed to a displacement of the Si^{4+} and O^{2-} ionic sublattices under the influence of the electric field. Crystallographic experiments have been performed under a periodically reversed electric field with four stages $E_+/0/E_-/0$ to avoid charge accumulation, and with low switching frequency (quasi-static mode). For fields of about $E_0 < 3 \text{ kV mm}^{-1}$, variations of Bragg peak intensities of a few percent were observed. The change of the fractional coordinates of the atoms in the unit cell changes the intensities of the Bragg reflections through the change of structure factor:

$$I(\mathbf{H}, E) \propto |F(\mathbf{H}, E)|^2 = \left| \sum_{j=1}^{N_{\text{at}}} f_j e^{2i\pi\mathbf{H}\cdot(\mathbf{r}_j + \Delta\mathbf{r}_j)} \right|^2. \quad (37)$$

We neglect in these expressions the atomic electron density polarization under the electric field, which would modify the atomic scattering factors f_j .

The modulation of the Bragg peak intensity was followed and modeled using the response ratios defined as the relative intensity variation in the perturbed ($E \neq 0$) and unperturbed crystal ($E = 0$) using a least-squares refinement procedure:

$$\eta(\mathbf{H}, E) = \frac{I(\mathbf{H}, E) - I(\mathbf{H}, E = 0)}{I(\mathbf{H}, E = 0)}. \quad (38)$$

The results of the experiment indicate that the bond distances Si–O are very little affected, but both a deformation and a reorientation of rigid SiO_4 tetrahedra are induced

by the electric field [102, 103]. These distortions increase slightly the dipole components of the Si–O–Si fragments along the field direction, which is consistent with the small values of the piezoelectric coefficients of α -quartz.

The transient atomic displacements during a resonant vibration of α -quartz have been investigated through time-resolved X-ray diffraction measurements at the beamline BL02B1 of the Spring-8 synchrotron facility. The specificity of the experiment is that a single crystal of quartz was made vibrating in resonance with its thickness-shear vibration (resonance frequency of $f_0 = 30$ MHz) to amplify the physical phenomenon and render it possible to measure with X-ray diffraction. Applying an electric field in this special direction distorts the trigonal unit cell to a triclinic one; the distortion may be quantified by the values of the angles α , β and γ with respect to the nonprimitive C -centered orthorhombic unit cell ($a = 4.91$ Å, $b = 8.50$ Å, $c = 5.40$ Å, and $\alpha = \beta = \gamma = 90^\circ$). The time profile of the experiment is illustrated in Figure 43. It was imposed by the fixed frequency 26.1 kHz of the single electron bunch of the synchrotron storage ring. Short 50 ps X-ray pulses were isolated using a high-speed mechanical chopper. A sine-wave electric field of varying amplitude ($E_0 < 0.2$ kV mm $^{-1}$) was applied perpendicular to the faces of the quartz crystal with a frequency f close to f_0 to drive the resonant vibration. The time-dependent crystal structure was investigated over one complete period of electric field by varying the time delay Δt .

The angles β and γ change according to a sine wave with a period of $f_0^{-1} = 33$ ns, whereas the other lattice constants a , b , c , α do not change appreciably. The maximum of angular distortion varies linearly with the applied electric field amplitude E_0 . This

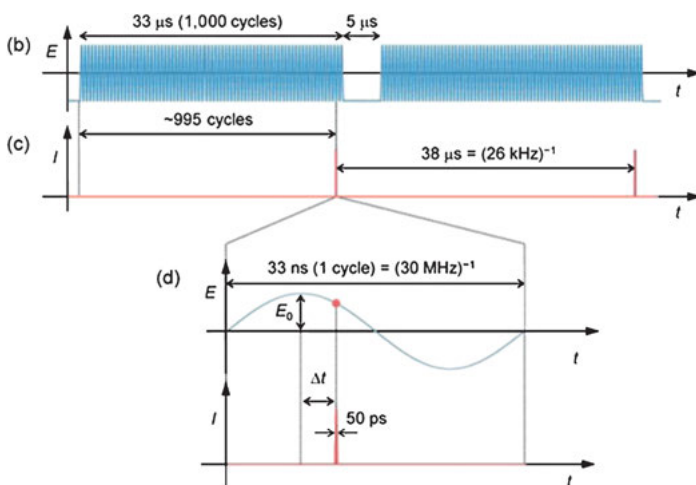


Figure 43: Schematic of the time-resolved experiment with hybrid alternating electric field (b) and repetitive short-pulse X-rays (d). The applied electric field consists of a sequence of 1000 cycles of a 30 MHz sine wave repeated periodically and separated by $5 \mu\text{s}$. Short-pulse X-rays with a pulse width of 50 ps and repetitive frequency of 26.1 kHz are used as a probe. Reproduced from [104], with the permission of AIP Publishing.

resonant lattice vibration is observed only in a narrow frequency band as shown in Figure 44. The amplitude and phase behaviors are consistent with the Lorentzian distribution and arctangent curve as a function of the frequency of a harmonic oscillator under driving and damping forces (see the fitting in Figure 44).

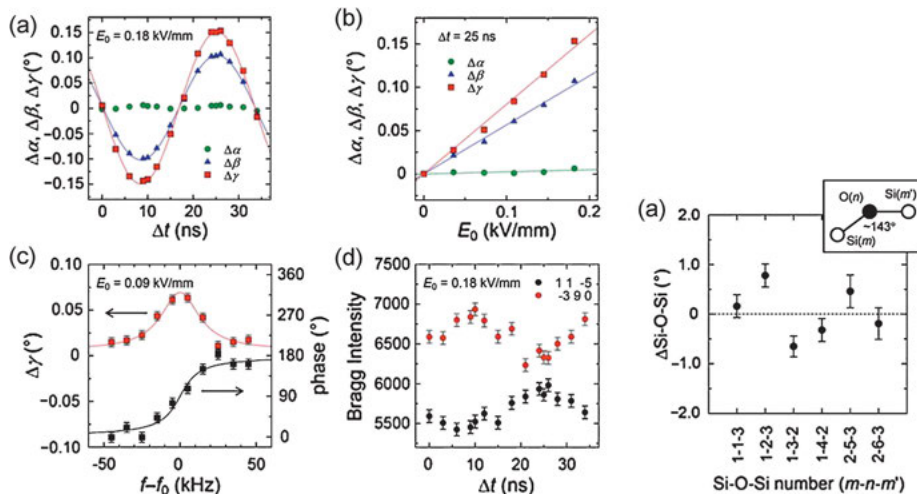


Figure 44: Unit cell parameters and Bragg intensity of α -quartz vibrating under alternating electric fields along the Y' -axis. Left: (a) Change of α, β, γ as a function of time under the resonant alternating electric field with $f = f_0$ and $E_0 = 0.18$ kV/mm. (b) Change of α, β, γ at $\Delta t = 25$ ns as a function of E_0 . (c) Changes of the amplitude and phase of the $\Delta\gamma$ sine curve of (a) as a function of the frequency shift ($f - f_0$). (d) Change of intensity of the (11-5) and (-390) Bragg reflections as a function of Δt . Right: Structural changes: change of the Si-O-Si angles. Reproduced from [104], with the permission of AIP Publishing.

Associated atomic motions in the unit cell were detected as changes of Bragg peak intensity (Figure 44) with the same frequency as the driving electric field. Crystal structures at the maximum of distortion ($\Delta t = 9$ ns and $\Delta t = 25$ ns) were determined by a least-squares refinement over 3 700 measured Bragg reflections. The strained triclinic unit cell of quartz contains three crystallographically independent SiO_4 tetrahedra (labeled 1-3 in Figure 44). No change in Si-O distances and O-Si-O angles were detected, indicating that the SiO_4 tetrahedra are hardly distorted by the driven resonant lattice strain. On the contrary, Si-O-Si angles, bridging SiO_4 tetrahedra, show significant distortions from the ideal 143.66° in the nondistorted trigonal structure. This bending vibration results from the response of each local Si-O-Si dipole moment, which behaves synchronized to the applied periodic electric field.

This time-resolved X-ray diffraction experiment highlights that the response of a quartz piezoelectric crystal to an applied resonant electric field can be traced back to the atomic displacements with a nanosecond time resolution. A complete structural dynamics can be mapped out.

In addition to electric field stimuli, the structural dynamics in piezoelectric and ferroelectric solids have been probed using ultrafast laser pulses to initiate strain waves, which can be further probed by time-resolved X-ray diffraction techniques [105–108]. The idea is to design a thin layer of ferroelectric material deposited on a layer of a metallic electrode used as a transducer (for instance, SrTiO₃). The metallic electrode is excited by femtosecond light pulses, leading to a quasi-instantaneous temperature rise. The resulting heat expansion is limited by the speed of sound and proceeds within picoseconds. This launches a strain wave in the ferroelectric material. The propagation of the strain wave is then investigated through the shift of the Bragg peak position. The in-plane and out-of-plane structural dynamics of PZT and PbTiO₃ have been studied that way [105–107].

3.7 Dynamics of long-range ordering from time-resolved X-ray crystallography

We have seen at the beginning of this chapter that X-ray diffraction on single crystals is characterized by the crystal scattering factor $F_{\text{crystal}}(\mathbf{H})$ (equation (17)), which is the product of the unit-cell scattering factor by the interference function $F_{\text{crystal}}(\mathbf{H}) = \Gamma(\mathbf{H}) \times F(\mathbf{H})$, where $\Gamma(\mathbf{H})$ describes long-range ordering and periodicity of the crystal. A modification of the crystal periodicity has direct consequences on the X-ray diffraction pattern, as illustrated in Figure 9 (h) for a unit cell doubling resulting from a dimerization process. As a consequence, a detailed time-resolved X-ray diffraction study of the temporal evolution of the interference function has the potential to provide evidences of transient changes in long-range structural ordering of a crystal. This is related to case (h) in Figure 9.

Transition metal oxides represent a very important class of materials in solid state physics; their ground-state properties are driven by a balance among several correlated processes, such as orbital and charge ordering, magnetism (spin), and lattice degrees of freedom [109]. Mixed valence manganites with perovskite structure provide illustrative examples of this delicate interplay, leading to very rich phase diagrams characterized by phase transitions and the appearance of interesting physical properties such as magnetic ordering or colossal magnetoresistance. Time-resolved X-ray diffraction analyses have been performed on crystalline thin films and single crystals of doped manganites to probe the individual dynamics of the orbital, charge, and lattice parameters [110–113]. Among others, the half-doped Pr_{0.5}Ca_{0.5}MnO₃ has been subject to specific attention. It undergoes a phase transition around $T_o = 250$ K, below which charge ordering occurs connected to orbital ordering as depicted in Figure 45 (b) with a symmetry lowering from *Pbnm* space group at high temperature to *P2₁/m* space group below the phase transition. The formation of a charge-ordered state is manifested by the charge-density modulation at the Mn site with localization of Mn³⁺ and Mn⁴⁺ cations, whereas orbital ordering leads to an alternating pattern of

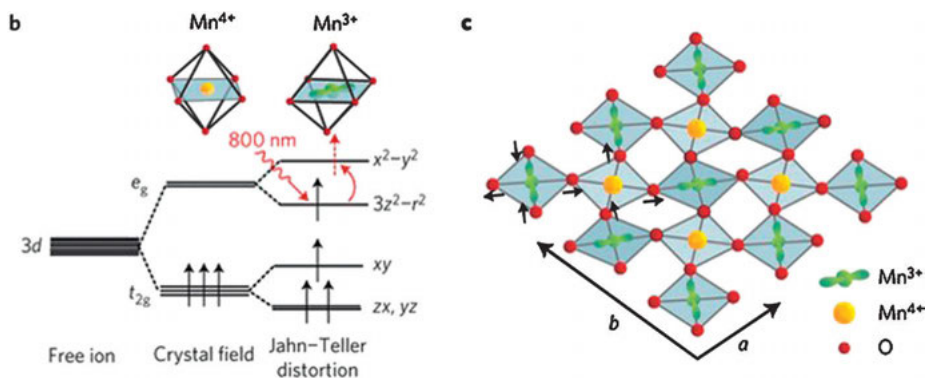


Figure 45: (b) Electron configuration of Mn⁴⁺ ions and splitting of the 3d states for Mn³⁺ ions under the Jahn–Teller effect associated with distortions of the oxygen octahedra at the Mn³⁺ sites in Pr_{0.5}Ca_{0.5}MnO₃. The red arrows indicate the photoinduced transition. (c) Schematic of the structure within the (*ab*) plane in the charge and orbital ordered state. Orbital ordering induces a doubling of the unit cell along the *b*-axis and a symmetry change from orthorhombic *Pbnm* to monoclinic *P2₁/m* [110]. Reprinted by permission from Macmillan Publishers Ltd, copyright (2014).

occupied orbitals within the crystallographic (*ab*) plane. The modulation is commensurate with the lattice periodicity at low temperature, characterized by a doubling of the unit cell along the *b*-axis (Figure 45 (c)). It has been reported that the modulation changes to incommensurate in a temperature range just below the transition temperature T_0 [114]. In the commensurate phase, the diffraction pattern exhibits superlattice reflections, reflecting the additional periodicity of the charge and orbital degrees of freedom, and Jahn–Teller lattice distortion. The main reflections ($0k0$) with k even characterize the average basis structure. Superstructure reflections can be classified in three classes, each sensitive to a specific component of the phase transition: with k odd, ($0k/20$) reflections are sensitive to orbital order and Jahn Teller distortion, ($0k0$) reflections are sensitive to the charge order, and ($hk/2l$) reflections measure the overall structural distortion.

Time-resolved X-ray diffraction has been performed using the XFEL source at the Linac Coherent Light Source (LCLS) at the SLAC National Accelerator Laboratory. Optical pulses of 55 fs with a wavelength of 800 nm excited the sample with a repetition rate of 120 Hz. X-ray probe pulses of 50 fs were focused on the sample [110]. The X-ray energy was tuned in the vicinity of the Mn K edge using a silicon (111) monochromator to adopt resonance conditions allowing discrimination of the charge and orbital order [115]. The optical excitation at 800 nm mainly excite the Mn³⁺ intrasite transition which drives the Jahn–Teller distortion depicted in Figure 45 (b). This photoinduced electronic excitation leads to an ultrafast change of the atomic potential, allowing further structural changes. Time-resolved X-ray diffraction data for various selected reflections as functions of pump laser fluence are shown in Figure 46 (a–c). The observed dynamics show a fast component, which cannot be resolved given the experimental

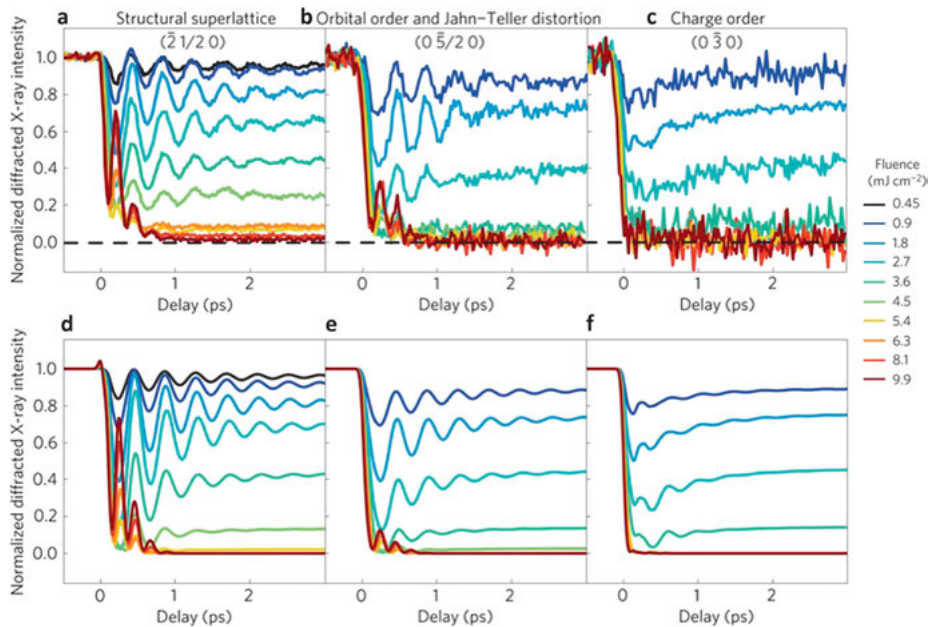


Figure 46: Measured (a–c) and simulated (d–f) evolution of the normalized diffracted X-ray intensities for three superlattice reflections. (a, d) The $(\bar{2}\frac{1}{2}0)$ reflection, which is sensitive to structural distortion only. (b, e) The $(0\frac{5}{2}0)$ reflection, which is sensitive to orbital ordering. (c, f) The $(0\bar{3}0)$ reflection which is sensitive to charge ordering [110]. Reprinted by permission from Macmillan Publishers Ltd, copyright (2014).

resolution, and a strong 2.45 THz modulation attributed to a coherent optical phonon mode triggered by the ultrafast pump pulse. The almost vanishing intensity of all the superstructure reflections is the signature of photoinduced disappearance of orbital and charge order, known as orbital and charge-order melting. This is unambiguous evidence that the lattice symmetry has changed at high pump fluence. The oscillation and therefore coherent motions persist only for a short time at high fluence before the phase transition is completed. The diffraction data has been modeled appropriately using a time-dependent order parameter formalism (Figure 46 (d–f)).

As shown in this example, the enhancement of the scattered X-ray signal at very specific positions in reciprocal space (Bragg positions) owing to crystal periodicity (reflected by the interference function $\Gamma(\mathbf{H})$) allows probing in real time the dynamics of long-range ordering of various degrees of freedom in a crystal and therefore evaluate the coupling between them. Half-doped $\text{Pr}_{0.5}\text{Ca}_{0.5}\text{MnO}_3$ is a specific case, exhibiting a commensurate superstructure associated with a unit-cell doubling below the phase transition. The dynamics of charge density waves, which are commensurate or incommensurate spatial modulations of the electron density accompanied by a collective lattice distortion in a crystal, have been studied using similar time-resolved X-ray or

electron diffraction experiments [116–119]. Nonthermal melting and transition to long-lived modulated states in the picosecond time scale have been revealed by monitoring the temporal dependence of the intensity, position, and profile of relevant superlattice reflections related to the charge density waves.

3.8 Going beyond the structural dynamics from time-resolved X-ray diffraction

Along this chapter, we have seen that time-resolved X-ray scattering (solution scattering and crystal diffraction) can provide detailed information on the structural dynamics of solids and liquids at time scales that cover several orders of magnitude from hundreds of femtosecond to seconds.

Recalling that X-rays are scattered by the electrons of the sample, the X-ray scattered signal in a given stationary experiment is directly related to the 3D electron density distribution by the Fourier transform of the complex structure factor:

$$\begin{aligned}\rho(\mathbf{r}) &= \frac{1}{V} \sum_{\mathbf{H}} F(\mathbf{H}) e^{-2i\pi\mathbf{H}\cdot\mathbf{r}} \\ &= \frac{1}{V} \sum_{\mathbf{H}} |F(\mathbf{H})| e^{i\varphi(\mathbf{H})} e^{-2i\pi\mathbf{H}\cdot\mathbf{r}}\end{aligned}\quad (39)$$

with the experimentally measured intensity being proportional to the square of the structure factor modulus,

$$I(\mathbf{H}) \propto |F(\mathbf{H})|^2. \quad (40)$$

In a structural analysis, the assumption of neutral independent atoms (IAM: independent atom model) is generally considered, so that atomic nuclear positions are directly assigned to regions of high electron density accumulations. This simple IAM approximation is valid for structural purposes only and completely neglects interatomic and intermolecular bonding. Using accurate X-ray diffraction experiments, the equilibrium time-averaged electron distribution can be determined in a crystalline solid with high degree of precision and high level of spatial resolution (typically, 0.1 Å). In practice, the method uses a sophisticated atomic centered multipolar modeling to uncover the deformation of the atomic electron clouds to form chemical bonding [2]. This approach is nowadays very mature and used almost routinely for getting numerous chemical, biological, and physical insights on ground state or unperturbed systems. In terms of experimental conditions, the requirements are quite drastic:

- High accuracy (high signal-to-noise ratio) on the measured Bragg peak intensity since the deformation of the valence electron density is a tiny effect.
- Completeness of the measured Bragg reflection data set (complete coverage of reciprocal space) to avoid series termination in equation (39) and therefore artefacts in the modeled electron density distribution.

- Short X-ray wavelength (hard X-rays) to extend the Fourier summation as far as possible in the reciprocal space to achieve subangstrom resolution in the direct space modeled electron density distribution.

Probing the changes in the electron density distribution in a time-resolved manner would extend the investigated dynamics much beyond a purely structural picture, providing access to additional electronic degrees of freedom. Recovering the transient 3D electron density distribution is nevertheless a very challenging task if we consider the aforementioned requirements:

- The sensitivity of time-resolved diffraction experiments, that is, the detectable changes in Bragg peak intensity $\Delta I/I_0 = (I(t) - I_0)/I_0$ depends on the stability of the pump–probe scheme parameters, such as pump intensity, probe intensity, focusing position on the sample, overlap of pump and probe pulses on the sample, stability of the controlled delay, etc.
- Photon counting statistics of the X-ray detection system combined with the X-ray flux of the source limit the detectability of weak intensity changes.
- Completeness of the reciprocal space coverage has proved feasible with millisecond to picosecond experiments performed at synchrotron radiation facilities, given the large literature on the subject (see, for instance, the example of the bacterial blue light receptor PYP, Section 3.3). On the contrary, measuring a complete sphere of reciprocal space with femtosecond time-resolution with single crystal diffraction experiments is a current challenge.

In addition, such experiments raise a fundamental question. In the time-resolved extension of the X-ray scattering process, the electron density $\rho(\mathbf{r})$ in equation (39) is replaced by a time-dependent analogue $\rho(\mathbf{r}, t)$. Assuming that the X-ray pulse duration is longer than the dynamical time scale of the electron wave packets, the electronic wave packet remains unchanged before and after the scattering process, and the usual treatment applies by just considering time as a new parameter. The outcome of an experiment should be the electron density distribution at different time delays after triggering the perturbation. This is the semiclassical approximation. For ultrashort X-ray pulses, typically in the femtosecond time regime, a full quantum theory of light–matter interactions has to be used. This is out of the scope of the present chapter; general concepts to treat this problem have been proposed in the literature [120–123].

Pioneering experiments in the frame of the semiclassical approximation have been performed using time-resolved powder X-ray diffraction with a table-top laser-driven plasma source at the Max Born Institute in Berlin. In addition to the purely structural dynamics, these experiments have provided new pictures of the spatial rearrangement of electronic charges within electronically excited crystals. The very first experiments concerned ionic materials $(\text{NH}_4)_2\text{SO}_4$, KH_2PO_4 , LiBH_4 , LiH , and NaBH_4 [124–129]. The reconstructed time-dependent electron density distributions $\rho(\mathbf{r}, t)$ reveal important ultrafast phenomena:

- Transient charge density maps in ammonium sulfate $(\text{NH}_4)_2\text{SO}_4$ reveal concerted charge transfer from the sulfate anion and proton transfer from the ammonium cation within 100 fs, further periodically modulated by low-frequency lattice phonon modes with modification of the hydrogen bond geometry [124, 125].
- In potassium dihydrogen phosphate KH_2PO_4 , a pronounced photoinduced charge transfer from the potassium atom to the oxygen atoms of the H_2PO_4^- ions is characterized by the transient charge density maps. This charge relocation is modulated by low-frequency lattice modes, coherently excited upon photoexcitation. The results can explain the ultrafast dynamic response of such ionic ferroelectric materials [126].
- In LiBH_4 , an anion-to-cation charge transfer is evidenced, leading to a transient electric polarization induced by the high optical field of the pump laser [127]. Comparisons have been made with the similarly characterized photoinduced charge transfer in LiH and NaBH_4 [128, 129]. LiH behaves differently from the series, the charge being shifted from Li to H, enhancing the ionicity of the material.

We illustrate here in more detail the approach using the photoinduced charge transfer process in the crystals of $[\text{Fe}(\text{bpy})_3]^{2+}(\text{PF}_6^-)_2$ mapped by femtosecond X-ray powder diffraction. The crystal structure of $[\text{Fe}(\text{bpy})_3]^{2+}(\text{PF}_6^-)_2$ is shown in Figure 48 (a). The diffraction experimental setup is illustrated in Figure 14. In solution, optical excitation of the molecular entities $[\text{Fe}(\text{bpy})_3]^{2+}$ populates the singlet metal-to-ligand-charge-transfer states ($^1\text{MLCT}$), from which the system decays via intersystem crossing into a high-spin quintet state (5T_2) on a sub-150 fs time scale. In the here considered femtosecond X-ray powder diffraction, the sample, consisting of a crystalline powder, is excited with sub-50 fs laser pulses at 800 nm initiating the photoinduced charge-transfer process, which is probed by diffracting 100 fs $\text{Cu K}\alpha$ pulses at 8.04 keV from the excited powder at variable pump–probe time delay. For each time delay, the diffraction pattern consists of Debye–Scherrer rings, which are radially integrated to provide the pattern (intensity as a function of diffraction angle 2θ) given in Figure 47,

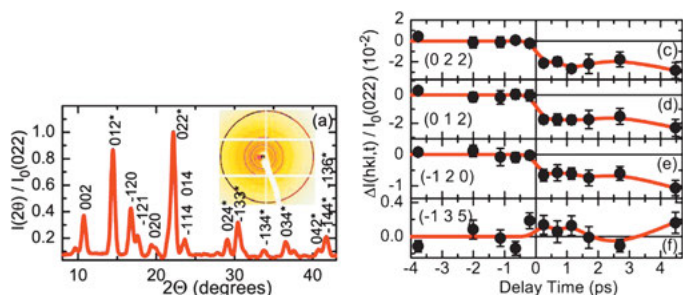


Figure 47: Left: powder X-ray diffraction pattern recorded using the X-ray plasma source (integration time of 8 hours). Right: transient changes of Bragg peak intensity as a function of time delay between the optical pump pulse and X-ray probe pulse. Reproduced from [130], with the permission of AIP Publishing.

left. It consists of nearly 20 well-separated Bragg peaks, whose intensity is determined by profile fitting as a function of time delay (Figure 47, right). Pronounced intensity changes of a few percent are characterized.

The electron density maps have been computed at various time delays by the Fourier transform of the corresponding structure factor moduli derived from the measured Bragg intensities, using the Maximum Entropy Method formalism to retrieve the structure factor phases. The map derived from the data at a pump–probe delay of 250 fs is given in Figure 48 (b). It highlights a charge transfer from Fe to the bpy

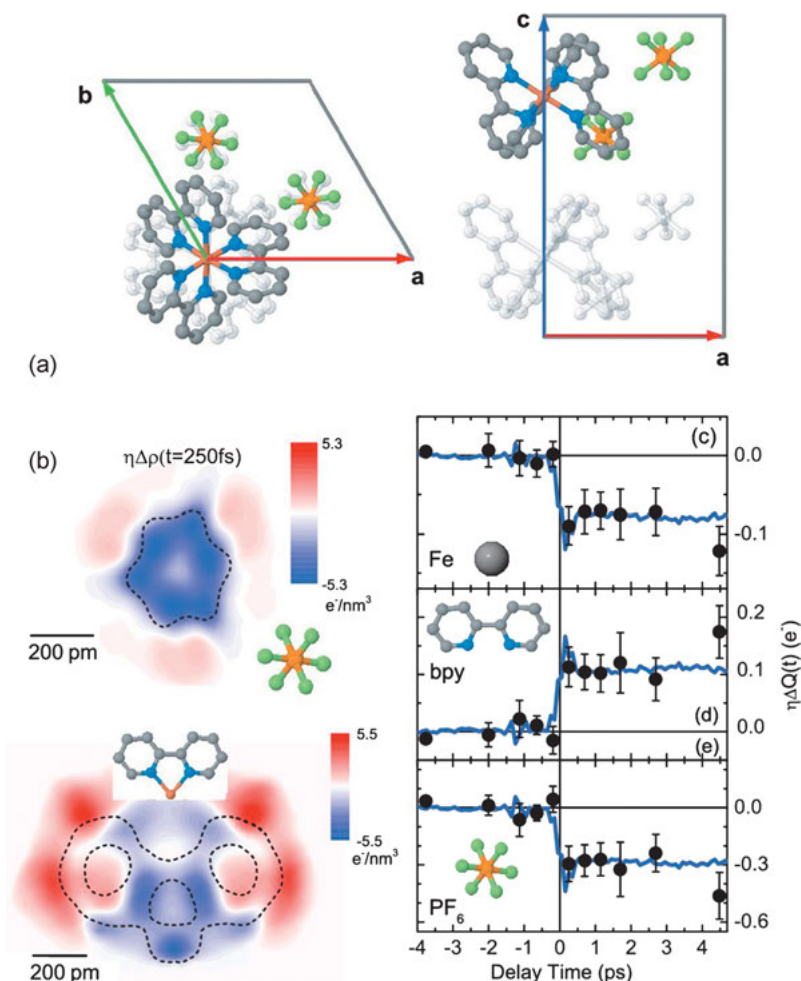


Figure 48: (a) Unit cell of $[\text{Fe}(\text{bpy})_3]^{2+}(\text{PF}_6)_2$. (b) Contour plots of the change of electron density distribution at 250 fs pump–probe delay. The dashed line indicates the stationary electron density. (c)–(e) Transient changes of the electron density integrated over fragment subvolumes Fe, bpy, and hexafluorophosphate counter-ion. Reproduced from [131], with the permission of AIP Publishing.

unit together with an increase in the Fe–bpy distance, as usually observed for 1A_1 to 5T_2 transition in Fe^{II} spin-crossover complexes. A net charge transfer from the PF_6^- counter-ion is also evidenced by a negative difference electron density at the PF_6^- position. The charge transfer has been further traced by integrating the difference electron density over space regions of the different structural fragments: Fe, bpy, and PF_6^- (Figure 48 (c)). The overall transferred charge is quite large, implying a nonlocal effect, attributed to the formation of polarons within the crystal lattice (polarization of the surrounding of photoexcited charge-transfer species).

From the results attained so far we can conclude that a real atomic resolution appropriate for a sophisticated multipolar modeling is currently out of reach, but obtaining detailed information on the transient 3D electron density distribution is nevertheless possible. Fragment integrated charges, as derived in the previous example, can highlight charge-transfer processes. Fantastic new insights on photoinduced mechanisms, such as charge transfer, dipole enhancement, bond formation and breaking, and exciton dynamics, may thus be revealed. Investigating early photoinduced electron transfer events before the nuclear degrees of freedom have yet adapted to the electronic configuration of the excited state is an exciting perspective, which would open new opportunities for chemical reactions to be imaged in real time through diffraction techniques.

4 Perspectives

In view of the important progresses we might anticipate for the near future, structural dynamics is probably only at its infancy. Many interesting progresses are already on the way.

Time-resolved electron diffraction offers an important alternative to time-resolved X-ray diffraction. It is a very mature approach, which achieves routinely time resolutions of hundreds of femtoseconds. Electrons have scattering cross-sections about five orders of magnitude higher than X-rays, which decreases the penetration depth into matter, an obvious limitation, but allows measurements to be performed on diluted systems, for instance, in the gas phase. Time-resolved electron diffraction has been very efficient in the studies of the temporal evolution of chemical reactions, giving direct evidence on the dynamical evolution of relaxation pathways from the excited states. Phase transitions, such as the photoinduced metal–insulator transition in vanadium dioxide, have also been the subject of investigations. Ultrafast electron diffraction will rapidly advance to cover the attosecond time domain by compression of femtosecond electron packets [132]. Although the nuclear motions can occur as fast as femtoseconds, the electron dynamics span the attosecond time regime. A methodology has been proposed for attosecond electron imaging and diffraction, and numerical simulations confirm the feasibility of the approach under realistic experimental conditions. In parallel, attosecond Laue X-ray diffraction has been envisioned at XFEL

sources. The fundamental idea relies on the Heisenberg uncertainty principle, according to which a bandwidth of X-rays should be generated at attosecond time scale, rendering possible Laue diffraction experiments in the serial crystallography approach.

There have been technological revolutions in the past decades in the development of high-energy-accelerator-based coherent X-ray sources at third-generation synchrotron radiation facilities and XFELs. These sources emit ultrabright X-rays with a high degree of coherence allowing new imaging possibilities to be set up [133]. Several coherent diffraction imaging methods in transmission and reflection modes have been developed. The general procedure is to illuminate an object with a coherent laser-like beam and collect the scattered X-rays with an area detector and a high spatial resolution on the detector. Using appropriate phase retrieval algorithms, the image of the object can be reconstructed. The possibilities of such methods for time-resolved structural analysis is evidenced by the three-dimensional imaging of the generation and subsequent evolution of coherent acoustic phonons in individual gold nanocrystals on the picosecond time scale performed with a femtosecond XFEL source [134]. Besides time-resolved experiments, this method has a high potential for the structural analysis of noncrystalline and/or individual objects, including biological materials, cells, and viruses, albeit at present with a limited spatial resolution >10 nm. Using XFEL, coherent diffraction imaging has already been applied to study individual viruses or biological nanocomposites.

A chemical reaction transforms molecules from one structure to another with interatomic bond making and breaking being essential processes. Understanding the chemical dynamics that connect structures and function along a reaction pathway remains extremely challenging. Time-resolved X-ray solution scattering has the potential to really improve our understanding of chemical reaction pathways. The increasing accuracy in the measurements show that detailed structural information at atomic resolution can be achieved with current third-generation synchrotrons in the liquid phase. This is on the way to be extended to time-resolved X-ray scattering studies of chemical reaction dynamics in diluted gases at intense XFELs. The very first experiment of this kind considered the ultrafast ring-opening reaction of 1,3-cyclohexadiene to form linear 1,3,5-hexatriene, a prototype reaction for the understanding of a large class of organic reactions [135]. Combined with *ab initio* structure calculations, transient features in the X-ray scattering pattern have been assigned to short-lived intermediates defining the whole molecular trajectory of the reaction. These remarkable results demonstrate the capability of capturing molecular motions with atomic spatial resolution and femtosecond time resolution in the gas phase.

Bibliography

- [1] S. Kobatake, S. Takami, H. Muto, T. Ishikawa, and M. Irie. Rapid and reversible shape changes of molecular crystals on photoirradiation. *Nature*, 446:778–781, 2007.

- [2] P. Coppens. *X-ray Charge Densities and Chemical Bonding*. Oxford Science Publications, London, 1997.
- [3] K. H. Kim, J. Kim, J. H. Lee, and H. Ihee. Topical review: molecular reaction and solvation visualized by time-resolved X-ray solution scattering: structure, dynamics, and their solvent dependence. *Struct. Dyn.*, 1:011301, 2014.
- [4] J. G. Kim, T. W. Kim, J. Kim, and H. Ihee. Protein structural dynamics revealed by time-resolved X-ray solution scattering. *Acc. Chem. Res.*, 48:2200–2208, 2015.
- [5] T. K. Kim, J. H. Lee, M. Wulff, Q. Kong, and H. Ihee. Spatiotemporal kinetics in solution studied by time-resolved x-ray liquidography (solution scattering). *Chem. Phys. Chem.*, 10:1958–1980, 2009.
- [6] H. Ihee. Visualizing solution-phase reaction dynamics with time-resolved x-ray liquidography. *Acc. Chem. Res.*, 42:356–366, 2009.
- [7] H. Ihee, M. Wulff, J. Kim, and S.-I. Adachi. Ultrafast x-ray scattering: structural dynamics from diatomic to protein molecules. *Int. Rev. Phys. Chem.*, 29:453–520, 2010.
- [8] M. Cammarata, M. Lorenc, T. K. Kim, J. H. Lee, Q. Y. Kong, E. Pontecorvo, M. Lo Russo, G. Schiro, A. Cupane, M. Wulff, and H. Ihee. Impulsive solvent heating probed by picosecond x-ray diffraction. *J. Chem. Phys.*, 124:124504, 2006.
- [9] I. I. Vorontsov and P. Coppens. On the refinement of time-resolved diffraction data: comparison of the random-distribution and cluster-formation models and analysis of the light-induced increase in the atomic displacement parameters. *J. Synchrotron Radiat.*, 12:488–493, 2005.
- [10] S. Pillet, V. Legrand, M. Souhassou, and C. Lecomte. Kinetics of light-induced first-order phase transformation in molecular solids: $\text{Fe}(\text{btr})_2(\text{NCS})_2\text{H}_2\text{O}$. *Phys. Rev. B*, 74:140101, 2006.
- [11] L. D. Chapman, R. Colella, and R. Bray. X-ray diffraction studies of acoustoelectrically amplified phonons. *Phys. Rev. B*, 27:2264–2277, 1983.
- [12] M. Herzog, A. Bojahr, J. Goldshteyn, W. Leitenberger, I. Vrejoiu, D. Khakhulin, M. Wulff, R. Shayduk, P. Gaal, and M. Bargheer. Detecting optically synthesized quasi-monochromatic sub-terahertz phonon wavepackets by ultrafast X-ray diffraction. *Appl. Phys. Lett.*, 100:094101, 2012.
- [13] A. M. Lindenberg, I. Kang, S. L. Johnson, T. Missalla, P. A. Heimann, Z. Chang, J. Larsson, P. H. Bucksbaum, H. C. Kapteyn, H. A. Padmore, R. W. Lee, J. S. Wark, and R. W. Falcone. Time-resolved X-ray diffraction from coherent phonons during a laser-induced phase transition. *Phys. Rev. Lett.*, 84:111–114, 2000.
- [14] J. Larsson, A. Allen, P. H. Bucksbaum, R. W. Falcone, A. Lindenberg, G. Naylor, T. Missalla, D. A. Reis, K. Scheidt, A. Sjögren, P. Sondauss, M. Wulff, and J. S. Wark. Picosecond X-ray diffraction studies of laser-excited acoustic phonons in InSb. *Appl. Phys. A*, 75:467–478, 2002.
- [15] K. Sokolowski-Tinten and D. von der Linde. Ultrafast phase transitions and lattice dynamics probed using laser-produced X-ray pulses. *J. Phys. Condens. Matter*, 16:R1517–R1536, 2004.
- [16] K. Sokolowski-Tinten, C. Blome, J. Blums, A. Cavalerri, C. Dietrich, A. Tarasevitch, I. Uschmann, E. Förster, M. Kammler, M. Horn von Hoegen, and D. von der Linde. Femtosecond X-ray measurement of coherent lattice vibrations near the Lindemann stability limit. *Nature*, 422:287–289, 2003.
- [17] M. S. Schmokel, R. Kaminski, J. B. Benedict, and P. Coppens. Data scaling and temperature calibration in time-resolved photocrystallographic experiments. *Acta Crystallogr., Sect. A*, 66:632–636, 2010.
- [18] M. Hada and J. Matsuo. Ultrafast X-ray sources for time-resolved measurements. *X-Ray Spectrom.*, 41:188–194, 2012.

- [19] R. Kaminski, G. Nottingham, and P. Coppens. An optical chopper for generation of short X-ray pulses to allow in-house time-resolved photocrystallography. *J. Appl. Crystallogr.*, 47:1765–1768, 2014.
- [20] A. G. Stepanov and C. P. Hauri. Short x-ray pulses from third-generation light sources. *J. Synchrotron Radiat.*, 23:141–151, 2016.
- [21] M. Gembicky, D. Oss, R. Fuchs, and P. Coppens. A fast mechanical shutter for submicrosecond time-resolved synchrotron experiments. *J. Synchrotron Radiat.*, 12:665–669, 2005.
- [22] M. Cammarata, L. Eybert, F. Ewald, W. Reichenbach, M. Wulff, P. Anfinrud, F. Schotte, A. Plech, Q. Kong, M. Lorenc, B. Lindenau, J. Rübiger, and S. Polachowksi. Chopper system for time resolved experiments with synchrotron radiation. *Rev. Sci. Instrum.*, 80:015101, 2009.
- [23] S. Nozawa, S. I. Adachi, J. I. Takahashi, R. Tazaki, L. Guérin, M. Daimon, A. Tomita, T. Sato, M. Chollet, E. Collet, H. Cailleau, S. Yamamoto, K. Tsuchiya, T. Shioya, H. Sasaki, T. Mori, K. Ichiyanagi, H. Sawa, H. Kawata, and S. Y. Koshihara. Developing 100 ps-resolved X-ray structural analysis capabilities on beamline NW14A at the photon factory advanced ring. *J. Synchrotron Radiat.*, 14:313–319, 2007.
- [24] R. W. Schoenlein, S. Chattopadhyay, H. H. W. Chong, T. E. Glover, P. A. Heimann, C. V. Shank, A. A. Zholents, and M. S. Zolotarev. Generation of femtosecond pulses of synchrotron radiation. *Science*, 287:2237–2240, 2000.
- [25] A. A. Zholents and M. S. Zolotarev. Femtosecond X-ray pulses of synchrotron radiation. *Phys. Rev. Lett.*, 76:912–915, 1996.
- [26] P. Beaud, S. L. Johnson, A. Streun, R. Abela, D. Abramsohn, D. Grolimund, F. Krasniqi, T. Schmidt, V. Schlott, and G. Ingold. Spatiotemporal stability of a femtosecond hard-x-ray undulator source studied by control of coherent optical phonons. *Phys. Rev. Lett.*, 99:174801, 2007.
- [27] S. Khan, K. Holldack, T. Kachel, R. Mitzner, and T. Quast. Femtosecond undulator radiation from sliced electron bunches. *Phys. Rev. Lett.*, 97:074801, 2006.
- [28] F. Zamponi, Z. Ansari, C. v. Korff Schmising, P. Rothhardt, N. Zhavoronkov, M. Woerner, T. Elsaesser, M. Bargheer, T. Trobitzsch-Ryll, and M. Haschke. Femtosecond hard X-ray plasma sources with a kilohertz repetition rate. *Appl. Phys. A*, 96:51–58, 2009.
- [29] F. Zamponi, Z. Ansari, M. Woerner, and T. Elsaesser. Femtosecond powder diffraction with a laser-driven hard X-ray source. *Opt. Express*, 18:947–961, 2010.
- [30] C. Rischel, A. Rousse, I. Uschmann, P.-A. Albouy, J.-P. Geindre, P. Audebert, J.-C. Gauthier, E. Förster, J.-L. Martin, and A. Antonetti. Femtosecond time-resolved X-ray diffraction from laser-heated organic films. *Nature*, 390:490–4921, 1997.
- [31] C. Rose-Petruck, R. Jimenez, T. Guo, A. Cavalerri, C. W. Siders, F. Raksi, J. A. Squier, B. C. Walker, K. R. Wilson, and C. P. J. Barty. Picosecond–milliangström lattice dynamics measured by ultrafast X-ray diffraction. *Nature*, 398:310–312, 1999.
- [32] V. Arora, S. Bagchi, M. Gupta, J. A. Chakera, A. Gupta, P. A. Naik, P. Chaddah, and P. D. Gupta. Study of strain propagation in laser irradiated silicon crystal by time-resolved diffraction of K- α X-ray probe of different photon energies. *J. Appl. Phys.*, 114:023302, 2013.
- [33] J. Liu, J. Wang, B. Shan, C. Wang, and Z. Chang. An accumulative X-ray streak camera with sub-600-fs temporal resolution and 50-fs timing jitter. *Appl. Phys. Lett.*, 82:3553–3555, 2003.
- [34] Z. Chang, A. Rundquist, J. Zhou, M. M. Murnane, H. C. Kapteyn, X. Liu, B. Shan, J. Liu, L. Niu, M. Gong, and X. Zhang. Demonstration of a sub-picosecond X-ray streak camera. *Appl. Phys. Lett.*, 69:133–135, 1996.
- [35] T. Ejdrup, H. T. Lemke, K. Haldrup, T. N. Nielsen, D. A. Arms, D. A. Walko, A. Miceli, E. C. Landahl, E. M. Dufresne, and M. M. Nielsen. Picosecond time-resolved laser pump/X-ray probe experiments using a gated single-photon-counting area detector. *J. Synchrotron Radiat.*, 16:387–390, 2009.

- [36] P. Fertey, P. Alle, E. Wenger, B. Dinkespiler, O. Cambon, J. Haines, S. Hustache, K. Medjoubi, F. Picca, A. Dawiec, P. Breugnon, P. Delpierre, C. Mazzoli, and C. Lecomte. Diffraction studies under in situ electric field using large-area hybrid pixel XPAD detector. *J. Appl. Crystallogr.*, 46:1151–1161, 2013.
- [37] R. Nuske, C. v. Korff Schmising, A. Jurgilaitis, H. Enquist, and H. Navirian. Time-resolved X-ray scattering from laser-molten indium antimonide. *Rev. Sci. Instrum.*, 81:013106, 2010.
- [38] L. X. Chen. Taking snapshots of photoexcited molecules in disordered media by using pulsed synchrotron X-rays. *Angew. Chem., Int. Ed.*, 43:2886–2905, 2004.
- [39] A. Gruverman, D. Wu, and J. F. Scott. Piezoresponse force microscopy studies of switching behavior of ferroelectric capacitors on a 100-ns time scale. *Phys. Rev. Lett.*, 100:097601, 2008.
- [40] E. D. Mishina, N. E. Sherstyuk, V. I. Stadnichuk, A. S. Sigov, V. M. Mukhorotov, Y. I. Golovko, A. van Etteger, and Th. Rasing. Nonlinear-optical probing of nanosecond ferroelectric switching. *Appl. Phys. Lett.*, 83:2402–2404, 2003.
- [41] E. Zolotoyabko, J. P. Quitana, B. H. Hoerman, and B. W. Wessels. Fast time-resolved X-ray diffraction in BaTiO₃ films subjected to a strong high-frequency electric field. *Appl. Phys. Lett.*, 80:3159–3161, 2002.
- [42] A. Katrusiak. High-pressure crystallography. *Acta Crystallogr., Sect. A*, 64:135–148, 2008.
- [43] N. J. Brooks, B. L. L. E. Gauthé, N. J. Terrill, S. E. Rogers, R. H. Templer, O. Ces, and J. M. Seddon. Automated high pressure cell for pressure jump X-ray diffraction. *Rev. Sci. Instrum.*, 81:064103, 2010.
- [44] K. Ichiyangi and K. G. Nakamura. Structural dynamics of materials under shock compression investigated with synchrotron radiation. *Metals*, 6:17, 2016.
- [45] K. D. Liss, T. d'Almeida, M. Kaiser, R. Hock, A. Magerl, and J. F. Eloy. Time-resolved X-ray diffraction study of laser-induced shock and acoustic waves in single crystalline silicon. *J. Appl. Phys.*, 106:044914, 2009.
- [46] Y. Hironaka, A. Yazaki, F. Saito, K. G. Nakamura, K.-I. Kondo, H. Takenaka, and M. Yoshida. Evolving shock-wave profiles measured in a silicon crystal by picosecond time-resolved X-ray diffraction. *Appl. Phys. Lett.*, 77:1967–1969, 2000.
- [47] J. Hu, K. Ichiyangi, T. Doki, A. Goto, T. Eda, K. Norimatsu, S. Harada, D. Horiuchi, Y. Kabasawa, S. Hayashi, S. i. Uozumi, N. Kawai, S. Nozawa, T. Sato, S.-I. Adachi, and K. G. Nakamura. Complex structural dynamics of bismuth under laser-driven compression. *Appl. Phys. Lett.*, 103:161904, 2013.
- [48] M. G. Gorman, R. Briggs, E. E. McBride, A. Higginbotham, B. Arnold, J. H. Eggert, D. E. Fratanduono, E. Galtier, A. E. Lazicki, H. J. Lee, H. P. Liermann, B. Nagler, A. Rothkirch, R. F. Smith, D. C. Swift, G. W. Collins, J. S. Wark, and M. I. McMahon. Direct observation of melting in shock-compressed bismuth with femtosecond X-ray diffraction. *Phys. Rev. Lett.*, 115:095701, 2015.
- [49] D. H. Kalantar, J. F. Belak, G. W. Collins, J. D. Colvin, H. M. Davies, J. H. Eggert, T. C. Germann, J. Hawreliak, B. L. Holian, K. Kadau, P. S. Lomdahl, H. E. Lorenzana, M. A. Meyers, K. Rosolankova, M. S. Schneider, J. Sheppard, J. S. Stölken, and J. S. Wark. Direct observation of the alpha–epsilon transition in shock-compressed iron via nanosecond x-ray diffraction. *Phys. Rev. Lett.*, 95:075502, 2005.
- [50] A. Schropp, R. Hoppe, V. Meier, J. Patommel, F. Seiboth, Y. Ping, D. G. Hicks, M. A. Beckwith, G. W. Collins, A. Higginbotham, J. S. Wark, H. J. Lee, B. Nagler, E. C. Galtier, B. Arnold, U. Zastrau, J. B. Hastings, and C. G. Schroer. Imaging shock waves in diamond with both high temporal and spatial resolution at an XFEL. *Sci. Rep.*, 5:11089, 2015.
- [51] P. Ferrer, I. da Silva, J. Rubio-Zuazo, B. F. Alfonso, C. Trobajo, S. Khainakov, J. R. Garcia, S. Garcia-Granda, and G. R. Castro. A flow-through reaction cell for in situ X-ray diffraction and

- absorption studies of heterogeneous powder–liquid reactions and phase transformations. *J. Synchrotron Radiat.*, 19:93–100, 2012.
- [52] D. Wang, U. Weierstall, L. Pollack, and J. Spence. Double-focussing mixing jet for XFEL study of chemical kinetics. *J. Synchrotron Radiat.*, 21:1364–1366, 2014.
- [53] T. E. Stevens, J. Kuhl, and R. Merlin. Coherent phonon generation and the two stimulated Raman tensors. *Phys. Rev. B*, 65:144304, 2002.
- [54] A. Subedi, A. Cavalleri, and A. Georges. Theory of nonlinear phononics for coherent control of solids. *Phys. Rev. B*, 89:220301, 2014.
- [55] M. Först, C. Manzoni, S. Kaiser, Y. Tomioka, Y. Tokura, R. Merlin, and A. Cavalleri. Nonlinear phononics as an ultrafast route to lattice control. *Nat. Phys.*, 7:854–856, 2011.
- [56] S. L. Johnson, P. Beaud, E. Vorobeva, C. J. Milne, E. D. Murray, S. Fahy, and G. Ingold. Non-equilibrium phonon dynamics studied by grazing-incidence femtosecond x-ray crystallography. *Acta Crystallogr., Sect. A*, 66:157–167, 2009.
- [57] R. I. Tobey, D. Prabhakaran, A. T. Boothroyd, and A. Cavalleri. Ultrafast electronic phase transition in $\text{La}_{1/2}\text{Sr}_{3/2}\text{MnO}_4$ by coherent vibrational excitation: evidence for nonthermal melting of orbital order. *Phys. Rev. Lett.*, 101:197404, 2008.
- [58] M. Rini, R. Tobey, N. Dean, J. Itatani, Y. Tomioka, Y. Tokura, R. W. Schoenlein, and A. Cavalleri. Control of the electronic phase of a manganite by mode-selective vibrational excitation. *Nature*, 449:72–74, 2007.
- [59] M. Först, R. Mankowsky, and A. Cavalleri. Mode selective control of the crystal lattice. *Acc. Chem. Res.*, 48:380–387, 2015.
- [60] N. Casaretto, S. Pillet, E. E. Bendeif, D. Schaniel, A. K. E. Gallien, P. Klüfers, and T. Woike. Multiple light-induced no linkage isomers in the dinitrosyl complex $[\text{RuCl}(\text{NO})_2(\text{PPh}_3)_2]\text{BF}_4$ unravelled by photocrystallographic and IR analysis. *IUCr*, 2:35–44, 2015.
- [61] K. H. Kim, H. Ki, K. Y. Oang, S. Nozawa, T. Sato, J. Kim, T. K. Kim, J. Kim, S.-I. Adachi, and H. Ihee. Global reaction pathways in the photodissociation of I_3^- ions in solution at 267 and 400 nm studied by picosecond X-ray liquidography. *Chem. Phys. Chem.*, 14:3687–3697, 2013.
- [62] A. Plech, M. Wulff, S. Bratos, F. Mirloup, R. Vuilleumier, F. Schotte, and P. A. Anfinrud. Visualizing chemical reactions in solution by picosecond x-ray diffraction. *Phys. Rev. Lett.*, 92:125505, 2004.
- [63] S. Jun, J. H. Lee, J. Kim, J. Kim, K. H. Kim, Q. Kong, T. K. Kim, M. Lo Russo, M. Wulff, and H. Ihee. Photochemistry of Hg_2Br_2 in methanol investigated using time-resolved x-ray liquidography. *Phys. Chem. Chem. Phys.*, 12:11536–11547, 2010.
- [64] T. K. Kim, M. Lorenc, J. H. Lee, M. Lo Russo, J. Kim, M. Cammarata, Q. Kong, S. Noel, A. Plech, M. Wulff, and H. Ihee. Spatiotemporal reaction kinetics of an ultrafast photoreaction pathway visualized by time-resolved liquid x-ray diffraction. *Proc. Natl. Acad. Sci.*, 103:9410–9415, 2006.
- [65] M. Christensen, K. Haldrup, K. S. Kjaer, M. Cammarata, M. Wulff, K. Bechgaard, H. Weihe, N. H. Harrit, and M. M. Nielsen. Structure of a short-lived excited state trinuclear Ag–Pt–Pt complex in aqueous solution by time-resolved X-ray scattering. *Phys. Chem. Chem. Phys.*, 12:6921–6923, 2010.
- [66] M. Christensen, K. Haldrup, K. Bechgaard, R. Feidenhans'l, Q. Kong, M. Cammarata, M. Lo Russo, M. Wulff, N. Harrit, and M. M. Nielsen. Time-resolved x-ray scattering of an electronically excited state in solution. structure of the $^3A_{2u}$ state of tetrakis- μ -pyrophosphitodiplatinate(II). *J. Am. Chem. Soc.*, 131:502–508, 2008.
- [67] K. Haldrup, G. Vanko, W. Gawelda, A. Galler, G. Doumy, A. M. March, E. P. Kanter, A. Bordage, A. Dohn, T. B. van Driel, K. S. Kjaer, H. T. Lemke, S. E. Canton, J. Uhlrig, V. Sundström, L. Young, S. H. Southworth, M. M. Nielsen, and C. Bressler. Guest-host interactions investigated by

- time-resolved x-ray spectroscopies and scattering at MHz rates: solvation dynamics and photoinduced spin transition in aqueous $\text{Fe}(\text{bipy})_3^{2+}$. *J. Phys. Chem.*, 116:9878–9887, 2012.
- [68] K. H. Kim, J. Kim, K. Y. Oang, J. H. Lee, D. Grolimund, C. J. Milne, T. J. Penfold, S. L. Johnson, A. Galler, T. W. Kim, J. G. Kim, D. Suh, J. Moon, J. Kim, K. Hong, L. Guérin, T. K. Kim, M. Wulff, C. Bressler, and H. Ihee. Identifying the major intermediate species by combining time-resolved x-ray solution scattering and x-ray absorption spectroscopy. *Phys. Chem. Chem. Phys.*, 17:23298–23302, 2015.
- [69] K. Haldrup, M. Christensen, M. Cammarata, Q. Kong, M. Wulff, S. O. Mariager, K. Bechgaard, R. Feidenhans'l, N. Harrit, and M. M. Nielsen. Structural tracking of a bimolecular reaction in solution by time-resolved x-ray scattering. *Angew. Chem., Int. Ed.*, 48:4180–4184, 2009.
- [70] J. H. Lee, M. Wulff, S. Bratos, J. Petersen, L. Guérin, J.-C. Leicknam, M. Cammarata, Q. Kong, K. B. Moller, and H. Ihee. Filming the birth of molecules and accompanying solvent rearrangement. *J. Am. Chem. Soc.*, 135:3255–3261, 2013.
- [71] K. H. Kim, J. G. Kim, S. Nozawa, T. Sato, K. Y. Oang, T. W. Kim, H. Ki, J. Jo, S. Park, C. Song, T. Sato, K. Ogawa, T. Togashi, K. Tono, M. Yabashi, T. Ishikawa, J. Kim, R. Ryoo, J. Kim, H. Ihee, and S.-I. Adachi. Direct observation of bond formation in solution with femtosecond X-ray scattering. *Nature*, 518:385–389, 2015.
- [72] V. Srajer, T. Teng, T. Ursby, C. Pradervand, Z. Ren, S. Adachi, W. Schildkamp, D. Bourgeois, M. Wulff, and K. Moffat. Photolysis of the carbon monoxide complex of myoglobin: nanosecond time-resolved crystallography. *Science*, 274:1726–1729, 1996.
- [73] V. Srajer, Z. Ren, T. Teng, M. Schmidt, T. Ursby, D. Bourgeois, C. Pradervand, W. Schildkamp, M. Wulff, and K. Moffat. Protein conformational relaxation and ligand migration in myoglobin: a nanosecond to millisecond molecular movie from time-resolved Laue X-ray diffraction. *Biochemistry*, 40:13802–13815, 2001.
- [74] C. D. M. Hutchison, M. Kaucikas, J. Tenboer, C. Kupitz, K. Moffat, M. Schmidt, and J. J. van Thor. Photocycle populations with femtosecond excitation of crystalline photoactive yellow protein. *Chem. Phys. Lett.*, 654:63–71, 2016.
- [75] U. K. Genick, G. E. O. Borgstahl, K. Ng, Z. Ren, C. Pradervand, P. M. Burke, V. Srajer, T.-Y. Teng, W. Schildkamp, D. E. McRee, K. Moffat, and E. D. Getzoff. Structure of a protein photocycle intermediate by millisecond time-resolved crystallography. *Science*, 275:1471–1475, 1997.
- [76] B. Perman, V. Srajer, Z. Ren, T.-Y. Teng, C. Pradervand, T. Ursby, D. Bourgeois, F. Schotte, M. Wulff, R. Kort, K. Hellingwerf, and K. Moffat. Energy transduction on the nanosecond time scale: early structural events in a xanthopsin photocycle. *Science*, 279:1946–1950, 1998.
- [77] H. Ihee, S. Rajagopal, V. Srajer, R. Pahl, S. Anderson, M. Schmidt, F. Schotte, P. A. Anfinrud, M. Wulff, and K. Moffat. Visualizing reaction pathways in photoactive yellow protein from nanoseconds to seconds. *Proc. Natl. Acad. Sci.*, 102:7145–7150, 2005.
- [78] F. Schotte, H. Sun Cho, V. R. I. Kaila, H. Kamikubo, N. Dashdorj, E. R. Henry, T. J. Graber, R. Henning, M. Wulff, G. Hummer, M. Kataoka, and P. A. Anfinrud. Watching a signaling protein function in real time via 100-ps time-resolved Laue crystallography. *Proc. Natl. Acad. Sci.*, 109:19256–19261, 2012.
- [79] T. W. Kim, J. H. Lee, J. Choi, K. H. Kim, L. J. van Wilderen, L. Guerin, Y. Kim, Y. O. Jung, C. Yang, J. Kim, M. Wulff, J. J. van Thor, and H. Ihee. Protein structural dynamics of photoactive yellow protein in solution revealed by pump–probe X-ray solution scattering. *J. Am. Chem. Soc.*, 134:3145–3153, 2012.
- [80] H. S. Cho, F. Schotte, N. Dashdorj, J. Kyndt, and P. A. Anfinrud. Probing anisotropic structure changes in proteins with picosecond time-resolved small-angle X-ray scattering. *J. Phys. Chem. B*, 117:15825–15832, 2013.
- [81] S. Boutet, L. Lomb, G. J. Williams, T. R. M. Barends, A. Aquila, R. B. Doak, U. Weierstall, D. P. DePonte, J. Steinbrener, R. L. Shoeman, M. Messerschmidt, A. Barty, T. A. White,

- S. Kassemeyer, R. A. Kirian, M. M. Seibert, P. A. Montanez, C. Kenney, R. Herbst, P. Hart, J. Pines, G. Haller, S. M. Gruner, H. T. Philipp, M. W. Tate, M. Hromalik, L. J. Koerner, N. van Bakel, J. Morse, W. Ghonsalves, D. Arnlund, M. J. Bogan, C. Coleman, R. Fromme, C. Y. Hampton, M. S. Hunter, L. C. Johansson, G. Katona, C. Kupitz, M. Liang, A. V. Martin, K. Nass, L. Redecke, F. Stellato, N. Timneanu, D. Wang, N. A. Zatsepin, D. Schafer, J. Defever, R. Neutze, P. Fromme, J. C. H. Spence, H. N. Chapman, and I. Schlichting. High-resolution protein structure determination by serial femtosecond crystallography. *Science*, 337:362–364, 2012.
- [82] I. Schlichting. Serial femtosecond crystallography: the first five years. *IUCr*, 2:246–255, 2015.
- [83] J. Tenboer, S. Basu, N. Zatsepin, K. Pande, D. Milathianaki, M. Frank, M. Hunter, S. Boutet, G. J. Williams, J. E. Koglin, D. Oberthuer, M. Heymann, C. Kupitz, C. Conrad, J. Coe, S. Roy-Chowdhury, A. Weierstall, D. James, D. Wang, T. Grant, A. Barty, O. Yefanov, J. Scales, C. Gati, C. Seuring, V. Srajer, R. Henning, P. Schwander, R. Fromme, A. Ourmazd, K. Moffat, J. J. van Thor, J. C. H. Spence, P. Fromme, H. Chapman, and M. Schmidt. Time-resolved serial crystallography captures high-resolution intermediates of photoactive yellow protein. *Science*, 346:1242–1246, 2014.
- [84] K. Pande, C. D. M. Hutchison, G. Groenhof, A. Aquila, J. S. Robinson, J. Tenboer, S. Basu, S. Boutet, D. P. DePonte, M. Liang, T. A. White, N. A. Zatsepin, O. Yefanov, D. Morozov, D. Oberthuer, C. Gati, G. Subramanian, D. James, Y. Zhao, J. Koralek, J. Brayshaw, C. Kupitz, C. Conrad, S. Roy-Chowdhury, J. D. Coe, M. Metz, P. L. Xavier, T. D. Grant, J. E. Koglin, G. Ketawala, R. Fromme, V. Srajer, R. Henning, J. C. H. Spence, A. Ourmazd, P. Schwander, U. Weierstall, M. Frank, P. Fromme, A. Barty, H. N. Chapman, K. Moffat, J. J. van Thor, and M. Schmidt. Femtosecond structural dynamics drives the trans/cis isomerization in photoactive yellow protein. *Science*, 352:725–729, 2016.
- [85] A. Cannizzo, C. J. Milne, C. Consani, W. Gawelda, Ch. Bressler, F. van Mourik, and M. Chergui. Light-induced spin crossover in Fe(II)-based complexes: the full photocycle unraveled by ultrafast optical and X-ray spectroscopies. *Coord. Chem. Rev.*, 254:2677–2686, 2010.
- [86] E. Collet, N. Moisan, C. Baldé, R. Bertoni, E. Trzop, C. Laulhé, M. Lorenc, M. Servol, H. Cailleau, A. Tissot, M.-L. Boillot, T. Graber, R. Henning, P. Coppens, and M. Buron le Cointe. Ultrafast spin-state photoswitching in a crystal and slower consecutive processes investigated by femtosecond optical spectroscopy and picosecond X-ray diffraction. *Phys. Chem. Chem. Phys.*, 14:6192–6199, 2012.
- [87] M. Lorenc, C. Balde, W. Kaszub, A. Tissot, N. Moisan, M. Servol, M. Buron-Le-Cointe, H. Cailleau, P. Chasle, P. Czarnecki, M. L. Boillot, and E. Collet. Cascading photoinduced, elastic, and thermal switching of spin states triggered by a femtosecond laser pulse in an Fe(III) molecular crystal. *Phys. Rev. B*, 85:054302, 2012.
- [88] R. Bertoni, M. Lorenc, A. Tissot, M.-L. Boillot, and E. Collet. Femtosecond photoswitching dynamics and microsecond thermal conversion driven by laser heating in Fe(III) spin-crossover solids. *Coord. Chem. Rev.*, 282–283:66–76, 2015.
- [89] M. Lorenc, J. Hébert, N. Moisan, E. Trzop, M. Servol, M. Buron le Cointe, H. Cailleau, M. L. Boillot, E. Pontecorvo, M. Wulff, S. Koshihara, and E. Collet. Successive dynamical steps of photoinduced switching of a molecular Fe(II) spin-crossover material by time-resolved x-ray diffraction. *Phys. Rev. Lett.*, 103:028301, 2009.
- [90] P. J. Chupas, K. W. Chapman, and P. L. Lee. Application of an amorphous silicon-based area detector for high-resolution, high-sensitivity and fast time-resolved pair distribution function measurements. *J. Appl. Crystallogr.*, 40:463–470, 2007.
- [91] M. A. Newton, K. W. Chapman, D. Thompsett, and P. J. Chupas. Chasing changing nanoparticles with time-resolved pair distribution function methods. *J. Am. Chem. Soc.*, 134:5036–5039, 2012.

- [92] D. Saha, K. M. O. Jensen, C. Tyrsted, E. D. Bojesen, A. H. Mamakhel, A.-C. Dippel, M. Christensen, and B. B. Iversen. In situ total X-ray scattering study of WO_3 nanoparticle formation under hydrothermal conditions. *Angew. Chem., Int. Ed.*, 53:3667–3670, 2014.
- [93] D. Saha, E. D. Bojesen, K. M. O. Jensen, A.-N. Dippel, and B. B. Iversen. Formation mechanisms of Pt and Pt_3Gd nanoparticles under solvothermal conditions: an in situ total X-ray scattering study. *J. Phys. Chem. C*, 119:13357–13362, 2015.
- [94] C. Tyrsted, N. Lock, K. M. O. Jensen, M. Christensen, E. D. Bojesen, H. Emerich, G. Vaughan, S. J. L. Billinge, and B. B. Iversen. Evolution of atomic structure during nanoparticle formation. *IUCr*, 1:165–171, 2014.
- [95] K. M. O. Jensen, H. L. Andersen, C. Tyrsted, E. D. Bojesen, A.-C. Dippel, N. Lock, S. J. L. Billinge, B. B. Iversen, and M. Christensen. Mechanisms for iron oxide formation under hydrothermal conditions: an in situ total scattering study. *ACS Nano*, 8:10704–10714, 2014.
- [96] J.-L. Mi, K. M. O. Jensen, C. Tyrsted, M. Bremholm, and B. B. Iversen. In situ total X-ray scattering study of the formation mechanism and structural defects in anatase TiO_2 nanoparticles under hydrothermal conditions. *CrystEngComm*, 17:6868–6877, 2015.
- [97] R. Tazaki, D. Fu, M. Itoh, M. Daimon, and S. Koshihara. Lattice distortion under an electric field in BaTiO_3 piezoelectric single crystal. *J. Phys. Condens. Matter*, 21:215903, 2009.
- [98] D. Issenmann, S. Schleaf, S. Ibrahimkuty, G. Buth, T. Baumbach, A. Plech, M. Beyer, and J. Demsar. Lattice dynamics of laser excited ferroelectric BaTiO_3 . *Acta Phys. Pol. A*, 121:319–323, 2012.
- [99] C. Moriyoshi, S. Hiramoto, H. Ohkubo, Y. Kuroiwa, H. Osawa, K. Sugimoto, S. Kimura, M. Takara, Y. Kitanaka, Y. Noguchi, and M. Miyayama. Synchrotron radiation study on time-resolved tetragonal lattice strain of BaTiO_3 under electric field. *Jpn. J. Appl. Phys.*, 50:09NE05, 2011.
- [100] C. Moriyoshi and Y. Kuroiwa. Time-resolved measurements of lattice strain in ferroelectric crystals induced by application of electric field: single crystal diffraction study. *Trans. Am. Crystallogr. Assoc.*, 170–181, 2013.
- [101] A. Grigoriev, D.-H. Do, D. M. Kim, C.-B. Eom, B. Adams, E. M. Dufresne, and P. G. Evans. Nanosecond domain wall dynamics in ferroelectric $\text{Pb}(\text{Zr},\text{Ti})\text{O}_3$ thin films. *Phys. Rev. Lett.*, 96:187601, 2006.
- [102] J. Davaasambuu, A. Pucher, V. Kochin, and U. Pietsch. Atomistic origin of the inverse piezoelectric effect in $\alpha\text{-SiO}_2$ and $\alpha\text{-GaPO}_4$. *Europhys. Lett.*, 62:834–840, 2003.
- [103] R. Guillot, P. Fertey, N. K. Hansen, P. Allé, E. Elkaim, and C. Lecomte. Diffraction study of the piezoelectric properties of low quartz. *Eur. Phys. J. B*, 42:373–380, 2004.
- [104] S. Aoyagi, H. Osawa, K. Sugimoto, A. Fujiwara, S. Takeda, C. Moriyoshi, and Y. Kuroiwa. Atomic motion of resonantly vibrating quartz crystal visualized by time-resolved x-ray diffraction. *Appl. Phys. Lett.*, 107:201905, 2015.
- [105] D. Schick, A. Bojahr, M. Herzog, P. Gaal, I. Vrejoiu, and M. Bargheer. Following strain-induced mosaicity changes of ferroelectric thin films by ultrafast reciprocal space mapping. *Phys. Rev. Lett.*, 110:095502, 2013.
- [106] C. v. Korff Schmising, M. Bargheer, M. Kiel, N. Zhavronkov, M. Woerner, T. Elsaesser, I. Vrejoiu, D. Hesse, and M. Alexe. Coupled ultrafast lattice and polarization dynamics in ferroelectric nanolayers. *Phys. Rev. Lett.*, 98:257601, 2007.
- [107] D. Daranciang, M. J. Highland, H. Wen, S. M. Young, N. C. Brandt, H. Y. Hwang, M. Vattilana, M. Nicoul, F. Quirin, J. Goodfellow, T. Qi, I. Grinberg, D. M. Fritz, M. Cammarata, D. Zhu, H. T. Lemke, D. A. Walko, E. M. Dufresne, Y. Li, J. Larsson, D. A. Reis, K. Sokolowski-Tinten, K. A. Nelson, A. M. Rappe, P. H. Fuoss, G. B. Stephenson, and A. M. Lindenberg. Ultrafast photovoltaic response in ferroelectric nanolayer. *Phys. Rev. Lett.*, 108:087601, 2012.

- [108] K. Istomin, V. Kotaidis, A. Plech, and Q. Kong. Dynamics of the laser-induced ferroelectric excitation in BaTiO₃ studied by X-ray diffraction. *Appl. Phys. Lett.*, 90:022905, 2007.
- [109] N. Nagaosa and Y. Tokura. Orbital physics in transition metal oxides. *Science*, 288:462–468, 2000.
- [110] P. Beaud, A. Caviezel, S. O. Mariager, L. Rettig, G. Ingold, C. Dornes, S. W. Huang, J. A. Johnson, M. Radovic, T. Huber, T. Kubacka, A. Ferrer, H. T. Lemke, M. Chollet, D. Zhu, J. M. Glowina, M. Sikorski, A. Robert, H. Wadati, M. Nakamura, M. Kawasaki, Y. Tokura, S. L. Johnson, and U. Staub. A time-dependent order parameter for ultrafast photoinduced phase transitions. *Nat. Mater.*, 13:923–927, 2014.
- [111] H. Ichikawa, S. Nozawa, T. Sato, A. Tomita, K. Ichiyangi, M. Chollet, L. Guerin, N. Dean, A. Cavalleri, S.-I. Adachi, T.-H. Arima, H. Sawa, Y. Ogimoto, M. Nakamura, R. Tamaki, K. Miyano, and S.-Y. Koshihara. Transient photoinduced “hidden” phase in a manganite. *Nat. Mater.*, 10:101–105, 2014.
- [112] H. Ehrke, R. I. Tobey, S. Wall, S. A. Cavill, M. Först, V. Khanna, Th. Garl, N. Stojanovic, D. Prabhakaran, A. T. Boothroyd, M. Gensch, A. Mirone, P. Reutler, A. Revcolevschi, S. S. Dhesi, and A. Cavalleri. Photoinduced melting of antiferromagnetic order in La_{0.5}Sr_{1.5}MnO₄ measured using ultrafast resonant soft X-ray diffraction. *Phys. Rev. Lett.*, 106:217401, 2011.
- [113] A. Caviezel, U. Staub, S. L. Johnson, S. O. Mariager, E. Mohr-Vorobeva, G. Ingold, C. J. Milne, M. Garganourakis, V. Scagnoli, S. W. Huang, Q. X. Jia, S.-W. Cheong, and P. Beaud. Femtosecond dynamics of the structural transition in mixed valence manganites. *Phys. Rev. B*, 86:174105, 2012.
- [114] R. Kajimoto, H. Yoshizawa, Y. Tomioka, and Y. Tokura. Commensurate-incommensurate transition in the melting process of orbital ordering in Pr_{0.5}Ca_{0.5}MnO₃: a neutron diffraction study. *Phys. Rev. B*, 63:212407, 2001.
- [115] M. V. Zimmermann, J. P. Hill, D. Gibbs, M. Blume, D. Casa, B. Keimer, Y. Murakami, Y. Tomioka, and Y. Tokura. Interplay between charge, orbital and magnetic order in Pr_{1-x}Ca_xMnO₃. *Phys. Rev. Lett.*, 83:4872–4875, 1999.
- [116] M. Eichberger, H. Schafer, M. Krumova, M. Beyer, J. Demsar, H. Berger, G. Moriena, G. Sciaini, and R. J. D. Miller. Snapshots of cooperative atomic motions in the optical suppression of charge density waves. *Nature*, 468:799–802, 2010.
- [117] E. Mohr-Vorobeva, S. L. Johnson, P. Beaud, U. Staub, R. De Souza, C. Milne, G. Ingold, J. Demsar, H. Schaefer, and A. Titov. Nonthermal melting of a charge density wave in TiSe₂. *Phys. Rev. Lett.*, 107:036403, 2011.
- [118] C. Laulhé, L. Cario, B. Corraze, E. Janod, T. Huber, G. Lantz, S. Boulfaat, A. Ferrer, S. O. Mariager, J. A. Johnson, S. Grubel, A. Lubcke, G. Ingold, P. Beaud, S. L. Johnson, and S. Ravy. X-ray study of femtosecond structural dynamics in the 2D charge density wave compound 1T-TaS₂. *Physica B*, 460:100–104, 2015.
- [119] K. Haupt, M. Eichberger, N. Erasmus, A. Rohwer, J. Demsar, K. Rossnagel, and H. Schwoerer. Ultrafast metamorphosis of a complex charge-density wave. *Phys. Rev. Lett.*, 116:01640, 2016.
- [120] G. Dixit, J. M. Slowik, and R. Santra. Proposed imaging of the ultrafast electronic motion in samples using X-ray phase contrast. *Phys. Rev. Lett.*, 110:137403, 2013.
- [121] G. Dixit and R. Santra. Imaging ultrafast electronic motion by X-ray scattering. *J. Phys. Conf. Ser.*, 488:012009, 2014.
- [122] G. Dixit, J. M. Slowik, and R. Santra. Theory of time-resolved nonresonant X-ray scattering for imaging ultrafast coherent electron motion. *Phys. Rev. A*, 89:043409, 2014.
- [123] V. S. Yakovlev, M. I. Stockman, F. Krausz, and P. Baum. Atomic-scale diffractive imaging of sub-cycle electron dynamics in condensed matter. *Sci. Rep.*, 5:14581, 2015.

- [124] T. Elsaesser and M. Woerner. Photoinduced structural dynamics of polar solids studied by femtosecond X-ray diffraction. *Acta Crystallogr., Sect. A*, 66:168–178, 2010.
- [125] M. Woerner, F. Zamponi, Z. Ansari, J. Dreyer, B. Freyer, M. Prémont-Schwarz, and T. Elsaesser. Concerted electron and proton transfer in ionic crystals mapped by femtosecond X-ray powder diffraction. *J. Chem. Phys.*, 133:064509, 2010.
- [126] F. Zamponi, P. Rothhardt, J. Stingl, M. Woerner, and T. Elsaesser. Ultrafast large-amplitude relocation of electronic charge in ionic crystals. *Proc. Natl. Acad. Sci.*, 109:5207–5212, 2012.
- [127] J. Stingl, F. Zamponi, B. Freyer, M. Woerner, T. Elsaesser, and A. Borgschulte. Electron transfer in a virtual quantum state of LiBH_4 induced by strong optical fields and mapped by femtosecond X-ray diffraction. *Phys. Rev. Lett.*, 109:147402, 2012.
- [128] V. Juvé, M. Holtz, F. Zamponi, M. Woerner, T. Elsaesser, and A. Borgschulte. Field-driven dynamics of correlated electrons in LiH and NaBH_4 revealed by femtosecond X-ray diffraction. *Phys. Rev. Lett.*, 111:217401, 2013.
- [129] M. Woerner, M. Holtz, V. Juvé, T. Elsaesser, and A. Borgschulte. Femtosecond X-ray diffraction maps field-driven dynamics in ionic crystals. *Faraday Discuss.*, 171:373–392, 2014.
- [130] B. Freyer, F. Zamponi, V. Juvé, J. Stingl, M. Woerner, T. Elsaesser, and M. Chergui. Ultrafast inter-ionic charge transfer of transition-metal complexes mapped by femtosecond X-ray powder diffraction. *J. Chem. Phys.*, 138:144504, 2013.
- [131] T. Elsaesser and M. Woerner. Perspective: structural dynamics in condensed matter mapped by femtosecond X-ray diffraction. *J. Chem. Phys.*, 140:020901, 2014.
- [132] P. Baum and A. H. Zewail. Attosecond electron pulses for 4D diffraction and microscopy. *Proc. Natl. Acad. Sci.*, 104:18409–18414, 2007.
- [133] J. Miao, T. Ishikawa, I. K. Robinson, and M. M. Murnane. Beyond crystallography: diffractive imaging using coherent X-ray light sources. *Science*, 348:530–535, 2015.
- [134] J. N. Clark, L. Beitra, G. Xiong, A. Higginbotham, D. M. Fritz, H. T. Lemke, D. Zhu, M. Chollet, G. J. Williams, M. Messerschmidt, B. Abbey, R. J. Harder, A. M. Korsunsky, J. S. Wark, and I. K. Robinson. Ultrafast three-dimensional imaging of lattice dynamics in individual gold nanocrystals. *Science*, 341:56–59, 2013.
- [135] M. P. Minitti, J. M. Budarz, A. Kirrander, J. S. Robinson, D. Ratner, T. J. Lane, D. Zhu, J. M. Glowia, M. Kozina, H. T. Lemke, M. Sikorski, Y. Feng, S. Nelson, K. Saita, B. Stankus, T. Northey, J. B. Hastings, and P. M. Weber. Imaging molecular motion: femtosecond X-ray scattering of an electrocyclic chemical reaction. *Phys. Rev. Lett.*, 114:255501, 2015.

Bruce D. Patterson

Ultrafast science

Keywords: XFEL, coherent phonons, correlated X-ray scattering, nonlinear X-ray optics

Introduction

With the development of dedicated synchrotron facilities beginning in the 1970s, X-ray sources underwent dramatic improvement, bringing new possibilities for investigating matter with X-rays, as illustrated in the previous chapters. The average source brightness, defined as photons per time, area, solid angle, and bandwidth, of a modern synchrotron beamline exceeds that of a laboratory source by more than ten orders of magnitude, and as we have seen, a pulse duration as short as tens of picoseconds permits the study of rapid changes in the sample under investigation. In 2009, X-ray source characteristics made a quantum leap with the advent of the LINAC Coherent Light Source (LCLS), the world's first X-ray Free-Electron Laser (XFEL), at the reconfigured Stanford Linear Accelerator Center in Menlo Park, California. In contrast to the synchrotron, which emits quasi-continuously, the XFEL emits intense short pulses of radiation at a typical repetition rate of 100 Hz. These pulses are extremely intense, with a peak brightness more than ten orders of magnitude greater than that of a state-of-the-art synchrotron, and they have a very short duration, less than 100 fs. Furthermore, since emission occurs on average into fewer than 1.5 optical modes, the radiation has a high transverse coherence. Disadvantages of XFEL radiation are a relatively poor longitudinal coherence – the relative bandwidth of the emitted X-rays is typically 0.1% – and large pulse-to-pulse fluctuations in the central wavelength, spectral shape, and integrated pulse energy. But perhaps the most important limitation of a typical XFEL compared to a synchrotron is that whereas a synchrotron simultaneously supplies radiation to 20 or so beamlines, at an XFEL, only one or two experiments can operate at a time.

These properties of XFEL radiation allow novel applications and call for novel measurement techniques. A large class of XFEL experiments are characterized as “diffract-before-destroy.” A 20-fs XFEL pulse containing 10^{11} 10 keV hard X-ray photons implies a peak power of 8 GW, and, when focused to a $5 \times 5 \mu\text{m}^2$ spot, produces a peak fluence of $6.4 \mu\text{J}/\mu\text{m}^2$. Liquid water has an absorption length for 10 keV photons of 2 mm, and hence the maximum absorbed energy density is $20 \text{ eV}/\text{nm}^3$, which eventually produces a destructive temperature rise of almost 800 °C.

The key here is the word “eventually”: destruction of the sample is effectively delayed due to the finite atomic velocities of the exploding sample. Figure 1 shows a simulation [1] of an XFEL pulse striking a single protein molecule. Note that during

<https://doi.org/10.1515/9783110433920-006>

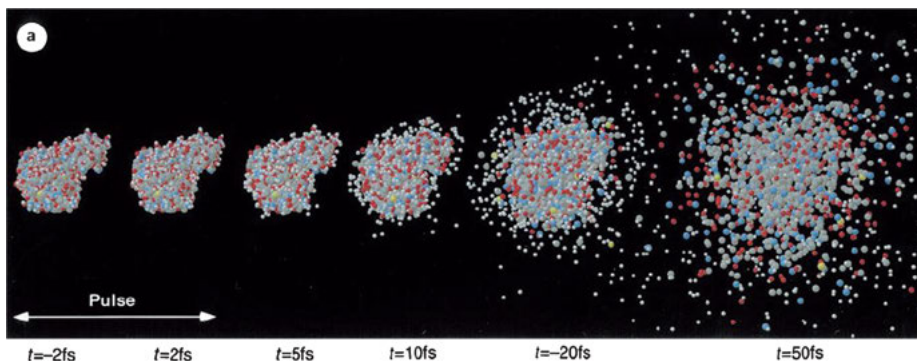


Figure 1: A simulation of a 2-fs FWHM XFEL pulse of 3×10^{12} 12 keV photons per 100 nm diameter focus spot striking a single lysozyme protein molecule [1]. The dots represent individual atoms: white, H; grey, C; blue, N; red O; yellow S. Note that the 2-fs XFEL pulse effectively samples an undisturbed molecule, the basis of “diffract-before-destroy.” Reprinted by permission from Macmillan Publishers Ltd.

a sufficiently short duration XFEL pulse, the inertia of the atoms causes the molecule to remain largely intact, in principle allowing the collection of diffraction scattering patterns that reflect the structure of the unperturbed molecule. In a sense, the short XFEL pulse “outruns” the radiation damage inflicted to the sample. For a protein sample, modern synchrotron beamlines are sufficiently bright that severe sample damage occurs within seconds, generally requiring the sample to be cryogenically cooled and severely limiting the amount of data that can be acquired from a small sample. Diffract-before-destroy at an XFEL avoids these limitations, but it requires that the sample be replaced by an identical copy prior to each shot, e.g., introduced as a stream of particles carried by a gas or liquid jet or prepositioned on the surface of a sample holder and scanned by the incoming beam. Furthermore, since each sample has a different orientation, sophisticated sorting software is required to analyze the orientation of each shot and to combine the information from many shots into a consistent data set, which is then analyzed to yield the desired structural information.

In principle, individual molecules can serve as identical samples for a diffract-before-destroy experiment, and a long-term goal of several XFEL research groups is to determine the atomic-scale structure of protein molecules in this way. Principal problems are presently the lack of sufficient peak X-ray intensity to orient a single-shot diffraction pattern and uncontrolled background scattering from the carrier material.

One of the most successful applications of short-wavelength XFEL pulses to date has, however, been “serial protein crystallography,” in which diffract-and-destroy experiments are performed on nanometer-size protein crystals (for a review, see, e.g., [2]). For many protein systems, these can be made in large numbers and can be introduced into the XFEL beam in a liquid jet of compatible solvent, and the crystalline Bragg reflections produce sufficiently strong diffraction spots to orient single-shot patterns. Since it is not yet possible to synchronize the delivery of individual nanocrystals

with the arrival of the XFEL pulses, a relatively large amount of protein material is wasted, but the advantages of the technique are the effective avoidance of radiation damage and the avoidance of cryogenic cooling. A further advantage of using crystalline samples in a diffract-before-destroy experiment is the “self-termination” effect of Bragg scattering [3]: Even if an XFEL pulse is longer in duration than the time required for the sample to be destroyed, scattering from the perturbed sample during the latter part of the pulse produces only a weak diffuse background to the strong Bragg scattering from the intact crystal during the early part of the pulse.

However, dramatic changes in the electronic structure – excitation and ionization – may occur on the time scale of the XFEL pulse duration, and since it is the electrons that scatter the X-rays (“Thompson scattering”), there can be important consequences for the diffraction pattern. For the case of serial crystallography using protein nanocrystals, careful simulation [4] has shown that the resulting diffraction pattern reflects an “effective” scattering strength for each atom, which is modified from that of an unperturbed atom. Since this effective form factor changes with pulse fluence and duration, we can in principle use this effect to control the atomic visibility and hence to obtain information on the crystallographic phase. We note here that in Hamburg, Germany, a laboratory-based XFEL is under development, incorporating THz accelerating modules and an optical undulator [5]. The resulting sub-fs pulses should effectively “outrun” even electronic damage in the sample.

A possible attractive alternative to single-particle imaging with an XFEL for structural studies is offered by the “cross-correlation” technique, described in Section 2 of this chapter, which allows structural studies of a randomly positioned and oriented ensemble of identical particles.

The combination at an XFEL of short-wavelength short-pulse duration and high peak intensity leads to another class of experiments: “pump–probe” investigations of dynamic processes on the atomic scale [6]. Here, a “pump” signal creates a nonequilibrium situation in the sample under investigation, and after a suitable delay, the sample is “probed” using the XFEL pulse. By repeating the experiment, either with the same sample after it has returned to equilibrium or with a copy of the original sample, and by using a different pump–probe delay interval, a “molecular movie” can be effectively constructed, frame by frame. The sample may be a collection of photosensitive molecules, which can be efficiently and promptly excited by a short, intense electromagnetic pulse with a suitable wavelength (UV, Vis, IR, or perhaps even terahertz), the range of delays can be chosen to bracket typical chemical reaction and electronic deactivation times (ps), and the probe experiment can be a scattering experiment (such as serial crystallography, single-particle imaging, or diffuse scattering [7]) or a spectroscopic measurement (X-ray absorption or emission spectroscopy [6, 8]). Important results have been obtained with pump–probe photo-chemistry at XFELs on both inorganic and organic catalytic systems [9].

A special case of pump–probe experiments involves the photoexcitation of atomic vibrations and subsequent probing using X-rays. This has been demonstrated with

XFELs for the case of molecules in solution [10, 11], but most work has involved photoexcited lattice vibrations in solids, the so-called “coherent phonons.” These experiments are discussed in Section 1. A further special case of pump–probe, perhaps with a delay interval of zero, uses the nonlinear interaction of two intense X-ray pulses or an X-ray and an optical pulse. Two examples of the nonlinear interactions using X-rays are discussed in Section 3: stimulated X-ray Raman scattering and X-ray optical sum-frequency generation. The chapter closes with a semirigorous mathematical explanation of XFEL operation, a short description of existing and planned XFEL facilities and an outlook on the future of XFEL science.

1 Time-resolved X-ray diffraction studies of photoexcited coherent phonons

1.1 Electronic time scales in condensed matter

The properties of materials are principally determined by the electrons that bind together their constituent atoms. As described in earlier chapters, the ground-state characteristics of matter, i.e., the molecular and crystal structure and the response to low-energy thermal, electrical, and magnetic perturbations, are generally well understood. To a large degree, this understanding is based on the Born–Oppenheimer approximation: because atomic nuclei are much heavier than the electrons, it is assumed that the electrons react instantaneously to a perturbation and that the nuclei move in a self-consistent field produced by an electron distribution that is in local and temporal equilibrium. But upon closer examination, we find that perturbed electrons do not respond instantaneously and, furthermore, that competitive processes on ultrafast time scales determine important dynamical properties – in particular, regarding chemical (e.g., catalytic) and optical properties.

The most convenient method of quickly creating a nonequilibrium electron distribution – excited electrons and holes – in condensed matter is irradiation by an intense optical laser pulse. It is then interesting to consider the timescales for energy distribution and relaxation of such excited carriers and how they ultimately equilibrate with the motion of the atomic nuclei. The timescale for electron–electron interactions is of the order of the plasma frequency ν_p of an electron gas with a density appropriate to that of condensed matter, $n_{el} \approx 5 \times 10^{29} \text{ e}^-/\text{m}^3$:

$$\frac{1}{\nu_p} = 2\pi \sqrt{\frac{\epsilon_0 m_e}{n_{el} e^2}} \approx 0.16 \text{ fs.} \quad (1)$$

Upon excitation of a solid by photons with energy above the bandgap, electron–hole pairs are created. These will then diffuse, with a diffusion constant of the order of that

for a low-density plasma: $D_p \approx 40 \text{ cm}^2/\text{s}$ [12]. For a typical optical absorption length $l_{\text{abs}} \approx 100 \text{ nm}$, the carriers leave the absorption region on a timescale

$$\tau_{\text{diff}} = \frac{l_{\text{abs}}^2}{D_p} \approx 250 \text{ fs.} \quad (2)$$

Ultimately, the electrons and holes will recombine, either radiatively or nonradiatively. Near-bandgap electron–hole pairs in semiconductors have lifetimes spanning the timescales of ns to ms [13], whereas X-ray-initiated core electron excitations have lifetimes in the range 10 ps–0.1 fs [14].

In this section, we describe how ultrafast X-ray diffraction (XRD) can be used to indirectly probe electron dynamics following photoexcitation of the sample. The nonequilibrium electron distribution modifies the interatomic bonding forces, and if the duration of the optical pulse is shorter than a typical vibration period of the host atoms (100 fs), then lattice vibrations are generated, which may be detected by ultrafast X-ray diffraction. Sufficiently intense excitation may even produce displacement amplitudes close to or exceeding the “Lindemann stability limit” (approximately 15% of the nearest-neighbor distance [15]), resulting in “nonthermal melting.”

1.2 Coherent phonon generation in bismuth

Lattice vibrations in solids are coupled to electronic excitations via the electron–phonon interaction; basically, a lattice distortion influences the electric susceptibility, and vice versa, giving rise to impulsive stimulated Raman scattering [16, 17]. In stimulated Raman scattering, SRS (Figure 2(a)), an “excitation” wave with frequency ω_1 brings the system from the ground state g to a real or virtual highly excited state e , and a simultaneous “stimulation” wave with somewhat lower frequency ω_2 causes a

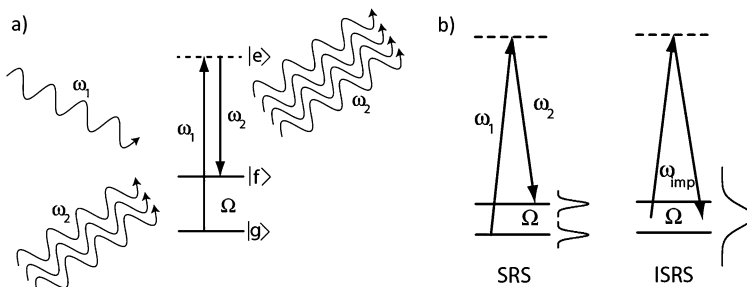


Figure 2: (a) Inelastic stimulated Raman scattering (SRS) of two optical frequency components ω_1 and ω_2 , based on the electron–phonon coupling between electronic and lattice degrees of freedom, generates a phonon of frequency Ω via a virtual highly excited state e . (b) A single, sufficiently short-duration optical pulse may contain both frequency components ω_1 and ω_2 , resulting in “impulsive” stimulated Raman (ISRS) scattering and the generation of coherent phonons.

stimulated decay to a low-lying excited state f . The result is the creation of a phonon excitation with frequency $\Omega = \omega_1 - \omega_2$ and the coherent amplification of the stimulation wave ω_2 . In impulsive stimulated Raman scattering, ISRS (Figure 2 (b)), a single broadband wave with center frequency ω_{imp} , e.g., obtained from a single pulse of sufficiently short duration, provides both excitation and stimulation. A good reference for SRS and other nonlinear optical effects is the book by Boyd [18].

The creation with SRS of a phonon excitation may be understood in terms of a sudden, optically induced change in the atomic potential of the lattice, which produces a nonequilibrium state, in which a significant fraction of the atoms in a crystal begin to vibrate in phase about a new equilibrium position (“displacive excitation”). If this excitation occurs in phase in the entire sample, then we speak of a coherent nonequilibrium quantum state, also known as a “Glauber” state [19]. In this section, we describe the detection of the Glauber state via ultrafast time-resolved XRD, but the associated periodic modulation of the electric susceptibility implies that the Raman interaction can also be used to optically detect coherent phonons, e.g., via the time-dependent optical reflectivity.

A large literature exists on optically generated and detected coherent phonons in bismuth. The choice of bismuth is due to its structural simplicity, its low optical phonon frequencies and its strong electron–phonon interaction. To observe atomic-scale features of coherent phonon creation and decay within the unit cell of the crystal, ultrafast pump–probe X-ray diffraction (XRD) is required, using a short-duration optical pump pulse followed a variable delay later by a short-duration hard X-ray pulse. Although most ultrafast XRD studies of coherent phonons have to date been performed using laser-plasma sources [20] and sliced synchrotron beams [21], the intense, subpicosecond pulses of the XFEL are now preferred.

At room temperature, bismuth has the rhombohedral $A7$ structure [22] ($a = 4.7461 \text{ \AA}$, $\alpha = 57.23^\circ$) with a two-atom basis at

$$\mathbf{r}_{0\pm} = \pm a(\xi_0, \xi_0, \xi_0) \quad (3)$$

with $\xi_0 = 0.2334$ (Figure 3 (b)). This value is the result of a small Peierls distortion (Figure 3 (a)) of a perfect cubic structure ($\alpha = 60^\circ$, $\xi_0 = 0.25$). Cubic bismuth would be a metal with a half-filled conduction band; the Peierls distortion lowers the total free energy (electronic plus elastic) and reduces the electron density of states at the Fermi level; this interaction between crystal structure and electron density is the origin of the strong electron–phonon interaction in this material.

An optical phonon periodically displaces the atoms according to

$$\mathbf{r}_{\pm} = \mathbf{r}_{0\pm} \pm \mathbf{u}(t). \quad (4)$$

For $\mathbf{u}(t)$ parallel to the [111] crystal axis, the phonon mode is A_{1g} ; there are also two additional modes, denoted E_g , with motion perpendicular to [111].

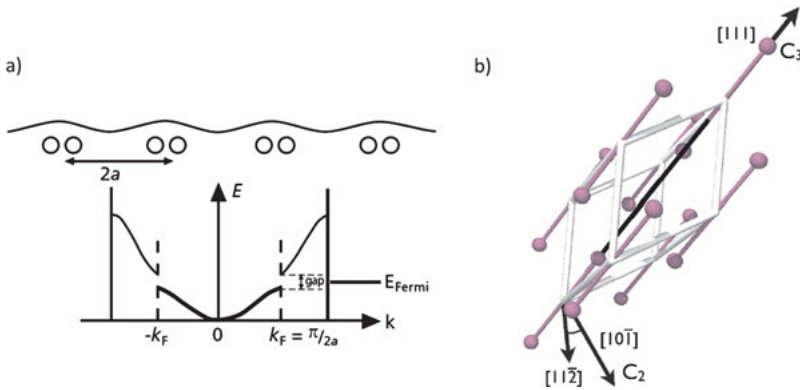


Figure 3: (a) The Peierls instability [23]. Under special circumstances, it may be energetically favorable for a metallic crystal to undergo a spontaneous lattice distortion, forming atomic dimers and doubling the crystal unit cell. In the reciprocal space, the Brillouin zone is halved, and a gap opens at the Fermi level, causing a lowering of the electronic energy, which more than compensates the increase in elastic energy. In bismuth, such a Peierls coupling between the lattice and electronic degrees of freedom is responsible for the large electron–phonon interaction. (b) The unit cell of Bi, indicating the two-atom basis oriented along the [111] direction [24]. Reprinted with permission from the American Physical Society.

The electronic excitation caused by a short-duration optical laser pulse suddenly changes the electron distribution among bonding and antibonding states and hence alters the interatomic potential. This results in a new equilibrium neighbor distance, producing a displacively excited coherent A_{1g} phonon, which corresponds to oscillations with amplitude $a\delta_{||}(0)$ along the three-fold axis (Figure 4 (a)). The subsequent atomic displacements then are

$$\mathbf{u}(t) = a\delta_{||}(t)(1, 1, 1). \tag{5}$$

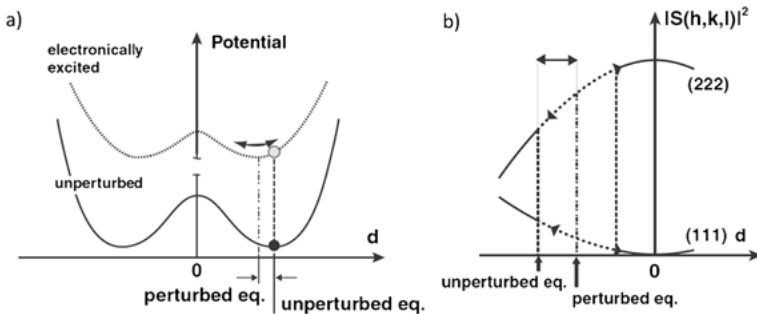


Figure 4: (a) The displacive excitation of coherent A_{1g} phonons by the inelastic scattering of intense pulses of optical radiation [21]. (b) The atomic displacements for the A_{1g} optical phonon in Bi produce changes in the diffracted X-ray intensity, which are opposite for the 111 and 222 reflections [21].

1.3 X-ray diffraction observation of coherent phonons in Bi

The diffracted X-ray intensity for Bi, corresponding to a Bragg reflection with reciprocal lattice vector $G_{hkl} = \frac{2\pi}{a}(hkl)$, is given by

$$I_{hkl} \propto |S_{hkl}|^2 \propto \cos^2(\mathbf{G}_{hkl} \cdot \mathbf{r}_+) \exp(-\langle (\mathbf{u} \cdot \mathbf{G}_{hkl})^2 \rangle), \quad (6)$$

where the exponential term is the Debye–Waller factor. For the A_{1g} optical phonon mode and symmetrical reflections hhh , we thus have (disregarding for the moment the Debye–Waller term):

$$\begin{aligned} I_{hhh}(t) &\propto \cos^2\{6\pi h[\xi + \delta_{\parallel}(t)]\} \\ &\approx \cos^2(6\pi h\xi) - 6\pi h \sin(12\pi h\xi)\delta_{\parallel}(t) \\ &= \begin{cases} 0.095 - 11.0\delta_{\parallel}(t), & 111, \\ 0.657 + 35.8\delta_{\parallel}(t), & 222, \end{cases} \end{aligned} \quad (7)$$

where a Taylor expansion in δ_{\parallel} has been truncated at the linear term; see Figure 4 (b).

In a “slicing” source of ultrashort X-ray pulses, an optical laser pulse is used to deflect a short-duration section of the circulating electron bunch at a synchrotron, allowing the extraction of a short but low-intensity X-ray pulse [25]. Using such a source, a single crystal of Bi was pumped with 800 nm, 1.4 mJ/cm² light pulses of 115 fs duration, and probed at glancing incidence with 7.1 keV X-ray pulses of 140 fs duration [26, 27]. The resulting changes measured in the intensities of the X-ray diffraction Bragg reflections are shown as functions of pump–probe delay in Figure 5 (a). Strong

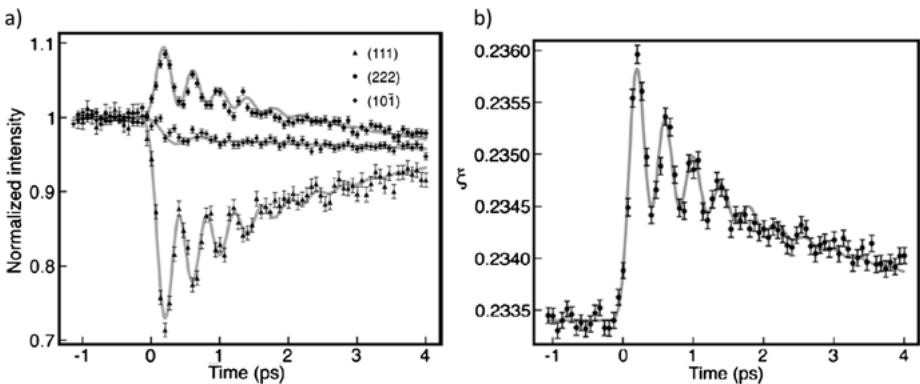


Figure 5: (a) Time-dependent changes in X-ray diffraction intensities from photo-pumped Bi, showing, for the 111 and 222 reflections, oscillations attributable to displacively excited coherent A_{1g} optical phonons [26]. (b) The atomic position parameter $\xi(t)$ for the A_{1g} coherent optical phonon, extracted from the 111 and 222 diffraction data from Figure 4 (a) [26]. Note that this atomic-scale information cannot be obtained from optical reflectivity measurements. Reproduced with permission of the International Union of Crystallography.

oscillations from coherent A_{1g} optical phonons are seen for the 111 and 222 reflections – as predicted, the oscillations are 180° out of phase. Using equation (7), the atomic position parameter $\xi(t) = \xi_0 + \delta_{\parallel}(t)$ can be extracted from these data (see Figure 5 (b)); the fitted oscillation frequency is 2.65 THz, the peak-to-peak vibration amplitude is 2.7 pm, and the exponential damping time, due to a combination of electronic relaxation and diffusion, is 2.9 ps. It should be noted that a direct measurement of the phonon vibration amplitude is only possible with time-resolved XRD. As will be discussed further, such experiments demonstrate a decrease in the A_{1g} frequency with increasing pump fluence due to “electronic softening” of the atomic potential.

1.4 Density functional theory calculations of photoexcited phonon dynamics

Phonon dynamics in a solid are determined by the potential energy surface seen by the atoms. This surface is accessible using the density functional theory (DFT) described in an earlier chapter [28–31]. The pertinent phonon frequencies can be computed, e.g., using a supercell “frozen phonon” formalism or via dynamical force matrices in “density functional perturbation theory” (DFPT) [32].

To compute the atomic potential in photoexcited Bi as a function of degree of electronic excitation (see Figure 6 (a)), Murray et al. [28] used the “constrained DFT” technique [33], in which the valence band occupation at each point in the Brillouin zone

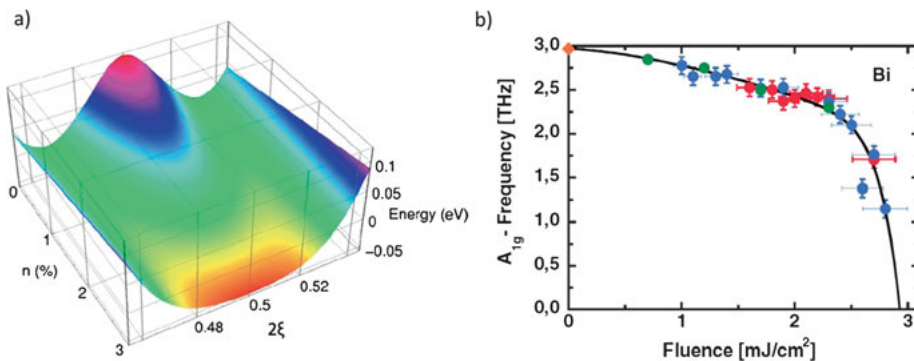


Figure 6: (a) The atomic potential energy for symmetric (A_{1g}) optical $k = 0$ phonons in Bi as a function of the atomic coordinate 2ξ and the fractional electron–hole plasma density n [28]. Note the shift of the potential minimum (responsible for a displacive phonon excitation) and electronic softening (responsible for an excitation-dependent phonon frequency) with increasing n at low excitation levels and ultimately the disappearance of the $2\xi_0 = 0.5$ potential barrier upon strong excitation (predicting a photoinduced structural phase transition). Reprinted with permission from the American Physical Society. (b) A compilation of the dependence of A_{1g} coherent optical phonon frequencies on the excitation pump fluence, measured with X-ray techniques [20]. Reproduced with the permission of AIP Publishing.

is weighted by a Fermi–Dirac distribution with temperature $k_B T = 0.5$ eV, such that the average energy per electron–hole, 1.5 eV, is equal to the pump photon energy. This assumes sufficiently rapid electron–electron scattering to assure a local equilibrium. Separate values for the chemical potential for electrons and holes were constrained in such a way as to guarantee the assumed photoexcited electron–hole plasma density n . The figure shows the atomic potential energy as a function of n and the atomic coordinate 2ξ , which was fit to the expression

$$E(n, x) = \sum_{i=0}^8 \sum_{j=0}^2 a_{ij} (2\xi - 0.5)^{2i} n^j. \quad (8)$$

At small values of n , the computed optical phonon frequency undergoes an approximately linear “electronic softening” with increasing n , in good agreement with experiment (Figure 6 (b)). Although the potential is clearly anharmonic, particularly at high photoexcitation, the authors of the study claim that the most significant effect on the phonon frequency at low excitation levels is a general photoexcited flattening or “electronic softening.” At sufficiently high excitation, it is predicted that the potential barrier $2\xi_0 = 0.5$ disappears, indicating a photoinduced structural phase transition.

1.5 Asymmetric photo-excitation of TO coherent E_g phonons

We have seen that the hhh (and in particular, the 111) Bragg reflections in Bi are sensitive to the A_{1g} phonon mode, with longitudinal vibrations along the three-fold C_3 symmetry axis (Figure 3 (b)). The *transverse* E_g phonon mode involves atomic motion perpendicular to this axis, e.g., along the two-fold C_2 axis, and if we include such motion, then the atomic displacement vector in equation (4) now becomes

$$\mathbf{u}(t) = a\delta_{\parallel}(t)(1, 1, 1) + a\delta_{\perp}(t)(1, 0, \bar{1}) \quad (9)$$

with the corresponding 111 and 001 diffracted intensities

$$\begin{aligned} I_{111} &\propto \cos^2 \{6\pi[\xi + \delta_{\parallel}(t)]\}, \\ I_{001} &\propto \cos^2 \{2\pi[\xi + \delta_{\parallel}(t) - \delta_{\perp}(t)]\}. \end{aligned} \quad (10)$$

Note that the 111 reflection is only sensitive to A_{1g} displacements, but that a 001 measurement makes also the E_g mode accessible.

Johnson et al. [27] have performed time-resolved pump–probe XRD measurements on Bi with a flexible geometry, allowing observations of both 111 and 001 diffractions with optical pump pulses whose polarization can be varied with respect to the C_3 direction (i.e., the pump polarization can include a component perpendicular to the crystal symmetry axis). Analysis of this experiment resulted in the transverse atomic oscillations as a function of the sample temperature shown in Figure 7. The absorbed

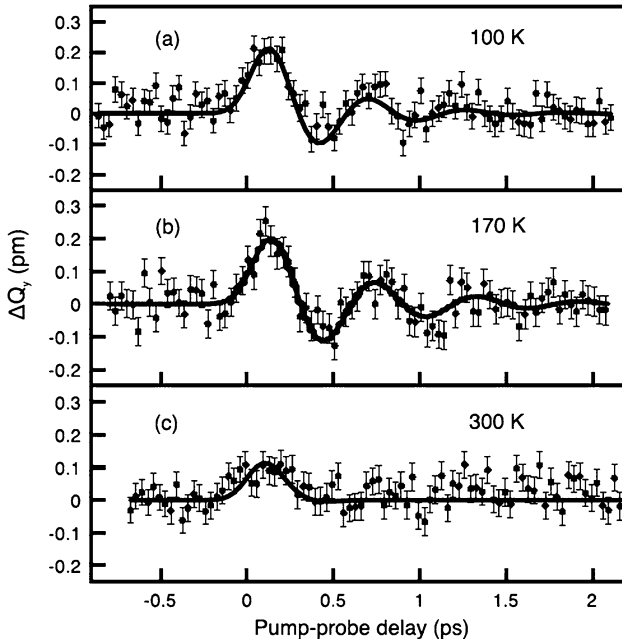


Figure 7: Temperature-dependent transverse optical phonon (E_g) oscillations in Bi, excited with a pump polarization component perpendicular to the C_3 symmetry axis and extracted using equation (10) from combined 111 and 001 diffraction measurements [27]. The plots show the transverse atomic displacement $a\delta_{\perp}(t)$. Reprinted with permission from the American Physical Society.

pump fluence $1.6 \text{ mJ}/\text{cm}^2$ was similar to that used for the A_{1g} data in Figure 5. Compared to the A_{1g} oscillations, notice for E_g : the lower oscillation frequency (1.8–1.9 THz vs 2.65 THz), the much smaller and temperature-dependent peak-to-peak oscillation amplitude (0.2–0.1 pm vs 2.7 pm) and the shorter damping time (0.3–0.1 ps vs 2.9 ps), together with the fact that the E_g vibrations oscillate with a sine curve about zero, whereas A_{1g} shows a vertically offset cosine curve. As discussed both qualitatively [27] and quantitatively [34, 31], these features are compatible with a model for E_g phonon photoexcitation, in which a transversely polarized pump pulse produces a short-lived asymmetric electron distribution (Figure 8). This asymmetric distribution causes the phase-shifted E_g oscillations, and its rapid (fs) temperature-dependent decay to a symmetric distribution explains the small, T -dependent E_g phonon oscillation amplitude.

1.6 Squeezed-state coherent phonons

In a further study of ultrafast pump–probe XRD in photoexcited bismuth, Johnson et al. [24] observed oscillations in the diffracted intensity from the $(10\bar{1})$ and $(11\bar{2})$

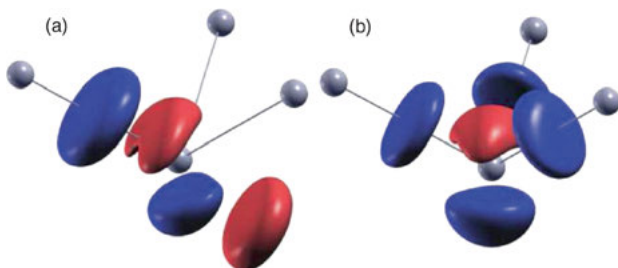


Figure 8: Transient changes in valence electron distributions, computed using DFT, for optical pump pulses polarized along (a) the asymmetric $[10\bar{1}]$ and (b) the symmetric $[111]$ crystal directions [31]. The red and blue isosurfaces indicate regions where the electron density is respectively increased and decreased by $0.0002 \text{ e}/a_{\text{Bohr}^3}$. A short-lived asymmetric electron distribution is believed to be responsible for the excitation of E_g phonon vibrations. Reprinted with permission from the American Physical Society.

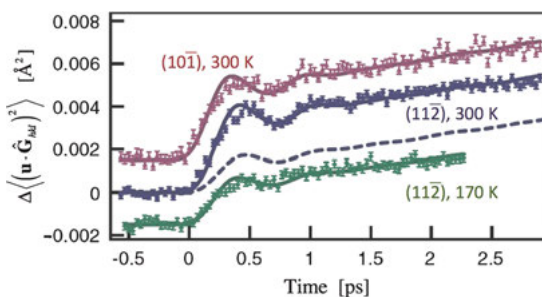


Figure 9: The time-dependent change in the direction-projected mean-square atomic displacement for the $(10\bar{1})$ and the $(11\bar{2})$ diffraction planes in Bi [24]. The curves have been displaced vertically. The dashed curve is a DFT simulation for the $(11\bar{2})$ plane at room temperature. Reprinted with permission from the American Physical Society.

planes. Although the corresponding reciprocal lattice vectors are perpendicular to $[111]$, and hence such data may be expected to show oscillations characteristic of the E_g phonon mode, the authors argue [24] that these will be unobservably weak. Instead, they assign the observed oscillations to variations in the Debye–Waller factor in equation (6) and extract from the experimental data the time-dependent change in the projected variances $\Delta\langle(\mathbf{u} \cdot \hat{\mathbf{G}}_{hkl})^2\rangle$ (Figure 9).

An oscillation in the variance of the displacement of a harmonic oscillator (HO) occurs upon a sudden change (at $t = 0$) in the HO potential. For the $(10\bar{1})$ and the $(11\bar{2})$ diffraction data of Figure 9, this HO is believed to correspond to a weighted average of the phonon modes over the Brillouin zone [24]; in a model calculation, it is assumed that these mode frequencies, and hence the effective HO frequency, suddenly decrease upon optical pumping by the factor $\lambda = 0.88$. Such a sudden softening of the HO potential implies that an HO wavefunction, which is an energy eigenfunction prior to

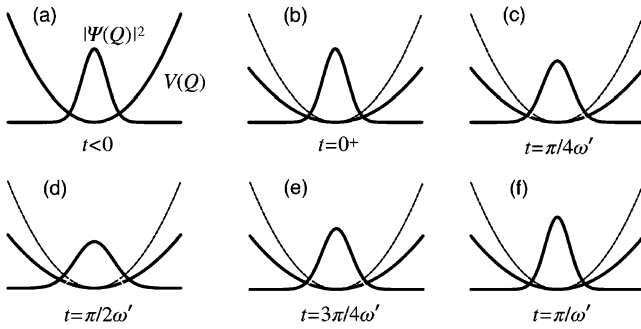


Figure 10: (a) A one-dimensional quantum harmonic oscillator (HO) with eigenfrequency ω in a potential $V(Q)$ (solid parabolic curve) is for times $t < 0$ in the energy eigenstate $\Psi(Q)$. (Q is the spatial coordinate.) (b) At time $t = 0$, the potential is suddenly softened to the eigenfrequency $\omega' = \lambda\omega < \omega$; the HO state is no longer an eigenstate. (c–f) For times $t > 0$, the Q -variance oscillates at the frequency $2\omega'$. From [26]. Reproduced with permission of the International Union of Crystallography.

$t = 0$, is at later times no longer an eigenfunction and hence shows a variance which oscillates at twice the new effective HO frequency (Figure 10).

A simple demonstration of this behavior for a suddenly softened one-dimensional quantum harmonic oscillator has been given by [35, 36]. The wavefunction at $t = 0^+$ is identical to that for $t < 0$:

$$\psi(x, 0) = \left(\frac{m\omega}{\pi\hbar}\right)^{1/4} e^{-\frac{m\omega}{2\hbar}x^2}, \tag{11}$$

and this wavefunction implies the following initial expectation values and variances:

$$\begin{aligned} \langle x(0) \rangle &= 0, \\ \langle p(0) \rangle &= -i\hbar \left\langle \frac{d}{dx} \right\rangle = 0, \\ \langle x(0)p(0) \rangle &= \frac{i\hbar}{2}, \\ \langle p(0)x(0) \rangle &= -\frac{i\hbar}{2}, \\ \Delta x^2(0) &= \langle x^2(0) \rangle - \langle x(0) \rangle^2 = \frac{\hbar}{2m\omega}, \\ \Delta p^2(0) &= \langle p^2(0) \rangle - \langle p(0) \rangle^2 = \frac{\hbar m\omega}{2}, \\ \Delta x(0)\Delta p(0) &= \frac{\hbar}{2}. \end{aligned} \tag{12}$$

At $t = 0^+$, the HO eigenfrequency is assumed to undergo a slight instantaneous change from ω to $\lambda\omega$. In the Heisenberg picture, the Hamiltonian and equations of motion for $t > 0$ are given by

$$\hat{H} = \frac{\hat{p}}{2m} + \frac{m\lambda^2\omega^2\hat{x}^2}{2},$$

$$\begin{aligned}\frac{d\hat{x}}{dt} &= \frac{1}{i\hbar} [\hat{x}(t), \hat{H}] = \frac{\hat{p}(t)}{m}, \\ \frac{d\hat{p}}{dt} &= \frac{1}{i\hbar} [\hat{p}(t), \hat{H}] = -m\lambda^2\omega^2\hat{x}(t),\end{aligned}\quad (13)$$

implying the following solutions for the position and momentum operators:

$$\begin{aligned}\hat{x}(t) &= \hat{x}(0) \cos \lambda\omega t + \frac{\hat{p}(0)}{m\lambda\omega} \sin \lambda\omega t, \\ \hat{p}(t) &= \hat{p}(0) \cos \lambda\omega t - m\lambda\omega\hat{x}(0) \sin \lambda\omega t.\end{aligned}\quad (14)$$

We square these and take expectation values to obtain the variances

$$\begin{aligned}\Delta x^2(t) &= \Delta x^2(0) \cos^2 \lambda\omega t + \frac{\langle \hat{p}^2(0) \rangle}{m^2\lambda^2\omega^2} \sin^2 \lambda\omega t, \\ \Delta p^2(t) &= \Delta p^2(0) \cos^2 \lambda\omega t + m^2\lambda^2\omega^2 \langle \hat{x}^2(0) \rangle \sin^2 \lambda\omega t,\end{aligned}\quad (15)$$

or

$$\begin{aligned}\Delta x^2(t) &= \frac{\Delta x^2(0)}{2} \left\{ \left(1 + \frac{1}{\lambda^2} \right) + \left(1 - \frac{1}{\lambda^2} \right) \cos 2\lambda\omega t \right\}, \\ \Delta p^2(t) &= \frac{\Delta p^2(0)}{2} \{ (1 + \lambda^2) + (1 - \lambda^2) \cos 2\lambda\omega t \}.\end{aligned}\quad (16)$$

Notice that the sudden decrease in eigenfrequency ($\lambda < 1$) causes the momentum variance to periodically drop below its value at $t = 0$. This effect is known as “squeezing” and is the subject of a large literature, in particular, with regard to the *photon* boson field [37].

1.7 Further X-ray investigations of photoexcited vibrations

Displacive-excited coherent optical phonons have also been observed with ultrafast XRD in several manganites [38, 39]. Also, photoexcited acoustic phonons can be generated in gold nanoparticles and observed with ultrafast XRD via periodic changes in the coherent diffraction features near crystal Bragg reflections [40]. Besides crystal diffraction peaks, atomic vibrations using time-resolved *diffuse* X-ray scattering can also be observed. In this way, acoustic phonons generated by photoinduced squeezing can be observed and analyzed to produce a wave-vector dependence of the electron–phonon interaction in germanium [41]. In addition, using time-resolved diffuse scattering from molecules in solution, two photoexcited oscillation frequencies (3 and 4 THz) have been observed of the 6 nitrogen atoms surrounding the central cobalt atom of organo-metallic molecules $[\text{Co}(\text{terpy})_2]^{2+}$ in water [11]. Molecular vibrations can also be observed using nontime-resolved X-ray spectroscopy by performing inelastic Raman scattering at X-ray wavelengths. Although it is not able to directly measure vibration amplitudes, this technique has the advantage over optical measurements of

elemental specificity – by measuring the inelastic energy losses for an incident photon energy close to a characteristic X-ray core excitation resonance we can enhance the sensitivity for vibrations that involve a particular element. In this way, at the 530 eV oxygen resonance in liquid acetone ($\text{C}_3\text{H}_6\text{O}$), the fundamental C–O stretch frequency, at 52 THz, can be observed along with nine higher harmonics [10]. Such observations can yield the shape of the possibly anharmonic interatomic potential energy surface.

2 Ultrafast correlated X-ray scattering on static molecules in solution

2.1 Protein structure from X-rays

Diffraction on crystalline samples, generally at a synchrotron source, is the standard X-ray-based method of determining the structure of biological macromolecules with atomic resolution (0.5–2 Å) [42]. However, this method has several drawbacks. The requirement of large ($>1000 \mu\text{m}^3$), high-quality crystals is often a major bottleneck, in particular, for proteins and protein complexes, which are also difficult to isolate and purify. Membrane proteins, which represent a significant fraction of both the human genome and of the targets for designer pharmaceuticals, are notoriously difficult to crystallize in three dimensions. Packing protein molecules in a crystal lattice introduces molecular contacts, which may induce significant structural perturbations. Radiation damage by the incident synchrotron beam typically limits the allowable exposure time of a protein crystal to the order of seconds. As mentioned in the Introduction to this chapter, the advent of serial femtosecond crystallography at X-ray free-electron lasers [2] has the potential of avoiding several of these drawbacks.

A lower resolution alternative (10–50 Å) to macromolecular X-ray diffraction from crystals is small-angle X-ray scattering (SAXS) on liquid solutions [43]. By introducing the liquid sample into the beam via a flowing liquid jet we are also able to perform synchronized optical pumping and SAXS probing to study photoinduced structural changes at time scales down to picoseconds [44].

In a SAXS experiment (Figure 11 (a)), incident monochromatic hard X-rays ($>5 \text{ keV}$) with incident wavevector $q_{\text{in}} = 2\pi/\lambda$, are scattered through an angle 2θ to an area detector. Because of the isotropy of the solvent and randomly-oriented macromolecules, the resulting scattering pattern $I(q)$, as a function of $q = |\mathbf{q}_{\text{out}} - \mathbf{q}_{\text{in}}|$, consists of concentric “Debye–Scherrer-like” rings, reflecting the structure factor of the scatterers. For elastic scattering ($q_{\text{out}} = q_{\text{in}}$), the scattering wavevector and the scattering angle are related by

$$q = \frac{4\pi \sin \theta}{\lambda}. \quad (17)$$

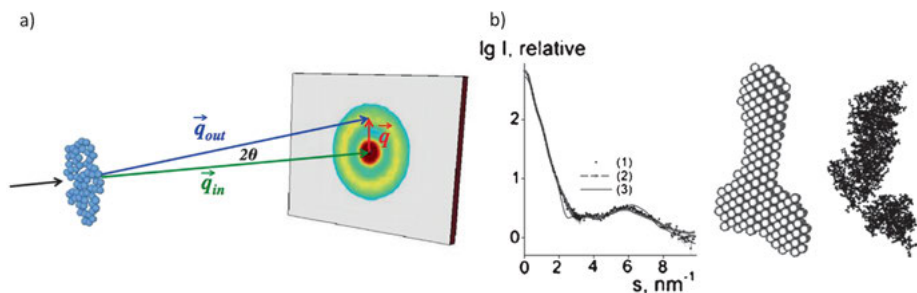


Figure 11: (a) The small-angle X-ray scattering (SAXS) geometry with the incident X-rays (black) scattering on a sample (light blue) to produce a ring-like pattern at the detector. We assume elastic scattering, implying incoming and outgoing wavevectors of equal magnitude ($q_{in} = q_{out} = 2\pi/\lambda$) and a scattering wavevector $q = 4\pi \sin \theta/\lambda$. (b) Extraction of a low-resolution 3D structure of a subunit of yeast V-ATPase from SAXS in solution under the assumption of uniform density [45]. The measured SAXS pattern of subunit C (curve 1, left) yielded the bead model (center), which corresponds to the calculated scattering pattern 2. The right-hand model and pattern 3 represent the known high-resolution structure of the structurally similar subunit H. Reproduced with permission of John Wiley & Sons.

In spite of their simple radial symmetry, the analysis of SAXS patterns has been developed to the point where using the assumed constraints such as uniform density, low-resolution molecular shapes may be determined [43] (Figure 11 (b)).

In 1977, Kam [46] described a possible extension of SAXS, which uses the fact that, for a finite number of static scattering molecules, the scattering patterns are not perfectly axially symmetric: they show intensity fluctuations, which can be analyzed in terms of correlation functions. Although, as the molecules change their orientations, these fluctuations vary from exposure to exposure, Kam argued that the correlation functions are specific to the molecular structure and can provide additional structural information, perhaps even down to atomic resolution.

A principal requirement of Kam's method is that the sample remains stationary during the X-ray exposure. According to the Stokes–Einstein–Debye relation [47], the reorientation time of a molecule in solution is given by

$$\tau_{\text{rot}} = \frac{4\pi\eta R_H^3}{3k_B T}, \quad (18)$$

where R_H is the *hydrodynamic radius* of the molecule, η is the viscosity of the solvent, k_B is the Boltzmann constant, and T is the temperature. The radius R_H , which includes the solvation shell around the molecule, is comparable to [48] the molecular *radius of gyration* R_g , which we will encounter later in this section. The value of R_H for the protein lysozyme is 1.9 nm [49], and the viscosity of water is 0.89 mPa s, implying a room-temperature reorientation time of 6.2 ns. The challenge is now to accumulate sufficient scattered X-ray counts in individual sub-ns SAXS exposures to allow the computation

of meaningful intensity correlation functions. This is just now becoming feasible with XFEL sources, and the technique has been named *correlated X-ray scattering* (CXS).

The following discussion of CXS is largely based on the excellent tutorial review by Kirian [50] and the publication by Malmerberg et al. [51], and the following assumptions are made: We assume that an incoming X-ray photon is scattered at most once in the sample (kinematic approximation), and we ignore inelastic processes and absorption. Further, we disregard background scattering from the solvent, which is to be subtracted from the experimentally observed patterns. We take the sample-detector distance to be much larger than the size of the sample (Fraunhofer limit), and by considering only small-angle scattering ($q \ll q_{\text{in}}$), we take the Ewald sphere to be flat. Finally, we avoid interparticle interference effects by assuming that although the coherence length of the incoming X-ray beam is larger than a single molecule, it is smaller than the intermolecule distance.

It should be noted that the CXS method, besides providing structural information on identical individual particles or molecules, can also be applied to the study of short-range order in colloidal suspensions. Furthermore, with repeated exposures, it is even possible to observe transient effects [52].

2.2 Model-independent analysis of SAXS data

Our goal is to determine from small-angle X-ray scattering the parameters that characterize the electronic charge density $\rho(\mathbf{r})$ of the molecule under study [51]. Of particular interest is the density autocorrelation function or *Patterson function*

$$\gamma(\mathbf{r}') = \int \rho(\mathbf{r})\rho(\mathbf{r} + \mathbf{r}')d\mathbf{r}, \quad (19)$$

the Fourier transform of which is proportional to the q -dependent scattered X-ray intensity from a single molecule,

$$I_1(\mathbf{q}) \propto \int_V \gamma(\mathbf{r})e^{i\mathbf{q}\cdot\mathbf{r}}d\mathbf{r}. \quad (20)$$

The sample consists of N identical molecules with random orientations ω . The exposure number k of such an ensemble produces the scattering pattern

$$I_{(k)}(\mathbf{q}) = \sum_{\alpha}^N I_1(\mathbf{q}; \omega_k^{\alpha}) \quad (21)$$

(the inclusion of the parameter ω_k^{α} specifies the orientation of the α th molecule for exposure number k), and an average over many such exposures yields the radially symmetric SAXS pattern

$$I_{\text{SAXS}}(q) = I_{\text{SAXS}}(\mathbf{q}) = \langle I_{(k)}(\mathbf{q}) \rangle$$

$$\begin{aligned}
 &= \left\langle \int \gamma(\mathbf{r}') e^{i\mathbf{q} \cdot R_\omega \mathbf{r}'} d\mathbf{r}' \right\rangle_\omega \\
 &= \int r^2 \bar{\gamma}(r) \frac{\sin(qr)}{qr} dr.
 \end{aligned} \tag{22}$$

Here, R_ω is a rotation matrix, and $\bar{\gamma}(r)$ is the rotationally averaged Patterson function. Due to this rotational averaging, $I_{\text{SAXS}}(q)$ can either be measured by averaging many brief exposures, each with frozen molecular orientations, or with a single long exposure, during which the molecules are allowed to rotate. An inverse transformation of $I_{\text{SAXS}}(q)$ yields $\bar{\gamma}(r)$:

$$\bar{\gamma}(r) \propto \int_0^\infty q^2 I_{\text{SAXS}}(q) \frac{\sin(qr)}{qr} dq, \tag{23}$$

from which the rotationally-averaged *pair density distribution function* $P(r)$, related to the pair distribution function discussed in an earlier chapter, is obtained:

$$P(r) = r^2 \bar{\gamma}(r). \tag{24}$$

A measure of the maximum linear dimension of the molecule, d_{max} , is given by the value of r for which $P(r)$ drops to zero. Further model-independent structural information is obtained [53] from a so-called *Guinier plot* of $\ln [I_{\text{SAXS}}(q)]$ vs q^2 . For small q , such a plot yields a straight line with slope

$$\frac{d \ln [I_{\text{SAXS}}(q)]}{d(q^2)} \approx -\frac{R_g^2}{3}. \tag{25}$$

Here R_g is the so-called *radius of gyration*, another measure of the molecular size, which is defined as the *rms* distance from each of the atoms of the molecule, weighted by its X-ray scattering factor, to their centroid.

As noted before (Figure 11 (b)), by incorporating additional constraints, such as the assumption of a uniform density inside the molecule, low-resolution shape information can be determined from SAXS data by iterative fitting.

2.3 Model-independent analysis of CXS data

The basic idea of CXS is that correlation function analysis of the short-duration measurements of the scattering from immobile molecules can provide additional structural information to that available from SAXS. Figure 12 shows how, from an experimental scattering exposure, one-, two-, and three-point correlation functions are computed [54]. The one-point correlation function is essentially SAXS. In the following, we concentrate on the two-point correlation function (Figure 12 (b)): For exposure number k , the counting rates at two pixels in the scattering detector correspond to the scattered intensities $I_{(k)}(\mathbf{q}_1)$ and $I_{(k)}(\mathbf{q}_2)$. The opening angle between the two q -vectors is $\Delta\phi$ (labeled ψ in Figure 12 (b)).

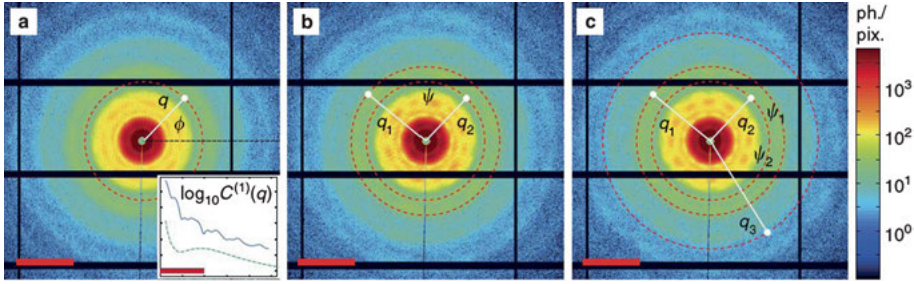


Figure 12: Scattering images and cross-correlation definition [54]. Three examples of the 3 751 different scattering images of the gold nanostructures of Figure 15 (d) on a logarithmic color scale. Superimposed on the patterns (a), (b), and (c) are parameters pertinent to computing the one-, two-, and three-point correlation functions, respectively. In frame (b), the opening angle between the scattering vectors \mathbf{q}_1 and \mathbf{q}_2 is labeled ψ ; in the present text, this angle is denoted $\Delta\phi$. The red dashed circles indicate the paths of azimuthal averaging. The inset in (a) shows the experimental $I_{\text{SAXS}}(q)$ (here denoted $C^{(1)}(q)$), where the green dashed curve is the subtracted background signal. The red bars correspond to a wave-vector interval $\Delta q = 0.1 \text{ nm}^{-1}$. Reprinted by permission from Macmillan Publishers Ltd.

We define the experimental two-point correlation function as the average over the many individual X-ray exposures k of the product of the two scattered intensities:

$$C_{\text{exp}}(\mathbf{q}_i, \mathbf{q}_j) = \langle I_{(k)}(\mathbf{q}_i) I_{(k)}(\mathbf{q}_j) \rangle_k. \quad (26)$$

The N -particle correlation function is an average over the product of two single-particle scattering intensities (first line of equation (27)): each particle has the unique orientation ω_k^α , where the indices $\alpha, \beta \in 1, N$ specify the particles, and k specifies the X-ray exposure. In the second line of the equation, we split the sums over particles into correlated quantities ($\alpha = \beta$) and uncorrelated quantities ($\alpha \neq \beta$), and in the third line, we take the limit of a large number of exposures:

$$\begin{aligned} C_N(\mathbf{q}_i, \mathbf{q}_j) &= \left\langle \sum_{\alpha\beta}^N I_1(\mathbf{q}_i; \omega_k^\alpha) I_1(\mathbf{q}_j; \omega_k^\beta) \right\rangle_k \\ &= \left\langle \sum_{\alpha}^N I_1(\mathbf{q}_i; \omega_k^\alpha) I_1(\mathbf{q}_j; \omega_k^\alpha) + \sum_{\alpha \neq \beta}^N I_1(\mathbf{q}_i; \omega_k^\alpha) I_1(\mathbf{q}_j; \omega_k^\beta) \right\rangle_k \\ &\rightarrow N \langle I_1(\mathbf{q}_i; \omega) I_1(\mathbf{q}_j; \omega) \rangle_\omega + (N^2 - N) \langle I_1(\mathbf{q}_i; \omega) \rangle_\omega \langle I_1(\mathbf{q}_j; \omega) \rangle_\omega. \end{aligned} \quad (27)$$

Note that the average of a product of uncorrelated quantities is equal to the product of their averages and that the first term is the correlation function for a single particle:

$$C_1(\mathbf{q}_i, \mathbf{q}_j) = \langle I_1(\mathbf{q}_i; \omega) I_1(\mathbf{q}_j; \omega) \rangle_\omega. \quad (28)$$

We then rearrange equation (27):

$$\begin{aligned} C_1(\mathbf{q}_i, \mathbf{q}_j) &= \frac{1}{N} C_{\text{exp}}(\mathbf{q}_i, \mathbf{q}_j) - (N-1) \langle I_1(\mathbf{q}_i; \omega) \rangle_\omega \langle I_1(\mathbf{q}_j; \omega) \rangle_\omega \\ &\approx \frac{1}{N} [C_{\text{exp}}(\mathbf{q}_i, \mathbf{q}_j) - I_{\text{SAXS}}(\mathbf{q}_i) I_{\text{SAXS}}(\mathbf{q}_j)]. \end{aligned} \quad (29)$$

Thus we find an important result: the single-particle correlation function can be determined from repeated measurements of many-particle diffraction patterns. The challenge remains to relate C_1 to the electron density $\rho(\mathbf{r})$ of a single particle.

What is the optimum number of particles N to be exposed in the X-ray pulses? The correlated scattering arises from the fluctuations in intensity around a ring of constant q in Figure 12 (b), which in turn are due to the fact that N is finite; these fluctuations will hence be strongest for small N . However, for small N , we have little or no scattering. It can be shown theoretically [50] and experimentally [54] that the signal-to-noise ratio, and hence the achievable spatial resolution in $\rho(\mathbf{r})$, is, to a good approximation, *independent* of N .

To extract structural information from C_1 , we take account of the axial geometry of the scattering arrangement (Figure 11 (a)), consider the symmetric case of $q = q_i = q_j$, and expand C_1 in terms of Legendre polynomials (the index n specifies the azimuthal pixel position around the ring with $q = \text{constant}$):

$$\begin{aligned} C_1(\mathbf{q}, \mathbf{q}) &\equiv C_1(q, \Delta\phi) \\ &= \langle I_{(k)}(q, \phi_n) I_{(k)}(q, \phi_n + \Delta\phi) \rangle_{k,n} \\ &= \frac{1}{4\pi} \sum_{l=0}^{l_{\max}} B_l(q) P_l(\cos \Delta\phi). \end{aligned} \quad (30)$$

The, as yet unknown, single-particle functions $\gamma(\mathbf{r})$ and $I_1(\mathbf{q})$ can be expanded in spherical harmonics Y_{lm} :

$$\begin{aligned} \gamma(\mathbf{r}) &= \sum_{lm} \gamma_{lm}(r) Y_{lm}(\hat{\mathbf{r}}), \\ I_1(\mathbf{q}) &= \int_V \gamma(\mathbf{r}) \exp(i\mathbf{q} \cdot \mathbf{r}) d\mathbf{r} \\ &= \sum_{lm} I_{lm}(q) Y_{lm}(\hat{\mathbf{q}}), \end{aligned} \quad (31)$$

and from equation (20), using the properties of the spherical harmonics [55] and the spherical Bessel functions j_l , we can relate I_{lm} and γ_{lm} :

$$I_{lm}(q) = 4\pi \int_0^{d_{\max}} \gamma_{lm}(r) r^2 j_l(qr) dr. \quad (32)$$

Friedel's law in crystallography states that in the single-scattering "kinematical" approximation and ignoring resonant scattering effects (which lead to complex atomic scattering factors), the scattering is symmetric in q : $I(\mathbf{q}) = I(-\mathbf{q})$. This implies that only even values of l are allowed in the expansion of equation (32).

If we consider the isotropic term

$$I_{00}(q) = 4\pi \int_0^{d_{\max}} \gamma_{00}(r) r^2 \frac{\sin(qr)}{qr} dr, \quad (33)$$

where

$$\gamma_{00}(r)r^2 \equiv \bar{\gamma}(r)r^2 = P(r), \quad (34)$$

then we again obtain the pair density distribution function.

According to Kam [46] and Saldin [56], the I_{lm} of equation (31) are related to the expansion coefficients of C_1 (equation (30)) by

$$B_l(q) = \sum_{l=-m}^m |I_{lm}(q)|^2, \quad (35)$$

and in the limit of small q , a Guinier-type expansion of equation (32) yields:

$$I_{lm}(q) \propto q^l \left(1 - \frac{q^2 R_{lm}^2}{2l+3} \right), \quad (36)$$

where the coefficients R_{lm} are related to the second-order multipole moment of the Patterson function:

$$R_{lm}^2 = \frac{\int_0^{d_{\max}} [\gamma(\mathbf{r})r^2] r^{l+2} Y_{lm}^*(\hat{\mathbf{r}}) d\mathbf{r}}{2 \int_0^{d_{\max}} [\gamma(\mathbf{r})r^2] r^l Y_{lm}^*(\hat{\mathbf{r}}) d\mathbf{r}}. \quad (37)$$

Equation (35) then implies

$$B_l(q) \propto \exp\left(2l \ln q - \frac{2q^2 R_l^2}{2l+3} \right), \quad (38)$$

where

$$R_l^2 = \frac{1}{2l+1} \sum_{l=-m}^l \mathbb{R}(R_{lm}^2). \quad (39)$$

Thus, a small- q Guinier analysis of $B_l(q)$, which, through equation (30), can be extracted from the experimentally determined single-particle correlation function $C_1(q, \Delta\phi)$ (Figure 12), yields a set of l -dependent effective radii R_l , instead of the single radius $R_g = R_0$ provided by SAXS. As an example, Malmerberg et al. [51] have performed simulations, which demonstrate that the quotient R_2/R_g can be used as a model-independent “shape descriptor” for the single particle (Figure 13). We thus see that an analysis of the two-point correlation measured with CXS can directly provide structural information going beyond that available from a SAXS measurement. As in the SAXS case (Figure 11 (b)), by imposing additional constraints, for example, on the positivity, the extent, the uniformity, and/or the symmetry of $\rho(\mathbf{r})$, it has been simulated by Donatelli et al. [57] that more information, at higher resolution, can also be obtained from CXS data (Figure 14). The dependence of the achievable resolution on the experimental parameters is also discussed in [57].

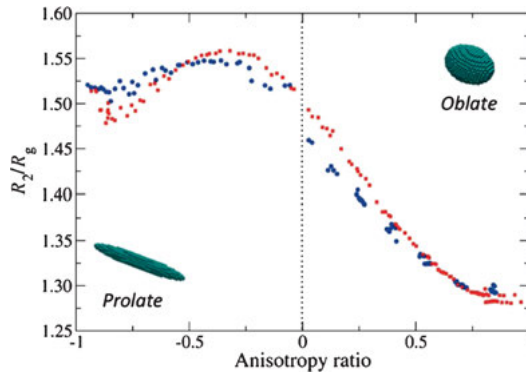


Figure 13: Example of a model-independent CSX shape descriptor for $l = 2$ [51]. The ratio R_2/R_g is plotted against the degree of anisotropy for ellipsoidal (black dots) and cylindrical (red squares) scatterers, allowing the identification of prolate or oblate features. Reproduced with permission of the International Union of Crystallography.

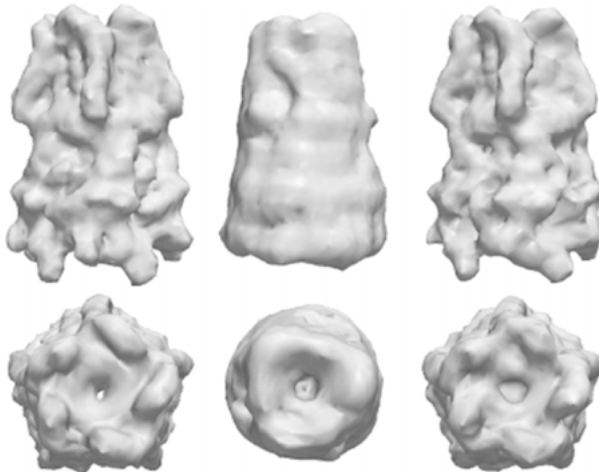


Figure 14: Reconstructions, in side (above) and top (below) views, of the pentameric ligand-gated ion channel (pLGIC) protein [57]. (Left) Original shape. (Center) Reconstruction from simulated CXS data, without imposing a symmetry constraint. (Right) CXS reconstruction, with the constraint of 5-fold symmetry.

2.4 The 2D case

It has been mathematically demonstrated [58] that, for random molecular alignment in three dimensions, it is not possible, in a model-independent fashion, to extract from the measured CXS correlations the effective scattering pattern $I_1(\mathbf{q})$ corresponding to a single particle. Had this been the case, it would have been possible, using standard iterative phasing algorithms [59], to realize Kam's original desire of directly determin-

ing the molecular electron density $\rho(\mathbf{r})$ from the measured CXS data. However, this is possible for particles aligned along a single axis parallel to the incident beam, as has been demonstrated experimentally for strongly scattering mesoscopic structures [54] (Figure 15). For such an alignment, we can write the two-point correlation function as a “ring cross-correlation,” which is a function of the scattering vector magnitudes q_i and q_j and their opening angle $\Delta\phi$ (denoted ψ in Figure 12 (b)), and which is a sum over the individual particles and is averaged over the exposures:

$$C(\mathbf{q}_i, \mathbf{q}_j) \equiv C(q_i, q_j, \Delta\phi) = \langle I_{(k)}(q_i, \phi_n) I_{(k)}(q_j, \phi_n + \Delta\phi) \rangle_{k,n}. \quad (40)$$

The experiment of Pedrini et al. [54] is described in Figure 15. To create a strongly scattering ensemble of identical but randomly oriented “particles” in two dimensions, many gold structures (350 nm across, 500-nm thick) were photolithographically generated on a thin silicon nitride membrane (Figure 15 (d)). Hard X-rays (6.2 keV) from a synchrotron were then scattered from this sample (Figure 15 (a)). To acquire many

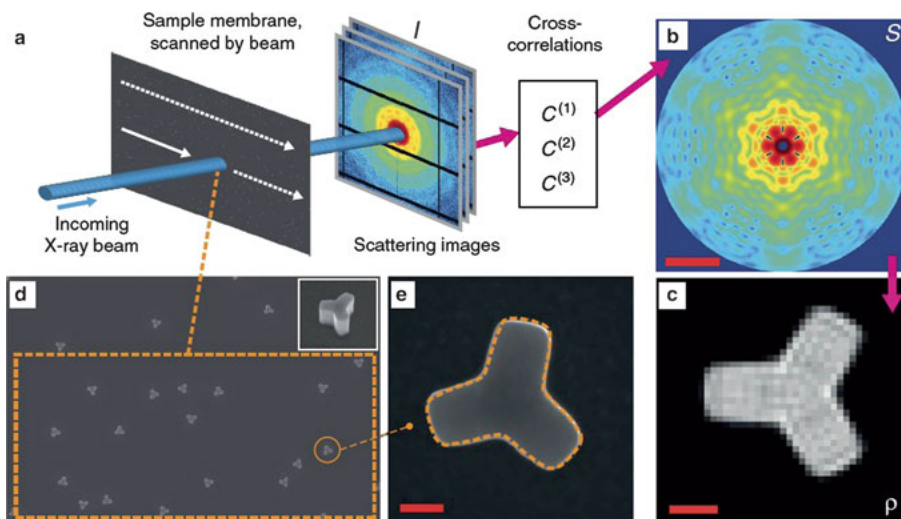


Figure 15: The 2D CXS experiment of Pedrini et al. [54]. Many stationary mesoscopic (350 nm across, 500-nm thick) three-legged gold structures were nanofabricated on a thin Si_3N_4 membrane with random orientations and placement. Many inequivalent CXS exposures were effectively made by acquiring scattering images for different positions of a tightly focused (dashed orange rectangle in frame d) 6.2 keV X-ray beam. From these scattering patterns, one-, two-, and three-point correlation functions were extracted and averaged, and, as described in the publication, the single-particle scattering function $I_1(q, \phi)$ could be extracted in a model-independent fashion (frame b, the red bar corresponds to 0.1 nm^{-1}). Finally, using standard iterative phase-retrieval techniques, the scattering function was inverted to yield the real-space image of a single particle (frame c), which shows a close resemblance to an electron microscope image (frame e). The red bars in (c) and (e) correspond to 100 nm. Reprinted by permission from Macmillan Publishers Ltd.

inequivalent exposures, 3 751 measurements were performed with different positions of the sample in the focused X-ray beam (dashed orange rectangle in Figure 15 (d)). For each exposure, one-, two- and three-point correlation functions were computed. The optimal size of a pixel for use in sampling the scattering pattern is the *Shannon pixel* [50], corresponding to a solid angle at the detector

$$\Delta\Omega = \left(\frac{\lambda}{2d_{\max}} \right)^2, \quad (41)$$

where d_{\max} is the largest molecular dimension. For ring cross-correlation with resolution $d_{\min} = 2\pi/q_{\max}$, this corresponds to a ring width $\Delta q = \pi/d_{\max}$ and a number of angular pixels in the outer ring of $N_{\Delta\phi} = 4\pi d_{\max}/d_{\min}$.

To obtain the (projected) real space image $\rho(r, \phi)$, we must (a) extract from $C_1(q_i, q_j, \Delta\phi)$ the single-particle diffraction pattern $I_1(q, \phi)$ and (b) determine the scattering phases necessary to invert $I_1(q, \phi)$ to the image $\rho(r, \phi)$. We begin by expanding the (as yet unknown) single-particle intensity in circular harmonics:

$$I_1(q, \phi) = \sum_m I_m(q) e^{im\phi} = \sum_m I_{-m}^*(q) e^{im\phi} = \sum_{m'} I_{m'}^*(q) e^{-im'\phi}. \quad (42)$$

Again, since I_1 is real, by Friedel symmetry, only even values of m are allowed, and $I_m(q) = I_{-m}^*(q)$. The single-particle correlation function can then be written as

$$\begin{aligned} C_1(q_i, q_j, \Delta\phi) &= \frac{1}{2\pi} \int I_1(q_i, \phi) I_1(q_j, \phi + \Delta\phi) d\phi \\ &= \sum_{m, m'} I_m(q_i) I_{m'}^*(q_j) e^{-im'\phi} \frac{1}{2\pi} \int e^{i(m-m')\phi} d\phi \\ &= \sum_m I_m(q_i) I_m^*(q_j) e^{-im\Delta\phi}. \end{aligned} \quad (43)$$

Taking the Fourier transform, we obtain

$$\begin{aligned} Q_m(q_i, q_j) &\equiv \frac{1}{2\pi} \int_0^{2\pi} C_1(q_i, q_j, \Delta\phi) e^{im\Delta\phi} d\Delta\phi \\ &= \sum_{m'} I_{m'}(q_i) I_{m'}^*(q_j) \frac{1}{2\pi} \int_0^{2\pi} e^{i(m-m')\Delta\phi} d\Delta\phi \\ &= I_m(q_i) I_m^*(q_j). \end{aligned} \quad (44)$$

Thus, from the ring *autocorrelations*, i.e., with $q_i = q_j = q$, we can obtain the *magnitudes* of the Fourier coefficients:

$$|I_m(q)| = \sqrt{Q_m(q, q)}. \quad (45)$$

Hence the first problem of constructing $I_1(q, \phi)$ from C_1 is one of phase-retrieval. Pedrini et al. [54] have shown that this can in principle be accomplished without

imposing real-space constraints, by using in addition the three-point correlations. Pedrini's resulting $I_1(q, \phi)$ is shown in Figure 15 (b). The stationary, relatively large, strongly scattering gold structures they used produced sufficient scattering to measure the three-point correlations at a synchrotron; for molecular scatters, an accurate measurement of higher-order correlations suffers from a low signal-to-noise ratio and will probably require an XFEL with high repetition rate [50].

The second problem, the inverse transformation of $I_1(q, \phi)$ to the real-space image $\rho(r, \phi)$ is also a phase-retrieval problem, which in this case can be solved by standard iterative techniques, incorporating, in addition to the reciprocal space constraint, real-space constraints, such as limiting the maximum size of the particle ("support") and requiring that $\rho(r, \phi) > 0$ everywhere ("positivity") [59]. Pedrini's resulting $\rho(r, \phi)$ (Figure 15 (c)) shows a strong resemblance to a scanning electron microscope image of one of the structures (Figure 15 (e)). We note that an elegant approach to *simultaneously* solving both phase retrieval problems (e.g., simultaneously refining $I_1(q, \phi)$ and $\rho(r, \phi)$), in the general framework of *iterative projection algorithms* has been proposed by [60].

3 Nonlinear X-ray optics

3.1 General considerations

The optical laser was invented in 1960, and its coherence, high spectral brightness, and short-duration pulses opened the floodgates for investigations of nonlinear optical and ultrafast phenomena: Second-harmonic generation was observed in 1961, sum-frequency generation and stimulated Raman scattering were observed in 1962, and picosecond mode-locked pulses were invented in 1963. The Nobel Prize for optical laser developments was awarded in physics to Townes, Basov, and Prokhorov in 1964. High peak-brightness X-ray pulses have now been available at XFELs since 2009, and work is underway to make use of nonlinear optical effects at X-ray wavelengths in novel spectroscopic applications; published observations include: an XFEL-pumped atomic laser using ionized Ne gas [61], amplified stimulated X-ray emission in silicon [62], second-harmonic X-ray generation in diamond [63], and optical/X-ray four-wave mixing using a transient grating [64]. Particularly interesting potential applications of nonlinear X-ray effects, highlighted in this section, are stimulated X-ray Raman scattering and nonlinear mixing of optical and X-ray wavelengths. Among the many textbooks on nonlinear optical phenomena, we note the excellent reference by Boyd [18].

The interaction of a polarizable material with a varying electric field produces a time-dependent electric polarization, which can be expanded as a power series in the

field strength:

$$\begin{aligned} P(t) &= \epsilon_0 [\chi^{(1)} E(t) + \chi^{(2)} E^2(t) + \chi^{(3)} E^3(t) + \dots] \\ &\equiv P^{(1)}(t) + P^{(2)}(t) + P^{(3)}(t) + \dots \end{aligned} \quad (46)$$

For a superposition of light waves, where the electric field consists of several oscillating components, the nonlinear terms in the polarization mix contributions with different frequencies, and the resulting Fourier components of the polarization are expressed in terms of the frequency-dependent nonlinear susceptibilities $\chi^{(s)}$:

$$P^{(s)}(\omega_k) = \epsilon_0 \chi^{(s)}(\omega_k = \omega_1 + \omega_2 + \dots + \omega_s) E(\omega_1) \dots E(\omega_s), \quad (47)$$

where the frequency ω_k can be any algebraic sum of the (positive and negative) frequencies that are active in the interaction.

Light-matter interactions are divided into two categories [18]:

- (a) A *parametric* (*p*) process, also called *passive* or *elastic*, leaves the material properties unchanged if we disregard a small energy dissipation in the intermediate state. The material thus acts as a catalyst for a change in the radiation fields.
- (b) In a *nonparametric* (*np*) process, also called *active* or *inelastic*, the material undergoes a large energy loss to or gain from the radiation field.

For parametric processes of any order, the source term on the right-hand side of equation (47) is proportional to the corresponding susceptibility, and for a nonparametric process, the cross-section for light scattering is proportional to the *imaginary part* of an odd-order susceptibility times the modulus squared of each field involved. Both types of interaction are generally enhanced by the presence of a nearby resonance. Materials with inversion symmetry have a vanishing second-order susceptibility. Examples of light-matter interactions are:

- (a) 1st-order *p*: light propagation with linear dispersion.
- (b) 1st-order *np*: single-photon absorption or emission.
- (c) 2nd-order *p*: second-harmonic generation, sum- and difference-frequency generation.
- (d) 3rd-order *np*: spontaneous and stimulated Raman scattering.
- (e) 3rd-order *p*: parametric four-wave mixing.

3.2 Stimulated Raman scattering at X-ray wavelengths

Conventional resonant inelastic X-ray scattering (RIXS) [65, 66] is a synchrotron-based, photon-in/photon-out, chemically specific spectroscopic method, which allows the study in solids of, e.g., intra-*d*-band charge-transfer and collective excitations [67], without the limitations of probing depth, low ambient EM-fields, sample conductivity and surface quality presented by photoemission. In spite of resonance

enhancement, the main drawback of RIXS is its low efficiency, generally 10^{-5} of elastic Rayleigh scattering.

Like its Raman scattering optical analog, the RIXS technique relies on *spontaneous* emission from a photoexcited state to produce the observed outgoing photon. RIXS and Raman scattering are 3rd-order nonparametric interactions. At sufficiently high incoming photon fluence, the efficiency of *stimulated* Raman scattering, another 3rd-order nonparametric process (Figure 2(a), Section 1) exceeds that of the spontaneous process, with gains in efficiency at optical wavelengths of up to 10^7 . Using ps–fs optical pulses, a variety of techniques have been devised of performing *time-dependent* stimulated Raman scattering. One of these, time-resolved coherent anti-Stokes Raman scattering (t-CARS), is shown schematically in Figure 16. Here, a first stimulated Raman scattering event (with excitation and stimulated waves ω_1 and ω_2) prepares the system in an excited state f , which may be a coherent superposition of two or more closely spaced (by $\delta\Omega$) states. If so, this superposition will develop during the experimentally variable time interval τ , exhibiting so-called “quantum beating.” At the end of this interval, a second stimulated Raman scattering event (ω_1 and ω_{AS}) projects the pertinent superposition onto the ground state g . Note that the first stimulated scattering event is a normal “Stokes” scattering ($\omega_1 > \omega_2$), and the second is an “anti-Stokes” scattering ($\omega_1 < \omega_{AS}$). The strength of the stimulated ω_{AS} signal may show damped oscillations as functions of the duration of the time interval τ , making the quantum beats visible and thus allowing a determination of the lifetime of the coherent excited state. A particularly attractive application of X-ray t-CARS would require additional flexibility in the configuration of multicolor incident X-ray waves. If the excitation process is made resonant with one atom (e.g., nitrogen) of, for example, an aminophenol (C_6H_7NO) molecule and the probe process with a different atom (e.g., oxygen), then we may be able to directly observe, in real time, an ultrafast co-

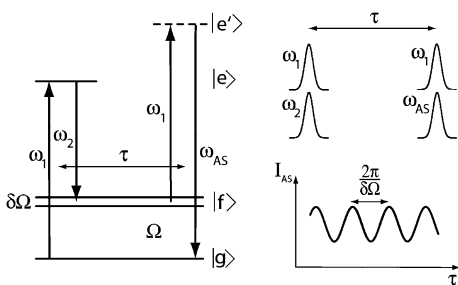


Figure 16: X-ray t-CARS, time-resolved coherent anti-stokes Raman scattering [68], is perhaps the “holy grail” of non-linear X-ray optics. It is based on two sequential stimulated Raman scattering events, separated by a variable time delay τ . As the delay is varied, the strength of the *anti-Stokes* signal ω_{AS} is predicted to show quantum beats, reflecting a coherent superposition of intermediate states $|f\rangle$. Taken as a single event, t-CARS may be considered to be an example of parametric four-wave mixing.

herent energy transfer across a molecule. The quantum-beating pattern observed in such an experiment may make visible interference effects arising from the quantum superposition of different transfer pathways [69].

We consider the feasibility of observing stimulated Raman scattering at X-ray wavelengths by comparing expressions for the cross-sections for spontaneous and stimulated Raman scattering to determine the minimum source characteristics for observing the latter [70]. Both spontaneous and stimulated Raman scatterings are governed by the third-order nonlinear susceptibility $\chi^{(3)}(\omega_2 = \omega_2 + \omega_1 - \omega_1)$. For the differential cross-section for stimulated Raman scattering, with incident beams at both ω_1 and ω_2 , Lee and Albrecht [71] derive the following expression:

$$\frac{d^2\sigma_{\text{stim}}}{d\Omega_2 d\omega_2} = \frac{32\pi^2 \hbar \omega_1 \omega_2}{\epsilon_0 c^2 N} F(\omega_2) \mathbb{J}(\chi^{(3)}), \quad (48)$$

where $d\Omega_2$ and $d\omega_2$ are the solid angle and bandwidth of the outgoing radiation, $F(\omega_2)$ is the incident ω_2 photon flux per unit scattered frequency, and N is the number of active atoms/volume. As discussed by these authors and others [72, 73], a spontaneous emission is identical to a stimulated emission in which the stimulating radiation arises from the *zero-point field* of the *black-body spectrum*. The Planck radiation law, which gives the number of emitted photons per second, area, steradian, and frequency interval, is

$$F_{\text{BB}}(\omega, T) \propto \frac{\omega^2}{c^2} \left(\frac{1}{e^{\frac{\hbar\omega}{k_B T}} - 1} + \frac{1}{2} \right). \quad (49)$$

For spontaneous optical radiation at room temperature, only the zero-point photons are of importance, and hence

$$F_{\text{spon}}(\omega_2) = F_{\text{BB}}(\omega_2, 0) \propto \frac{\omega_2^2}{c^2}. \quad (50)$$

With the correct numerical prefactors, Lee and Albrecht show that

$$\frac{d^2\sigma_{\text{spon}}}{d\Omega_2 d\omega_2} = \frac{\hbar \omega_1 \omega_2^3}{\pi \epsilon_0 c^4 N} \mathbb{J}(\chi^{(3)}). \quad (51)$$

We thus see that stimulated Raman scattering predominates over spontaneous Raman scattering (i.e., $\sigma_{\text{stim}} > \sigma_{\text{spon}}$) when the incident ω_2 flux exceeds that from the zero-point black-body radiation. Quantitatively, the stimulated and spontaneous Raman cross-sections derived by Lee and Albrecht [71] are equal for

$$F(\omega_2) = \frac{\omega_2^2}{32\pi^3 c^2}, \quad (52)$$

which, for a photon energy of 720 eV (the L_2 absorption edge of Fe), a Gaussian, bandwidth-limited pulse of FWHM duration $\Delta t = 2$ fs with an FWHM bandwidth of

$\hbar\Delta\omega = 0.9$ eV, and a focus spot of $(10\ \mu\text{m})^2$, corresponds to $4 \cdot 10^6$ photons/pulse. This may be supplied by an advanced XFEL. It should be noted that the efficient observation of stimulated X-ray Raman scattering requires that stimulated emission occurs before relaxation by competing deactivation processes, principally Auger decay. This necessitates to use simultaneous, extremely short-duration (i.e., femtoseconds, according to Ref. [14]) X-ray pulses at the two frequencies ω_1 and ω_2 . Perhaps, the sub-fs laboratory-scale XFEL foreseen in Ref. [5] could be of use here. The first evidence for stimulated X-ray Raman scattering has been observed in Ne gas [74], and effects in solids have been theoretically treated by Föhlisch and coworkers [75] and Stöhr and Scherz [76].

3.3 Enhancing the valence electron contribution to diffraction with X-ray/optical sum-frequency generation

A 2nd-order parametric nonlinear effect, which is also promising for XFEL applications, is sum-frequency generation (SFG). A shortcoming of structural studies of matter with X-ray diffraction is that X-rays are scattered by both the numerous tightly bound electrons in the atomic cores and the relatively fewer weakly bound valence electrons. For studies of chemical bonding effects, which depend sensitively on the spatial distribution of valence electrons, it would be advantageous if we could selectively enhance their contribution to X-ray scattering. A possible method of achieving this goal is offered by X-ray/optical sum-frequency generation, which produces an X-ray scattering signal only from those electrons that are polarized by the optical field.

Such X-ray/optical SFG has recently been demonstrated [77] at the LINAC Coherent Light Source XFEL (Figure 17 (a)). The second-order nonlinear SFG effect mixed 1.55 eV optical pulses (2-ps duration, 10^{10} W/cm²) with 8 keV X-ray pulses (80-fs duration), which were simultaneously incident on a diamond crystal. Momentum conservation was fulfilled with the aid of a Bragg reflection \mathbf{G} , and the frequency-shifted X-rays were discriminated with a high-resolution crystal analyzer. To interpret the strength of the measured sum-frequency signal (Figure 17 (b)), the authors use a two-component model, in which the electrons of diamond belong either to a spherically symmetric atomic fraction or to a nonspherically symmetric bond fraction. According to models of atomic binding in covalent semiconductors [78], the bond fraction principally contributes to the optical response. Under this assumption, Glover et al. [77] derive the following relation between the X-ray/optical SFG scattering factor $F_Q^{X/O}$ and $\delta\rho_Q(\mathbf{E}_{\text{light}})$, the Fourier component at wave-vector \mathbf{Q} of the light-induced charge density (in cgs units):

$$\delta\rho_Q(\mathbf{E}_{\text{light}}) = -i\mathbf{Q} \cdot \mathbf{E}_{\text{light}} \frac{3(\epsilon - 1)}{4\pi(\epsilon + 2)} F_Q^{X/O}, \quad (53)$$

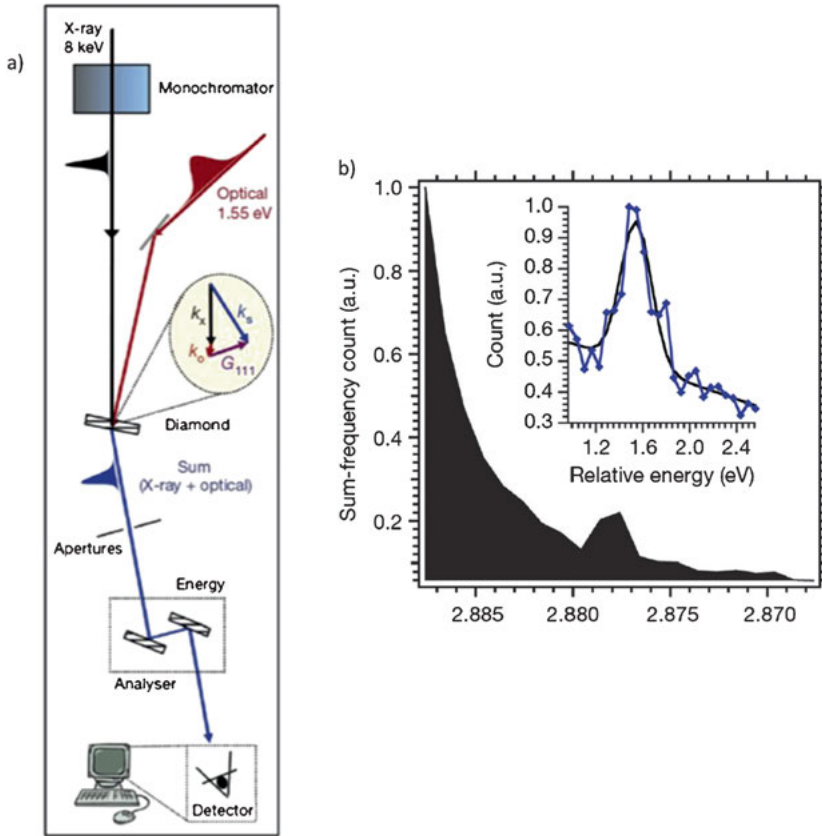


Figure 17: (a) The experimental setup used by Glover et al. [77] to measure the 111 Fourier component of the optically induced perturbation of the electron charge density in diamond. (b) The measured X-ray/optical SFG spectrum. The strength of the SFG peak, located 1.55 eV above the incident X-ray photon energy, implies a nonlinear conversion efficiency of $3 \cdot 10^{-7}$. Reprinted by permission from Macmillan Publishers Ltd.

where $\mathbf{E}_{\text{light}}$ is the optical electric field, ϵ is the dielectric constant, and the local nature of the electric field is accounted for via the Clausius–Mossotti relation. The measured SFG scattered intensity at the scattering vector $\mathbf{Q} = \mathbf{G}_{111} + \mathbf{k}_O$ (\mathbf{k}_O is the optical wave-vector) implies a nonlinear X-ray conversion efficiency of $3 \cdot 10^{-7}$. This corresponds to

$$\delta\rho_{111}(\mathbf{E}_{\text{light}}) = 0.84 \cdot 10^{-4} \text{ e}^-/\text{\AA}^3. \quad (54)$$

Support for the assumption that the bond charge is principally responsible for the optical response is given in Figure 18. A density-functional calculation of the ground-state valence charge density is shown in Figure 18(a), with a profile plotted along the [111] direction in Figure 18(d). Note that the valence charge is maximum at strong

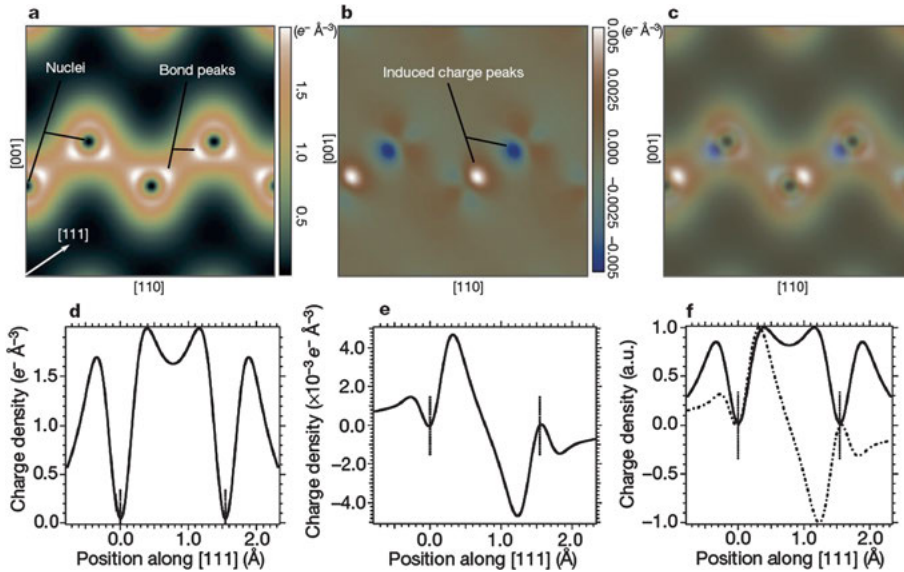


Figure 18: The results of density-functional calculations for diamond of (a, d) the ground-state valence charge density and (b, e) the changes induced in the valence charge density by a dc electric field of $2.7 \cdot 10^8$ V/m along the [111] direction. Superposing the two plots (c, f) demonstrates that the positions of the field-induced changes coincide with the local maxima (“bond peaks”) in the ground-state valence charge density [77]. Reprinted by permission from Macmillan Publishers Ltd.

“bond peaks,” on either side of the bond-center position. The change in charge density caused by applying a dc electric field of $2.7 \cdot 10^8$ V/m along the [111] direction is shown in Figures 18 (b) and (e) to produce localized positive and negative regions. This electric field is chosen to be equal to the amplitude of the [111] component of the optical electric field applied in the experiment. By superposing the ground-state density and the induced changes (Figures 18 (c) and (f)) we clearly see that electric field effects, and by extension the optical effects, are maximal along the interatomic bond. A Fourier analysis of the induced (static) valence charge density changes yields the value $\delta\rho_{111} = 1.07 \cdot 10^{-4} \text{ e}^-/\text{\AA}^3$, which is considered to be a quite good agreement with experiment (equation (54)). It is, of course, highly desirable to perform a true crystallographic mapping of the optically induced charge density at atomic resolution. This requires the measurement of many additional SFG Bragg reflections. It should be noted that since sum-frequency generation is a second-order nonlinear optical effect, by symmetry it should vanish in a centro-symmetric material such as diamond. In spite of this, it is observable due to the Doppler and Lorentz mechanisms: the first involving an acceleration by the X-ray electric field of the optically induced charge density and the second involving a “figure-8” motion of the electrons in the X-ray magnetic field [79].

4 The X-FEL operating principle

4.1 A graphical description of synchrotron radiation

In his introductory “Lectures on Physics,” Feynman gives an elegant graphical explanation of how synchrotron radiation is generated [80, 81]. Feynman considers an electron moving along the path $\mathbf{r}(\tau)$ as seen by an observer at the point (x, y, z) , and he distinguishes between τ , the time in the frame of the electron (the *emitter time*), and t , the time in observer’s frame (the *observer time*); $\mathbf{r}(\tau)$ is the *true* path of the electron, and $\mathbf{r}'(t)$ is the *apparent* path. Feynman gives a rigorous expression for the electric and magnetic fields of the moving electron:

$$\mathbf{E}(x, y, z) = \frac{e}{4\pi\epsilon_0} \left[\frac{\dot{\mathbf{r}}'}{r'^2} + \frac{r'}{c} \frac{d}{dt} \left(\frac{\dot{\mathbf{r}}'}{r'^2} \right) + \frac{1}{c^2} \frac{d^2 \dot{\mathbf{r}}'}{dt^2} \right],$$

$$\mathbf{B} = -\frac{1}{c} \dot{\mathbf{r}}' \wedge \mathbf{E}. \quad (55)$$

The first term in the electric field is the familiar $1/r^2$ Coulomb law, and the second term is a relativistic correction. Of interest here is the third, radiation term \mathbf{E}_{rad} , which in the far-field decreases more slowly as $1/r$. Complications arise from the appearance of the apparent position \mathbf{r}' and the observer time t , which, for relativistic motion, may differ dramatically from the true position \mathbf{r} and the emitter time τ . For example, suppose that we observe from the position $z = R_0$ the motion of an electron following the true trajectory $\mathbf{r}(\tau)$ in the vicinity of the origin. In Figure 19, the positions of the observer and electron are indicated (in two dimensions), along with the apparent position of the electron $\mathbf{r}'(x', z')$ and the corresponding unit vector $\hat{\mathbf{r}}'$. Note that $\hat{\mathbf{r}}'$ points from the observer toward the electron. For a distant observer ($x' \ll R_0, z' \approx -R_0$), we have

$$\hat{\mathbf{r}}' = \frac{x' \hat{\mathbf{x}} + z' \hat{\mathbf{z}}}{\sqrt{x'^2 + z'^2}} \approx \left(\frac{x'}{R_0} \right) \hat{\mathbf{x}} - \hat{\mathbf{z}}, \quad (56)$$

and the radiation term in the expression for \mathbf{E} becomes

$$\mathbf{E}_{\text{rad}} = \frac{e}{4\pi\epsilon_0 c^2} \frac{d^2 \dot{\mathbf{r}}'}{dt^2} \approx \frac{e}{4\pi\epsilon_0 c^2} \frac{d^2}{dt^2} \left(\frac{x'}{R_0} \right) \hat{\mathbf{x}}$$

$$\approx \frac{e}{4\pi\epsilon_0 c^2 R_0} a'_{\perp}(t) \hat{\mathbf{r}}_{\perp}. \quad (57)$$

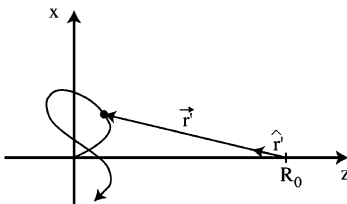


Figure 19: The motion of an electron near the origin is followed by an observer at $z = R_0$ [81]. Reproduced with the permission of the American Association of Physics Teachers.

Note that the radiation field decreases with distance as $1/R_0$, is perpendicular to the electron-observer direction, and is proportional to the transverse component $a'_\perp(t)$ of the apparent acceleration. From a distant vantage point at $z = R_0$, we consider the motion of an electron that follows the circular trajectory shown in Figure 20 (a). A segment of this trajectory near time zero corresponds to that in a bending magnet or near a pole of the FEL undulator. Because of the nonzero propagation time of light over the distance $R_0 - z$, the observer time t associated with the emitter time τ for an electron with coordinate $z(\tau)$ is given by

$$t = \tau + \frac{R_0}{c} - \frac{z(\tau)}{c}. \quad (58)$$

In what follows, we disregard the constant term R_0/c . As shown in Figure 20 (a), the true path $\mathbf{r}(\tau)$ of the electron is the dark “electron” circle. A point moving with the same angular velocity on the slightly larger “light” circle moves with speed c . In Figure 20 (b), we use a graphical method to construct from the true x -coordinate $x(\tau)$ (points) the apparent position $x'(t)$ (dark curve). Each of the $x(\tau)$ points is shifted in time to account for the light propagation. Consider, for example, point -4 . Because it is more distant from the observer than the origin, the apparent time is later than the true time, and we move the point in Figure 20 (b) to the right by the corresponding line segment in Figure 20 (a). Analogously, point $+5$ undergoes a shift to earlier time. The result for the apparent particle trajectory $x'(t)$ is a curtate cycloid. Of particular importance for synchrotron radiation is the sharp cusp in $x'(t)$, which occurs at the moment when the electron moves directly toward the observer ($t = 0$). At this point in the trajectory, the large apparent transverse acceleration causes the emission of an intense burst of synchrotron radiation. For a quantitative discussion of this radiation and an extension of these arguments to the case of a periodic magnetic undulator, see Ref. [81].

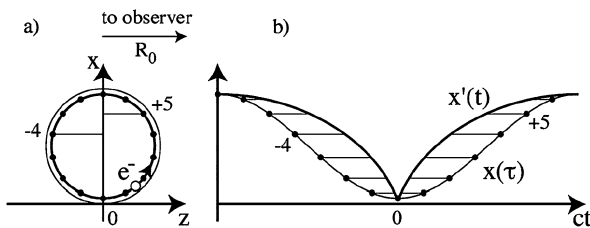


Figure 20: (a) An electron undergoes circular motion at an orbital “electron” radius r [81]. (b) Its apparent x -position $x'(t)$ is obtained from the true position $x(\tau)$ by a translation along the time-axis by the light propagation time z/c . This procedure yields a curtate cycloid for $x'(t)$, which is equivalent to the path traced out by the position of the electron at $t = 0$ as the diagram in (a) is unrolled along the circle with slightly larger (“light”) radius $R = r/\beta$. This figure is adapted from Ref. [80]. Reproduced with the permission of the American Association of Physics Teachers.

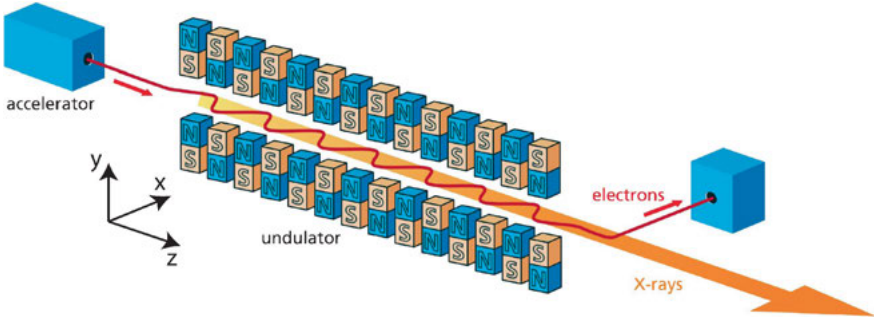


Figure 21: Schematic illustration of the components of an XFEL.

4.2 The XFEL microbunching instability

The principle of XFEL operation was invented and demonstrated with a prototype at Stanford University in the early 1970s by Madey [82]; for a detailed description, see [83]. The active medium in an XFEL consists of highly collimated bunches of relativistic electrons traversing a long magnetic undulator (see Figure 21). Contrary to the closed orbits of synchrotrons, where stochastic synchrotron radiation degrades the electron beam quality, the XFEL uses a linear accelerator (LINAC). A pulse of relativistic electrons with relativistic factor $\gamma = 1/\sqrt{1 - \beta^2} = 1/\sqrt{1 - v^2/c^2} \gg 1$ moves along an undulator, experiencing the periodic magnetic field $B_y = B_0 \cos(k_u z)$, where $k_u = 2\pi/\lambda_u$, and λ_u is the undulator period. The Lorentz force on the electron leads to the following equations of motion:

$$\begin{aligned} \gamma m \ddot{z} &= -e \dot{x} B_y, \\ \gamma m \ddot{x} &= e \dot{z} B_y. \end{aligned} \tag{59}$$

We first assume that $\dot{z} \approx \text{const} \equiv \bar{\beta} \gg \dot{x}$ and find:

$$\dot{x} = \frac{cK}{\gamma} \sin \omega_u t, \tag{60}$$

where $\omega_u = k_u \bar{\beta} c$, and the “undulator parameter” is defined as $K = \frac{eB_0 \lambda_u}{2\pi m c}$. Averaging over many undulator periods, we find

$$\langle \dot{z} \rangle = \langle \sqrt{\beta^2 c^2 - \dot{x}^2} \rangle = \left[1 - \frac{1}{2\gamma^2} \left(1 + \frac{K^2}{2} \right) \right] c \equiv \bar{\beta} c. \tag{61}$$

The x-oscillation causes emission of undulator radiation with wavelength λ . Consider in Figure 22 successive wavefronts, corresponding, from left to right, to emission at points B and A on the electron trajectory. From the figure we see that the condition for coherent superposition is $\lambda_u/\bar{\beta} = \lambda_u + \lambda$, where λ_u is the undulator period, and the

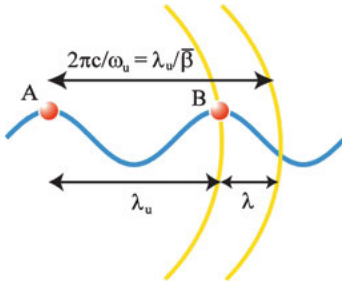


Figure 22: Coherent radiation wavefronts from successive undulator poles at A and B.

average value of the z-component of the electron velocity is

$$\bar{\beta}c = \left[1 - \frac{1}{2\gamma^2} \left(1 + \frac{K^2}{2} \right) \right] c. \quad (62)$$

We thus arrive at the “undulator equation” for the wavelength of the radiation:

$$\lambda = \frac{\lambda_u}{2\gamma^2} \left(1 + \frac{K^2}{2} \right). \quad (63)$$

At this resonant condition, the radiation overtakes the electrons by one wavelength per undulator period.

The major difference between undulator radiation at a synchrotron and at the XFEL is that the radiation field in the very long XFEL undulator becomes sufficiently strong to influence the electron trajectory. The electron energy is $W = \gamma mc^2$, which varies under the influence of the radiation field $E_x(t)$

$$\frac{dW}{dt} = -e\dot{x}(t)E_x(t). \quad (64)$$

This interaction is strongest when $|\dot{x}|$ is at its maximum, i.e., at the zero-crossings of the electron trajectory. Assuming plane-wave radiation, $E_x(t) = E_0 \cos(kz - \omega t + \psi_0)$, and using the expression for $\dot{x}(t)$ (equation (60)), we obtain

$$\frac{dW}{dt} = \frac{-eKcE_0}{2\gamma} (\sin \psi^+ - \sin \psi^-), \quad (65)$$

where $\psi^\pm = [(k \pm k_u)\bar{\beta}c - kc]t + \psi_0 = \psi_0 - ct[k(1 - \bar{\beta}) \mp k_u\bar{\beta}]$. Since ψ^- is always rapidly changing, the $\sin \psi^-$ contribution to $\frac{dW}{dt}$ averages to zero. A constant energy transfer between electrons and radiation occurs when $\psi^+ = \text{const}$, i.e., for

$$\begin{aligned} k(1 - \bar{\beta}) &= k_u\bar{\beta}, \\ \frac{2\pi}{\lambda}(1 - \bar{\beta}) &= \frac{2\pi}{\lambda_u}\bar{\beta} \approx \frac{2\pi}{\lambda_u}, \\ \lambda &= \lambda_u(1 - \bar{\beta}) = \frac{\lambda_u}{2\gamma^2} \left(1 + \frac{K^2}{2} \right). \end{aligned} \quad (66)$$

Thus, a constant energy transfer occurs for a radiation wavelength that satisfies the undulator equation (63).

Consider now the electron motion caused by the radiation field. The quantity $\psi = \psi^+$ is called the “ponderomotive phase,” and its time dependence is given by $\dot{\psi} = -k(1 - \bar{\beta})c + k_u \bar{\beta}c$. We define the relative energy “deviation” $\eta \equiv (\gamma - \gamma_r)/\gamma_r$ and the relative energy “detuning” $\Delta \equiv (\gamma_0 - \gamma_r)/\gamma_r$, where γ_r is the “resonant” value for which the undulator equation (63) is satisfied, γ_0 is the average value, and $\eta, \Delta \ll 1$. After some algebra, we obtain

$$\dot{\psi} = 2k_u c(\eta + \Delta). \tag{67}$$

On the other hand, the energy transfer is given by

$$\frac{dW}{dt} = -e\dot{x}E_x = -\frac{eKcE_0}{2\gamma_0} \sin \psi = mc^2\dot{\gamma} = mc^2\gamma_0\dot{\eta}, \tag{68}$$

implying that $\dot{\eta} = -\frac{eKcE_0}{2mcy_0^2} \sin \psi$. Taking a second time derivative, we obtain

$$\ddot{\psi} = -\Omega^2 \sin \psi, \tag{69}$$

which is the equation of motion for a physical pendulum with frequency $\Omega = \sqrt{\frac{ek_u KE_0}{m\gamma_0^2}}$.

The pendulum motion can be represented in a $(\psi, \dot{\psi})$ phase-space plot (Figure 23), where oscillatory and rotational trajectories are separated by a curve called the separatrix. Interaction in the XFEL undulator of a pulse of electrons with its own radiation field causes the initially uniform density distribution along the pulse to become modulated, with a period equal to the radiation wavelength λ . We see how this occurs by plotting electron trajectories in the phase space (Figure 24). The horizontal axis in Figure 24, the ponderomotive phase ψ , is essentially the z -coordinate of an electron in the pulse, in a coordinate system moving with the electrons at their average velocity $\bar{\beta}c$. A fraction of the pulse equal in length to somewhat more than twice the radiated

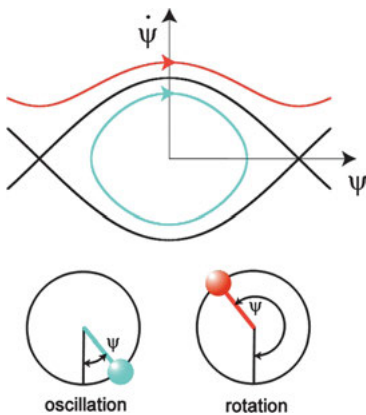


Figure 23: Oscillatory (blue) and rotational (red) motions of an electron in phase space is separated by the “separatrix” (black).

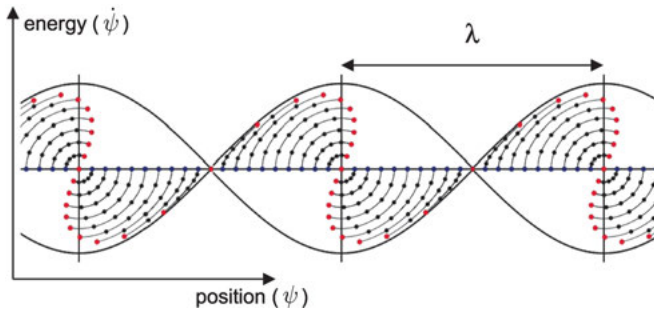


Figure 24: The development of an initially uniform electron distribution in phase space in the XFEL undulator (for zero detuning ($\Delta = 0$)). The ponderomotive phase ψ and its time derivative $\dot{\psi}$ effectively correspond to the position in a moving reference frame and the particle energy, respectively. At the point where “microbunches” are established (red), the undulator is terminated.

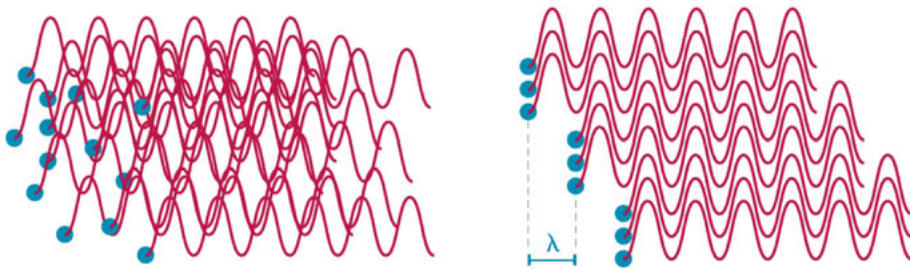


Figure 25: Schematic comparison of the incoherent radiation of randomly positioned electrons (left) and coherent radiation from microbunches (right).

wavelength λ is shown; the plot is repeated to the left and right. By equation (67) the vertical axis gives the deviation η of the electron energy from the resonant condition $\gamma = \gamma_r$. Dots show the successive positions of the initially uniformly distributed (blue) electrons. At the final situation shown (red), the approximate alignment of the dots at well-defined phases implies the formation of microbunches (Figure 25) and hence a strong density modulation of the pulse with a period equal to λ .

4.3 Self-amplified spontaneous emission

Whereas an electron pulse with randomly distributed electrons, as in a synchrotron, radiates incoherently, microbunching with periodicity λ , as occurs in the XFEL, results in coherent emission. For incoherent emission, the total radiated power $P_{\text{incoh}} = NP_1$ is the sum of that emitted by each of the N electrons in the pulse. For coherent emission, the radiated electric field $E_{\text{coh}} = NE_1$ adds up, implying a total power $P_{\text{coh}} = N^2P_1$, which is amplified by the factor N . For a typical pulse charge of 200 pC, $N \approx 10^9$!

XFEL operation thus proceeds as follows (Figure 26): the initially homogeneous electron pulse enters the undulator and spontaneously emits incoherent radiation. As the radiation field builds up, microbunching begins to develop, implying increasingly coherent emission and hence stronger microbunching and an exponential increase in the radiation power. It is arranged so that maximum microbunch modulation occurs at the end of the undulator, after which the electrons are discarded, and the radiation is directed to the experiment. This process is called ‘self-amplifying spontaneous emission’ (SASE).

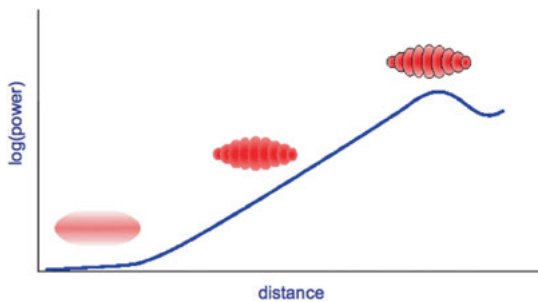


Figure 26: Schematic logarithmic plot of the X-ray power produced by an electron bunch as a function of distance it has travelled along the magnetic undulator. After an initial phase of “lethargic” growth of spontaneous undulator radiation, the initially homogeneous electron distribution in the bunch begins to form “microbunches.” These microbunches begin to radiate coherently, causing an exponential power increase and a sharper definition of the microbunches. If the undulator is extended beyond the position of optimal microbunching, then energy begins to flow back from the photon field to the electron motion, and the X-ray power decreases.

4.4 Worldwide XFEL facilities

The first hard X-ray free-electron laser (XFEL), the LINAC Coherent Light Source (LCLS) at the reconfigured Stanford linear accelerator, went into operation in April 2009 [84]. This was followed in June 2011 by the SACLA facility in Hyogo, Japan [85], and in October 2016 by the PAL facility in Pohang, South Korea [86]. Further XFELs presently under construction are the European XFEL in Hamburg, Germany [87], and the SwissFEL in Villigen-Würenlingen, Switzerland [88]. In addition, there are two operating soft X-ray lasers, FLASH in Hamburg, Germany [89], and FERMI in Trieste, Italy [90]. The pulse repetition rate of an XFEL is typically 100–120 Hz. By the use of superconducting acceleration technology the European XFEL will produce “macropulses” at 10 Hz, each of which consists of up to 2700 “micropulses,” at 220-ns intervals. The FERMI machine is quite special in that it uses a harmonic of an external optical laser to “seed” the XFEL emission. This results in a greatly improved FEL spectral stability and opens up novel possibilities for tailoring the FEL pulses. At the time of writing, the LCLS is undergoing an upgrade to a superconducting machine, and the SwissFEL

has demonstrated lasing at 25 nm and is constructing a second undulator beamline for soft X-rays.

5 Outlook

The self-amplification of spontaneous emission (SASE) mode of XFEL operation was presented in Section 4 of this chapter, and the applications of XFEL pulses highlighted in Sections 1–3 of the chapter for studying the structure and dynamics of condensed matter are based on this mode. It is expected that in the future, XFEL machines will go beyond simple SASE to offer significant improvement in performance and convenience.

The first XFELs have basically been single-user machines with only one experiment operating at any time. First experience has been made at the LCLS with spectral optical beam splitters, so-called “large-offset monochromators,” in which a thin diamond crystal introduced into the X-ray beam diffracts a portion of the beam to a branch beamline [91]; the majority of the radiation proceeds straight ahead to the principal user. A more attractive possibility for simultaneously supplying multiple users will be to generate and accelerate multiple electron bunches in the electron source and linear accelerator. Using a fast-switching magnet, individually configurable bunches can then be directed into two different undulators, allowing the independent choice of all relevant beam parameters.

Early XFELs have had pulse repetition rates of typically 100 Hz, limited by power requirements in the electron accelerator and by the thermal load on the X-ray optics. If the sample tolerates it, for example, in the gas phase or a rapidly flowing liquid stream, with improved detectors with faster frame rates, then a significantly higher repetition rate could bring a big advantage for so-called “photon-hungry” measurements. An example is the cross-correlation scattering technique discussed in Section 2. Some experiments would also benefit from a higher average photon intensity with a lower peak intensity, as would be provided by a high repetition rate machine with reduced electron charge per bunch. For power consumption reasons, an XFEL with high repetition rate must use superconducting acceleration technology [87].

A prominent example of a photon-hungry experiment is resonant inelastic X-ray scattering (RIXS) [67]. Here the well-defined incoming photon energy is scanned across sample resonances, and the inelastically scattered radiation is dispersed using a high-resolution spectrometer, allowing the selective excitation and observation of collective phenomena in the sample. Because of the narrow bandwidth required of the incoming beam and the low spectrometer acceptance, a high average X-ray intensity is a necessity. With short pulses at an XFEL and with optical pumping, pump–probe RIXS can be performed in a photoexcited nonequilibrium sample [8].

X-ray photoelectron spectroscopy (XPS), in which incoming photons eject characteristic photoelectrons dispersively detected in an electron spectrometer, is a versatile technique for investigating occupied electronic states [92]. Again, it would be intriguing to perform XPS at an XFEL in a pump–probe arrangement. But an intense X-ray pulse will generate many photoelectrons in a small area, and their mutual repulsion will severely degrade the measured photoelectron energy. This “space-charge” broadening can be reduced in a high-repetition-rate XFEL with high average but reduced peak intensity.

As noted earlier, SASE pulses are very intense, with short duration and high transverse coherence. But the longitudinal coherence and the reproducibility in terms of center wavelength and pulse energy are very poor. Reproducible, narrow bandwidth pulses can be produced by “seeding” the XFEL emission process: short-wavelength photons with a well-defined energy are injected along the electron beam as it traverses the undulator, inducing microbunching and radiation at a single desired wavelength. The seeding beam can be provided by a synchronized external laser, generally operating at a subharmonic of the XFEL emission. Laser-seeding allows versatile control of the FEL emission, but to date, it has only been demonstrated in the very soft extreme ultraviolet (XUV) wavelength range [90]. Alternatively, by introducing a wavelength filter half-way along the XFEL undulator and deflecting the electrons around it using a magnetic “chicane,” an XFEL can be “self-seeded,” as has been demonstrated at the LCLS at both hard [93] and soft [94] X-ray wavelengths. Presently, self-seeding suffers from large pulse energy fluctuations due to bunch-to-bunch variations in electron energy and by a broad spectral “pedestal” background from unfiltered SASE radiation.

Particularly promising options for XFEL machine development are based on manipulations of the electron beam prior to and during the emission process [95]. A position-dependent shift in kinetic energy (“chirp”) is imprinted on the electron bunch as it is accelerated, and the relative time delay between the bunch and the growing photon pulse is successively altered by small electron chicanes situated between the individual undulator modules. In this way, the XFEL photons in each module can, for example, interact with electrons that are as yet unperturbed by the FEL emission process (“fresh bunch”), and the result can be an extremely high peak XFEL power, perhaps reaching terawatts, a subfemtosecond pulse duration, or even multiple, multicolor pulses with a variable interpulse delay. The last of these could be highly attractive for the nonlinear X-ray methods discussed in Section 3. Even more ambitious schemes have been proposed for producing XFEL pulses and pulse trains with pulse durations entering the subattosecond domain [96]. The value of such pulses, for example, for time-resolved inner-shell electron spectroscopy, will, however, be limited by the time-energy uncertainty relation $\Delta E \Delta t (\text{FWHM}) \geq 1.8 \text{ fs eV}$: a 1 attosecond pulse has an energy bandwidth exceeding 1 800 eV.

However, the justification for further XFEL development and facility realization depends on a robust, blossoming palette of science applications. In the opinion of the author, the techniques highlighted in this chapter represent interesting candidates.

This Outlook concludes with comments on other promising XFEL techniques and applications.

As noted in the Introduction to this chapter, serial crystallography using nanometer-sized protein crystals that are renewed with each shot is presently among the most popular XFEL applications. Considering the XFEL emission spectrum, crystallography can benefit both from a narrower bandwidth for achieving higher structural resolution and from a broader bandwidth for increasing the number of observable reflections in a single shot [97]. A higher pulse intensity will also benefit crystallography: Diffraction of coherent radiation from a finite-sized crystal produces additional weak diffraction features between the Bragg reflections. A significantly improved signal-to-noise ratio from an increased incoming intensity, reduced background scattering, and improved detector performance may allow the use of these coherent diffraction features to determine the crystallographic phase [98]. Finally, as discussed in the Introduction, photosensitive proteins in crystalline form may be optically pumped and subsequently probed with the diffraction of short-duration X-ray pulses, yielding a molecular movie [99]. Here it should be recalled that since distortions propagate through a molecule with approximately the speed of sound (of order 1 nm/ps), structural changes on the XFEL time scale of 10 fs will be only 0.1 Å, necessitating a high experimental resolution.

Further interesting applications of time-resolved XFEL crystallography are the studies of materials under extreme conditions and of defect dynamics. “Ramp compression” by ns-duration optical laser pulses produces a high-pressure shock wave in a solid, accompanied by only a moderate temperature increase; a record pressure of 560 GPa has been recently achieved in iron [100]. In combination with powder diffraction from synchronized XFEL pulses, we then have the opportunity to investigate the structure of ultrahigh-pressure phases [101]. Ion-implantation into a solid is predicted to initiate a “defect cascade” of vacancy-interstitial clusters, which develops on the nanometer and picosecond length and time scales [102]. With a suitable synchronized ion-implantation pump, diffraction-based methods of defect characterization [103] and diffraction imaging may be used at the XFEL to follow the statistical behavior of such cascades.

The combination of spectroscopy and diffraction in a tandem experiment can dramatically increase the amount of obtainable information. Single-shot spectroscopic techniques, such as dispersively-detected X-ray emission spectroscopy [104] or the “high energy resolution off-resonant spectroscopy” (HEROS) technique [105] are particularly well suited to the XFEL, where a scan over energy is often unrealistic. Optimizing ultrafast photoinduced catalytic reactions at the surface of nanoparticles in solution may be of vital importance to the development of renewable energy sources and time-dependent measurements at an XFEL, both of the crystallography of the nanoparticle (using the pair-distribution function) and of the chemical spectroscopy of the surface reaction, could supply important information not available with other techniques [106].

Bibliography

- [1] R. Neutze, R. Wouts, D. van der Spoel, E. Weckert, and J Hajdu. Potential for biomolecular imaging with femtosecond x-ray pulses. *Nature*, 406:752–757, 2000.
- [2] B. D. Patterson. Crystallography using an x-ray free-electron laser. *Crystallogr. Rev.*, 20:242–294, 2014.
- [3] A. Barty, C. Caleman, A. Aquila, N. Timneanu, L. Lomb, T. A. White, J. Andreasson, D. Arnlund, S. Bajt, T. R. M. Barends, M. Barthelmess, M. J. Bogan, C. Bostedt, J. D. Bozek, R. Coffee, N. Coppola, J. Davidsson, D. P. DePonte, R. B. Doak, T. Ekeberg, V. Elser, S. W. Epp, B. Erk, H. Fleckenstein, L. Foucar, P. Fromme, H. Graafsma, L. Gumprecht, J. Hajdu, C. Y. Hampton, R. Hartmann, A. Hartmann, G. Hauser, H. Hirsemann, P. Holl, M. S. Hunter, L. Johansson, S. Kassemeyer, N. Kimmel, R. A. Kirian, M. Liang, F. R. N. C. Maia, E. Malmerberg, S. Marchesini, A. V. Martin, K. Nass, R. Neutze, C. Reich, D. Rolles, B. Rudek, A. Rudenko, H. Scott, I. Schlichting, J. Schulz, M. Marvin Seibert, R. L. Shoeman, R. G. Sierra, H. Soltau, J. C. H. Spence, F. Stellato, S. Stern, L. Strüder, J. Ullrich, X. Wang, G. Weidenspointner, U. Weierstall, C. B. Wunderer, and H. N. Chapman. Self-terminating diffraction gates femtosecond x-ray nanocrystallography measurements. *Nat. Photogr.*, 6:35–40, 2012.
- [4] S.-K. Son, H. N. Chapman, and R Santra. Multiwavelength anomalous diffraction at high x-ray intensity. *Phys. Rev. Lett.*, 107:218102, 2011.
- [5] F. X. Kärtner, F. Ahr, A.-L. Calendron, H. Çankaya, S. Carbajo, G. Chang, G. Cirmi, K. Dörner, U. Dorda, A. Fallahi, A. Hartin, M. Hemmer, R. Hobbs, Y. Hua, W. R. Huang, R. Letrun, N. Matlis, V. Mazalova, O. D. Mücke, E. Nanni, W. Putnam, K. Ravi, F. Reichert, I. Sarrou, X. Wu, A. Yahaghi, H. Ye, L. Zapata, D. Zhang, C. Zhou, R. J. D. Miller, K. K. Berggren, H. Graafsma, A. Meents, R. W. Assmann, H. N. Chapman, and P. Fromme. Axis: exploring the frontiers in attosecond x-ray science, imaging and spectroscopy. *Nucl. Instrum. Methods Phys. Res., Sect. A*, 829:24–29, 2016.
- [6] B. D. Patterson and R. Abela. Novel opportunities for time-resolved absorption spectroscopy at the x-ray free electron laser. *Phys. Chem. Chem. Phys.*, 12:5647–5652, 2010.
- [7] T. B. van Driel, K. S. Kjær, R. W. Hartsock, A. O. Dohn, T. Harlang, M. Chollet, M. Christensen, W. Gawelda, N. E. Henriksen, J. G. Kim, K. Haldrup, K. H. Kim, H. Ihee, J. Kim, H. Lemke, Z. Sun, V. Sundstro, W. Zhang, D. Zhu, K. B. Møller, M. M. Nielsen, and K. J. Gaffney. Atomistic characterization of the active-site solvation dynamics of a model photocatalyst. *Nat. Commun.*, 7:13678, 2016.
- [8] M. P. M. Dean, Y. Cao, X. Liu, S. Wall, D. Zhu, R. Mankowsky, V. Thampy, X. M. Chen, J. G. Vale, D. Casa, J. Kim, A. H. Said, P. Juhas, R. Alonso-Mori, J. M. Glownia, A. Robert, J. Robinson, M. Sikorski, S. Song, M. Kozina, H. Lemke, L. Patthey, S. Owada, T. Katayama, M. Yabashi, Y. Tanaka, T. Togashi, J. Liu, C. Rayan Serrao, B. J. Kim, L. Huber, C.-L. Chang, D. F. McMorro, M. Först, and J. P. Hill. Ultrafast energy- and momentum-resolved dynamics of magnetic correlations in the photo-doped Mott insulator Sr₂IrO₄. *Nat. Mater.*, 15:601–606, 2016.
- [9] M. Chergui. Ultrafast photophysics of transition metal complexes. *Acc. Chem. Res.*, 48:801–808, 2015.
- [10] Y.-P. Sun, F. Hennies, A. Pietzsch, B. Kennedy, T. Schmitt, V. N. Strocov, J. Andersson, M. Berglund, J.-E. Rubensson, K. Aidas, F. Gel'mukhanov, M. Odelius, and A. Föhlisch. Intramolecular soft modes and intermolecular interactions in liquid acetone. *Phys. Rev. B*, 84:132202, 2011.
- [11] E. Biasin, T. B. van Driel, K. S. Kjær, A. O. Dohn, M. Christensen, T. Harlang, P. Chabera, Y. Liu, J. Uhlig, M. Pápai, Z. Németh, R. Hartsock, W. Liang, J. Zhang, R. Alonso-Mori, M. Chollet, J. M. Glownia, S. Nelson, D. Sokaras, T. A. Assefa, A. Britz, A. Galler, W. Gawelda, C. Bressler, K. J. Gaffney, H. T. Lemke, K. B. Møller, M. M. Nielsen, V. Sundström, G. Vankó, K. Wärnmark,

- S. E. Canton, and K. Haldrup. Femtosecond x-ray scattering study of ultrafast photoinduced structural dynamics in solvated $[\text{Co}(\text{terpy})_2]^{2+}$. *Phys. Rev. Lett.*, 117:013002, 2016.
- [12] S. Hunsche, K. Wienecke, T. Dekorsy, and H. Kurz. Impulsive softening of coherent phonons in tellurium. *Phys. Rev. Lett.*, 75:1815–1818, 1995.
- [13] C. Kittel. *Introduction to Solid State Physics*. Wiley, New York, 1968.
- [14] M. O. Krause. Atomic radiative and radiationless yields for K and L shells. *J. Phys. Chem. Ref. Data*, 8:307–327, 1979.
- [15] M. Ross. Generalized Lindemann melting law. *Phys. Rev.*, 184:233–242, 1969.
- [16] T. E. Stevens, J. Kuhl, and R. Merlin. Coherent phonon generation and the two stimulated Raman tensors. *Phys. Rev. B*, 65:133304, 2002.
- [17] R. Merlin. Generating coherent THz phonons with light pulses. *Solid State Commun.*, 102:207–220, 1997.
- [18] R. W. Boyd. *Nonlinear Optics*. Elsevier, Amsterdam, 2008.
- [19] S. Howard and S. K. Roy. Coherent states of a harmonic oscillator. *Am. J. Phys.*, 55:1109–1117, 1987.
- [20] T. Elsaesser and M. Woerner. Perspective: structural dynamics in condensed matter mapped by femtosecond x-ray diffraction. *J. Chem. Phys.*, 140:020901, 2014.
- [21] P. Beaud, S. L. Johnson, E. Vorobeve, C. J. Milne, A. Caviezel, S. O. Mariager, R. A. De Souza, U. Staub, and G. Ingold. Ultrafast structural dynamics in condensed matter. *Chimia*, 65:308–312, 2011.
- [22] D. K. Seo and R. Hoffmann. What determines the structures of the group 15 elements. *J. Solid State Chem.*, 147:26–37, 1999.
- [23] R. E. Peierls. *Quantum Theory of Solids*. Oxford University Press, London, 2004.
- [24] S. L. Johnson, P. Beaud, E. Vorobeve, C. J. Milne, E. D. Murray, S. Fahy, and G. Ingold. Directly observing squeezed phonon states with femtosecond x-ray diffraction. *Phys. Rev. Lett.*, 102:175503, 2009.
- [25] R. W. Schoenlein, S. Chattopadhyay, H. H. W. Chong, T. E. Glover, P. A. Heimann, C. V. Shank, A. A. Zholents, and M. S. Zolotarev. Generation of femtosecond pulses of synchrotron radiation. *Science*, 287:2237–2240, 2000.
- [26] S. L. Johnson, P. Beaud, E. Vorobeve, C. J. Milne, E. D. Murray, S. Fahy, and G. Ingold. Non-equilibrium phonon dynamics studied by grazing-incidence femtosecond x-ray crystallography. *Acta Crystallogr., Sect. A*, 66:157–167, 2010.
- [27] S. L. Johnson, P. Beaud, E. Möhr-Vorobeve, A. Caviezel, G. Ingold, and C. J. Milne. Direct observation of non-fully-symmetric coherent optical phonons by femtosecond x-ray diffraction. *Phys. Rev. B*, 87:054301, 2013.
- [28] E. D. Murray, D. F. Fritz, J. K. Wahlstrand, S. Fahy, and D. A. Reis. Effect of lattice anharmonicity on high-amplitude phonon dynamics in photoexcited bismuth. *Phys. Rev. B*, 72:060301, 2005.
- [29] E. S. Zijlstra, L. L. Tatarinova, and M. E. Garcia. Laser-induced phonon–phonon interactions in bismuth. *Phys. Rev. B*, 74:220301, 2006.
- [30] E. D. Murray, S. Fahy, D. Prendergast, T. Ogitsu, D. M. Fritz, and D. A. Reis. Phonon dispersion relations and softening in photoexcited bismuth from first principles. *Phys. Rev. B*, 75:184301, 2007.
- [31] E. D. Murray and S. Fahy. First-principles calculation of femtosecond symmetry-breaking atomic forces in photoexcited bismuth. *Phys. Rev. Lett.*, 114:055502, 2015.
- [32] S. Baroni, P. Giannozzi, and A. Testa. Green's-function approach to linear response in solids. *Phys. Rev. Lett.*, 58:1861–1864, 1987.
- [33] P. Tangney and S. Fahy. Calculations of the A_1 phonon frequency in photoexcited tellurium. *Phys. Rev. Lett.*, 82:4340–4343, 1999.

- [34] J. J. Li, J. Chen, D. A. Reis, S. Fahy, and R. Merlin. Optical probing of ultrafast electronic decay in Bi and Sb with slow phonons. *Phys. Rev. Lett.*, 110:047401, 2013.
- [35] H. A. Gersch. Time evolution of minimum uncertainty states of a harmonic oscillator. *Am. J. Phys.*, 60:1024–1030, 1992.
- [36] C. Aslangul. Sudden expansion of a harmonic oscillator. *Am. J. Phys.*, 63:1021–1025, 1995.
- [37] V. V. Dodonov. Nonclassical states in quantum optics: a squeezed review of the first 75 years. *J. Opt. B*, 4:R1–R33, 2002.
- [38] A. Caviezel, U. Staub, S. L. Johnson, S. O. Mariager, E. Möhr-Vorobeva, G. Ingold, C. J. Milne, M. Garganourakis, V. Scagnoli, S. W. Huang, Q. X. Jia, S. W. Cheong, and P. Beaud. Femtosecond dynamics of the structural transition in mixed valence manganites. *Phys. Rev. B*, 86:174105, 2012.
- [39] A. Caviezel, S. O. Mariager, S. L. Johnson, E. Möhr-Vorobeva, S. W. Huang, G. Ingold, U. Staub, C. J. Milne, S. W. Cheong, and P. Beaud. Identification of coherent lattice modulations coupled to charge and orbital order in a manganite. *Phys. Rev. B*, 87:205104, 2012.
- [40] J. N. Clark, L. Beitra, G. Xiong, A. Higginbotham, D. M. Fritz, H. T. Lemke, D. Zhu, M. Chollet, G. J. Williams, M. Messerschmidt, B. Abbey, R. J. Harder, A. M. Korsunsky, J. S. Wark, and I. K. Robinson. Ultrafast three-dimensional imaging of lattice dynamics in individual gold nanocrystals. *Science*, 341:56–59, 2013.
- [41] M. Trigo, M. Fuchs, J. Chen, M. P. Jiang, M. Cammarata, S. Fahy, D. M. Fritz, K. Gaffney, S. Ghimire, A. Higginbotham, S. L. Johnson, M. E. Kozina, J. Larsson, H. Lemke, A. M. Lindenberg, G. Ndabashimiye, F. Quirin, K. Sokolowski-Tinten, C. Uher, G. Wang, J. S. Wark, D. Zhu, and D. A. Reis. Fourier-transform inelastic x-ray scattering from time- and momentum-dependent phonon–phonon correlations. *Nat. Phys.*, 9:790–794, 2013.
- [42] J. R. Heliwell. *Macromolecular Crystallography with Synchrotron Radiation*. Cambridge University Press, Cambridge, 1992.
- [43] D. I. Svergun and M. H. J. Koch. Small-angle scattering studies of biological macromolecules in solution. *Rep. Prog. Phys.*, 66:1735–1782, 2003.
- [44] M. Cammarata, M. Levantino, F. Schotte, P. A. Anfinrud, F. Ewald, J. Choi, A. Cupane, M. Wulff, and H. Ihee. Tracking the structural dynamics of proteins in solution using time-resolved wide-angle x-ray scattering. *Nat. Methods*, 5:881–886, 2008.
- [45] A. Armbrüster, D. I. Svergun, U. Coskun, S. Juliano, S. M. Bailer, and G. Grüber. Structural analysis of the stalk subunit Vma5p of the yeast V-ATPase in solution. *FEBS Lett.*, 570:119–125, 2004.
- [46] Z. Kam. Determination of macromolecular structure in solution by spatial correlation of scattering fluctuations. *Macromolecules*, 10:927–934, 1977.
- [47] P. Debye. *Polar Molecules*. Dover, New York, 1929.
- [48] C. M. Kok and A. Rudin. Relationship between the hydrodynamic radius and the radius of gyration of a polymer in solution. *Makromol. Chem.*, 2:655–659, 1981.
- [49] A. S. Parmar and M. Muschol. Hydration and hydrodynamic interactions of lysozyme: effects of chaotropic versus kosmotropic ions. *Biophys. J.*, 97:590–598, 2009.
- [50] R. A. Kirian. Structure determination through correlated fluctuations in x-ray scattering. *J. Phys. B*, 45:223001, 2012.
- [51] E. Malmerberg, C. A. Kerfeld, and P. H. Zwart. Operational properties of fluctuation x-ray scattering data. *IUCr*, 2:309–316, 2015.
- [52] P. Wochner, C. Gutt, T. Autenrieth, T. Demmer, V. Bugaev, A. D. Ortiz, A. Duri, F. Zontone, G. Grübel, and H. Dosch. X-ray cross correlation analysis uncovers hidden local symmetries in disordered matter. *Proc. Natl. Acad. Sci. USA*, 106:11511–11514, 2009.
- [53] W. H. De Jeu. *Basic X-Ray Scattering for Soft Matter*. Oxford University Press, London, 2016.

- [54] B. Pedrini, A. Menzel, M. Guizar-Sicairos, V. A. Guzenko, S. Gorelick, C. David, B. D. Patterson, and R. Abela. Two-dimensional structure from random multiparticle x-ray scattering images using cross-correlations. *Nat. Commun.*, 4:1647, 2013.
- [55] N. Baddour. Operational and convolution properties of three-dimensional Fourier transforms in spherical polar coordinates. *J. Opt. Soc. Am. A*, 27:2144–2155, 2010.
- [56] D. K. Saldin, V. L. Shneerson, R. Fung, and A. Ourmazd. Structure of isolated biomolecules obtained from ultrashort x-ray pulses: exploiting the symmetry of random orientations. *J. Phys. Condens. Matter*, 21:134014, 2009.
- [57] J. J. Donatelli, P. H. Zwart, and J. A. Sethian. Iterative phasing for fluctuation x-ray scattering. *Proc. Natl. Acad. Sci. USA*, 112:10286–10291, 2015.
- [58] V. Elser. Strategies for processing diffraction data from randomly oriented particles. *Ultramicroscopy*, 111:788–792, 2011.
- [59] J. R. Fienup. Phase retrieval algorithms: a comparison. *Appl. Optim.*, 21:2758–2769, 1982.
- [60] V. Elser. Three-dimensional structure from intensity correlations. *New J. Phys.*, 13:123014, 2011.
- [61] N. Rohringer, D. Ryan, R. A. London, M. Purvis, F. Albert, J. Dunn, J. D. Bozek, C. Bostedt, A. Graf, R. Hill, S. P. Hau-Riege, and J. J. Rocca. Atomic inner-shell X-ray laser at 1.46 nanometres pumped by an X-ray free-electron laser. *Nature*, 481:488–491, 2012.
- [62] M. Beye, S. Schreck, F. Sorgenfrei, C. Trabant, N. Pontius, C. Schüßler-Langeheine, W. Wurth, and A. Föhlisch. Stimulated x-ray emission for materials science. *Nature*, 501:191–194, 2013.
- [63] S. Shwartz, M. Fuchs, J. B. Hastings, Y. Inubushi, T. Ishikawa, T. Katayama, D. A. Reis, T. Sato, K. Tono, M. Yabashi, S. Yudovich, and S. E. Harris. X-ray second harmonic generation. *Phys. Rev. Lett.*, 112:163901, 2014.
- [64] F. Bencivenga, S. Baroni, C. Carbone, M. Chergui, M. B. Danailov, G. De Ninno, M. Kiskinova, L. Raimondi, C. Svetina, and C. Masciovecchio. Nanoscale dynamics by short-wavelength four wave mixing experiments. *New J. Phys.*, 15:123023, 2013.
- [65] M. Altarelli. Resonant x-ray scattering: a theoretical introduction. *Lect. Notes Phys.*, 697:201–242, 2006.
- [66] J.-E. Rubensson. RIXS dynamics for beginners. *J. Electron Spectrosc. Relat. Phenom.*, 110–111:135–151, 2000.
- [67] L. J. P. Ament, M. van Veenendaal, T. P. Devereaux, J. P. Hill, and J. van den Brink. Resonant inelastic x-ray scattering studies of elementary excitations. *Rev. Mod. Phys.*, 83:705–767, 2011.
- [68] S. Tanaka and S. Mukamel. Coherent x-ray Raman spectroscopy: a nonlinear local probe for electronic excitations. *Phys. Rev. Lett.*, 89:043001, 2002.
- [69] S. Mukamel, D. Abramavicius, L. Yang, W. Zhuang, I. V. Schweigert, and D. V. Voronine. Coherent multidimensional optical probes for electron correlations and exciton dynamics: from NMR to X-rays. *Acc. Chem. Res.*, 42:553–562, 2009.
- [70] B. D. Patterson. Resource Letter on Stimulated Inelastic X-Ray Scattering at an XFEL. Technical Report SLAC-TN-10-026, SLAC Tech. Note, 2010.
- [71] D. Lee and A. C. Albrecht. A unified view of Raman, resonance Raman and fluorescence spectroscopy. In R. J. H. Clark and R. E. Hester (Eds.), *Adv. IR and Raman Spect.*, volume 12, pages 179–213. Wiley, New York, 1985.
- [72] J. Mehra and H. Rechenberg. Planck's half-quanta: a history of the concept of zero-point energy. *Found. Phys.*, 29:91–132, 1999.
- [73] W. McCrea. Time, vacuum and cosmos. *Q. J. R. Astron. Soc.*, 27:137–152, 1986.
- [74] C. Weninger, M. Purvis, D. Ryan, R. A. London, J. D. Bozek, C. Bostedt, A. Graf, G. Brown, J. J. Rocca, and N. Rohringer. Stimulated electronic x-ray Raman scattering. *Phys. Rev. Lett.*, 111:233902, 2013.

- [75] A. Föhlisch, S. Schreck, and M. Beye. Implications of stimulated resonant x-ray scattering for spectroscopy, imaging, and diffraction in the regime from soft to hard x-rays. *J. Mod. Opt.*, 62:S41–S51, 2015.
- [76] J. Stöhr and A. Scherz. Creation of x-ray transparency of matter by stimulated elastic forward scattering. *Phys. Rev. Lett.*, 115:107402, 2015.
- [77] T. E. Glover, D. M. Fritz, M. Cammarata, T. K. Allison, S. Coh, J. M. Feldkamp, H. Lemke, D. Zhu, Y. Feng, R. N. Coffee, M. Fuchs, S. Ghimire, J. Chen, S. Shwartz, D. A. Reis, S. E. Harris, and J. B. Hastings. X-ray and optical wave mixing. *Nature*, 488:603–608, 2012.
- [78] B. B. Levine. Electrodynamic bond-charge calculation of nonlinear optical susceptibilities. *Phys. Rev. Lett.*, 22:787–790, 1969.
- [79] P. E. Eisenberger and S. L. McCall. X-ray parametric conversion. *Phys. Rev. Lett.*, 26:684–687, 1971.
- [80] R. P. Feynman, R. B. Leighton, and M. Sands. *The Feynman Lectures on Physics, volume 1, chapter 28*. Addison–Wesley, New York, 1963.
- [81] B. D. Patterson. A simplified approach to synchrotron radiation. *Am. J. Phys.*, 79:1046–1052, 2011.
- [82] J. M. J. Madey. Stimulated emission of bremsstrahlung in a periodic magnetic field. *J. Appl. Phys.*, 42:1906–1910, 1971.
- [83] C. Pellegrini, A. Marinelli, and S. Reiche. The physics of x-ray free-electron lasers. *Rev. Mod. Phys.*, 88:015006, 2016.
- [84] P. Emma, R. Akre, J. Arthur, R. Bionta, C. Bostedt, J. Bozek, A. Brachmann, P. Bucksbaum, R. Coffee, F.-J. Decker, Y. Ding, D. Dowell, S. Edstrom, A. Fisher, J. Frisch, S. Gilevich, J. Hastings, G. Hays, P. Hering, Z. Huang, R. Iverson, H. Loos, M. Messerschmidt, A. Miahnahri, S. Moeller, H-D Nuhn, G. Pile, D. Ratner, J. Rzepiela, D. Schultz, T. Smith, P. Stefan, H. Tompkins, J. Turner, J. Welch, W. White, J. Wu, G. Yocky, and J. Galayda. First lasing and operation of an ångström-wavelength free-electron laser. *Nat. Photon.*, 4:641–647, 2010.
- [85] T. Ishikawa, H. Aoyagi, T. Asaka, Y. Asano, N. Azumi, T. Bizen, H. Ego, K. Fukami, T. Fukui, Y. Furukawa, S. Goto, H. Hanaki, T. Hara, T. Hasegawa, T. Hatsui, A. Higashiya, T. Hirono, N. Hosoda, M. Ishii, T. Inagaki, Y. Inubushi, T. Itoga, Y. Joti, M. Kago, T. Kameshima, H. Kimura, Y. Kiri-hara, A. Kiyomichi, T. Kobayashi, C. Kondo, T. Kudo, H. Maesaka, X. M. Maréchal, T. Masuda, S. Matsubara, T. Matsumoto, T. Matsushita, S. Matsui, M. Nagasono, N. Nariyama, H. Ohashi, T. Ohata, T. Ohshima, S. Ono, Y. Otake, C. Saji, T. Sakurai, T. Sato, K. Sawada, T. Seike, K. Shirasawa, T. Sugimoto, S. Suzuki, S. Takahashi, H. Takebe, K. Takeshita, K. Tamasaku, H. Tanaka, R. Tanaka, T. Tanaka, T. Togashi, K. Togawa, A. Tokuhisa, H. Tomizawa, K. Tono, S. Wu, M. Yabashi, M. Yamaga, A. Yamashita, K. Yanagida, C. Zhang, T. Shintake, H. Kitamura, and N. Kumagai. A compact x-ray free-electron laser emitting in the sub-ångström region. *Nat. Photon.*, 6:540–544, 2012.
- [86] J. Choi, J. Y. Huang, H. S. Kang, M. G. Kim, C. M. Yim, T-Y Le, J. S. Oh, Y. W. Parc, J. H. Park, S. J. Park, I. S. Ko, and Y. J. Kim. Design of the PAL XFEL. *J. Korean Phys. Soc.*, 50:1372–1376, 2007.
- [87] M. Altarelli, R. Brinkmann, M. Chergui, W. Decking, B. Dobson, S. Düsterer, G. Grübel, W. Graeff, H. Graafsma, J. Hajdu, J. Marangos, J. Pflüger, H. Redlin, D. Riley, I. Robinson, J. Rossbach, A. Schwarz, K. Tiedtke, T. Tschentscher, I. Vartanants, H. Wabnitz, H. Weise, R. Wichmann, K. Witte, A. Wolf, M. Wulff, and M. Yurkov. XFEL, the European X-Ray Free-Electron Laser. Technical Report 2006-097, Technical Design Report DESY, Hamburg, 2006.
- [88] B. D. Patterson, P. Beaud, H. H. Braun, C. Dejoie, G. Ingold, C. Milne, L. Patthey, B. Pedrini, J. Szlachentko, and R. Abela. Science opportunities at the SwissFEL X-ray laser. *Chimia*, 68:73–78, 2014.

- [89] V. Ayvazyan, N. Baboi, I. Bohnet, R. Brinkmann, M. Castellano, P. Castro, L. Catani, S. Choroba, A. Cianchi, M. Dohlus, H. T. Edwards, B. Faatz, A. A. Fateev, J. Feldhaus, K. Flöttmann, A. Gamp, T. Garvey, H. Genz, C. Gerth, V. Gretchko, B. Grigoryan, U. Hahn, C. Hessler, K. Honkavaara, M. Hüning, R. Ischebeck, M. Jablonka, T. Kamps, M. Körfer, M. Krassilnikov, J. Krzywinski, M. Liepe, A. Liero, T. Limberg, H. Loos, M. Luong, C. Magne, J. Menzel, P. Michelato, M. Minty, U.-C. Müller, D. Nolle, A. Novokhatski, C. Pagani, F. Peters, J. Pflüger, P. Piot, L. Plucinski, K. Rehlich, I. Reyzl, A. Richter, J. Rossbach, E. L. Saldin, W. Sandner, H. Schlarb, G. Schmidt, P. Schmüser, J. R. Schneider, E. A. Schneidmiller, H.-J. Schreiber, S. Schreiber, D. Sertore, S. Setzer, S. Simrock, R. Sobierajski, B. Sonntag, B. Steeg, F. Stephan, K. P. Sytchev, K. Tiedtke, M. Tonutti, R. Treusch, D. Trines, D. Türke, V. Verzilov, R. Wanzenberg, T. Weiland, H. Weise, M. Wendt, I. Will, S. Wolff, K. Wittenburg, M. V. Yurkov, and K. Zapfe. Generation of GW radiation pulses from a VUV free electron laser operating in the femtosecond regime. *Phys. Rev. Lett.*, 88:104802, 2002.
- [90] E. Allaria, R. Appio, L. Badano, W. A. Barletta, S. Bassanese, S. G. Biedron, A. Borgia, E. Busetto, D. Castronovo, P. Cinquegrana, S. Cleva, D. Cocco, M. Cornacchia, P. Craievich, I. Cudin, G. D'Auria, M. Dal Forno, M. B. Danailov, R. De Monte, G. De Ninno, P. Delgiusto, A. Demidovich, S. Di Mitri, B. Diviacco, A. Fabris, R. Fabris, W. Fawley, M. Ferianis, E. Ferrari, S. Ferry, L. Froehlich, P. Furlan, G. Gaio, F. Gelmetti, L. Giannessi, M. Giannini, R. Gobessi, R. Ivanov, E. Karantzoulis, M. Lonza, A. Lutman, B. Mahieu, M. Milloch, S. V. Milton, M. Musardo, I. Nikolov, S. Noe, F. Parmigiani, G. Penco, M. Petronio, L. Pivetta, M. Predonzani, F. Rossi, L. Rumiz, A. Salom, C. Scafuri, C. Serpico, P. Sigalotti, S. Spampinati, C. Spezzani, M. Svandriik, C. Svetina, S. Tazzari, M. Trovo, R. Umer, A. Vascotto, M. Veronese, R. Visintini, M. Zaccaria, D. Zangrando, and M. Zangrando. Highly coherent and stable pulses from the FERMI seeded free-electron laser in the extreme ultraviolet. *Nat. Photonics*, 6:699–704, 2012.
- [91] Y. Feng, R. Alonso-Mori, T. R. M. Barends, V. D. Blank, S. Botha, M. Chollet, D. S. Damiani, R. B. Doak, J. M. Glowia, J. M. Koglin, H. T. Lemke, M. Messerschmidt, K. Nass, S. Nelson, I. Schlichting, R. L. Shoeman, Yu. V. Shvyd'ko, M. Sikorski, S. Song, S. Stoupin, S. Terentyev, G. J. Williams, D. Zhu, A. Robert, and S. Boutet. Demonstration of simultaneous experiments using thin crystal multiplexing at the Linac Coherent Light Source. *J. Synchrotron Radiat.*, 22:626–633, 2015.
- [92] C. Papp and H.-P. Steinrück. In situ high-resolution x-ray photoelectron spectroscopy – fundamental insights in surface reactions. *Surf. Sci. Rep.*, 68:446–487, 2013.
- [93] J. Amann, W. Berg, V. Blank, F.-J. Decker, Y. Ding, P. Emma, Y. Feng, J. Frisch, D. Fritz, J. Hastings, Z. Huang, J. Krzywinski, R. Lindberg, H. Loos, A. Lutman, H.-D. Nuhn, D. Ratner, J. Rzeplia, D. Shu, Yu. Shvyd'ko, S. Spampinati, S. Stoupin, S. Terentyev, E. Trakhtenberg, D. Walz, J. Welch, J. Wu, A. Zholents, and D. Zhu. Demonstration of self-seeding in a hard-x-ray free-electron laser. *Nat. Photonics*, 6:693–697, 2012.
- [94] D. Ratner, R. Abela, J. Amann, C. Behrens, D. Bohler, G. Bouchard, C. Bostedt, M. Boyes, K. Chow, D. Cocco, F. J. Decker, Y. Ding, C. Eckman, P. Emma, D. Fairley, Y. Feng, C. Field, U. Flechsig, G. Gassner, J. Hastings, P. Heimann, Z. Huang, N. Kelez, J. Krzywinski, H. Loos, A. Lutman, A. Marinelli, G. Marcus, T. Maxwell, P. Montanez, S. Moeller, D. Morton, H. D. Nuhn, N. Rodes, W. Schlotter, S. Serkez, T. Stevens, J. Turner, D. Walz, J. Welch, and J. Wu. Experimental demonstration of a soft x-ray self-seeded free-electron laser. *Phys. Rev. Lett.*, 114:054801, 2015.
- [95] E. Prat, M. Calvi, R. Ganter, S. Reiche, T. Schietinger, and T. Schmidt. Undulator beamline optimization with integrated chicanes for x-ray free-electron-laser facilities. *J. Synchrotron Radiat.*, 23:861–868, 2016.
- [96] D. J. Dunning, B. W. J. McNeil, and N. R. Thompson. Towards zeptosecond-scale pulses from x-ray free electron lasers. *Phys. Proc.*, 52:62–67, 2014.

- [97] C. Dejoie, L. B. McCusker, C. Baerlocher, R. Abela, B. D. Patterson, M. Kunz, and N. Tamura. Using a non-monochromatic microbeam for serial snapshot crystallography. *J. Appl. Crystallogr.*, 46:791–794, 2013.
- [98] J. C. H. Spence, R. A. Kirian, X. Wang, U. Weierstall, K. E. Schmidt, T. White, A. Barty, H. N. Chapman, S. Marchesini, and J. Holton. Phasing of coherent femtosecond x-ray diffraction from size-varying nanocrystals. *Opt. Express*, 19:2866–2873, 2011.
- [99] K. Pande, C. D. M. Hutchison, G. Groenhof, A. Aquila, J. S. Robinson, J. Tenboer, S. Basu, S. Boutet, D. P. DePonte, M. Liang, T. A. White, N. A. Zatsepin, O. Yefanov, D. Morozov, D. Oberthuer, C. Gati, G. Subramanian, D. James, Y. Zhao, J. Koralek, J. Brayshaw, C. Kupitz, C. Conrad, S. Roy-Chowdhury, J. D. Coe, M. Metz, P. L. Xavier, T. D. Grant, J. E. Koglin, G. Ketawala, R. Fromme, V. Šrajer, R. Henning, J. C. H. Spence, A. Ourmazd, P. Schwander, U. Weierstall, M. Frank, P. Fromme, A. Barty, H. N. Chapman, K. Moffat, J. J. van Thor, and M. Schmidt. Femtosecond structural dynamics drives the trans/cis isomerization in photoactive yellow protein. *Science*, 352:725–729, 2016.
- [100] Y. Ping, F. Coppari, D. G. Hicks, B. Yaakobi, D. E. Fratanduono, S. Hamel, J. H. Eggert, J. R. Rygg, R. F. Smith, D. C. Swift, D. G. Braun, T. R. Boehly, and G. W. Collins. Solid iron compressed up to 560 GPa. *Phys. Rev. Lett.*, 111:065501, 2013.
- [101] D. Milathianaki, S. Boutet, G. J. Williams, A. Higginbotham, D. Ratner, A. E. Gleason, M. Messerschmidt, M. M. Seibert, D. C. Swift, P. Hering, J. Robinson, W. E. White, and J. S. Wark. Femtosecond visualization of lattice dynamics in shock-compressed matter. *Science*, 342:220–223, 2013.
- [102] M. Samaras, P. M. Derlet, H. Van Swygenhoven, and M. Victoria. SIA activity during irradiation in nanocrystalline Ni. *J. Nucl. Mater.*, 323:213–219, 2003.
- [103] B. C. Larson. X-ray diffuse scattering near Bragg reflections for the study of clustered defects in crystalline materials. In I. Barabash, G. E. Ice, and E. A. Turchi (Eds.), *Diffuse Scattering and the Fundamental Properties of Materials*, page 139–160. Momentum Press, New York, 2009.
- [104] J. Kern, R. Alonso-Mori, R. Tran, J. Hattne, R. J. Gildea, N. Echols, C. Glöckner, J. Hellmich, H. Laksmono, R. G. Sierra, B. Lassalle-Kaiser, S. Koroidov, A. Lampe, G. Han, S. Gul, D. Difiore, D. Milathianaki, A. R. Fry, A. Miahnahri, D. W. Schafer, M. Messerschmidt, M. M. Seibert, J. E. Koglin, D. Sokaras, T. C. Weng, J. Sellberg, M. J. Latimer, R. W. Grosse-Kunstleve, P. H. Zwart, W. E. White, P. Glatzel, P. D. Adams, M. J. Bogan, G. J. Williams, S. Boutet, J. Messinger, A. Zouni, N. K. Sauter, V. K. Yachandra, U. Bergmann, and J. Yano. Simultaneous femtosecond x-ray spectroscopy and diffraction of photosystem II at room temperature. *Science*, 340:491–495, 2013.
- [105] J. Szlachetko, M. Nachtigal, J. Sa, J-C Dousse, J. Hozzowska, E. Kleymenov, M. Janousch, O. V. Safonova, C. König, and J. A. van Bokhoven. High energy resolution off-resonant spectroscopy at sub-second time resolution: (Pt(acac)₂) decomposition. *Chem. Commun.*, 48:10898–10900, 2012.
- [106] M. A. Newton, K. W. Chapman, D. Thompsett, and P. J. Chupas. Chasing changing nanoparticles with time resolved pair distribution function methods. *J. Am. Chem. Soc.*, 134:5036–5039, 2012.

Index

κ -formalism 6

Adler–Wiser formula 109

APW method 79

aspherical atomic form factor 7

asymmetric photo-excitation 230

atomic form factor 5, 17, 18

atomic structure 67

autocorrelation function of the time-averaged

electron density 38

average atomic form factor 40

average electron density 40

BaBiO₃

– atomic structure 89

– band structure 91

– density of states (DOS) 93

– difference electron density 92

– electronic structure 89

– partial charges 93

band structure

– of InSb 82

Born–Oppenheimer approximation 68

Bragg’s law 21

Bravais lattice

– centering operations 29

– reflection conditions 29

chemical short range order 46

coherence length 39

coherent diffraction 39

coherent phonon generation 225

conical intersections 119

conventional exchange-correlation functionals

72

correlated X-ray scattering 237

correlated X-ray scattering on static molecules in

solution 235

Coulomb interaction 69

Debye scattering equation 150

Debye–Waller factor 5, 31, 148

deformation electron density 8

density autocorrelation function 237

density functional theory 69

density of states

– of gold 83

DFT

– band structure 81

– basis sets 77

– codes 77

– density of states (DOS) 81

– difference density 87

– electric field gradient 86

– functionals 71

– magnetism 86

– relativistic effects 80

– structure optimization 84

dielectric

– dielectric constant 113

– dielectric function 112

– macroscopic dielectric function 112

– microscopic dielectric function 112

differential cross section 16

diffract-before-destroy 221

diffraction pattern

– of crystal with disorder 157

– of crystal with distorted domains 155

– of crystal with phonons 157

– of excited crystal 155

– of undistorted crystal 155

diffuse background intensity 32

diffuse scattering

– extended three-dimensional defects 48

– Huang 46

– planar defects 47

– point defects 47

– theory 43

– thermal 46

disorder

– displacement 45

– substitutional 44

disordered structures 42

– types 42

dynamic atomic electron density 147

dynamic structure factor 125

– of silicon 126

– of YBCO 129

elastic X-ray scattering 15

electric field gradient

– in YBCO 87

electron density 4, 69

- electron density
 - N-representable 71
 - of osmium 81
 - time-dependent 148
- electron energy-loss spectra
 - of graphene 124
 - of graphite 123
 - of silicon 120
- electronic density
 - time-dependent 102
- electronic excitations 101
- electronically excited crystals 206
- energy-loss function 113
 - of graphene 124
 - of silicon 121
- Ewald sphere 22
- exchange-correlation
 - exchange-correlation kernel 111
- exchange-correlation energy 69
- exchange-correlation kernel
 - adiabatic local-density approximation 111
 - random-phase approximation 111
- exchange-correlation potential 106
- excitation
 - excitation energies 110
 - neutral excitation energies 115
- excited electrons and holes 224

- Fourier transform of the electron density 18
- Fourier transform
 - properties 62
- Friedel's law 26
- frozen core approximation 78

- generalized four-dimensional Patterson function
 - 37
- generalized gradient approximation (GGA)
 - meta-GGA 72
- glide planes
 - glide components 30
 - reflection conditions 30
- ground state 154

- Hansen–Coppens model 6
- Hartree potential 106
- Hartree–Fock (HF) method 68
- Hohenberg and Kohn theorem 69
- Huang scattering 46
- Hubbard U 72
- hybrid functionals 72

- independent atom model (IAM) 4, 146
- inelastic stimulated Raman scattering 225
- inelastic X-ray scattering spectra
 - of silicon 126
 - of YBCO 129
- inelastic X-ray scattering spectroscopy 125
- intensity 16
- interaction between X-rays and matter 14
- interference function 153
- ionization potential (IP) 73

- Janak's theorem 74

- kernel
 - Bethe–Salpeter kernel 137
 - exchange-correlation kernel 109
 - long-range contribution 134
 - Nanoquanta kernel 136
- kinetic energy 69
- Kohn–Sham
 - Kohn–Sham equations 70
 - Kohn–Sham fictitious noninteracting system 110
 - Kohn–Sham orbitals 70
 - Kohn–Sham polarizability 109
 - Kohn–Sham scheme 70
 - potential 106
 - scheme 106
 - TDDFT Kohn–Sham equations 106
 - time-dependent Kohn–Sham equations 106
 - wavefunctions 106
- Koopmans theorem 73

- LAPW-method 78
- laser-driven plasma table-top sources 163
- lattice factor 20
- Laue classes 28
- linearized-augmented-plane-wave (LAPW) 78
- local density approximation (LDA) 72
- local-field effects 113

- many-body perturbation theory 76
- mean square displacement 32
- model-independent analysis of CXS data 238
- model-independent analysis of SAXS data 237
- molecular form factor 19
- multipolar model 6

- no local-field effects (NLF) 113
- nonlinear X-ray scattering 245
 - stimulated Raman scattering 246
 - X-ray/optical sum-frequency generation 249
- occupancy 41
- one-dimensional quantum harmonic oscillator 233
- one-point correlation function 239
- optical absorption 113
 - in silicon 131, 135
 - in argon 133, 137
 - of pristine cellulose 130
- orbital energies
 - of osmium 81
- pair density distribution function 238
- pair distribution function 49
 - 3D 57
 - analysis and refinement 55
 - data treatment 55
 - experiments 53
 - reduced 49
 - theory 49
 - ZnSe nanoparticles 58
- Patterson function 35, 237
- photo-Wilson plot 159
- photodifference map 172
- photodissociation of I_3^- 175
- photoexcited phonon dynamics 229
- polarizability 108
- probability density function 5, 31, 147
- projector-augmented-plane-wave (PAW) 78
- pump-probe approach 160
- pump-probe experiment 160
- reciprocal space 21
- Runge–Gross theorem 103
 - dependence on the initial state 105
 - limits 105
- satellite reflection 32
- scattered amplitude 19
 - of atom 18
 - of crystal 20
- scattered intensity 147
- scattering vector 17
- scissor operator 136
- self-amplified spontaneous emission 257
- shape descriptor 241
- single-electron picture
 - excitation spectra 94
 - optics 94
- single-particle functions 240
- single-particle scattering function 243
- size effect 46
- squeezed-state coherent phonons 231
- static atomic density 5
- static deformation electron density 9
- structure factor 4, 23
- structure factor
 - of excited state 154
- symmetry-causality paradox 107
- systematic extinctions 27
- TDDFT
 - acetylene molecule 117
 - codes 113
 - electron dynamics 117
 - exchange-correlation effects 125
 - He-atom 114
 - ion dynamics 117
 - local-field effects 120
 - linear response 107
- thermal diffuse scattering 46
- three-point correlation function 239
- time-dependent electron density distributions 206
- time-resolved experiment
 - 2D correlated X-ray scattering 243
 - general scheme 149
 - small-angle X-ray scattering (SAXS) 236
 - under electric field 196
 - X-ray/optical sum-frequency generation 250
 - X-ray pump-probe 160, 162
 - X-ray solution scattering 151
- time-resolved scattering
 - blue light receptor PYP 177
 - crystalline materials 153
 - electron by Electric field 166
 - excitation by pressure pulses 167
 - experimental methods 159
 - fast solution mixing 168
 - long-range ordering 202
 - mode-selective vibrational excitation 169
 - model case studies 169
 - nanoscale systems 191
 - noncrystalline samples 150

- optical excitation 165
- photoexcited coherent phonons 224
- photoinduced spin transitions 186
- photostationary state 169
- serial crystallography at XFEL facilities 185
- under applied external electric field 193
- X-ray detectors 164
- time-resolved X-ray diffraction photoexcited coherent phonons 224
- time-resolved X-ray solution scattering 173
- total energy
 - of osmium 84
- transient 3D electron density distribution 206
- two-point correlation function 239
- unit cell density 5
- unit cell scattering factor 153
- unit cell structure factor 20
- v-representability problem 105
- van der Waals forces 72
- X-ray scattering
 - elastic by single electron 16
- X-ray scattering formalism
 - time-resolved 146
- X-ray sources 161
- XFEL facilities 258
- XFEL microbunch instability 254
- XFEL operating principle 252